Pharmaceutical Crystallization Design Using Micromixers, Multiphase Flow, and Controlled Dynamic Operations

by

Mo Jiang

B.S. Biology, Tsinghua University, 2006
M.S. Chemical Engineering, University of Illinois at Urbana-Champaign, 2008

SUBMITTED TO THE DEPARTMENT OF CHEMICAL ENGINEERING IN PARTIAL FULFILLMENT OF THE REQUIREMENTS FOR THE DEGREE OF

Doctor of Philosophy
at the
MASSACHUSETTS INSTITUTE OF TECHNOLOGY

June 2015

Signature of Author: _____
Department of Chemical Engineering
March 20, 2015

Certified by: _____
Richard D. Braatz
Edwin R. Gilliland Professor of Chemical Engineering
Thesis Supervisor

Accepted by: _____
Richard D. Braatz
Edwin R. Gilliland Professor of Chemical Engineering
Chairman, Committee for Graduate Students

Pharmaceutical Crystallization Design Using Micromixers, Multiphase Flow, and Controlled Dynamic Operations

by

Mo Jiang

Submitted to the Department of Chemical Engineering on March 20, 2015 in Partial Fulfillment of the Requirements for the Degree of Doctor of Philosophy in Chemical Engineering

ABSTRACT

Crystallization is a key unit operation in the pharmaceutical industry. Control of crystallization processes can be challenging when undesirable phenomena such as particle attrition and breakage occur. This thesis describes the controlled crystallization of pharmaceuticals and amino acids for more efficient manufacturing processes and better efficacy of products. Crystallization equipment is designed so that (1) the undesirable phenomena do not occur at all, and/or (2) the phenomena that do occur are carefully controlled.

One key strategy is to exploit dual-impinging jets and multiphase flow to decouple nucleation and growth so that they can be individually controlled. Various configurations of micromixers were designed to provide controlled nucleation. Based on the dual-impinging-jet (DIJ) configuration, a physical explanation was provided for the discovery that a cooling micromixer can generate small crystals of uniform size and shape. An alternative design replaces the micromixing with the application of ultrasonication to decouple nucleation and flow rates. Based on these nucleation methods, a novel continuous crystallizer is designed where the slurry flow is combined with an air flow to induce a multiphase hydrodynamic instability that spontaneously generates slugs where the crystals continue to grow. These slugs are well-mixed without having the mixing blades in traditional crystallizer designs that induce undesirable uncontrolled crystallization phenomena.

Another key strategy is to increase the degrees of freedom in the dynamic operation of the crystallizers. In the slug-flow continuous crystallizer, extra degrees of freedom for control of the crystal growth are created by spatially varying the temperature profile along the tube. In a semi-continuous crystallizer configuration, continuous seeding using a DIJ mixer is combined with growth rate control in a stirred tank to experimentally demonstrate the manufacture of uniform-sized crystals. In addition, temperature-cycling experiments are designed in batch crystallizers to substantially change crystal shape with only a small number of cycles.

Experimental validation confirms that the proposed crystallizer designs reduce production time and equipment cost by orders of magnitude while suppressing secondary nucleation, attrition,

and aggregation/agglomeration—dominant but undesired phenomena that worsen the ability to control the properties of crystals produced by most existing crystallizer designs.

Thesis Supervisor:

Prof. Richard D. Braatz
Title: Edwin R. Gilliland Professor of Chemical Engineering

Thesis Committee Members:

Prof. Allan S. Myerson
Title: Professor of the Practice of Chemical Engineering

Prof. Bernhardt L. Trout
Title: Raymond F. Baddour, ScD, (1949) Professor of Chemical Engineering

ACKNOWLEDGEMENTS

I feel lucky that I chose Prof. Richard D. Braatz as my Ph.D. advisor. He not only transfers knowledge of process control, systems engineering, and particulate processes to us, but also cultivates self-motivation through patient mentoring and conveying a systems perspective that will aid our future success almost anywhere.

For beginning students, he spares no effort in encouraging their research and career interests, together with providing detailed knowledge and technical support. When I joined the group, Prof. Braatz gave a warmup mini-project to implement industrial-grade data-archiving software for a laboratory apparatus. To work properly, the project involved a large number of precise steps that had to be correct for the implementation to work. He decomposed the problem and explained each step in detail. Although unfamiliar with computer systems administration and computer-equipment communication (my background was experimental biology), I was able to accomplish the project goal within a week, after talking to experts and experimenting with frequent feedback from Prof. Braatz. He helped build up confidence in a natural way, not by words, but from gaining experience.

After Prof. Braatz provided a smooth and efficient start on research, I became more deeply involved in, fond of, and knowledgeable in my research area. When I designed a novel continuous-flow crystallizer that provided an unprecedented degree of control of the crystal size distribution, all previous knowledge of semi-continuous crystallizers and relevant analysis methods readily came to mind. Although most students mature to the point of becoming very independent in carrying out their research in their later years, we know that he is always there, happy to spend time in face-to-face discussion of data analysis and career options.

I also thank other committee members, Profs. Allan S. Myerson and Bernhardt L. Trout, and other professors for their valuable input and helpful interactions over the course of my thesis work. For example, a thesis committee member pointed out that it was not just enough to develop a new crystallization technology, and pushed the importance of precisely characterizing the class of crystallizations that would benefit from the technology (in the particular case, in question, the answer was "for fast-growing materials in the final crystallization step"). Through interactive teaching, Prof. Myerson also provided a solid systematic knowledge of pharmaceutical engineering and crystallization technology. The inspiration, guidance, and recommendations of my thesis committee members no doubt contributed to my eventual delivery of invited talks at more than a half dozen universities and conferences while I have been a Ph.D. student.

I thank Braatz Group members, past and present, especially: Dr. Mitsuko Fujiwara for the patient instruction and guidance for concentration control data collection experiments and data analysis coding; Dr. J. Carl Pirkle, Jr., Michael L. Rasche, Min Hao Wong, Zhilong Zhu, Mark C. Molaro, Dr. Xiaoxiang Zhu, and Dr. Jeremy VanAntwerp for helpful technical contribution and discussion; and Wenqing Tian, Lucas Foguth, Dr. Jingcai Cheng, Dr. Lixian Zhang, Dr. Eranda Harinath, Dr. Ali Mesbah, Dr. Ashlee N. Ford Versypt, Dr. Kwang-Ki Kim, Jang Hong, Benben Jiang, and Dr. Davide M. Raimondo for their support and company over all these years.

I also thank Yuran Wang, Yunzhi Gao, Chen Gu, Guolong Su, Jianjian Wang, Zeyuan Zhu, Dr. Jun Fu, Dr. Haitao Zhang, Dr. Keith Chadwick, Li Tan, Dr. Jun Xu, Mark Kebler, Dr. Patrick Heider, Christopher Testa, Andrew Ryan, Stephen K Wetzel, Ron Wiken, Wenzhen Yuan, Xiaodan Jia, Dr. Zhenya Zhu, Dr. Ying Diao, Dr. Liang Su, Brandon Reizman, Dr. Fei Guo, and Mike Healy for technical support and helpful discussions on experimental technique and coding,

and everyone else who have helped me in one way or another for my thesis work. All of these individuals went beyond the responsibilities of their jobs in their interactions with others.

My funding resources are acknowledged for financial support, namely, OSIsoft LLC, Abbott Laboratories (now AbbVie), Novartis Pharmaceuticals, and Takeda Pharmaceuticals.

Last but not least, I take this opportunity to express my gratitude to my family and friends who have supported me throughout my Ph.D., at the beginning of a challenging but wonderful journey.

TABLE OF CONTENTS

LIST OF FIGURES

LIST OF TABLES

1. INTRODUCTION TO CSD AND SHAPE CONTROL

Crystallization is a key unit operation in the pharmaceutical industry. The crystal size distribution (CSD) and shape can affect the efficacy of drug products (such as the amount of drug reaching the lungs from a nasal spray) as well as the efficiency of downstream processes such as filtration and milling. CSD control can be challenging when multiple simultaneous crystallization phenomena occur, such as growth, particle attrition and breakage, agglomeration, and primary and secondary heterogeneous nucleation.

After an introduction to the control of CSD (Section 1.1, details in Chapter 2), this thesis demonstrates the enhanced control of crystal size distribution and shape in the batch, semi-continuous, and continuous pharmaceutical crystallizers (Sections 1.2-1.4, details in Chapters 3-7). Each project started from the perspective of the whole system, whose configuration was designed based on requirements for the final product quality (Quality-by-Design). The system was then decomposed into subsystems that were understood in detail before adding more functionality and complexity.

1.1. Introduction to control of CSD with existing crystallizers

Successful Quality by Design (QbD) requires good comprehension and implementation of robust automatic process control. Chapter 2 discusses the role and application of control in QbD, with a primary emphasis on the crystallization of pharmaceuticals. Some successful industrial applications of automatic process control strategies are reviewed, as well as alternative control strategies that have been proposed for providing various tradeoffs between model fidelity, sensor inaccuracies, and robust performance. These strategies include feedback controllers based on solution concentration measurement via ATR-FTIR spectroscopy as well as measurements of particles in crystallizers based on in-process laser backscattering. The use of models for

crystallization kinetics to improve crystallizer designs, increase product quality, and reduce scale-up risk is also discussed, which is followed by simulation and experimental results that demonstrate how a target crystal size distribution can be obtained by combining continuous seeding with controlled crystal growth. [8] More detailed analysis of CSD control in advanced crystallizers is described in Chapters 3-7.

1.2. Enhanced control of crystal shape using well-designed temperature cycling

The evolution of particle shape is an important consideration in many industrial crystallization processes. Bad crystal shapes can cause operational problems downstream from the crystallizer (e.g., filtration, granulation, tableting). To monitor and optimize the shape of crystals, population balance models have been used which require the estimation of 2D growth and dissolution rates. Most past studies that estimated kinetics along multiple crystal axes in mixed-tank crystallizers were based on frequently sampling the slurry during crystallization, or employing imaging technology that only applies for low crystal number densities [9][10]. In contrast, Chapter 3 designs a single experiment (with temperature cycling) that substantially changes crystal shape with only a small number of cycles and allows the estimation of kinetic parameters in a two-dimensional PBM demonstrated to predict the crystal size and shape in another temperature cycling experiment.

The growth and dissolution of monosodium glutamate crystals of varying shapes are monitored using in-process Attenuated Total Reflection-Fourier Transform Infrared Spectroscopy, Focused Beam Reflectance Measurement (FBRM), Particle Vision and Measurement (PVM), and off-line optical microscopy. The growth and dissolution kinetics are estimated in a multidimensional population balance model (PBM) based on solute concentration and crystal dimension measurements. This model fitted the experimental data with a limited

number of parameters of small uncertainty. In addition, with the estimated kinetic parameters, the model was used to predict the crystal size and shape distribution in a different temperature-cycling experiment. In contrast to previous studies that have estimated kinetics along multiple crystal axes in mixed-tank crystallizers, this study implements dissolution terms in the multidimensional population balance model along multiple axes [11].

1.3. Enhanced control of CSD using a semi-continuous crystallizer design

Control of the size distribution (not necessarily the narrowest) of crystals is desired in the pharmaceutical industry to meet bioavailability requirements. The controllability of CSD is limited in industrial batch crystallizations, where seed crystals are added near the start of the batch. A theoretical study [3] predicted that the controllability of the crystal size distribution could be greatly increased by employing continuous seeding, where crystals are continuously fed to a well-mixed tank crystallizer at any time during the batch. Since uniform CSD is very difficult to achieve with batch cooling crystallization, this distribution was the target in Chapter 4 of an experimental demonstration of the crystallizer configuration with continuous seeding.

To experimentally demonstrate the enhanced control of CSD in a semi-continuous crystallizer, I combined continuous crystal seeding from a dual impinging jet (DIJ) mixer with a batch crystallizer operating under feedback control of the crystal growth rate. To generate seed crystals with a narrow size distribution, I developed a DIJ configuration that combines hot and cold saturated solutions. These seed crystals were further grown to a desired size in the stirred tank with suppressed nucleation that was instrumented with attenuated total reflection-Fourier transform infrared (ATR-FTIR) spectroscopy and FBRM. An automated system that followed preset supersaturation profiles by using feedback control was based on the construction of calibration models and the measurement of solubility and metastable limit [4].

Crystallization within DIJ mixers is useful, but not expected to be applicable to all combinations for all conditions, especially because the average supersaturation for a cooling DIJ mixer is usually not very high. Currently, whether any particular compound/solvent combination is suitable for use in a DIJ mixer has to be assessed by trial-and-error experimentation aided with experience. It would be useful at the early stage of research and development to be able to quickly identify compound-solvent combinations that cannot nucleate crystals within DIJ mixers, based on their physicochemical properties.

Chapter 5 develops a mathematical model for crystallization in a DIJ mixer that combines thermodynamics, kinetics, fluid dynamics, and heat and mass transfer [12]. The mathematical model is in the form of partial differential equations, simplified by exploiting symmetries and employing scaling analysis to generate one-dimensional analytical solutions for physical insights. Two-dimensional energy and molar balances are solved using COMSOL input with an analytical solution for the velocity field, to generate spatial distributions of temperature, concentration, and supersaturation near the hot-cold interface within a cooling DIJ mixer. The mathematical model provides guidance for modifying solvent and jet flow rates to increase the likelihood of continuously generating seed by mixing hot and cold saturated solutions in a DIJ mixer.

1.4. Enhanced control of CSD using a novel continuous-flow crystallizer design

Compared to batch and semibatch crystallizers, continuous-flow crystallizers have the potential for higher reproducibility, process efficiency, and flexibility, as well as lower capital and production cost. For higher process efficiency and reproducibility, many new continuous-flow crystallizer designs have been developed in recent years, including continuous oscillatory baffled crystallizers and continuous-flow tubular crystallizers. However, most of these

crystallizers are not specifically designed to provide many degrees of freedom for the control of crystal shape, size distribution, and polymorphic identity in the presence of process disturbances and variations in crystallization kinetics due to possible changes in the contaminant profile in the feed streams. Chapters 6 and 7 design a continuous-flow crystallizer that achieves maximum yield and controlled CSD with continuous cooling crystallization in the presence of process disturbances and variations in kinetics.

In order to achieve both maximum crystal yield and CSD control with high spatial and temporal uniformities, a novel continuous slug-flow crystallizer is operated in a hydrodynamically stable flow regime in which slugs of slurry are separated by slugs of gas in a tube. The residence time distribution of the slugs is equivalent to a set of small completely segregated batch reactors moving from the feed location to the exit. Each slug is well mixed through nondestructive liquid recirculation, rather than by a regular solid mixer, to reduce crystal attrition. Past knowledge of batch crystallizers is applied to continuously generate high-quality drug crystals, which enhanced the control of product CSD with properly tuned parameters within the design space. Unlike most other continuous-flow crystallizers that employ slugs, the proposed slug-flow crystallizer does not require a solvent/solvent separation operation afterwards, which further improves crystal product purity and process energy efficiency [7].

The crystallizer is designed so that nucleation and growth processes are decoupled to enhance the individual control of each phenomenon. Stable slugs will be generated with approximately uniform target sizes by mixing slurry and gas streams at proper flow rates for the specific mixer configuration in use. Nucleation methods are developed and implemented before slug formation (e.g., radial/coaxial mixers [7] and ultrasonication [13]) to generate seeds continuously with a controlled number density. After slug formation, an optimal cooling profile

can be applied to control the crystal growth rate, with temperature zones set up using peristaltic pumps and Proportional-Integral (PI) controllers.

2. THE ROLE OF AUTOMATIC PROCESS CONTROL IN QUALITY BY DESIGN

2.1. Introduction

The U.S. Food and Drug Administration defines Quality by Design (QbD) as "a systematic approach to pharmaceutical development that begins with predefined objectives and emphasizes product and process understanding and process control, based on sound science and quality risk management."[14] Pharmaceutical development includes the following elements: [14]

- Defining the target product profile while taking into account quality, safety, and efficacy of the drug compound. This profile considers the method of drug delivery, the form of the drug compound when delivered, the bioavailability of the drug once delivered, the dosage of the drug compound to maximize therapeutic benefits while minimizing side effects, and the stability of the product.
- Identifying potential critical quality attributes of the drug product. All of the drug product characteristics that have an impact on product quality must be determined so these attributes can be studied and controlled.
- Determining the critical quality attributes of the components (e.g., drug compound, excipients) needed for the drug product to be of desired quality.
- Selecting a process capable of manufacturing the drug product and its components;
- Identifying a strategy for controlling the process to reliably achieve the target product profile.

Most pharmaceuticals manufacturing processes include at least one crystallizer for purification of intermediates or the final active pharmaceutical ingredient (Figure 2.1), and usually for producing crystals to be compacted with excipients to form a tablet. The bioavailability and tablet stability depend on the crystal structure, size, and shape distribution

(Figure 2.2). Typical objectives in the operation of intermediate and final crystallizations are to maximize chemical purity and yield and to produce crystals that do not cause operations problems in downstream processing. An important consideration in many crystallization concerns polymorphism, which occurs when a chemical compound can adopt different crystal structures. Polymorphs are the same molecular species but have different packing of molecules within the crystal structure (see Figure 2.3 for an example) [15], [16]. Another common occurrence is solvatomorphism or pseudo-polymorphism, which is when varying amounts of solvent molecules can be incorporated within the crystal structure, to form crystal solvates of different composition. Different polymorphs or solvatomorphs can have very different physical properties (e.g., solubility, bioavailability, shelf-life), and hence very different efficacy. The control of crystal polymorphism is required for the manufacturing process to achieve the QbD objectives and for regulatory compliance. The most stable polymorph is typically achievable with sufficient process time and suitable crystallization conditions. Metastable polymorphs are more challenging to manufacture reliably with a key challenge being to prevent transformation to more stable forms.

A QbD approach for the development of pharmaceutical crystallization processes involves two consecutive steps:

1. Design of a target crystal size distribution (CSD) and polymorphic form based on bioavailability and delivery needs (Figure 2.4);
2. Design a manufacturing-scale crystallizer to produce the target CSD based on simulation models that account for all potential scale-up issues such as non-ideal mixing (Figure 2.5) [17].

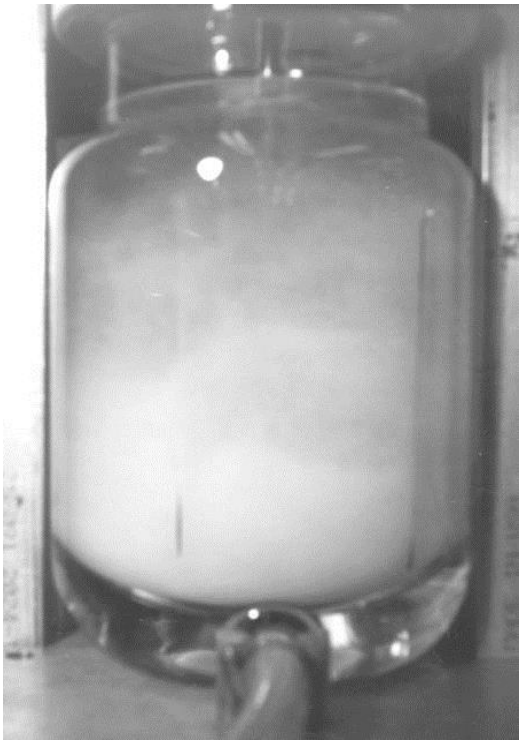

Figure 2.1. A photograph of a bench-scale crystallizer with a jacket for temperature control. Supersaturation in pharmaceutical crystallizers is usually induced by cooling and/or antisolvent addition.

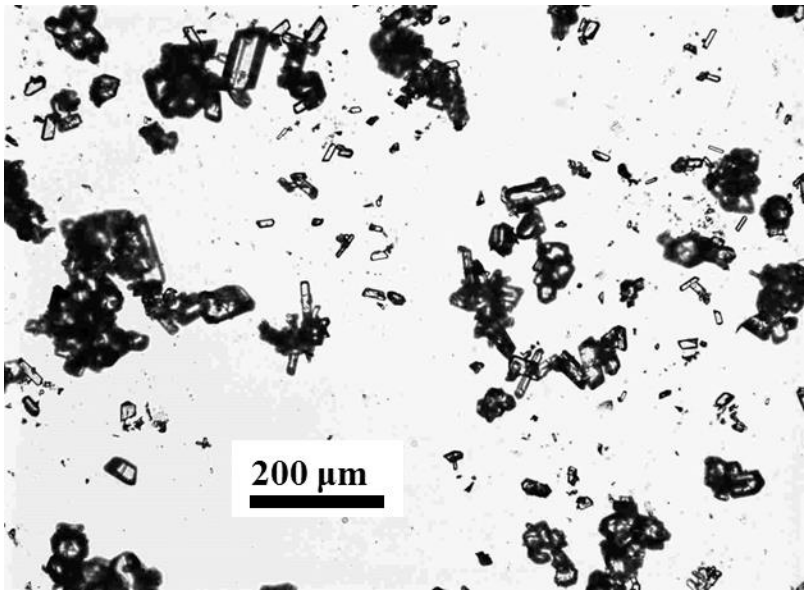

Figure 2.2. A photograph of some pharmaceutical crystals produced from a crystallizer that was inadequately controlled, showing potential variations in size and shape.

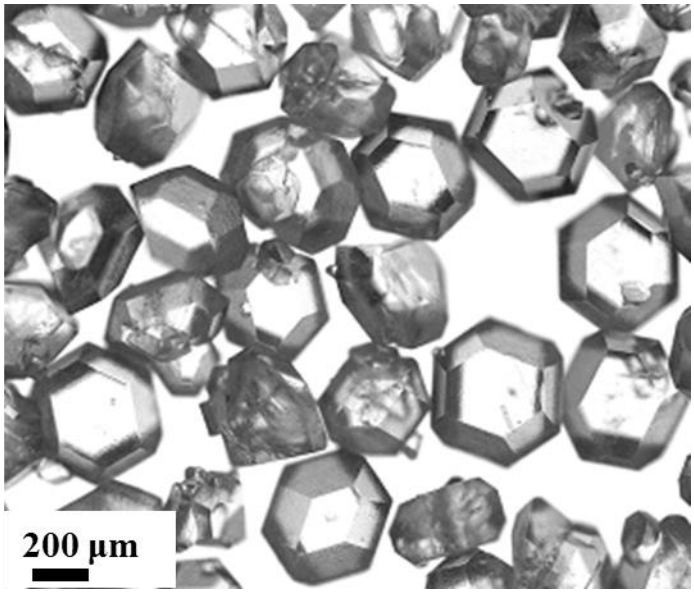

(a)

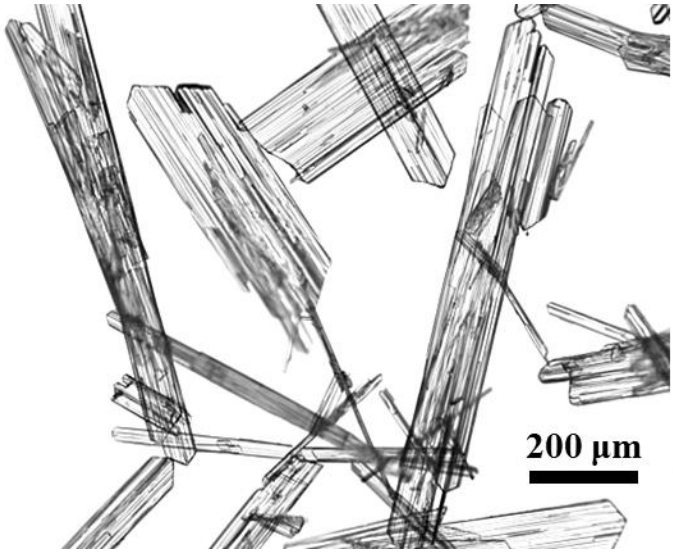

(b)

Figure 2.3. (a) α polymorph (metastable form, prismatic shape) and (b) β polymorph (stable form, needlelike platelet shape) crystals of L-glutamic acid. The two polymorphs show different crystal morphologies.

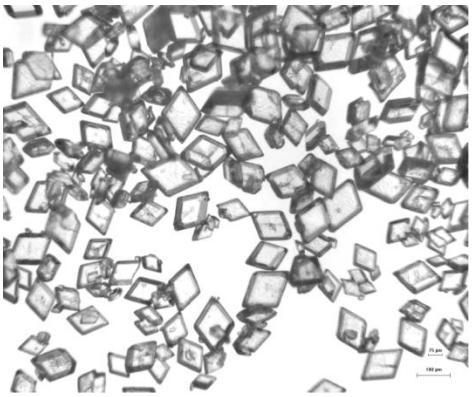

Figure 2.4. An example of a potential target crystal size distribution and polymorphic form.

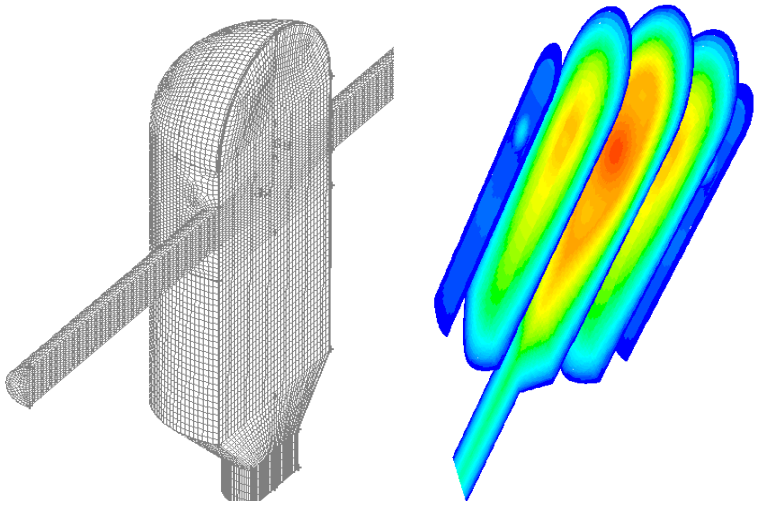

Figure 2.5. Example simulation results of the spatial distribution of turbulent Reynolds number in a confined dual impinging jet mixer. Such mixers can be used to generate sub 10-micron crystals for many solute/solvent systems.

Many crystallizer designs for Step 2 are based on the creation of a highly intense mixing zone operating at high supersaturation to produce crystal seeds for subsequent growth [3], [18]–[24]. Step 1 requires first finding all of the polymorphs by crystallizing the pharmaceutical compounds in many different solvents with many different supersaturation methods and trajectories, and the identification of crystallization kinetics from the small quantity of

pharmaceutical compounds available for process development. Such investigations can be facilitated by high-throughput microfluidics platforms that can provide information on polymorphism, solubility, and kinetics even at very high supersaturation difficult to achieve in other systems (Figures 2.6 and 2.7) [1], [25]–[33]. A more advanced version of the high-throughput platform in Figures 2.6 and 2.7 allows information to be collected in parallel using chips comprised of 144 wells (each 30 nanoliters in volume) with crystal detection performed using optical spectroscopy (Figure 2.8). Further developed versions of these microfluidic array chips allow for in situ identification of polymorph identity via Raman spectroscopy or X-ray diffraction.

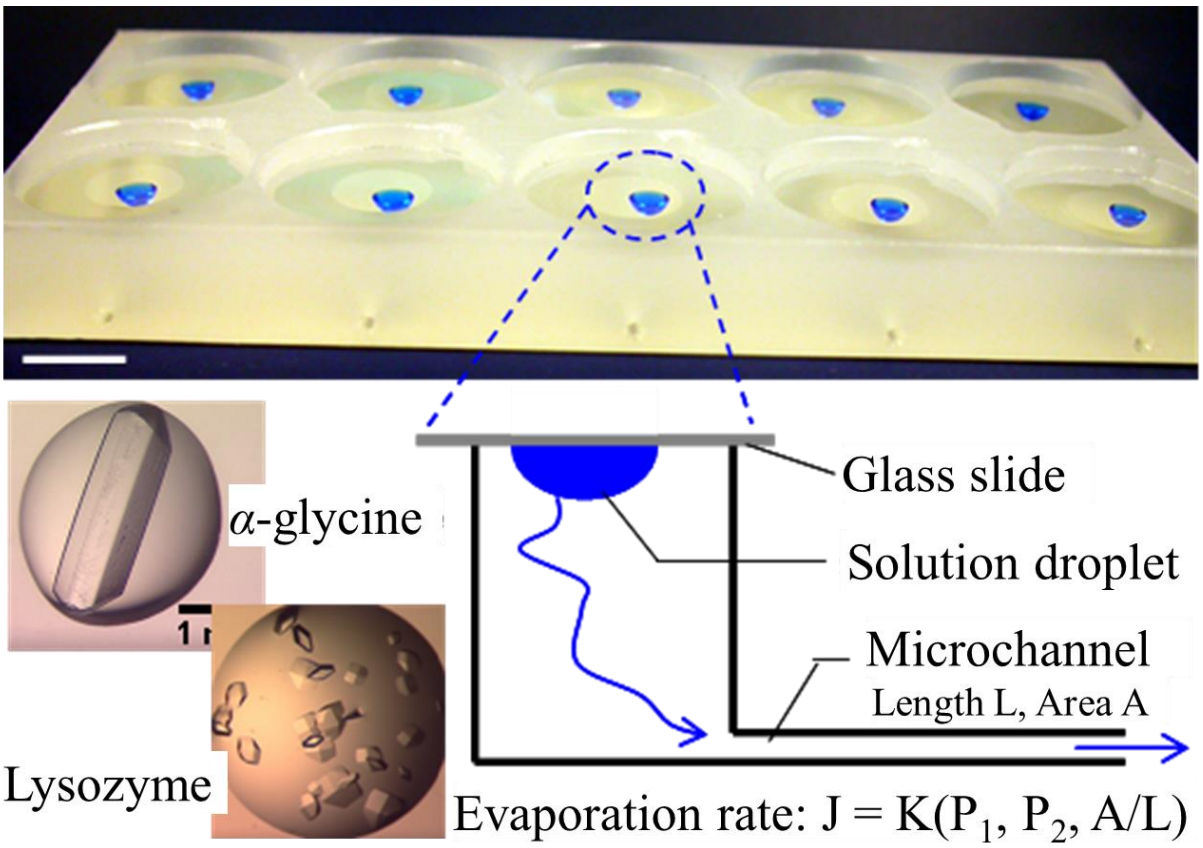

Figure 2.6. A microfluidic platform that uses evaporation to generate supersaturation in 2–10 microliter-sized droplets in microwells. The rate of evaporation (*J*), and thereby the

supersaturation profile, is set by the dimensions of the channel (cross-sectional area *A* and length *L*) that connects the well with the ambient environment.

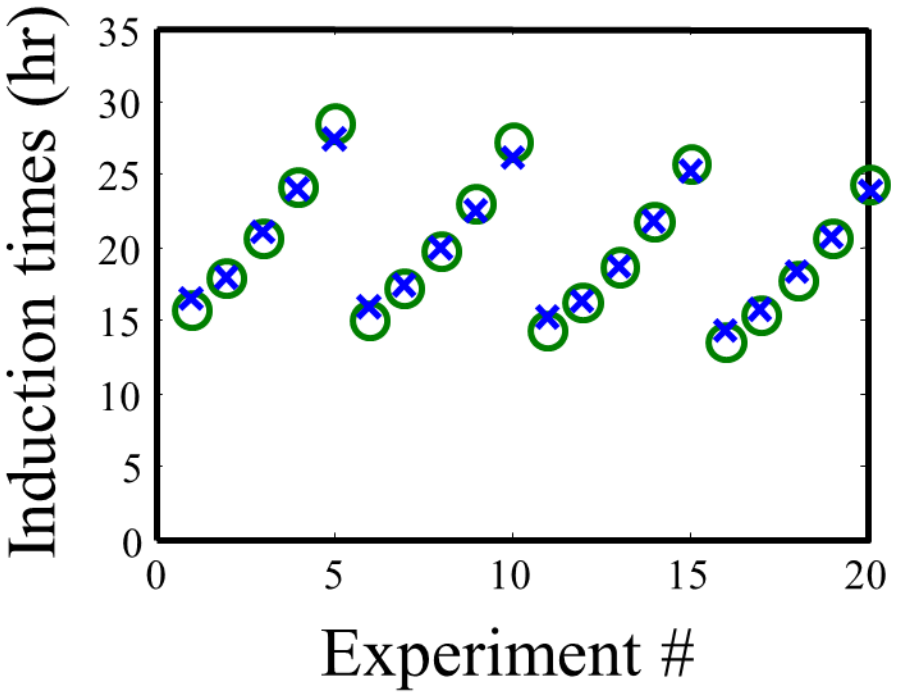

Figure 2.7. A comparison of induction times measured in wells in a microfluidic platform (crosses) with predictions of a first-principles model (circles) with nucleation kinetics estimated from the microfluidic data at high supersaturation. A detailed study demonstrated that these nucleation kinetic parameters resulted in accurate predictions of induction times in subsequent experiments.

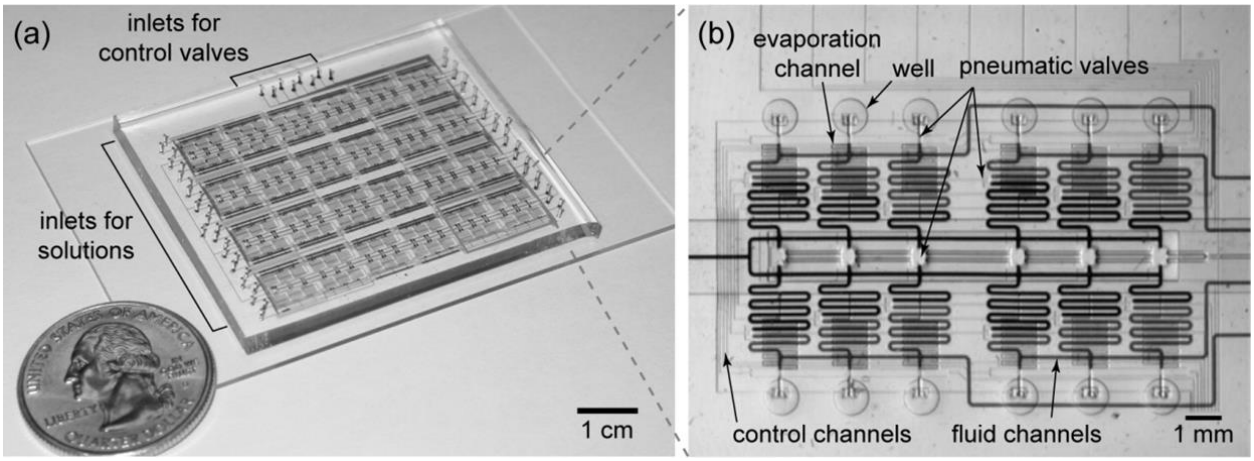

Figure 2.8. A high-throughput microfluidic chip for protein and pharmaceutical crystallization that enables 144 induction time experiments to be conducted in parallel with different precipitants and different solute concentrations: (a) a micrograph of the microfluidic chip, which contains 8 inlets for pressurized control lines, 48 inlets for different precipitants, and one inlet for the target protein or pharmaceutical, (b) a micrograph of the microfluidic components used for metering solutions and controlling evaporation of solvent [1]. The target molecule and precipitant are metered into serpentine channels, and the ratio of each component is controlled by the placement of a pneumatic valve. After filling, the solutions are dispensed into a well that is connected to an evaporation channel. The dimensions of the evaporation channel control the rate of evaporation.

After the target product profile is defined and critical quality attributes identified, a control strategy can be identified. The elements of a control strategy include:[14]

- Control of the input material attributes, such as the drug substance and excipients, based on an understanding of their impact on the processing or product quality;
- Product specifications, which define the objective of the control strategy;
- Controls for unit operations that have an impact on the downstream processing or end-product quality, such as crystallizers in which poor control of the output crystal size distribution can result in problems in downstream operations such as washing, filtering, drying, and/or tableting;

- A monitoring program such as regular testing of intermediates and product for verifying drug product quality and the accuracy of multivariate prediction models.

The controls for unit operations include not only the design of feedback controllers but also other considerations associated with the integration of sensors, process design, and control required to move from input materials to optimized process design, such as:[34]

- Sensors, experimental design, and data analysis;
- Process automation;
- First-principles modeling and simulation;
- Design of operations to form a consistent product.

The remainder of this chapter provides a more detailed description of the QbD approach for the development of pharmaceutical crystallization processes, namely,

- The design of robust control strategies;
- Some example applications of automatic feedback control;
- The role of kinetics modeling;
- An example idea for a deeper QbD approach.

2.2. The design of robust control strategies

A well-studied control objective in crystallization is to minimize the secondary nucleation of crystals that may cause potential problems in downstream filtering operations by minimizing the ratio of nucleation mass to seed mass (n/s) over the temperature profile [35]–[38]

$$\min_{T(t)} \left\{ \frac{\text{nucleation mass}}{\text{seed mass}} \right\} \tag{2.1}$$

The control objective is related to the temperature profile through a population balance model [39][40] for the crystals in the slurry:

$$\frac{\partial f}{\partial t} + G(C,T)\frac{\partial f}{\partial L} = B(C,T)\delta(L) \tag{2.2}$$

where $f(L,t)$ is the crystal size distribution which is a function of the crystal size L and time t, G is the growth rate and B is the nucleation rate which are assumed to be functions of the solute concentration C and the temperature T, and δ is the Dirac delta function. The solute concentration is described by its mass balance

$$\frac{\mathrm{d}C}{\mathrm{d}t} = -3\alpha G(C,T)\int_0^\infty f(L,t)dL \tag{2.3}$$

where α is a conversion factor. The temperature profile must satisfy constraints due to equipment limitations

$$\begin{aligned} T_{\min} \le T(t) \le T_{\max} \\ R_{\min} \le \frac{\mathrm{d}T(t)}{\mathrm{d}t} \le R_{\max} \end{aligned} \tag{2.4}$$

where $T_{\min}$, $T_{\max}$, $R_{\min}$, and $R_{\max}$ are user-specified scalars. The crystallization must also satisfy a constraint to ensure a high enough batch yield:

$$C(t_{\text{final}}) \le C_{\text{final,max}} \tag{2.5}$$

where t_{final} is the time in which the batch ends and $C_{\text{final,max}}$ is the limit on the concentration at t_{final}. A common practice in the crystallization control literature is to solve optimizations (2.1) to (2.5) while ignoring uncertainties in the nucleation and growth kinetics [37], [41], [42].

This example shows that the robustness of the control strategy can be very strongly affected by uncertainties. A linear cooling profile results in n/s = 10.7, while numerical solution of the optimization (2.1) to (2.5) improves the n/s to 8.5, which is a 21% reduction in the nucleation mass to seed mass (Figure 2.9). All of the improvements due to optimization can be lost due to uncertainties in crystallization kinetics. In particular, the n/s can be as large as 14.6 for realistic

uncertainties in the nucleation and growth kinetics, [43] which is much worse than performing no optimization at all. The poor robustness can be understood in terms of the crystallization phase diagram. When only the temperature is measured in the control strategy, uncertainties in the crystallization kinetics can cause the pathway in the phase diagram to drift across the metastable limit, which results in uncontrolled crystallization (upper dashed pathway in Figure 2.10). While not all crystallizations are as sensitive to model uncertainties, this example as well as many others [44]–[46] illustrate that uncertainties cannot be safely ignored and it is important to design feedback controllers that are insensitive to these model uncertainties.

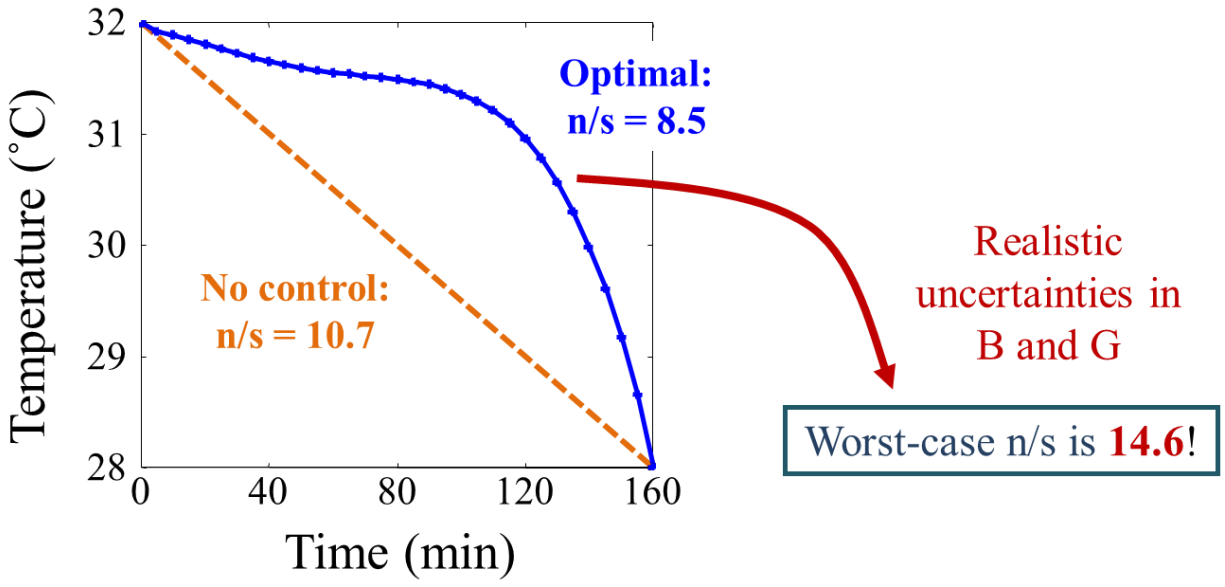

Figure 2.9. Temperature profiles for seeded cooling crystallizations. Optimal control that ignores uncertainties predicts a 21% improvement in n/s (from 10.7 to 8.5) that can be completely lost due to uncertainties (from 10.7 to 14.6).

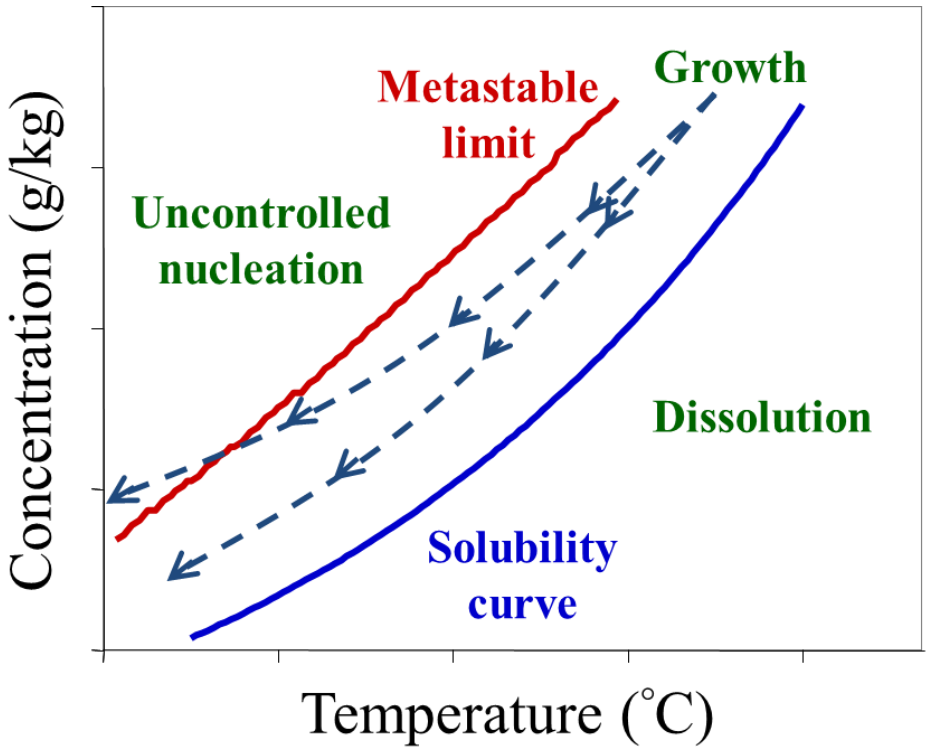

Figure 2.10. Phase diagram for crystal dissolution, growth, and uncontrolled nucleation showing robust and non-robust operational trajectories. A control strategy that is insensitive to model uncertainties must keep the operational trajectory between the solubility curve and metastable limit.

State-of-the-art in situ sensor technologies [47]–[74] (Figure 2.11) provide additional information that can be employed in real-time to produce more robust control strategies. For example, a strategy that is much less sensitive to uncertainties in the kinetics employs feedback control based on in situ solute concentration measurement obtained by ATR-FTIR spectroscopy to follow the desired pathway in the crystallization phase diagram (lower dashed pathway in Figure 2.10). Detailed theoretical analyses indicate that this feedback control strategy more robustly operates the crystallizer at constant growth and low nucleation rates [75], [76], which

has been demonstrated in numerous experimental implementations at universities and pharmaceutical companies [4], [7], [75], [77]–[79].

(a)

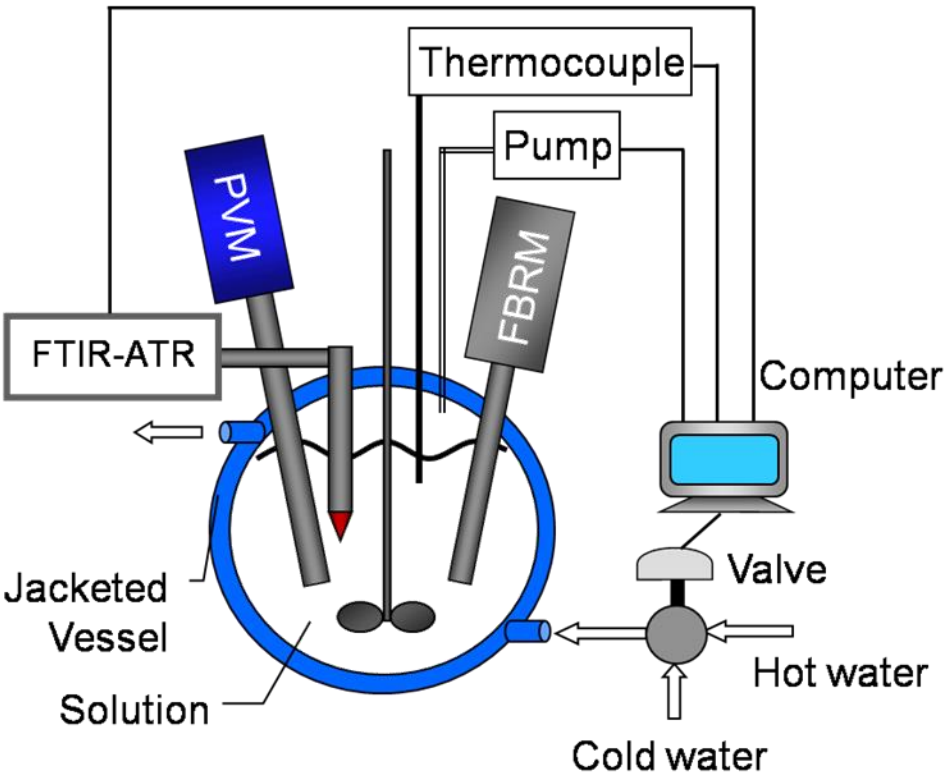

(b)

Figure 2.11. (a) A photograph and (b) a schematic of crystallization laboratory setup with state-of-the-art *in situ* sensor technologies that enable the development of robust control strategies. ATR-FTIR refers to Attenuated Total Reflection FTIR spectroscopy, FBRM refers to Focused Beam Reflectance Measurement (laser backscattering), and PVM refers to Particle Vision and Measurement (in situ video microscopy).

2.3. Some example applications of automatic feedback control

Figure 2.12 shows some sample results in which automatic feedback control was applied to a Merck pharmaceutical with very high secondary nucleation kinetics [78]. The feedback control system tracks any desired trajectory in the crystallization phase diagram, including constant absolute or relative supersaturation (Figure 2.12a). The extent of nucleation was simultaneously monitored by tracking the total counts/sec measured in real-time using in situ laser backscattering (Figure 2.12b). The input to the feedback control system was the solubility curve

and the metastable limit obtained by an automated system with software implemented in Visual Basic and Matlab, using a similar crystallizer and sensor technology as shown in Figure 2.11 (without the PVM).

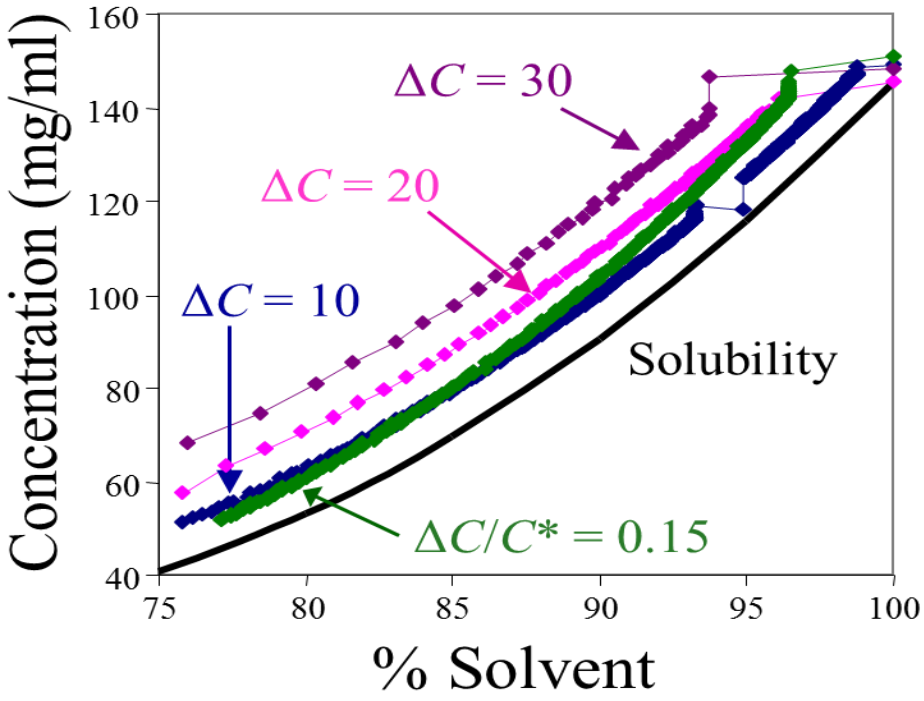

(a)

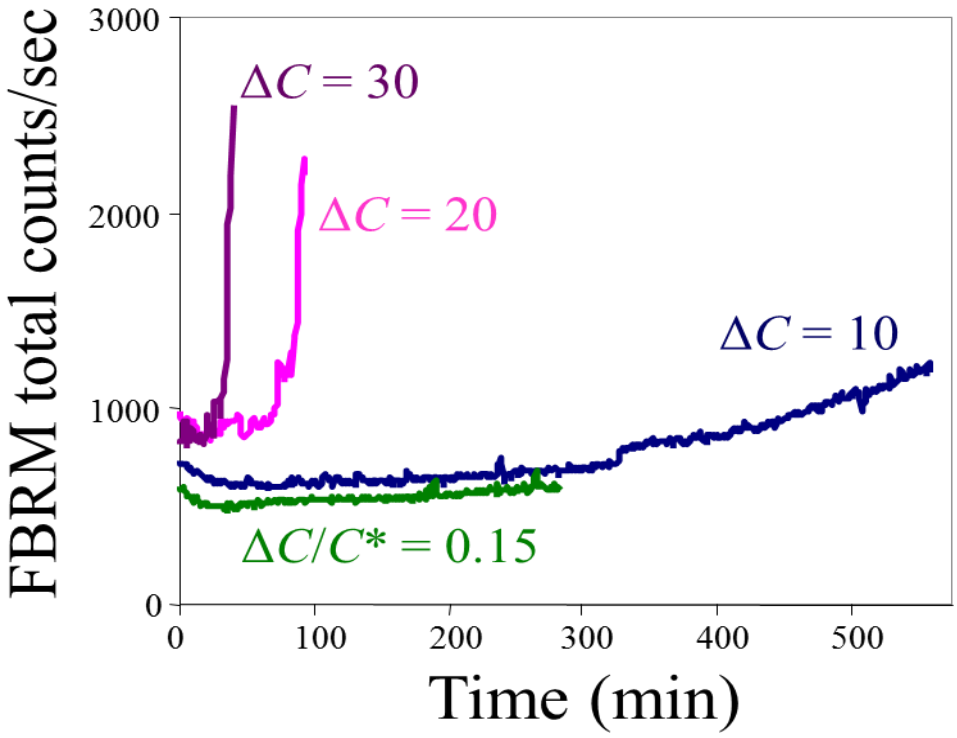

(b)

Figure 2.12. Automatic feedback control of the batch crystallization of a Merck compound: (a) concentration control at constant absolute and relative supersaturation; (b) secondary nucleation monitored by FBRM total counts per second.

The initial three runs at constant supersaturation were run automatically, followed by inspection of the total counts/sec that indicated different secondary nucleation levels at different absolute supersaturation. An absolute supersaturation ΔC = 30 mg/ml resulted in excessive nucleation within an hour whereas ΔC = 20 mg/ml resulted in excessive nucleation after 70 min. An absolute supersaturation ΔC = 10 mg/ml resulted in a long batch time with slow increase in nucleation near the end of the batch. These observations motivated the selection of a pathway in the crystallization phase diagram with a constant relative supersaturation of 0.15, which has a similar supersaturation as ΔC = 20 mg/ml in the early portion of the batch in which no nucleation

was observed, and a somewhat lower supersaturation at 10 mg/ml near the end of the batch to suppress nucleation then. The constant relative supersaturation pathway resulted in about half of the batch time as the ΔC = 10 mg/ml pathway while also having less nucleation. The automated system enabled a rapid convergence to controlled batch crystallization operations with minimum user input. The temperature time profile resulting from the feedback control of concentration can be implemented subsequently using simple temperature controllers.

Another demonstration of automatic feedback control is for the crystallization of polymorphs of L-glutamic acid (Figures 2.3 and 2.13). The α-polymorph is easier to process in downstream operations, whereas manufacture of the stable β-polymorph crystals is more reliably produced by operating between the solubility curves of the two polymorphs (Figure 2.14). Operating an unseeded crystallizer at various cooling rates produced crystals of both polymorphs, with widely varying proportions (Figure 2.15). This objective of this experimental study was to produce crystals of pure single polymorphic form.

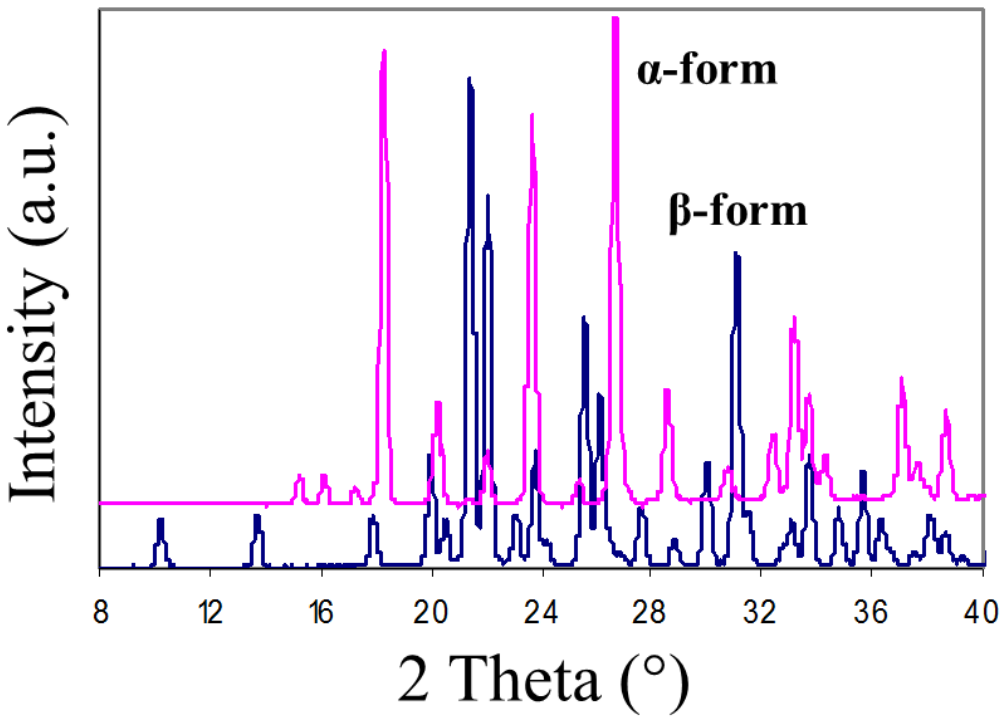

Figure 2.13. Powder X-ray diffraction patterns for the metastable α (upper curve) and stable β (lower curve) polymorphic forms of L-glutamic acid.

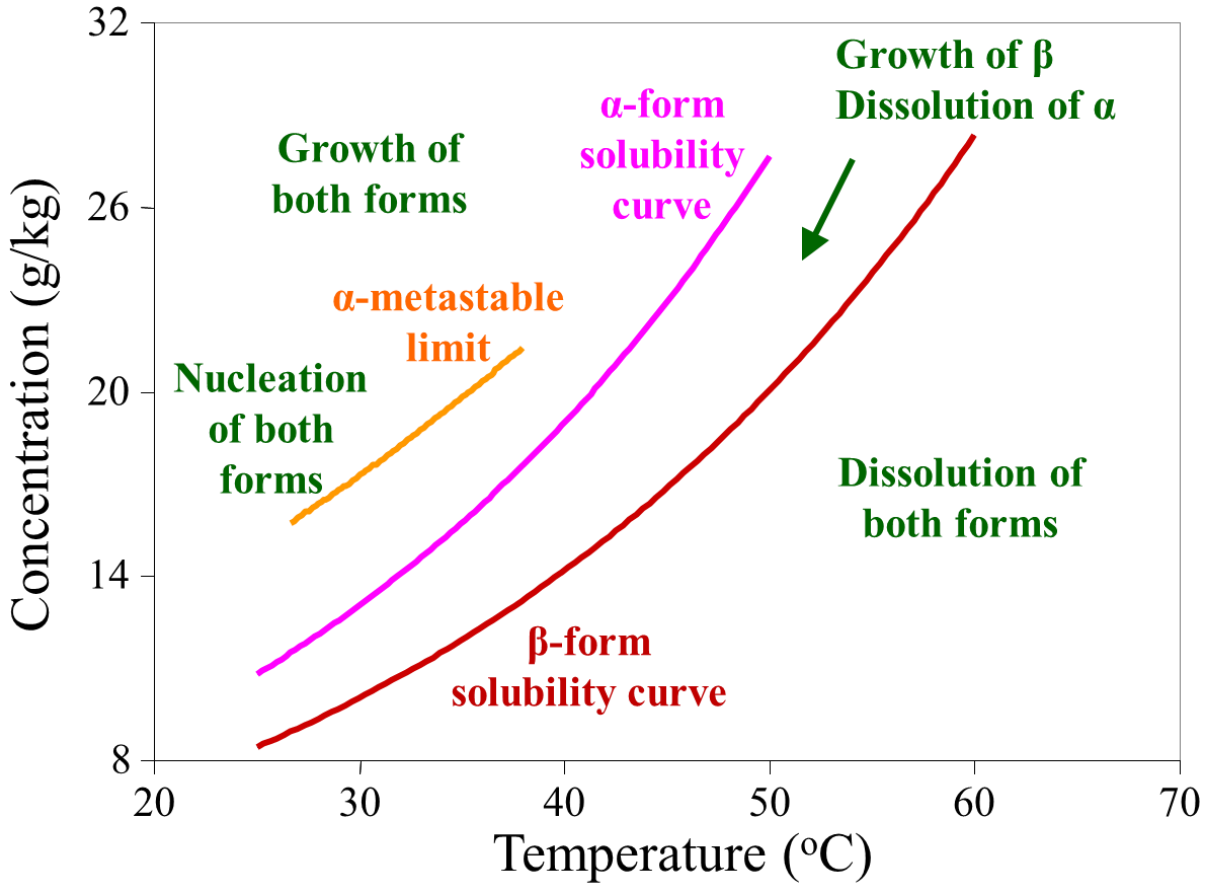

Figure 2.14. Crystallization phase diagram for L-glutamic acid. For such a monotropic system, β-form crystals grow and α-form crystals dissolve in the region between the solubility curves of the α- and β-forms.

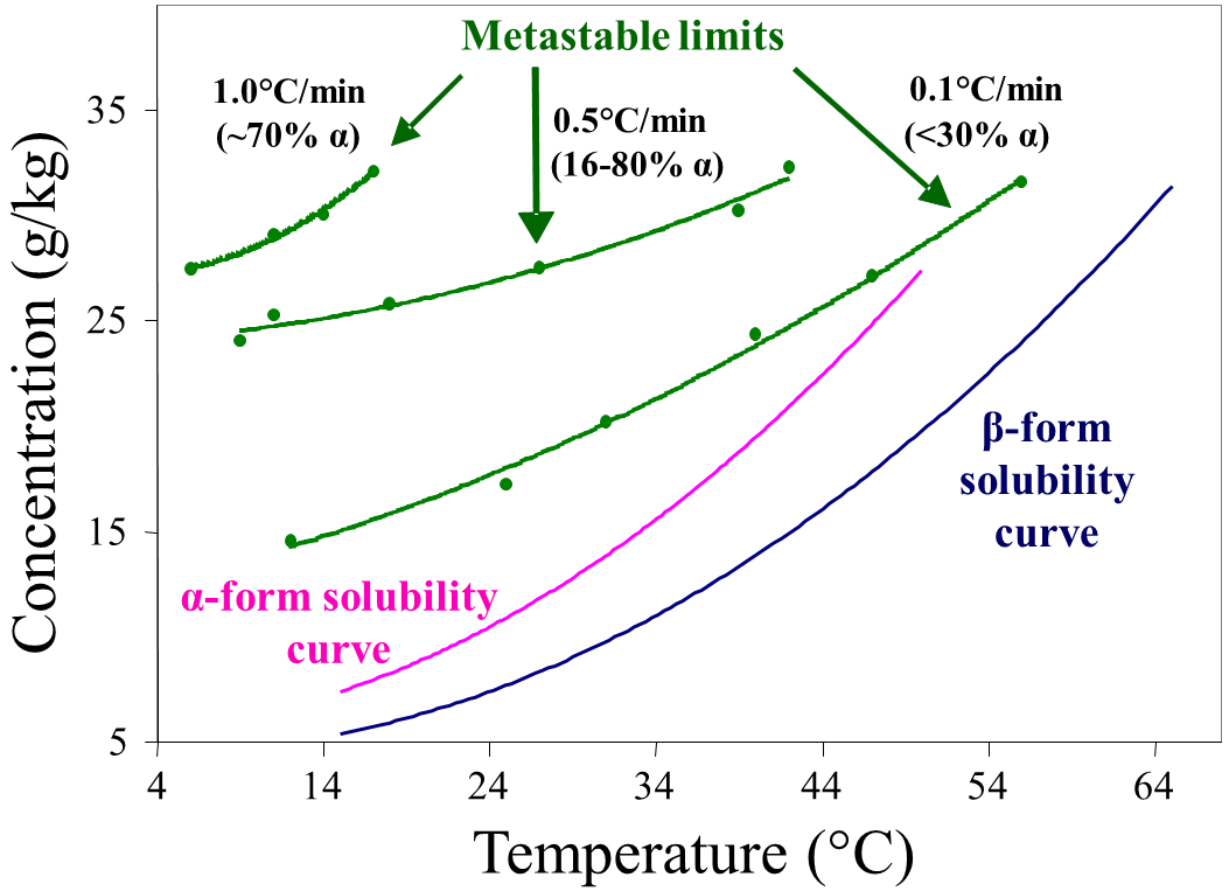

Figure 2.15. Crystallization phase diagram for L-glutamic acid, showing metastable limits at various cooling rates (0.1, 0.5, and 1.0 °C/min) with corresponding polymorphic portions of nuclei.

Pure stable β-polymorph crystals in an unseeded crystallizer can be achieved at any cooling rate, as long as the operations in the last portion of the batch remain for a long enough time between the two solubility curves (Figure 2.16). The batch time can be reduced by maximizing the supersaturation while operating between the two solubility curves, by increasing the temperature after the initial mixture of α- and β-polymorph crystals are produced by rapid cooling. The products were large β-polymorph crystals (Figure 2.16).

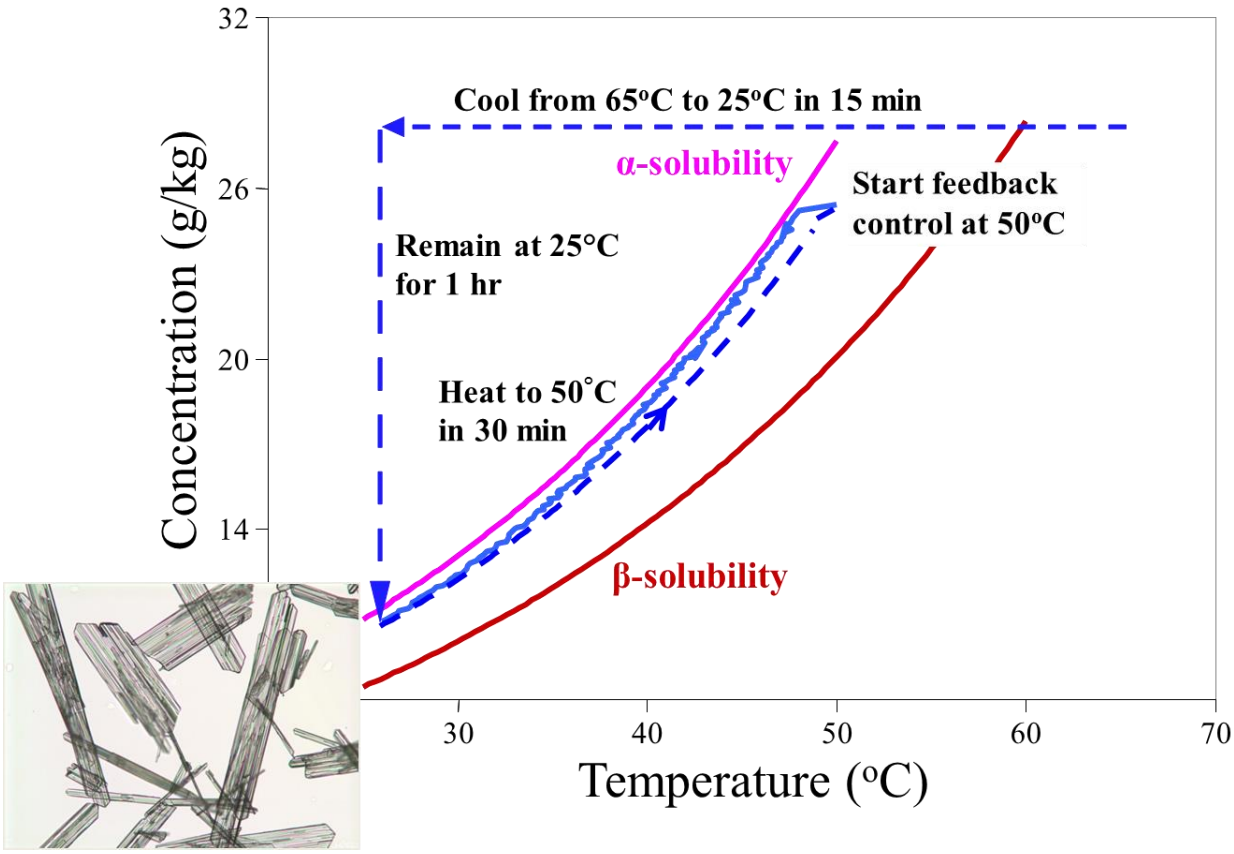

Figure 2.16. Controlled operations to manufacture the L-glutamic acid stable β-polymorph. The operation begins with a quick cooling from 65°C to 25°C to generate nuclei, followed by holding the temperature at 25°C for 1 hour to deplete supersaturation to maximize surface area of crystals, then a quick heating to 50°C (while operating between the two solubility curves) to reach a much higher temperature to increase the growth rate of the β-form crystals. The last step is to apply concentration feedback control (solid lines) to grow larger β-form product crystals.

The manufacture of the metastable α-polymorph crystals requires operation above the solubility curves for both forms (Figure 2.14), but not at such a high supersaturation that nucleation of the stable β-polymorph crystals occurs. The most reliable operation is to seed with the metastable crystals while cooling to operations above the solubility of the α-polymorph while remaining below the metastable limit (Figure 2.17). Seeding with α-polymorph crystals is required because the initial unseeded operation produced a mixture of α- and β-polymorph

crystals for the full range of cooling rates (Figure 2.15), which would always result in a large quantity of β-polymorph crystals at the end of the batch.

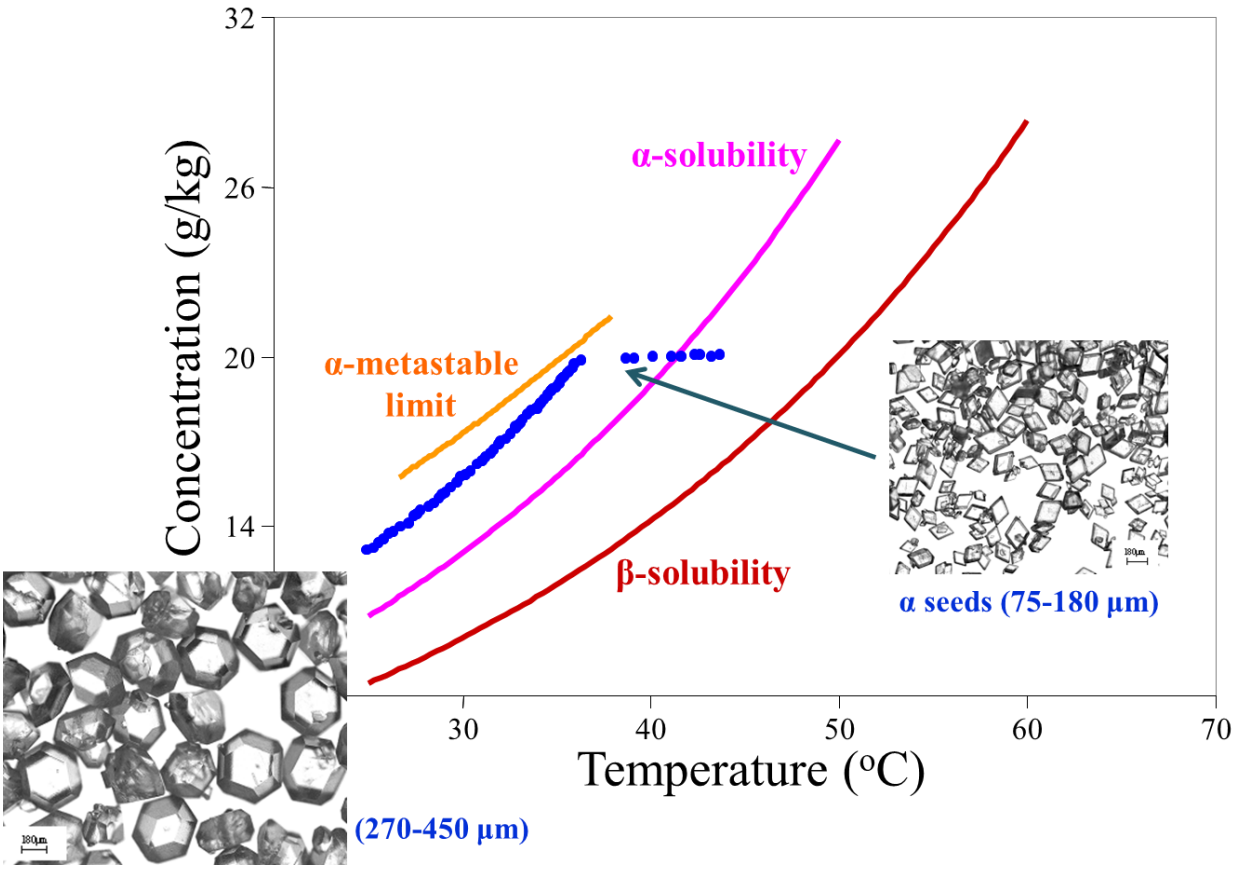

Figure 2.17. Controlled operations to manufacture a pure batch of metastable α-form crystals of L-glutamic acid. α-form seeds (75–180 µm in size) are grown to large sizes (270–450 µm in size) by following an operational trajectory between the α-form solubility curve and the α-form metastable limit.

Automatic feedback control can be employed to force the crystallizer to follow a desired pathway within the desired operating window of the crystallization phase diagram, to produce large metastable crystals without the addition of any additives (Figure 2.17) [80]. The same approach has been used to robustly manufacture stable and metastable solvatomorphs [81].

These experimental implements also demonstrate how in situ sensor technologies can be used to design and implement a robust control strategy.

The feedback control of concentration to follow a target pathway in the crystallization phase diagram (Figure 2.18b) has several advantages over the application of a pre-determined temperature or antisolvent addition profile (Figure 2.18a): [75], [76], [82]

- Lower costs and process development times;
- Lower trial-and-error experimentation;
- Insensitivity to most variations in kinetics and most disturbances.

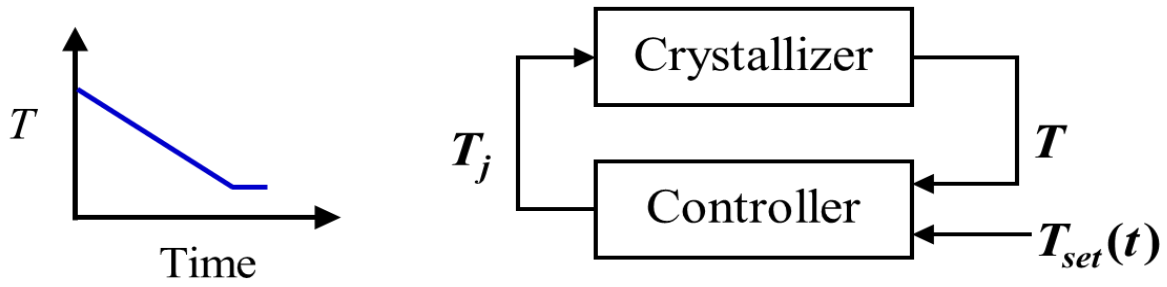

(a)

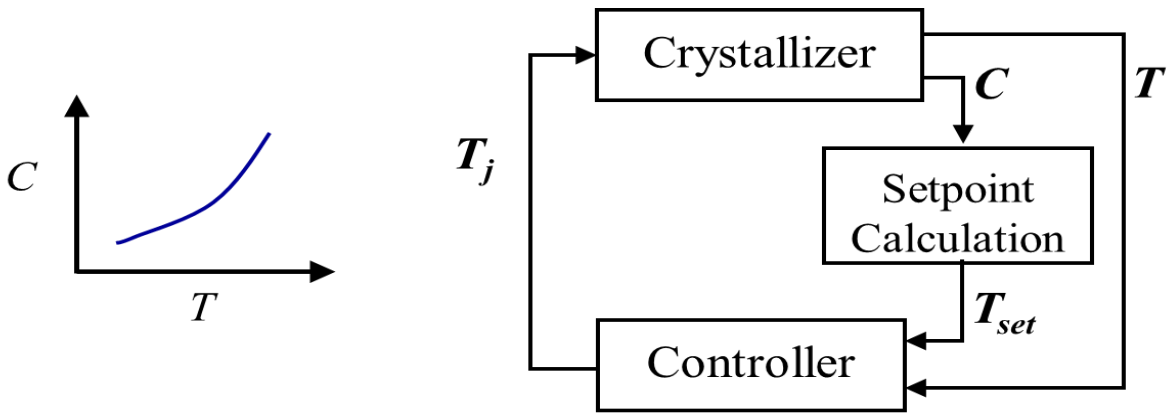

(b)

Figure 2.18. Implementations of (a) temperature control and (b) concentration feedback control for cooling crystallization. The implementations for antisolvent crystallization are similar, with T replaced by % solvent.

Concentration feedback control can result in high variability in the batch time, which is indirectly used as an extra degree of freedom to produce the reduced sensitivity. A drawback of both control approaches in Figure 2.18, as well as nearly all other crystallization control approaches described in the literature, is sensitivity to variations in the solubility due to impurities. The simplest way to deal with impurities is to have fine control of the input material attributes, which is one of the tenets of the QbD approach [14]. Unfortunately, often the chemical feed streams for pharmaceutical production are outsourced and suppliers are switched or remain the same but modify their operations, which results in a change in the impurity profile for the input materials to the crystallizer. For pharmaceutical-solvent combinations in which only one form occurs, alternative feedback control strategies have been developed that employ in situ laser backscattering measurements so as to be insensitive to variations in the solubility as well as other disturbances [82]–[85]. It will be interesting to see whether such approaches can be modified to reduce their weaknesses, such as reduced molecular purity of the product crystals, and how well these approaches can be extended to various types of polymorphic crystallizations.

2.4. The role of kinetics modeling

The aforementioned robust control strategies are insensitive to variations in crystallization kinetics and actually did not require a determination of explicit expressions for the crystallization kinetics. Instead, information on nucleation and growth kinetics were incorporated implicitly through the position of the metastable limit within the crystallization phase diagram (Figure 2-10). Explicit models for the crystallization kinetics can still be very useful, in particular, in improving the characteristics of the seed crystals and in reducing risk during scale-up from bench

to manufacturing scale. The quantity and size distribution of seed crystals can be optimized from first-principles population balance models that incorporate the crystallization kinetics [36]. These same models can be coupled with computational fluid dynamics (CFD) simulations to identify potential scale-up problems, revise batch operations (such as seeding or antisolvent addition rates) to improve operations at the manufacturing scale, and optimize process equipment such as the geometries and physical locations of baffles and feed streams [17], [86].

Non-ideal mixing is a common scale-up problem in batch crystallizers. Many industrial researchers apply vanilla CFD simulation to try to describe some of the effects of imperfect mixing, but simulation codes that do not include a population balance model for the crystals do not adequately describe all of the crystallization phenomena important in manufacturing operations. A typical manufacturing-scale crystallizer as shown in Figure 2.19 involves processes that encompass a wide range of length scales, which include crystal nucleation (<1 micron), crystal growth (from sub-micron to hundreds of microns), micromixing (less than the size of a grid cell in a CFD simulation), and macromixing (up to meters)—such systems are multi-scale [87]. High resolution simulations [88], [89] of pharmaceutical crystallizers that couple micromixing, macromixing, and population balance models can provide insights that would be difficult to observe in experiments. For example, Figure 2.20 shows such a simulation of an antisolvent crystallization in which increased nucleation was seen near the mixing blade at intermediate times, which was due to increased mixing intensity [86]. Observing the source of nuclei is rarely possible in a large-scale crystallizer.

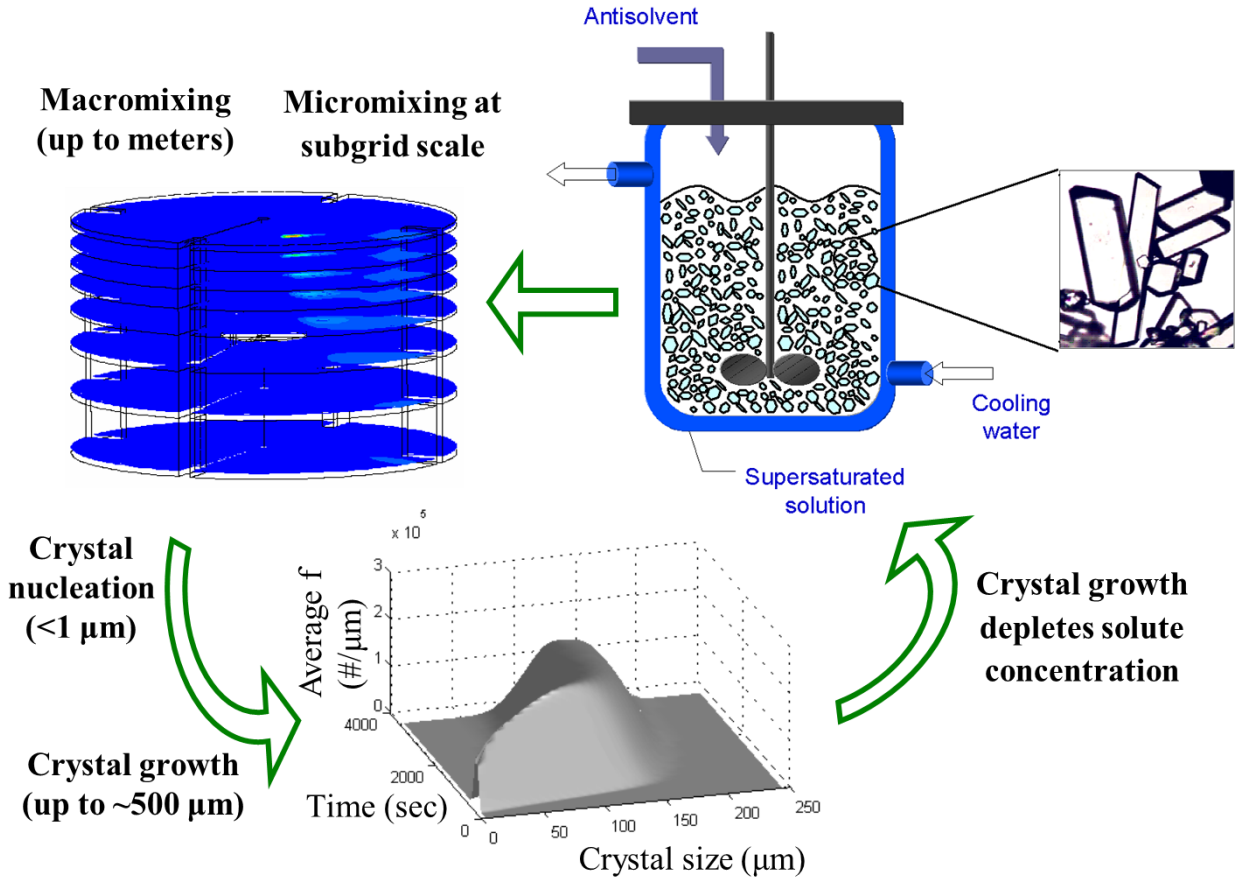

Figure 2.19. A manufacturing-scale crystallizer couples phenomena (micromixing, macromixing, nucleation, and growth) over a wide range of length scales (sub-micron to meter scale).

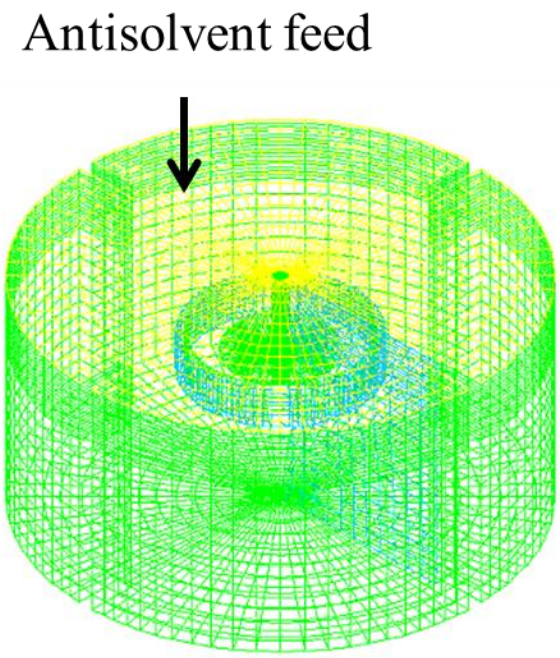
Antisolvent feed

(a)

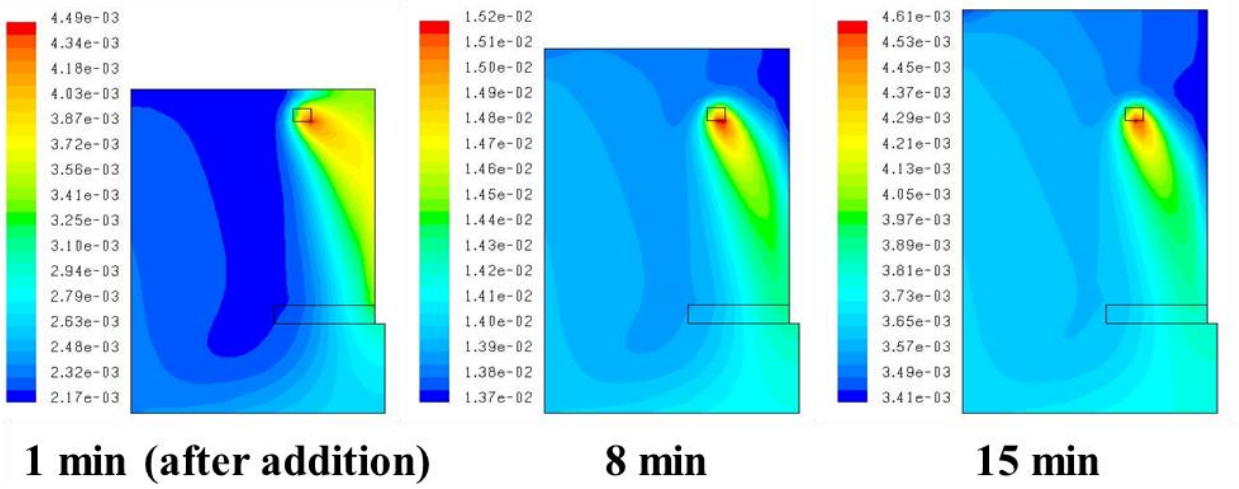
4.49e-03
4.34e-03
4.18e-03
4.03e-03
3.87e-03
3.72e-03
3.56e-03
3.41e-03
3.25e-03
3.10e-03
2.94e-03
2.79e-03
2.63e-03
2.48e-03
2.32e-03
2.17e-03
1.52e-02
1.51e-02
1.50e-02
1.49e-02
1.48e-02
1.47e-02
1.46e-02
1.45e-02
1.44e-02
1.43e-02
1.42e-02
1.41e-02
1.40e-02
1.39e-02
1.38e-02
1.37e-02
4.61e-03
4.53e-03
4.45e-03
4.37e-03
4.29e-03
4.21e-03
4.13e-03
4.05e-03
3.97e-03
3.89e-03
3.81e-03
3.73e-03
3.65e-03
3.57e-03
3.49e-03
3.41e-03
1 min (after addition)
8 min
15 min

(b)

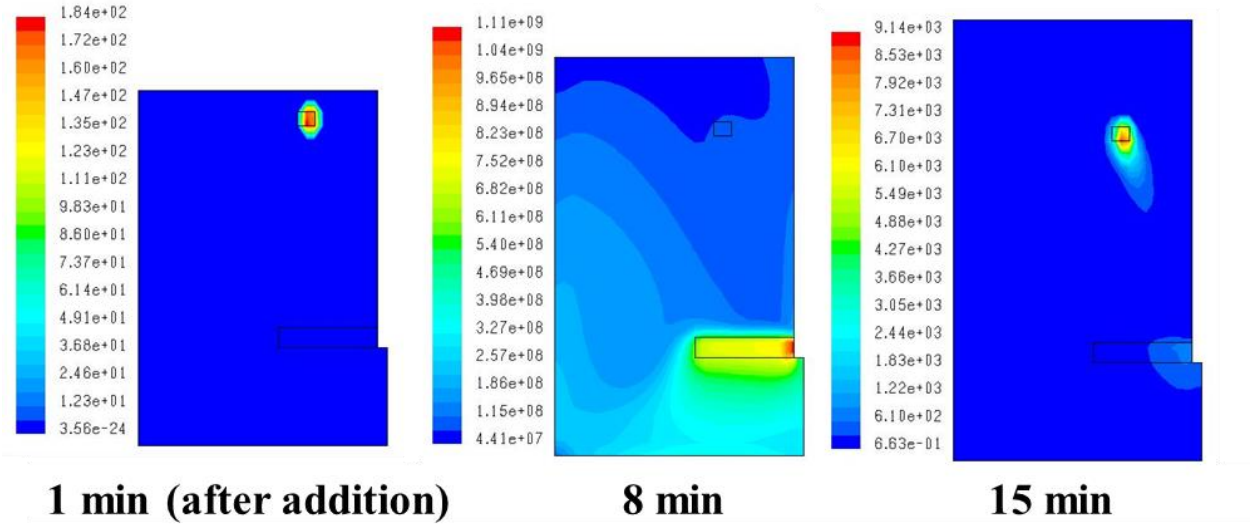

(c)

Figure 2.20. Simulation results for antisolvent crystallization in a stirred-tank crystallizer with imperfect mixing. (a) The grid cells at the start of the simulation, with increased number of cells near the blade and the feed position shown, with the topmost cells increasing in size as antisolvent raises the level of slurry in the tank. (b) Supersaturation and (c) nucleation rate spatial distributions within the crystallizer at 1, 8, and 15 minutes after the start of antisolvent addition. The highest supersaturation level exists close to the upper right corner for all three time spots. The highest nucleation rate happens at similar places as the supersaturation ones for 1 and 15 minutes, but very close to the mixing blade (on the lower right edge) for 8 minutes.

2.5. An example idea for a deeper QbD approach

The above discussions were mostly focused on the design of a crystallizer that manufacture large uniform-sized crystals while minimizing nucleation, which is motivated by the fact that large crystals are easier to wash, filter, and dry. Most crystallizers in the pharmaceutical industry add seeds at the beginning of batch, with the remainder of the control strategy specified by optimization of cooling and/or antisolvent addition.

An idea that has been explored has been the continuous addition of seed crystals during a batch, to provide extra degrees of freedom to enable the manufacture of crystals with a targeted size distribution that is not necessarily large uniform-size crystals [3]. For many pharmaceutical-

solvent combinations, the application of high supersaturation enables the manufacture of very small seed crystals with a narrow size distribution, which can be coupled with a jacketed stirred-tank crystallizer to subsequently grow these crystals to a desired size (Figure 2.21). For some systems, high quality seed crystals can be manufactured by performing cooling crystallization within a DIJ mixer, in which the fluids in the two jets are saturated solutions of the same solvent at two different temperatures (Figure 2.22).

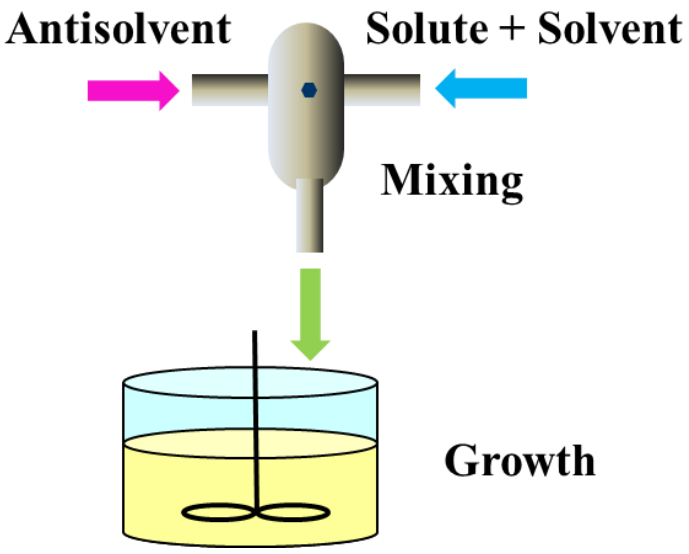

Figure 2.21. A schematic of antisolvent crystallization occurring within a confined DIJ mixer operating at high supersaturation that continuously produces seed crystals that enter a stirred tank. The high supersaturation in the DIJ mixer is generated in a mixing zone where opposing streams from two jets (containing saturated solution and antisolvent, respectively) collide. A feedback control system operates the stirred-tank crystallizer at lower supersaturation so that only crystal growth (no nucleation) occurs.

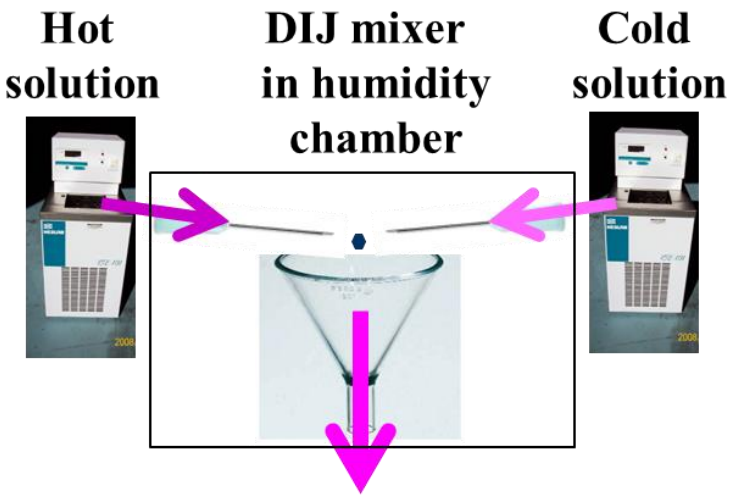

Figure 2.22. A free-surface cooling DIJ mixer forms crystals by combining hot and cold saturated solutions. The entire system is located within a humidity chamber to minimize evaporation.

For either mode of supersaturation generation, many target CSDs can be achieved by manipulating seed generation continuously using a DIJ mixer [3]. The slurry exiting the DIJ mixer is directed into the aging vessel with crystal growth rate optimally controlled to get as close as possible to the target size distribution. A unimodal crystal size distribution is easily obtained by continuously manipulating the inlet jet velocities of the DIJ mixer throughout the batch, to continuously vary the seeding (Figure 2.23). The inlet velocities were computed by solution of the optimization

$$\min_{v_{\text{jet}}(t)} \left\| f_{\text{target}}(L) - f(L, t_{\text{final}}) \right\| \tag{2.6}$$

where f_{target} is the target crystal size distribution, v_{jet} is the inlet velocities for the two jets, and || || is the integral of the square of its argument over the crystal dimension L. This optimization was numerically solved subject to the constraints

$$\frac{\partial f(L,t)}{\partial t} + G\frac{\partial f(L,t)}{\partial L} = f_{\text{jet}}(L, t; v_{\text{jet}}(t)) \tag{2.7}$$

$$v_{\text{jet,min}} \leq v_{\text{jet}}(t) \leq v_{\text{jet,max}} \tag{2.8}$$

where f_{jet} is the CSD of the crystals existing the DIJ mixer, which was computed using a coupled model for micromixing, macromixing, and population balance within the DIJ mixer [3], and $v_{\text{jet,min}}$ and $v_{\text{jet,max}}$ are user-specified scalars set to satisfy constraints on the DIJ mixer operation. Equation (2.7) is the population balance model for the stirred tank operating under a constant growth rate by using feedback control of the concentration.

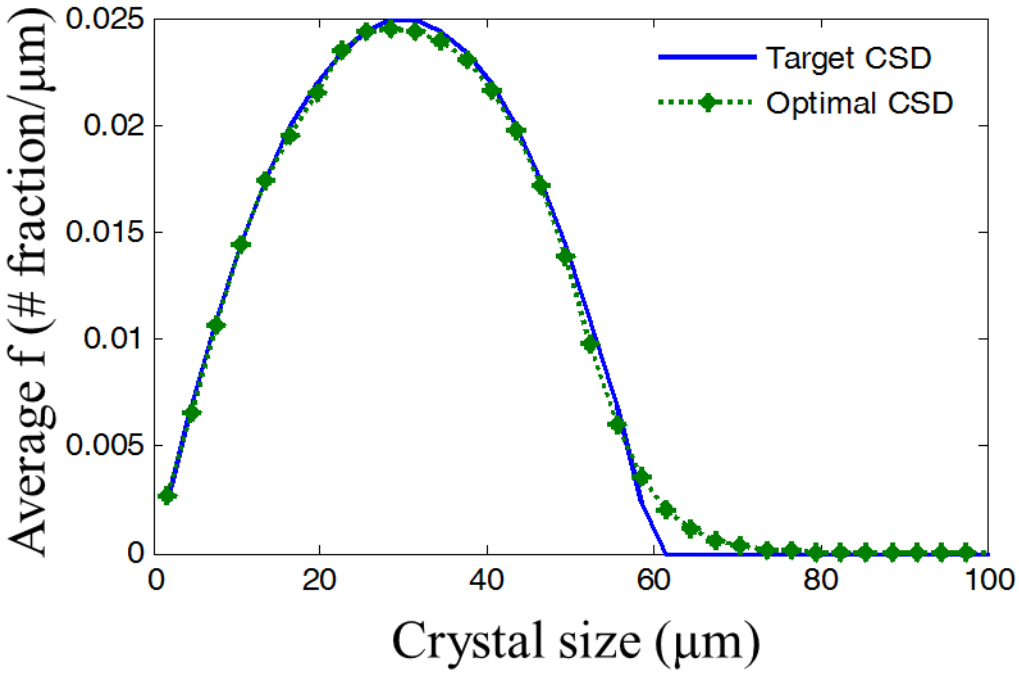

(a)

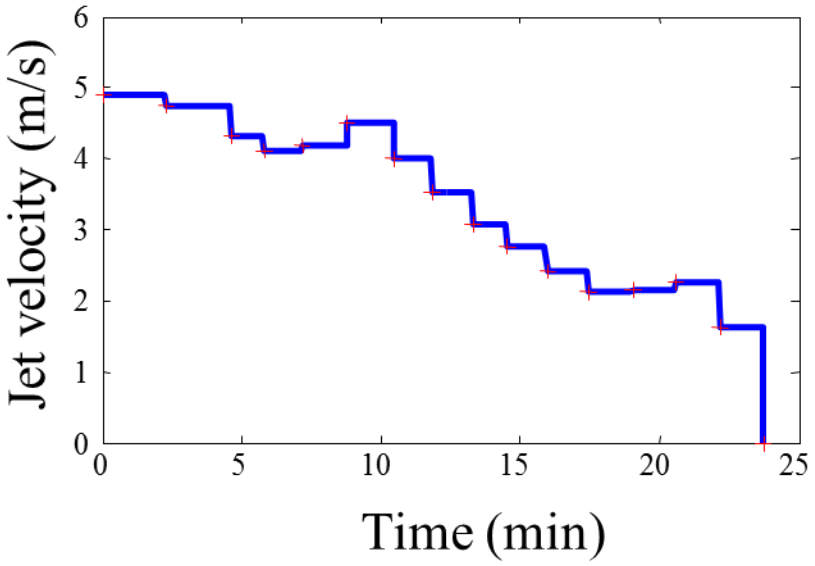

(b)

Figure 2.23. (a) Comparison of a unimodal target CSD (line) with the CSD (dash star) achieved by optimization of continuously varying inlet velocities to a DIJ mixer coupled to an stirred tank (simulation results). (b) The time profile of inlet jet velocities for the simulated achievable CSD, with the jets constrained to have the same inlet velocity.

The largest deviation between the target CSD and the nearest achievable CSD in Figure 2.23 occurs at the largest crystal size where the CSD drops to zero. Simulation results for other target CSDs also show the largest deviation occurring wherever the target CSD is sharp. The most challenging unimodal target CSD is a uniform distribution, with the optimal inlet jet velocities being close to a uniform distribution–a constant value of particle numbers per unit length between some minimum and maximum size (Figure 2.24). Theoretical analysis [3] indicates that the proposed control strategy is reasonably robust to variations in the inlet jet velocity profiles, which was tested experimentally by attempting to achieve a nearly uniform CSD by using a constant inlet jet velocity followed by a sharp drop to zero, to approximate the profile in Figure 2.24b. The experimental implementation resulted in a CSD very close to the CSD determined by simulations to most closely match a uniform distribution. Similar to the simulated achievable

CSD, the experimentally achieved CSD also has the largest deviation with the target uniform distribution at the largest crystal size (sharp side). In addition to the inlet jet velocity (Figures 2.23b and 2.24b), the supersaturation trajectory can be optimized over time, to take advantage of the ability to robustly control the supersaturation (e.g., Figure 2.12a and 2.17) [4].

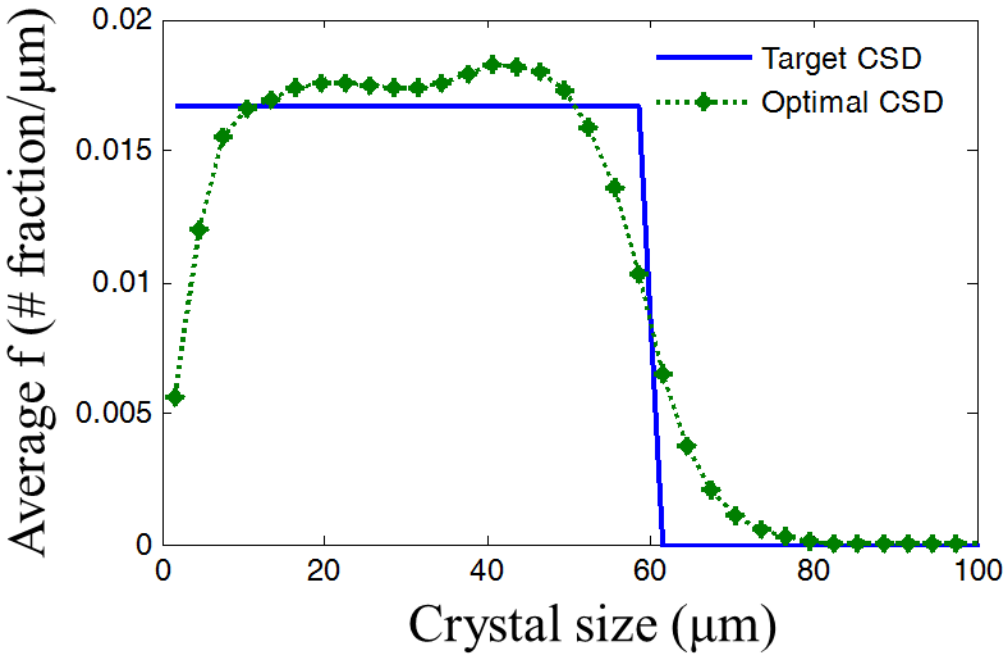

(a)

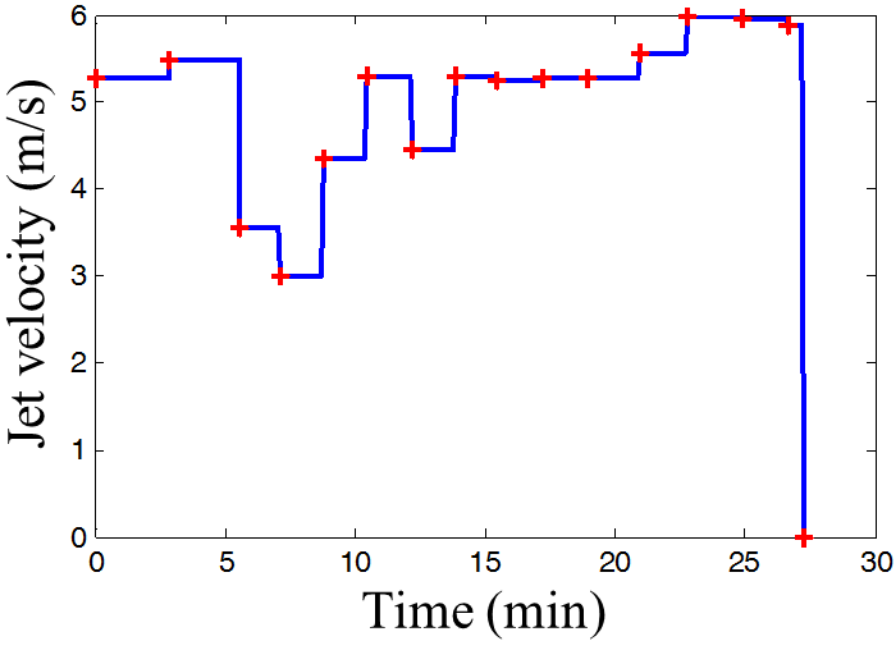

(b)

Figure 2.24. (a) Comparison of a uniform target CSD (line) with the CSD (dash star) achieved by optimization of continuously varying inlet velocities to a DIJ mixer coupled to an aging tank (simulation results). (b) The time profile of inlet jet velocities for the simulated achievable CSD, with the jets constrained to have the same inlet velocity.

2.6. Summary

This chapter discusses the role and application of automatic control in Quality by Design with examples taken from pharmaceutical crystallization. Microfluidic platforms were discussed as a technology for early-stage pharmaceutical process development to screen for polymorphs, identify desirable process parameters such as choice of solvents, and to rapidly determine key properties such as solubility and crystallization kinetics. Throughout the drug development and manufacturing processes, automatic feedback control can be employed together with microfluidic platforms and/or process sensor technology to reduce process/product sensitivity to uncertainties and disturbances for control of such properties as crystal size distribution [4], [7],

[11] and polymorphism. The key points were illustrated by simulation results and experimental implementations. Kinetics modeling was described as a step towards improving process designs, especially for reducing risk during scale-up by quantifying the effects of non-ideal mixing on product quality. A deeper QbD approach to pharmaceutical crystallization was described that designs controlled operations to obtain a target product CSD. Other advanced approaches are described in details in later chapters.

3. MODIFICATION OF CRYSTAL SIZE AND SHAPE USING DEEP TEMPERATURE CYCLING

3.1. Introduction

A large proportion of crystallizations from solution produce rod-like crystals, which can cause problems in downstream process operations. One effective method for modifying the crystal shape and size is to introduce molecular additives [90]–[92], which have the potential problem of contaminating the product. An alternative method of shape modification is to optimally control the supersaturation trajectory or by cycling between positive and negative supersaturations to take advantage of different relative dependencies along the crystal axes of growth and dissolution [93]–[100]. A very large change in the crystal shape has been reported with 20 to 80 temperature cycles, both theoretically and experimentally [97], [101]. This article experimentally demonstrates that a large change in crystal size and aspect ratio is possible with a reduced number of temperature cycles (e.g., 3 to 6).

Many efforts have been directed towards the construction of multidimensional population balance models suitable for the design of process operations to optimize crystal shape [58], [98], [102]–[110]. These models require the estimation of growth kinetics along multiple axes, with most methods based on sampling the slurry during crystallization, or on employing imaging technology [9], [10], [55], [56], [60], [93], [111]–[115]. A commercial instrument that has been used for in-situ measurement of the crystal shape distribution is Particle Vision and Measurement (PVM) [67]. Focused Beam Reflectance Measurement (FBRM) is commonly available in crystallization laboratories, but it is not possible to construct an arbitrary two-dimensional crystal size distribution (2D CSD) from measurements of the chord length distribution (CLD) obtained by an FBRM. The CLD data is not sufficiently informative for

accurate quantitative correlation to a 2D CSD, even with a design limiting the variety of CSDs with a set seed mass and supersaturation profile.

To identify dissolution and growth kinetic parameters in a 2D population balance model (PBM), this article uses solute concentrations determined using ATR-FTIR spectroscopy [53], [64], [116] and mean crystal lengths and widths from microscope images [88], [89], [105], [117], [118]. Trends in mean crystal width, length, and aspect ratio in intermediate times were measured using FBRM. The initial crystal size distributions in the PBM were determined from PVM measurements. Compared to the previously published multidimensional PBMs, the PBM in this article includes dissolution kinetics. The PBM is used to predict the crystal size and shape distribution in a temperature-cycling experiment with a different supersaturation profile.

3.2. Experimental and numerical methods

This section summarizes experimental methods for characterization of the solute concentration and mean length and width for monosodium glutamate (MSG) crystals in aqueous solution by attenuated total reflection-Fourier transform infrared (ATR-FTIR) spectroscopy, chemometrics, Focused Beam Reflectance Measurement® (FBRM), Particle Vision and Measurement® (PVM), and optical microscopy. Then we describe a two-dimensional population balance model for the growth and dissolution of rod-like crystals, and the numerical algorithms for simulation of the model and for estimation of the growth and dissolution kinetics along the length and width dimensions of the crystals.

3.2.1. Experimental setup

The solute was monosodium glutamate (MSG, from Ajinomoto, with DSC and TGA data in Figs. 3.S1 and 3.S2), whose crystals are rod-like in shape. The solvent was deionized (DI) water. Within the experimental temperature range and solvent, MSG crystallizes as a monohydrate

[119]. Crystallizations were carried out in two 100-ml cylindrical glass vessels were placed side by side in an EasyMax crystallization platform. Due to the inability to place all probes within one vessel due to space limitations, one vessel had PVM (Lasentec V819L) and S-series FBRM probes and the other vessel had ReactIR and G-series FBRM probes. This study utilized chord length data measured every 10 seconds with the G-series (G400) FBRM probe and iC FBRM 4.2.65 Beta software. Infrared spectra for MSG in DI water were collected once every minute in a stirred crystallizer by an in-situ ReactIR™ probe with iC IR 4.2 software (ReactIR™ 15 FTIR reaction analysis system) with 256 scans collected for each spectrum and DI water at 25°C used for the background spectrum. Metal overhead stirrers were continuously operated at rotational speed of 150–200 rpm, which was just enough to well suspend the crystals. The temperatures of both crystallizers were measured every 2 seconds and adjusted through the solid-state thermostat embedded in the EasyMax platform controlled with iControl EasyMax 4.1 software. Off-line optical images were taken of the crystal slurry or crystals obtained by vacuum filtration by polarized microscopes (Leica DM2500 and Zeiss Axiovert 200) with a digital camera (Leica DFC 400 Color).

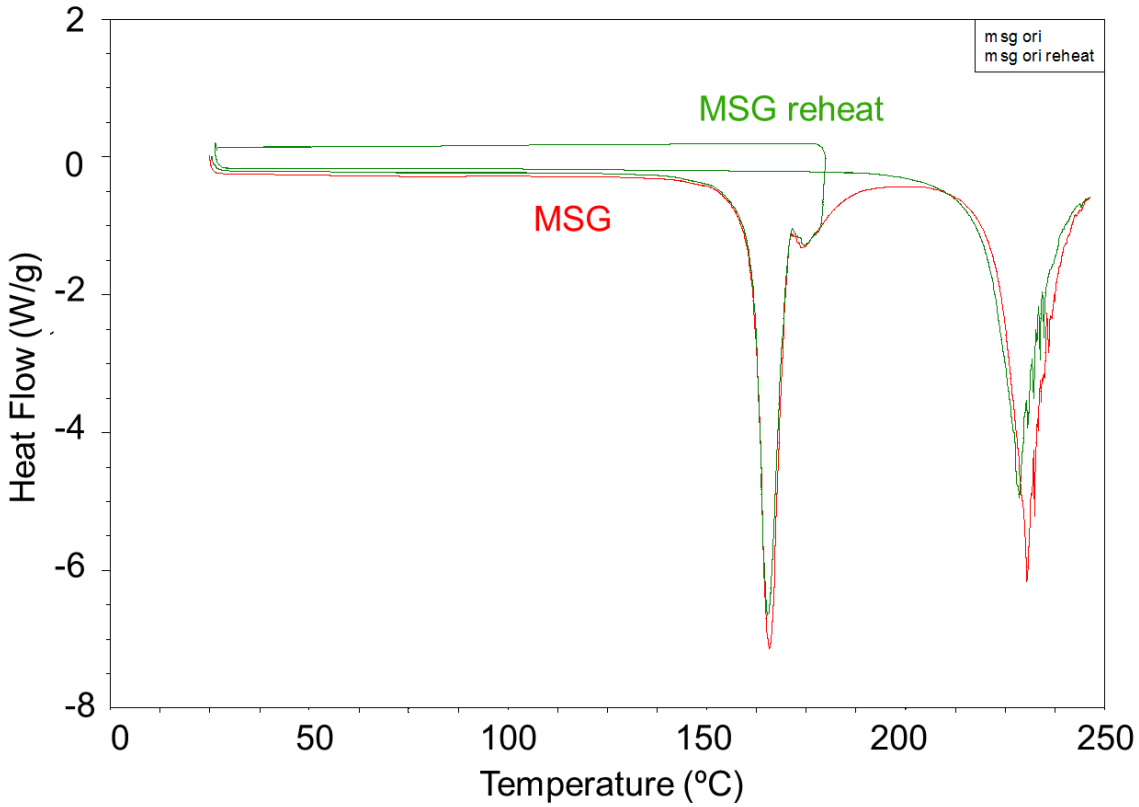

Figure 3.S1. Differential Scanning Calorimetry (DSC) of MSG crystals. The red line is for the original MSG crystals with two characteristic peaks. After heating to 180°C, holding, and then cooling to 25°C, the MSG loses the peak at about 162°C (green line), which provides evidence that the peak at about 162°C was associated with water incorporated into the crystals.

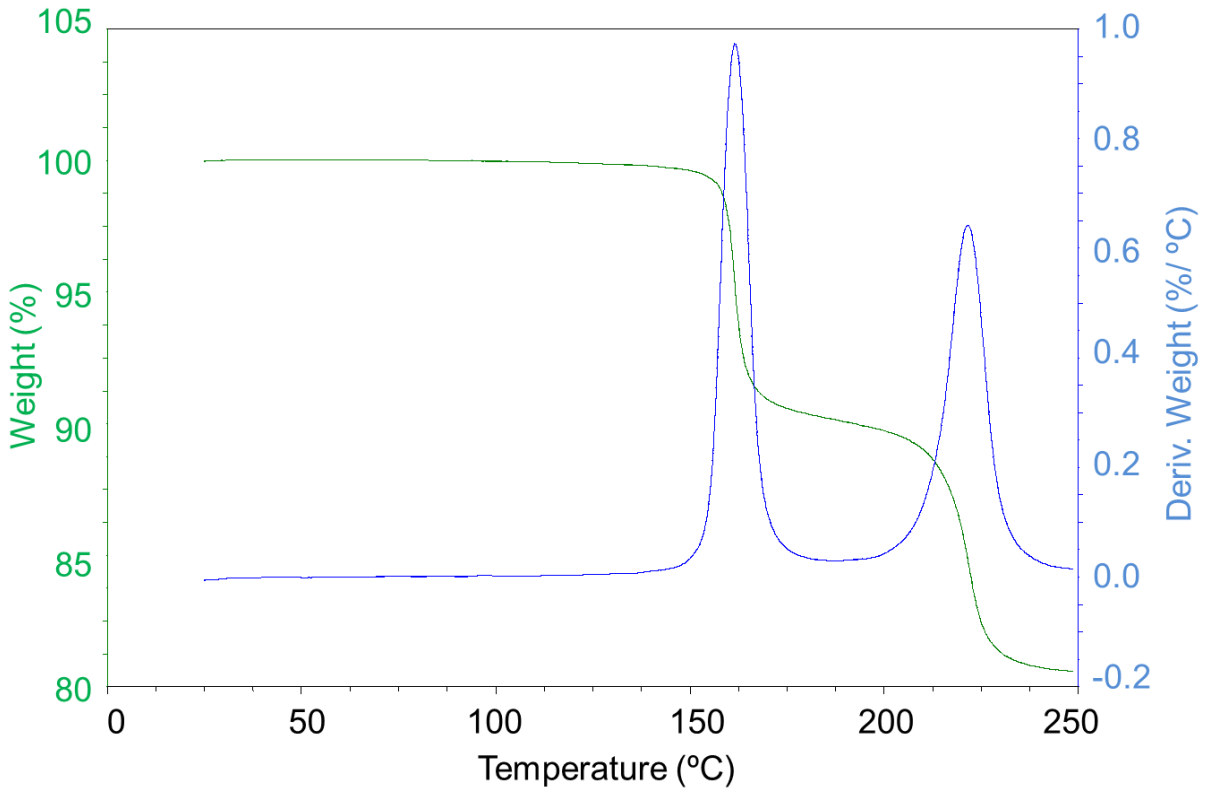

Figure 3.S2. Thermogravimetric Analysis (TGA, Q5000 V3.8 Build 256) of MSG crystals. The ratio of solid weight loss (10%) after 160°C (green line) coincides with the loss of one mole of combined water from the monohydrate form of MSG (with molecular weight = 187.11 g/mol).

3.2.2. Microscope images for measuring mean crystal length and width

During two temperature-cycling experiments, slurry samples of 2 ml were collected from the crystallizer at certain times during the cycles when the slurry was at the lowest temperature so as to reduce potential size changes during the off-line measurement of the mean crystal length and width by optical microscope. The mean length and width of crystals were measured from the microscope images.

3.2.3. IR calibration for solute concentration

The two crystallizers were cooled at a constant rate of 0.5 °C/min for different known MSG concentrations (Table 3.1) in 120 grams of aqueous solution, while being measured with in-situ

ReactIR spectroscopy and FBRM. Each decrease in the solute concentration was achieved by dosing solvent followed by equilibration after measurements were taken for a higher concentration, all controlled with a procedure pre-set in the EasyMax software. The FBRM total counts/sec were at very low level throughout the calibration experiments, confirming that nucleation was negligible during these IR calibration experiments (that is, the metastable limit was not crossed).

Table 3.1. ReactIR calibration samples for in-situ solute concentration measurement.

Calibration sample	Solute concentration (g/g solvent)	Temperature range (°C)	Number of spectra
Cs1	0.7937	65.0–48.3	34
Cs2	0.7576	55.0–37.9	35
Cs3	0.7246	44.9–32.1	26
Cs4	0.6944	35.0–22.7	25

IR absorbance spectra after DI water background subtraction and baseline offset were exported from the iC IR 4.2 software. Five chemometrics methods detailed by Togkalidou et al. [116] were applied to the absorbance spectra in the range 1200–1800 cm^{-1} with known solute concentrations and temperatures to construct a linear calibration model for measurement of the solute concentration:

$$C = \sum_{j=1200}^{1800} w_j a_j + w_T T + w_0 \tag{3.1}$$

where C is the solute concentration (g MSG/g water), a_j is the absorbance at frequency j (cm^{-1}), T is the temperature (°C), and w_j, w_T, and w_0 are regression coefficients. Representative infrared spectra and the regression coefficients are in Fig. 3.1, with the equipment and procedures being the same as for other solute-solvent systems [54], [77]. The calculations were

carried out using in-house Matlab 5.3 code (The Mathworks, Inc.). Standard Principal Component Regression with a noise level of 0.015 gave the smallest 95% prediction interval of ± 0.0055 g/g solvent. The regression coefficient plot in Fig. 3.1b does not show any spikes that would indicate overfitting, and is relatively flat except for frequencies where there are large peaks, as expected.

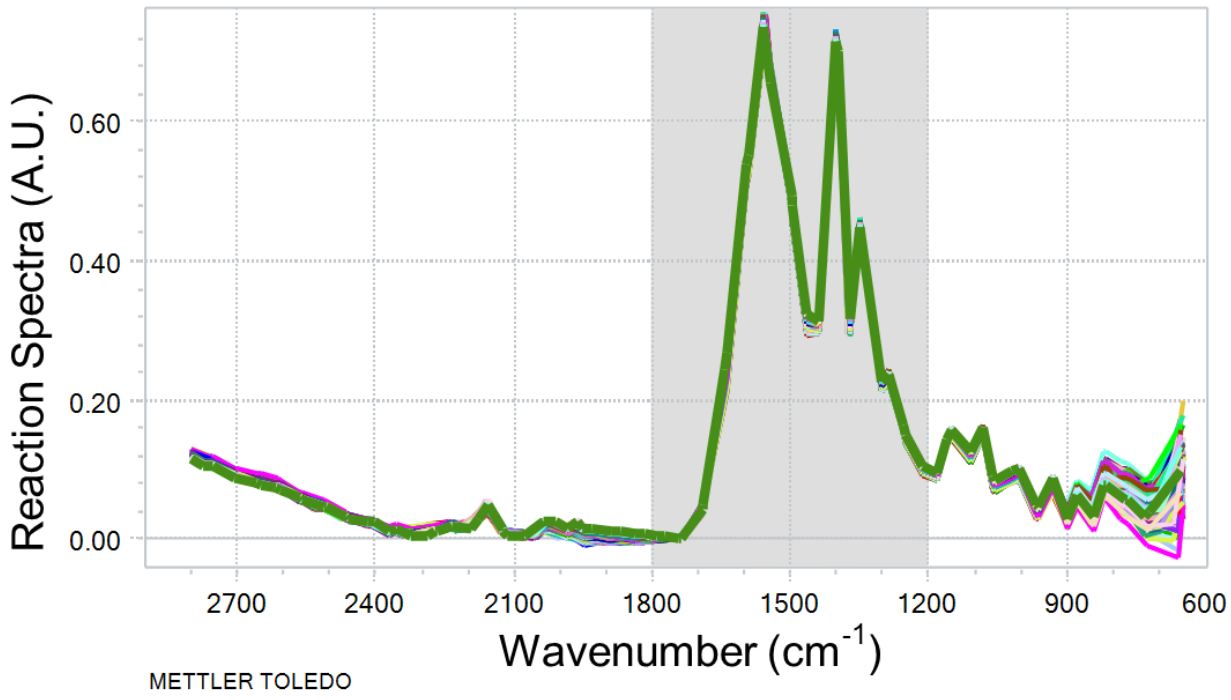

(a)

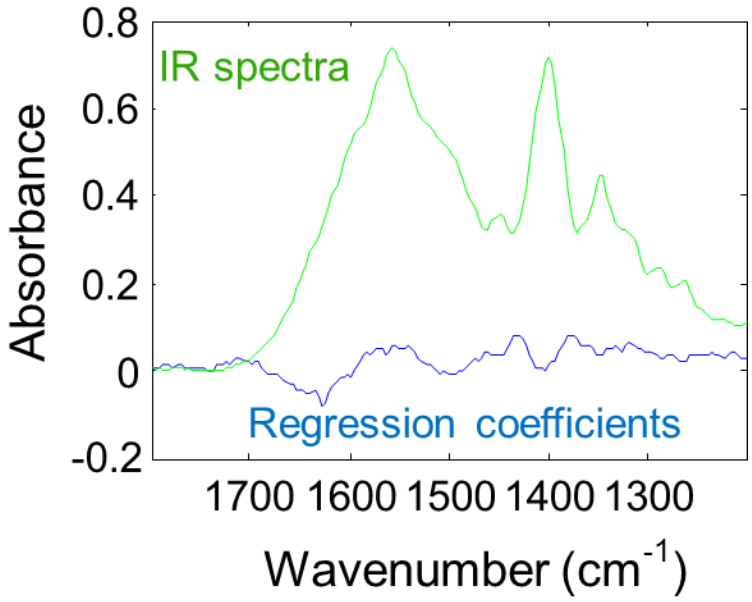

(b)

Figure 3.1. (a) Representative FTIR spectra of MSG aqueous samples used for calibration. (b) Regression coefficients of the calibration model relating absorbances to solute concentration.

3.2.4. Temperature-cycling experiments for kinetics estimation and model validation

The cycling experiment that produced the measurements of mean crystal length and width and solute concentration used for kinetics estimation followed this procedure (Fig. 3.2):

1. Add 66.6 g MSG (milled with IKA mill Werke MP 10) to 60 ml DI water.
2. Stir at 25ºC for 5 minutes.
3. Heat to 65ºC at a rate of 2 ºC/min.
4. Hold for one hour to fully equilibrate.
5. Cool to 35ºC at a rate of 10 ºC/hour.
6. Hold at 35ºC for 30 minutes.
7. Heat to 65ºC at a rate of 2 ºC/min.

8. Repeat the cooling/hold/heating cycle in Steps 5 to 7 three more times before end of experiment.

The milling of the seed crystals to produce more surface area for growth did not change the hydration state of the MSG crystals (Fig. 3.S3). The heating rate in Fig. 3.2 was set high because dissolution kinetics are much faster than growth kinetics, which was observed in the preliminary experiments by observing the infrared spectra abruptly stop changing when the temperature was held at a constant value after heating. The cooling rate was set to be just slow enough to suppress nucleation based on analysis of PVM and optical microscopy images collected during preliminary experiments.

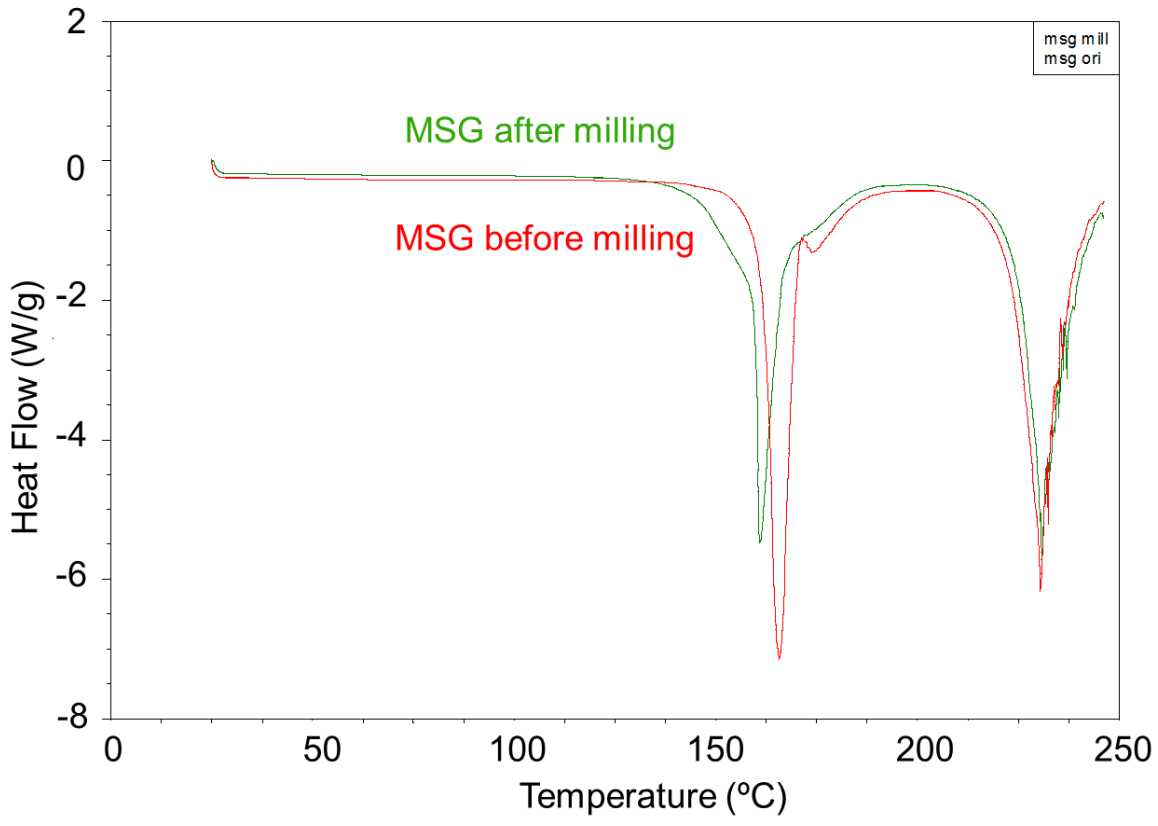

Figure 3.S3. DSC data of MSG crystals before (red line) and after (green line) milling. The characteristic peak associated with MSG did not change, and the peak associated with combined

water (170°C) remained, which indicated that the MSG did not lose its monohydrate during milling.

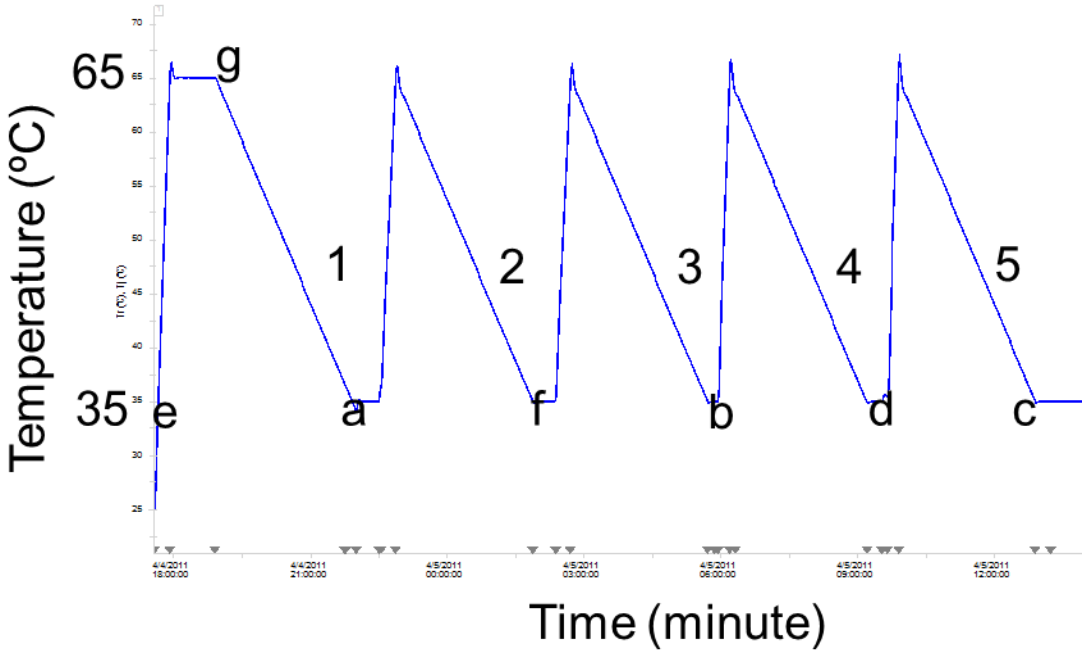

Figure 3.2. The temperature profile for the estimation temperature-cycling experiment (5 cycles).

Past studies have demonstrated a very large change in the crystal shape with 20 to 80 temperature cycles [97], [101]. In this study, the temperature range was chosen to be much greater (65°C − 35°C = 30°C) so that a large crystal mass dissolves and then grows during each cycle, to generate a larger change in crystal shape during each cycle. The very high heating rate during the dissolution state of each cycle, and the use of a cooling rate nearly as high as possible while avoiding nucleation, enable a larger number of cycles to be completed in the same time period.

The mean crystal length and width were validated in another temperature-cycling experiment that followed the same experimental procedure, but with 7 cycles, a lower temperature range,

and no solute concentration measurement. These different experimental conditions were expected to lead to different amounts of change in crystal size and shape for the two experiments.

3.2.5. Simulation and optimization codes for kinetics estimation and CSD prediction

Experimental data (e.g., size of time step, number of time steps, initial liquid concentration and solvent mass) were input to a Matlab simulation-optimization code that estimated kinetic parameters based on an initial estimate obtained from an initial set of simulation runs in which one parameter was changed at a time based on physical intuition on the effect of each parameter on the solute concentration and mean crystal length and width profiles. The 2D population balance model included size-dependent dissolution and growth terms,

$$\begin{aligned} &\frac{\partial f}{\partial t}+\frac{\partial}{\partial L}\left(G_L f\right)+\frac{\partial}{\partial W}\left(G_W f\right)=0, \quad \text{for } S \geq 0 \\ &\frac{\partial f}{\partial t}-\frac{\partial}{\partial L}\left(D_L f\right)-\frac{\partial}{\partial W}\left(D_W f\right)=0, \quad \text{for } S<0 \end{aligned} \tag{3.2}$$

where f is the 2D population density, S is the absolute supersaturation, t is time, the growth and dissolution rates in the length L and width W directions are assumed to be 2D generalizations of the 1D equations [120], i.e.,

$$\begin{aligned} G_L &= k_{GL0}\exp\left(-\frac{\Delta E}{RT}\right)S^{g_L}(1+\delta_{GL}L) \\ G_W &= k_{GW0}\exp\left(-\frac{\Delta E}{RT}\right)S^{g_W}(1+\delta_{GW}W) \\ D_L &= \frac{k_{DL}(-S)^{d_L}}{L^{\gamma}} \\ D_W &= \frac{k_{DW}(-S)^{d_W}}{W^{\gamma}} \end{aligned} \tag{3.3}$$

and the δ_{ij} and γ define size-dependencies. The two-dimensional population balance model (3.2) was combined with a solute mass balance and solved using a multidimensional method of characteristics algorithm [121], [122]. All but six of the kinetic parameters were set to fixed

values as described in the caption to Table 3.2, with the remaining six parameters determined by applying successive quadratic programming to minimize the sum-of-squared-deviations between the model predictions and experiments,

$$\min_{\underline{\theta}\le\theta\le\bar{\theta}} \frac{1}{\sigma_C^2}\sum_{i=1}^{N_C} C_{measured}(t_i) - C_{model}(t_i;\theta)^{\,2} + \sum_{k=1}^{4}\frac{1}{\sigma_{L,k}^2} L_{measured}(t_k) - L_{model}(t_k;\theta)^{\,2} + \sum_{k=1}^{4}\frac{1}{\sigma_{W,k}^2} W_{measured}(t_k) - W_{model}(t_k;\theta)^{\,2} \tag{3.4}$$

where

$$\underline{\theta} = \begin{bmatrix} \ln k_{GW0} & \ln k_{GL0} & g_W & g_L & \ln k_{DW} & \ln k_{DL} \end{bmatrix}^{\mathrm{T}} \tag{3.5}$$

is the vector of fitted model parameters, N_C is the number of concentration measurements, σ is the standard deviation of each measurement error, and the subscripts *C*, *L*, and *W* refer to the solute concentration and mean crystal length and width, respectively. These coefficients weigh the relative confidence in the measurements of solute concentration and mean crystal length and width, to produce parameter estimates that are unbiased with minimum variance assuming that the errors have zero expectation and are uncorrelated with each other and the independent variables [123].

Table 3.2. Kinetic parameters estimated from fitting data from the estimation temperature-cycling experiment or set with justifications.[a]

Parameters	Optimal values	Units	Fitted or fixed parameter
k_{GL0}	6.4×10^{13}	(μm)(g water)^2/(min)(g MSG)^2	Fitted
g_L	2.00	Dimensionless	Fitted
δ_{GL}	0	1/μm	Fixed
k_{GW0}	2.3×10^{13}	(μm)(g water)^2/(min)(g MSG)^2	Fitted
g_W	2.00	Dimensionless	Fitted

δ_{GW}	0	1/μm	Fixed
k_{DL}	4.4×10^{6}	$(\mu m)^2$(g water)/(min)(g MSG)	Fitted
k_{DW}	1.6×10^{6}	$(\mu m)^2$(g water)/(min)(g MSG)	Fitted
d_L	1	dimensionless	Fixed
d_W	1	dimensionless	Fixed
γ	1	dimensionless	Fixed
ΔE	71.24	kJ/mol	Fixed

[a]The lower and upper bounds for the growth exponents g_L and g_W were 1 and 2, as specified by theory [41]. The dissolution exponents d_L and d_W were set equal to 1 to be consistent with the assumption of mass-transfer-limited dissolution [124], and the size-dependencies in the growth rates, δ_{GL} and δ_{GW} were set to zero as nonzero values did not significantly improve the fit to data. The average activation energy 71.24 kJ/mol in G_W and G_L expressions was estimated from [53]. The value of γ was selected to capture the trends in the increase in mean crystal length and width (Fig. 3.9b). Varying the value of the dependency of the dissolution rate on the crystal dimensions, γ in (3.3), above 1 did not affect the quality of fit much (comparison not shown). Although it could be argued from physical grounds that the dissolution rate in the length direction should be better modeled as being dependent on the size in the width direction and vice versa, swapping these dependencies did not improve the quality of the model's fit to data.

Uncertainties in the parameter estimates were quantified using standard methods whose applications to crystallization are well established [41]. With the vector of predicted variables

$$\underline{Y} = \begin{bmatrix} C_1 & C_2 & \cdots & C_{N_C} & L_1 & L_2 & L_3 & L_4 & W_1 & W_2 & W_3 & W_4 \end{bmatrix}^{\mathrm{T}}, \tag{3.6}$$

the sensitivity matrix for this system is

$$\underline{\underline{F}} = \left.\frac{\partial \underline{Y}}{\partial \underline{\theta}}\right|_{\underline{\theta}^*} = \begin{bmatrix} \frac{\partial C_1}{\partial \ln k_{GW0}} & \frac{\partial C_1}{\partial \ln k_{GL0}} & \frac{\partial C_1}{\partial g_W} & \frac{\partial C_1}{\partial g_L} & \frac{\partial C_1}{\partial \ln k_{DW}} & \frac{\partial C_1}{\partial \ln k_{DL}} \\ \frac{\partial C_2}{\partial \ln k_{GW0}} & \frac{\partial C_2}{\partial \ln k_{GL0}} & \frac{\partial C_2}{\partial g_W} & \frac{\partial C_2}{\partial g_L} & \frac{\partial C_2}{\partial \ln k_{DW}} & \frac{\partial C_2}{\partial \ln k_{DL}} \\ \vdots & \vdots & \vdots & \vdots & \vdots & \vdots \\ \frac{\partial C_{N_C}}{\partial \ln k_{GW0}} & \frac{\partial C_{N_C}}{\partial \ln k_{GL0}} & \frac{\partial C_{N_C}}{\partial g_W} & \frac{\partial C_{N_C}}{\partial g_L} & \frac{\partial C_{N_C}}{\partial \ln k_{DW}} & \frac{\partial C_{N_C}}{\partial \ln k_{DL}} \\ \frac{\partial L_1}{\partial \ln k_{GW0}} & \frac{\partial L_1}{\partial \ln k_{GL0}} & \frac{\partial L_1}{\partial g_W} & \frac{\partial L_1}{\partial g_L} & \frac{\partial L_1}{\partial \ln k_{DW}} & \frac{\partial L_1}{\partial \ln k_{DL}} \\ \vdots & \vdots & \vdots & \vdots & \vdots & \vdots \\ \frac{\partial L_4}{\partial \ln k_{GW0}} & \frac{\partial L_4}{\partial \ln k_{GL0}} & \frac{\partial L_4}{\partial g_W} & \frac{\partial L_4}{\partial g_L} & \frac{\partial L_4}{\partial \ln k_{DW}} & \frac{\partial L_4}{\partial \ln k_{DL}} \\ \frac{\partial W_1}{\partial \ln k_{GW0}} & \frac{\partial W_1}{\partial \ln k_{GL0}} & \frac{\partial W_1}{\partial g_W} & \frac{\partial W_1}{\partial g_L} & \frac{\partial W_1}{\partial \ln k_{DW}} & \frac{\partial W_1}{\partial \ln k_{DL}} \\ \vdots & \vdots & \vdots & \vdots & \vdots & \vdots \\ \frac{\partial W_4}{\partial \ln k_{GW0}} & \frac{\partial W_4}{\partial \ln k_{GL0}} & \frac{\partial W_4}{\partial g_W} & \frac{\partial W_4}{\partial g_L} & \frac{\partial W_4}{\partial \ln k_{DW}} & \frac{\partial W_4}{\partial \ln k_{DL}} \end{bmatrix} \tag{3.7}$$

where $\underline{\theta}^*$ is the vector of optimal parameter estimates (values listed in Table 3.2). Each element of $\underline{\underline{F}}$ was calculated by the two-point central finite difference formula and used to construct an estimate of the parameter covariance matrix

$$\underline{\underline{V_\theta^{-1}}} = \underline{\underline{F}}\,\underline{\underline{V_\varepsilon^{-1}}}\,\underline{\underline{F}}^{\mathrm{T}}, \tag{3.8}$$

given the measurement error covariance matrix

$$\underline{\underline{V_\varepsilon}} = \mathrm{diag}(\sigma_C^2 \underline{\underline{I_{N_C}}}, \sigma_{L,1}^2, \sigma_{L,2}^2, \sigma_{L,3}^2, \sigma_{L,4}^2, \sigma_{W,1}^2, \sigma_{W,2}^2, \sigma_{W,3}^2, \sigma_{W,4}^2)\,. \tag{3.9}$$

3.3. Results and discussion

3.3.1. Evolution of crystal dimensions for the temperature-cycling experiments

In the estimation temperature-cycling experiment, the FBRM statistics had not converged to a stable oscillation even after five cycles (Fig. 3.3), with the square-weighted mean chord length at the end of each cycle increasing with cycle number, indicating that each cycle continues to increase the size of the crystals. The increase in the ratio of the mean cube-weighted and square-weighted mean chord length (blue line in Fig. 3.3) is associated with a change in the mean aspect

ratio (Table 3.3). The trends agreed with the off-line microscope images (see Fig. 3.4) and PVM images (see Fig. 3.5), which clearly showed that each cycle continued to increase the mean crystal length, width, and aspect ratio. The same trends are seen in the FBRM statistics and off-line microscope images for the validation temperature-cycling experiment (see Figs. 3.6 to 3.7). While past modeling results for temperature cycling of a single crystal indicated that the crystal shape can significantly continue to change after many cycles [97], [99], an interesting aspect of the experimental data for the crystal size and shape distribution in Figs. 3.3 to 3.7 is that deep cycling enables the mean crystal dimensions to significantly increase at the end of each cycle.

Table 3.3. Mean aspect ratio and standard deviations from microscope measurements for the 5-cycle experiment.[a]

	Cycle 1a	Cycle 3b	Cycle 4d	Cycle 5c
Mean aspect ratio	2.555	3.244	3.936	4.660
Standard deviation	0.076	0.159	0.187	0.243

[a]The sampling points (e.g., 1a, 3b) are shown in Fig. 3.2.

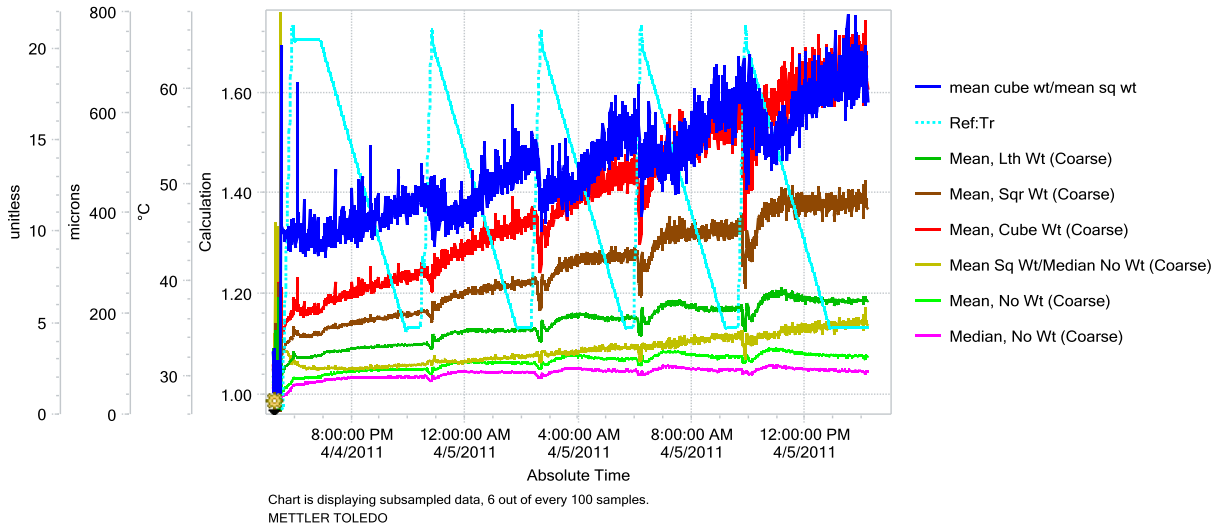

Figure 3.3. Mean chord length for various length weightings (none, length, square, and cubic) for the estimation temperature-cycling experiment. All of the mean chord lengths show a periodic change following temperature cycles (cyan line) starting from the plateau of the first cycle (when the slurry is equilibrated). Various length-weighted average chord lengths indicate that the crystal dimensions increase as the cycle number increases, and the ratio of mean cube-weighted to square-weighted mean sizes indicate that the mean aspect ratio increases as the cycle number increases. To better visualize the trends and variations, the chart displays 6 out of every 100 data points.

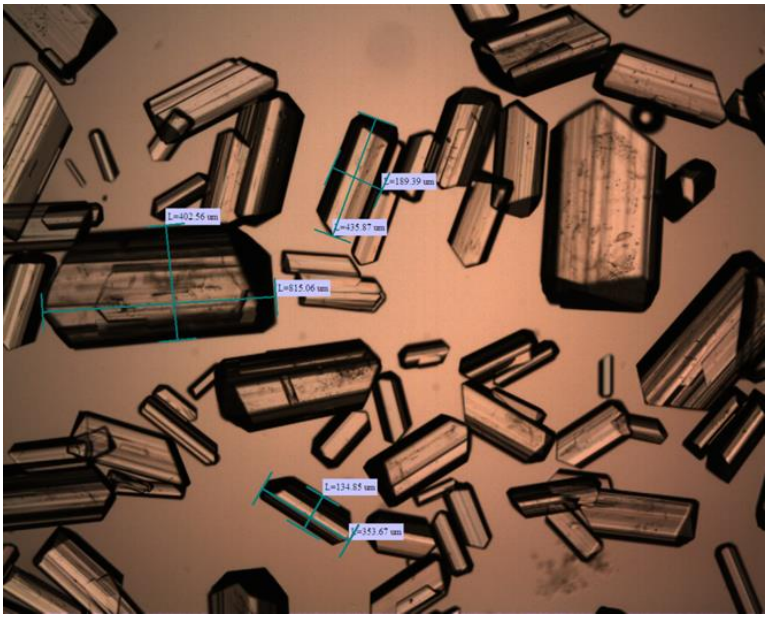

(a)

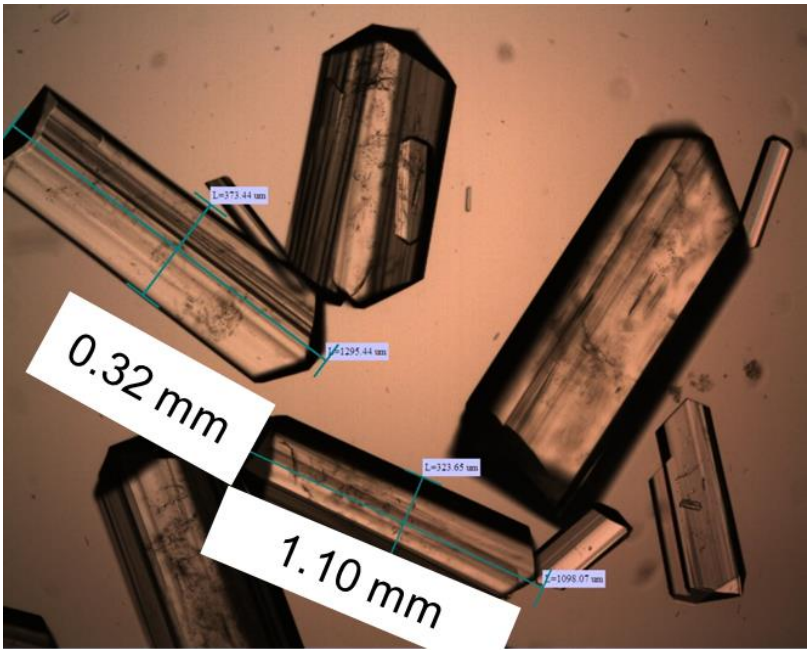

(b)

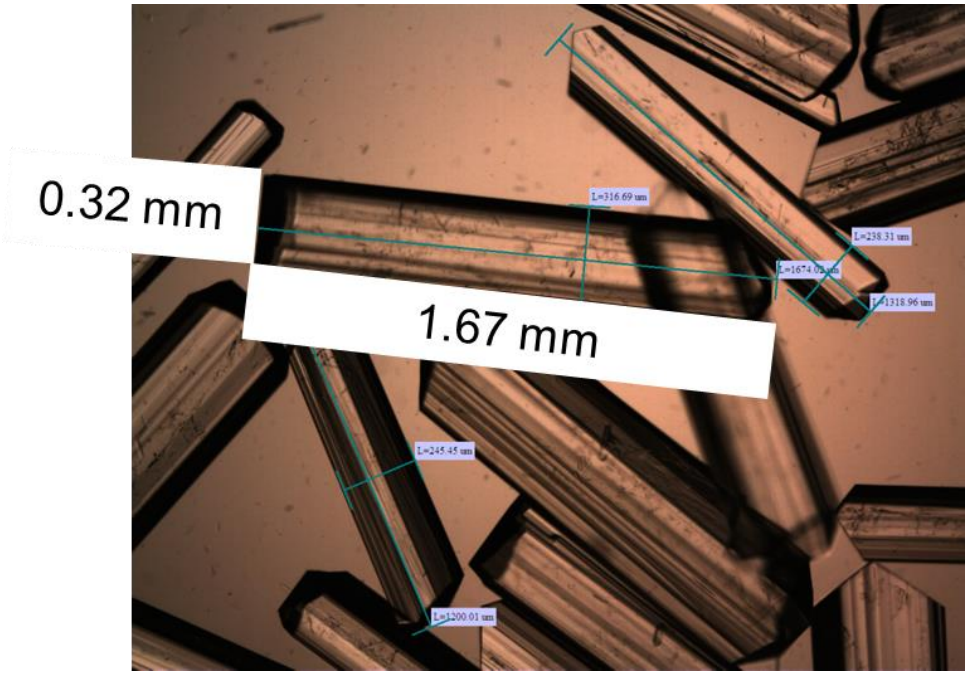

(c)

Figure 3.4. Microscopy images (with polarizers) of MSG slurry for samples collected at 35°C in the estimation temperature-cycling experiment at (a) cycle 1a, (b) cycle 3b, and (c) cycle 5c. The timing of the sampling points is shown in Fig. 3.2.

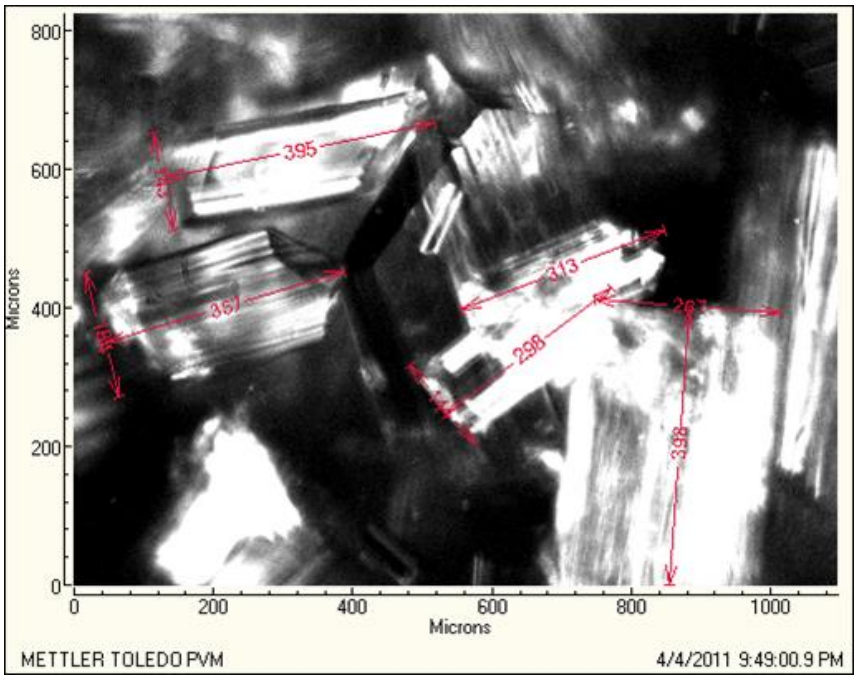
800
600
400
200
0
Microns
0
200
400
600
800
1000
Microns
395
313
357
298
398
METTLER TOLEDO PVM
4/4/2011 9:49:00.9 PM

(a)

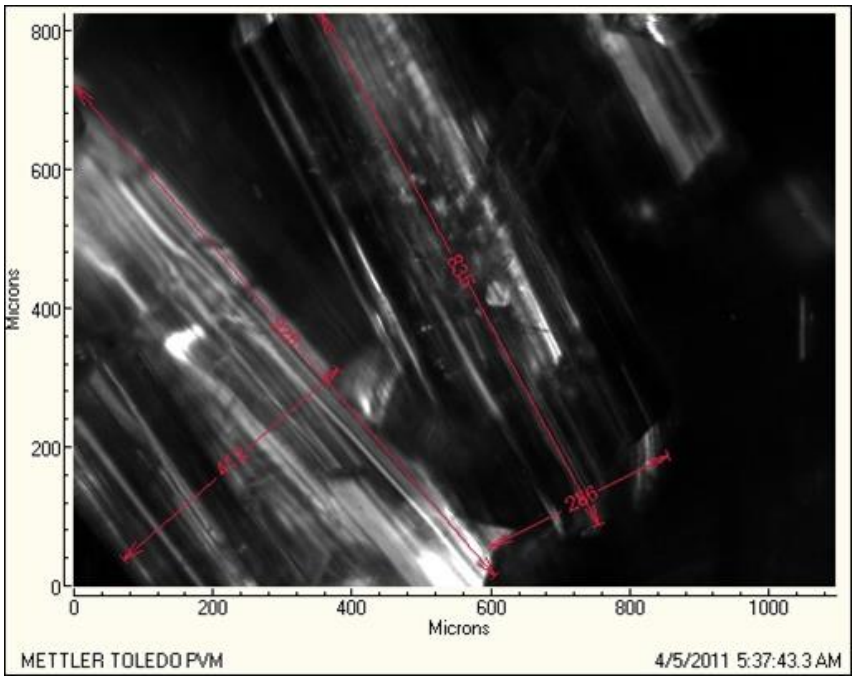
800
600
400
200
0
Microns
0
200
400
600
800
1000
Microns
835
286
METTLER TOLEDO PVM
4/5/2011 5:37:43.3 AM

(b)

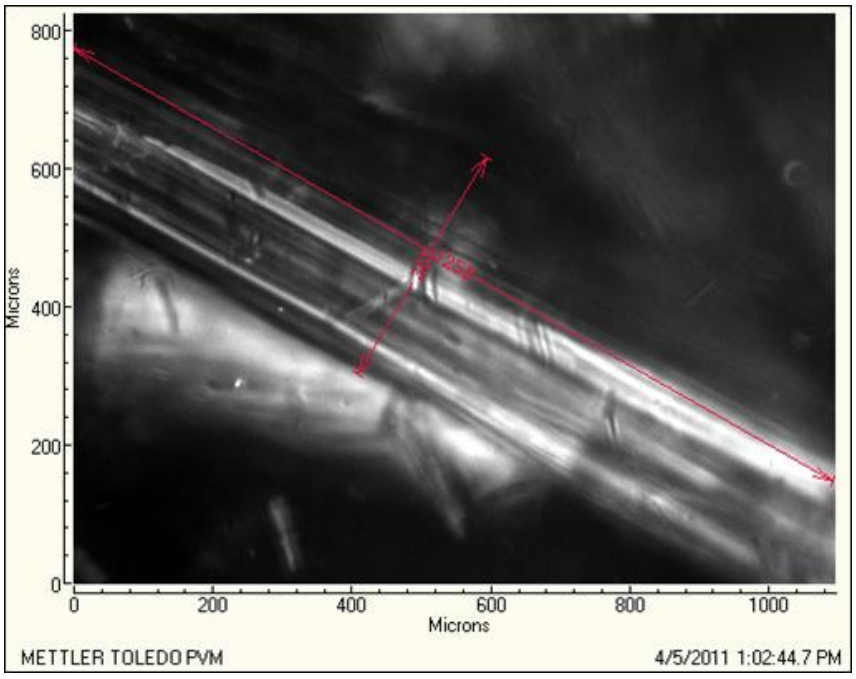

(c)

Figure 3.5. PVM images of MSG slurry at 35°C in the estimation temperature-cycling experiment at (a) cycle 1a, (b) cycle 3b, and (c) cycle 5c. The timing of the measurement points is shown in Fig. 3.2. The PVM images show that crystals grow larger as the cycle number increases, with some crystals growing larger than the image frame of PVM, such as in the fifth cycle. No secondary nuclei were observed in any of the PVM images collected during the experiments.

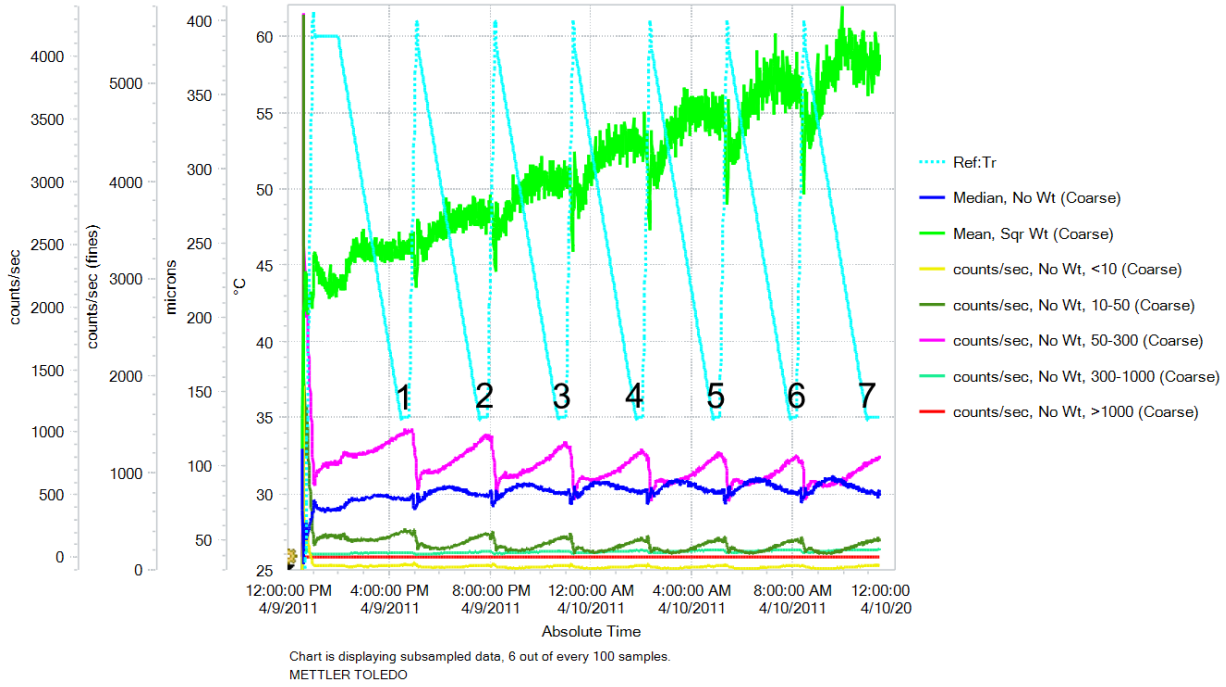

Figure 3.6. G400 FBRM (macro mode, which was called 'coarse mode' in earlier versions of the FBRM software) counts/sec statistics and temperature for the validation temperature-cycling experiment with samples collected at the end of the first, second, third, and seventh cycles (at 35°C, timing of the four sampling points shown with cycle numbers). The validation experiment shows periodic changes in FBRM statistics as the temperature cycles, with a decrease in the measured number of smaller chord lengths (< 300 μm) and an increase in mean square-weight size with cycle number.

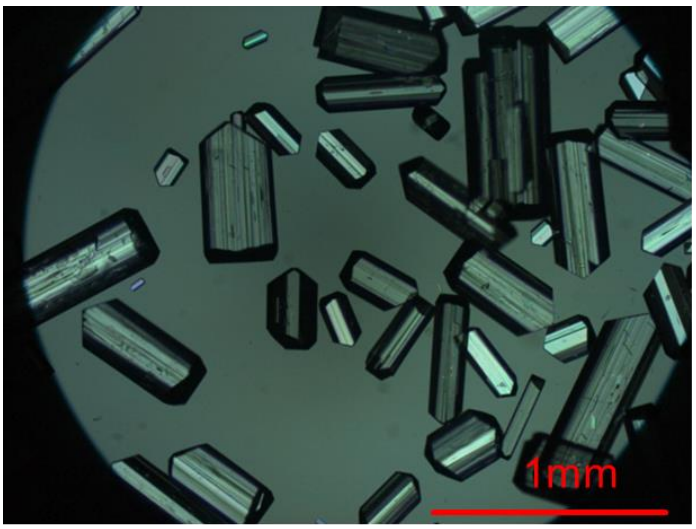

(a)

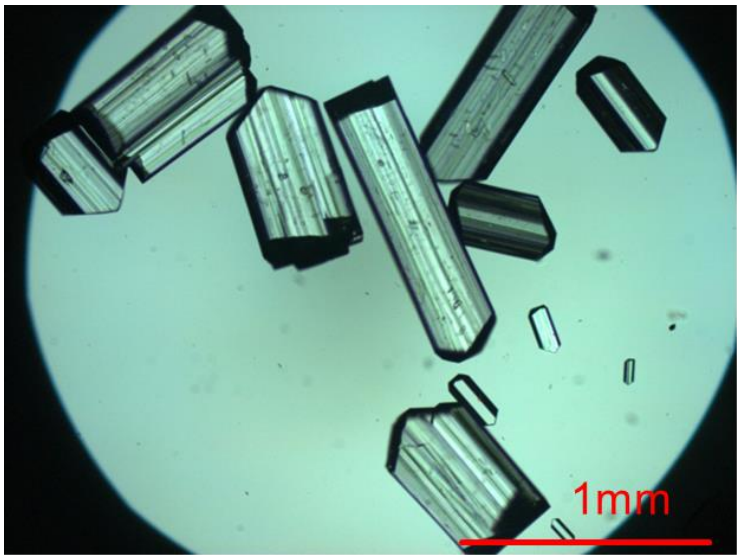

(b)

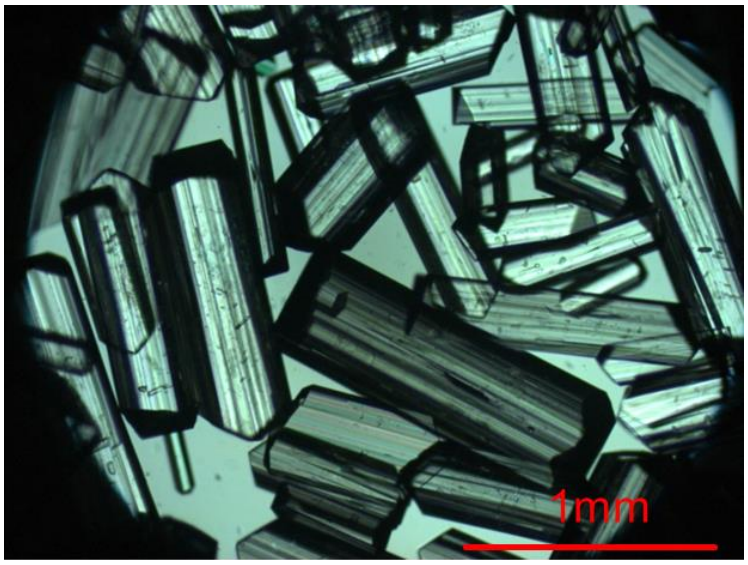

(c)

Figure 3.7. Microscopy images (with polarizers) of slurry of MSG crystals in aqueous solution for the validation temperature-cycling experiment at the end of (a) cycle 1, (b) cycle 3, and (c) cycle 7.

We will see in the solute concentration measurements in Section 3.3.2 that the solute concentration at the lowest temperature, when the slurry samples are collected, increases little from one cycle to the next. Since the total quantity of solute molecules is constant, the total mass of crystals when samples are collected changes slowly with cycle number, which suggests that the increase in the crystal dimensions after each cycle is mostly explained by a reduction in the total number of crystals during each dissolution step. For this reduction to occur, a significant fraction of the crystals becomes small enough to completely dissolve in each cycle. This observation implies that the CSD must become broader during each cycle, which can only occur in the PBM (3.2) if the growth and/or dissolution rates are size dependent. Most reported dissolution rate expressions are size-dependent [120] whereas most reported growth rates are size-independent [41], so these assumptions were made in this article.

3.3.2. Evolution of crystal dimensions and solute concentration for the estimation temperature-cycling experiment

The solute concentration during the estimation temperature-cycling experiment is shown in Fig. 3.8. For the first cycle, the temperature was held constant immediately after the first heating ramp, to enable a qualitative assessment of the dissolution rate. The solution concentration reaches a constant value shortly after the temperature is held constant, indicating that the dissolution rate is fast enough for the solute concentration to quickly reach steady-state (and hence the saturated concentration).

The solute concentration at the highest temperature (~65°C) is almost the same for each cycle (Fig. 3.8, where each narrow peak arises from overshooting of the temperature at each transition between heating to cooling), and the supersaturation is largely consumed before the next heating stage (Fig. 3.9a). Given that the solute conditions are essentially the same at the start of each

cooling stage, the increase of solute concentration at the end of each cooling stage (35°C, see Fig. 3.8), must be associated with a decrease in the overall crystal mass grown during each cycle. As the average supersaturation during each cooling stage increases (thus the growth rate increases [40]) with cycle number (Fig. 3.9a), the decrease in the overall crystal mass grown is explained by a reduction in the amount of crystal surface area in each subsequent cycle. This analysis is consistent with a decrease in the total number of crystals at the end of each cycle, as the crystals become larger, as seen in the FBRM statistics and PVM and optical microscopy images (Figs. 3.3 to 3.5).

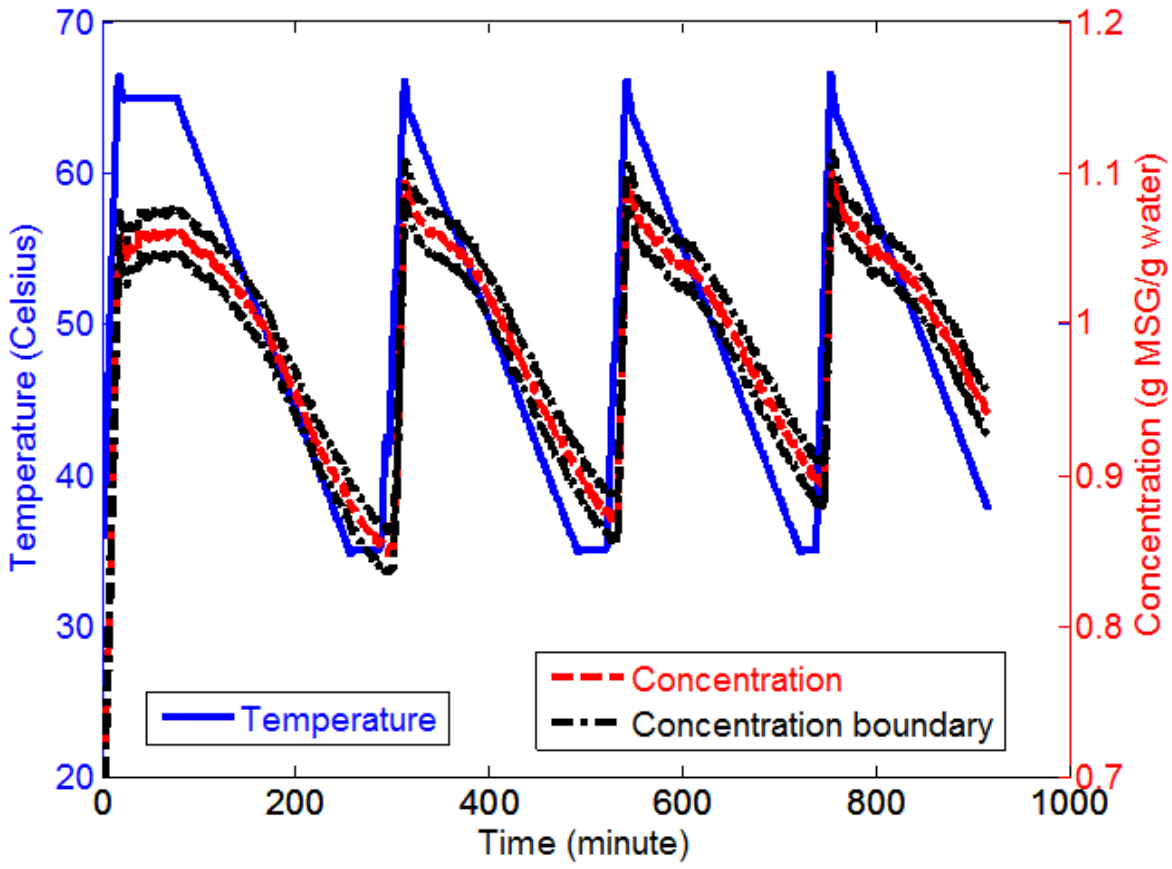

Figure 3.8. Solute concentration profile over time for the estimation temperature-cycling experiment. The time range covers the first four cycles. Beyond that time range (after point 4g in Fig. 3.2), there was no FTIR equipment available. The distance along the vertical axis between

red and black lines is σ_C in (3.4), which is the predicted standard deviation of solute concentration.

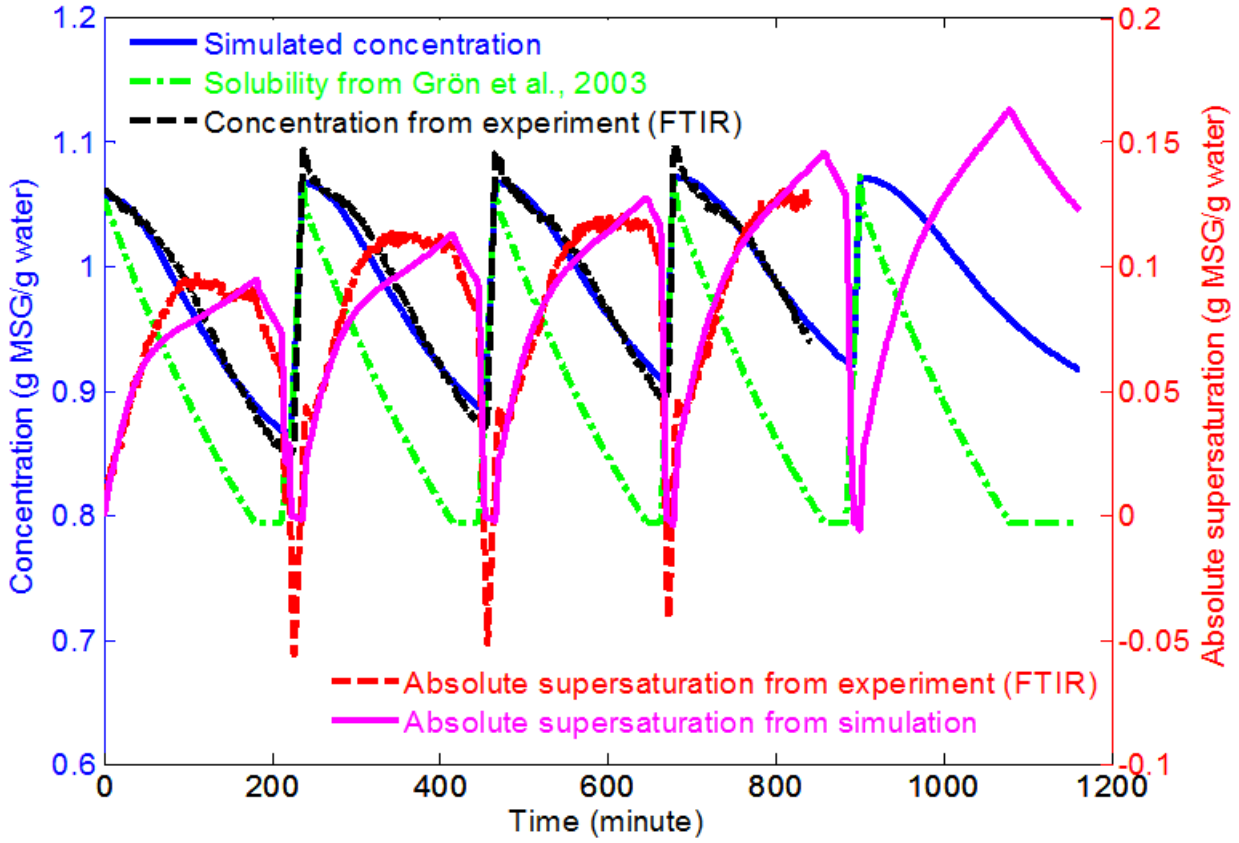

(a)

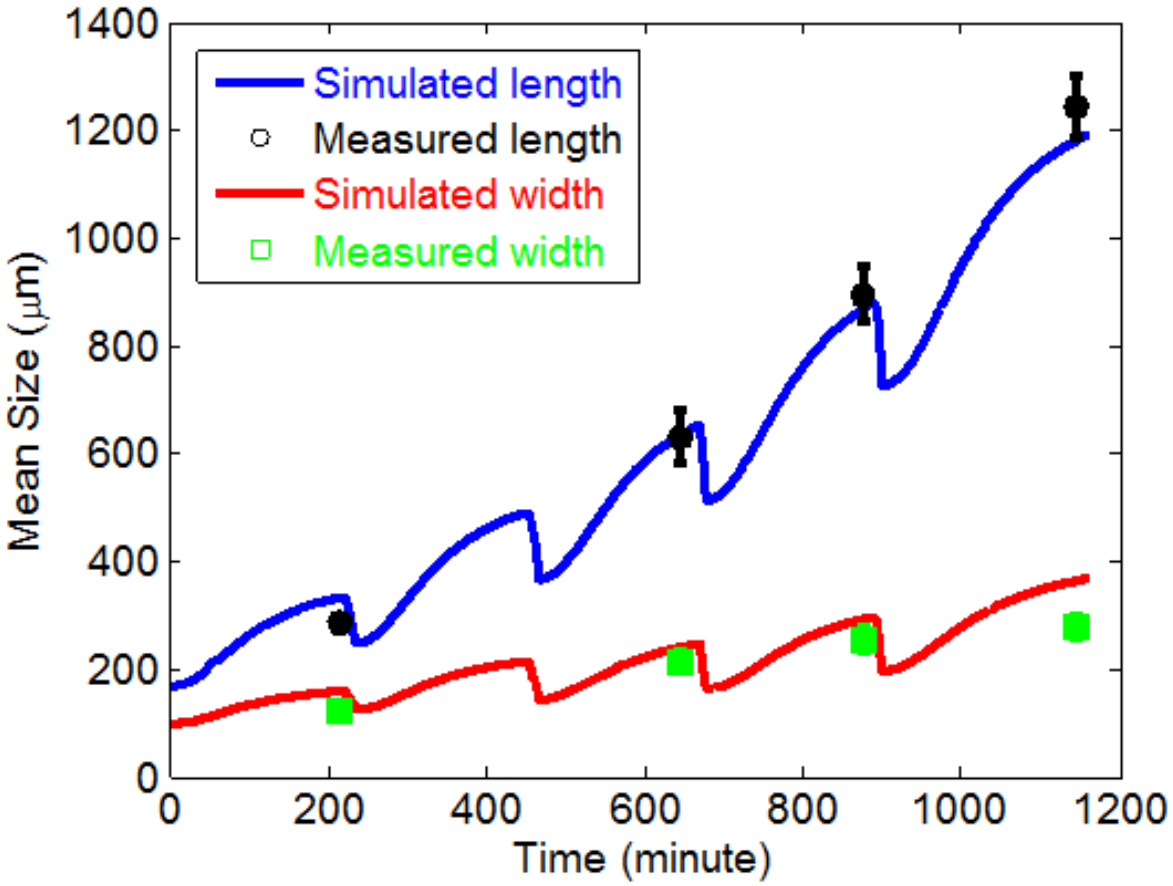

(b)

Figure 3.9. Comparison between experimental data and model predictions using the kinetic parameters in Table 3.2 for the estimation temperature-cycling experiment for (a) solute concentration and absolute supersaturation (the solubility, which is computed based on the implemented temperature, uses the same vertical axis as the solute concentration), and (b) mean crystal length (experiment: black circle; model: blue line) and width (experiment: green square; model: red line).

The use of the in-situ measurements of the solute concentration and crystal mean length and width to estimate the dissolution and growth kinetics is described next.

3.3.3. Simulation and prediction of CSDs with estimated kinetic parameters

The two-dimensional dissolution and growth kinetic parameters determined by the application of least-square estimation to the data from the estimation temperature-cycling

experiment are reported in Table 3.2, with comparisons between model predictions and experiments in Fig. 3.9. The estimated parameters for the growth and dissolution rates in Table 3.2 have values that are consistent with theory [40], [120]. About half of the model parameters were set based on theory or experimental studies by other groups, as described in the caption of Table 3.2, and the simulation parameters are in Table 3.4. The solute concentration from the population balance model (3.2) tracks the experimental value, including the slow increase in the minimum solute concentration in each cycle (Fig. 3.9a). The mean crystal length and widths from the model also track the optical microscopy measurements quite closely through all of the cycles, with somewhat larger deviations for the ratio of the mean length and mean width (Fig. 3.9b).

Table 3.4. Parameters used in the numerical simulation of the population balance model (3.2) in the estimation temperature-cycling experiment.

Variable	Description	Values	Units
Δt	Time step	0.05	minute
ΔW	mesh size for the width	5.0	μm
ΔL	mesh size for the length	5.0	μm
$C(0)$	initial solute concentration	1.0558	g MSG/g water
M_s	mass of solvent (water)	begins with 60.0	g
	times that slurry sample was collected	215, 645, 875, 1145	minute
T	real-time temperature	35.0 to 65.0	°C
	number of temperature points	1162	dimensionless

The kinetic parameters in Table 3.2 were used to predict the mean crystal length and width (Fig. 3.10) in another temperature-cycling experiment (e.g., the 7-cycle validation experiment,

detailed in Section 3.2.4 and Table 3.5). The predictions closely track the experimental data throughout the temperature cycles (Fig. 3.10), except at the 7th cycle, which is consistent with the accumulation of the effects of model uncertainties on model predictions that would be expected in any process that has states whose values continue to drift over time. The mean crystal length prediction is especially accurate, with negligible prediction error for cycles 1, 2, and 3 and <10% prediction error at Cycle 7. The mean crystal width and the ratio of length to width have larger deviations. The crystal size distributions at the sampling times were also calculated (Figs. 3.11 to 3.12) based on the estimated kinetic parameters (Table 3.2). The CSDs from the PBM grow wider with cycle number, which is consistent with having size-dependent dissolution rates in the model, and consistent with experimental measurements (Table 3.7). The trends in mean width, length, and aspect ratio in Fig. 3.10 and Table 3.6 agree with FBRM CLD data (Fig. 3.6).

Table 3.5. Parameters used in the numerical simulation of the population balance model (3.2) in the validation temperature-cycling experiment.

Variable	Description	Values	Units
Δt	Time step	0.05	minute
ΔW	mesh size for the width	5.0	μm
ΔL	mesh size for the length	5.0	μm
$C(0)$	initial solute concentration	1.0024	g MSG/g water
M_s	mass of solvent (water)	begins with 60.0	G
	times that slurry sample was collected	199, 379, 567, 1297	Minute
T	real-time temperature	35.0 to 60.0	°C
	number of temperature points	1318	dimensionless

Table 3.6. Mean aspect ratio and standard deviations from microscope measurements for the 7-cycle experiment.[a]

	Cycle 1	Cycle 2	Cycle 3	Cycle 7
Mean aspect ratio	2.349	2.399	2.622	2.835
Standard deviation	0.064	0.050	0.059	0.053

[a]The sampling points are defined in Fig. 3.6.

Table 3.7. Crystal length and width measurement from the 7-cycle validation experiment.[a]

Cycle number	Minimum width (μm)	Maximum width (μm)	Minimum length (μm)	Maximum length (μm)	Range of width (μm)	Range of length (μm)	Number of crystals
1	17.0	345.3	38.0	1056.5	328.3	1018.5	201
2	25.6	389.8	36.9	1295.5	364.2	1258.6	287
3	26.8	474.8	81.0	1176.7	448.0	1095.7	138
7	40.2	651.2	160.5	1505.2	611.0	1344.7	187

[a]The cycle numbers are defined in Fig. 3.3.

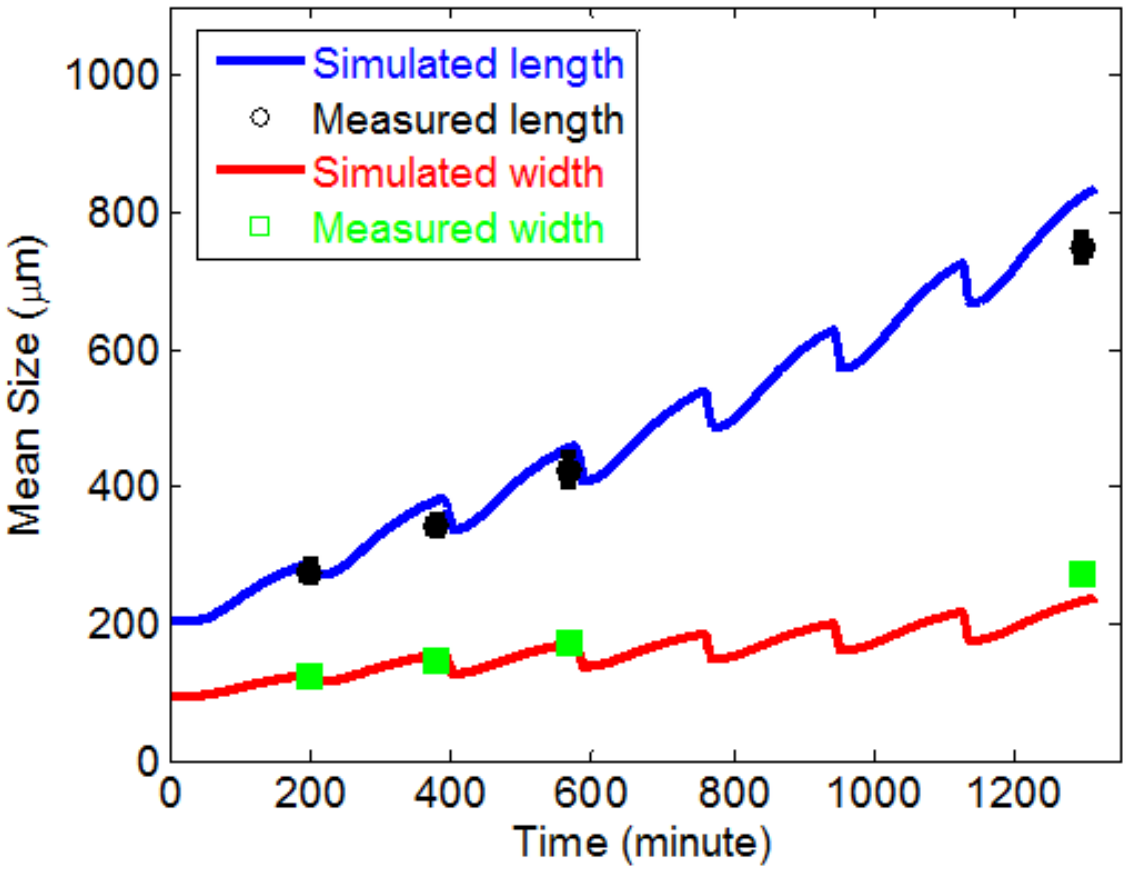

Figure 3.10. Comparison between experimental data and model predictions using the kinetic parameters in Table 3.2 for the estimation in the validation temperature-cycling experiment (7 cycles) for the mean crystal length (experiment: black circle; model: blue line) and width (experiment: green square; model: red line). The model expected errors in the mean crystal length and width are reported in Table 3.9. The measurement error bars in the plot are the sample standard deviations computed by resampling the crystal size measurements.

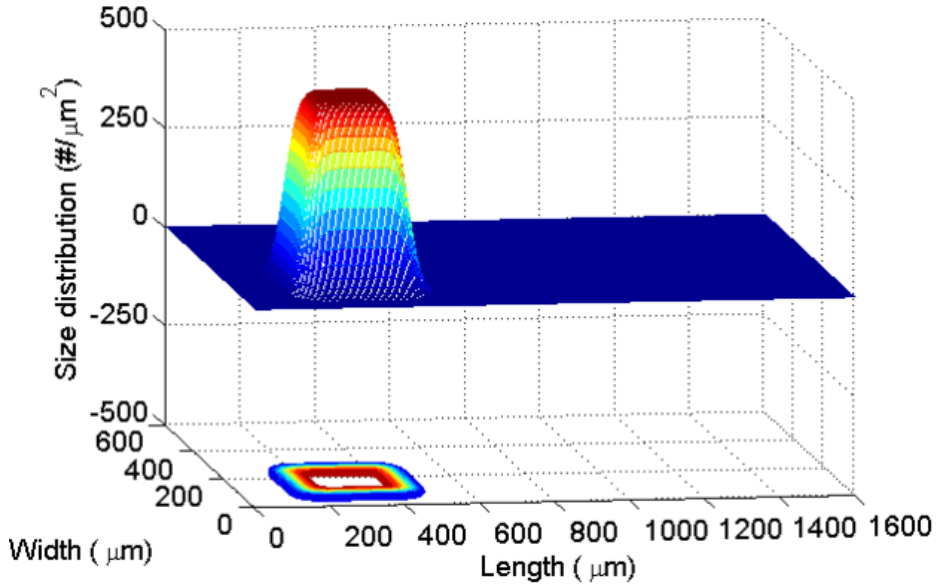
500
250
0
-250
-500
Size distribution (#/μm2)
600
400
200
0
Width (μm)
0
200
400
600
800
1000
1200
1400
1600
Length (μm)

(a)

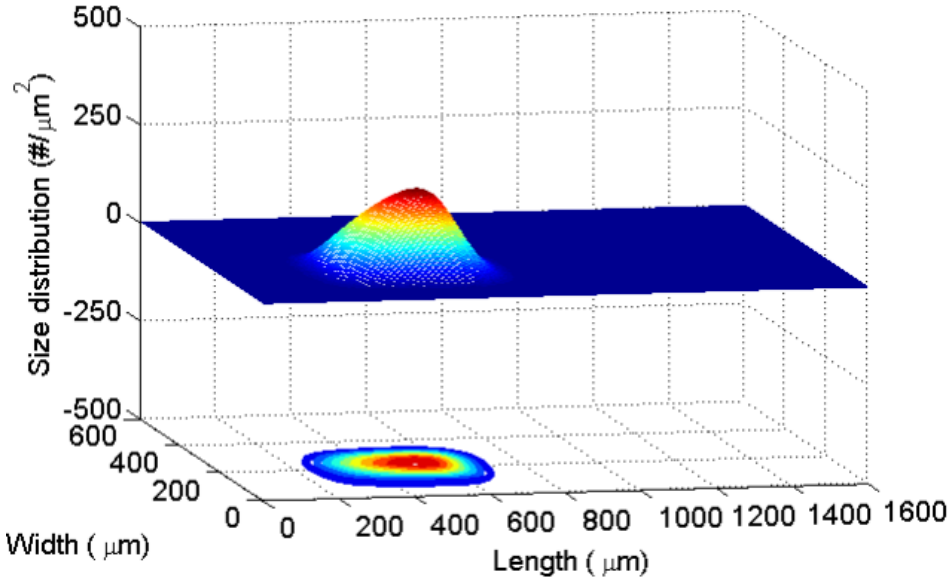
500
250
0
-250
-500
Size distribution (#/μm2)
600
400
200
0
Width (μm)
0
200
400
600
800
1000
1200
1400
1600
Length (μm)

(b)

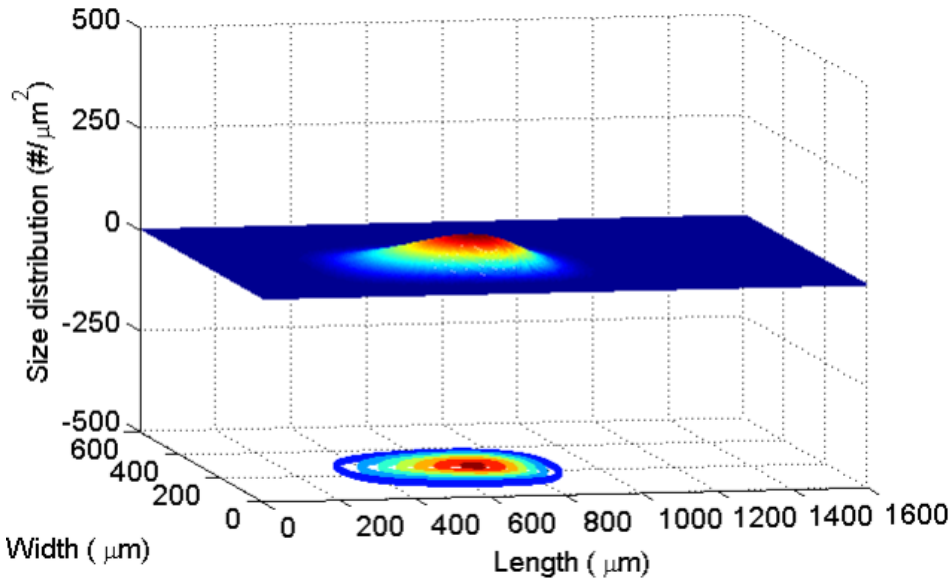
500
250
0
-250
-500
Size distribution (#/μm2)
600
400
200
0
Width (μm)
0
200
400
600
800
1000
1200
1400
1600
Length (μm)

(c)

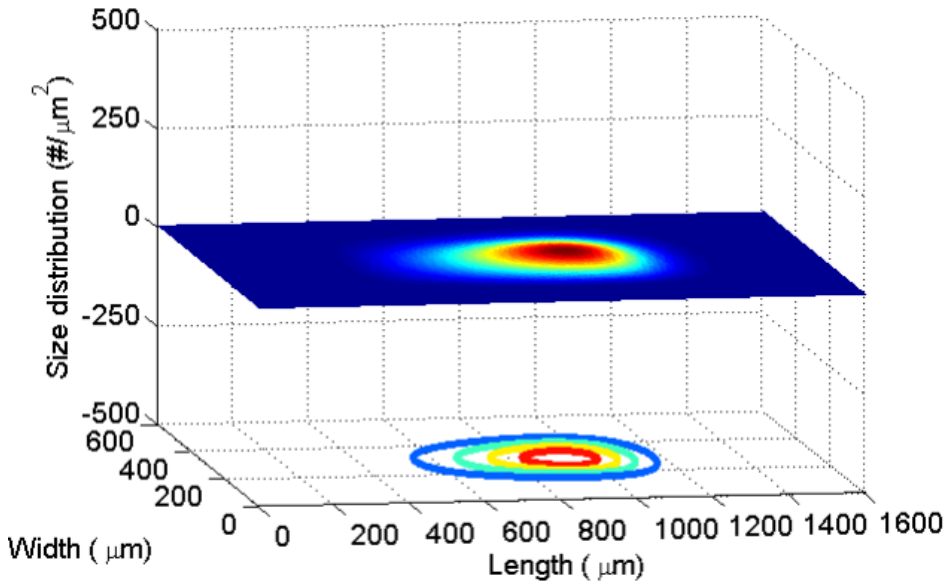
500
250
0
-250
-500
Size distribution (#/μm2)
600
400
200
0
Width (μm)
0
200
400
600
800
1000
1200
1400
1600
Length (μm)

(d)

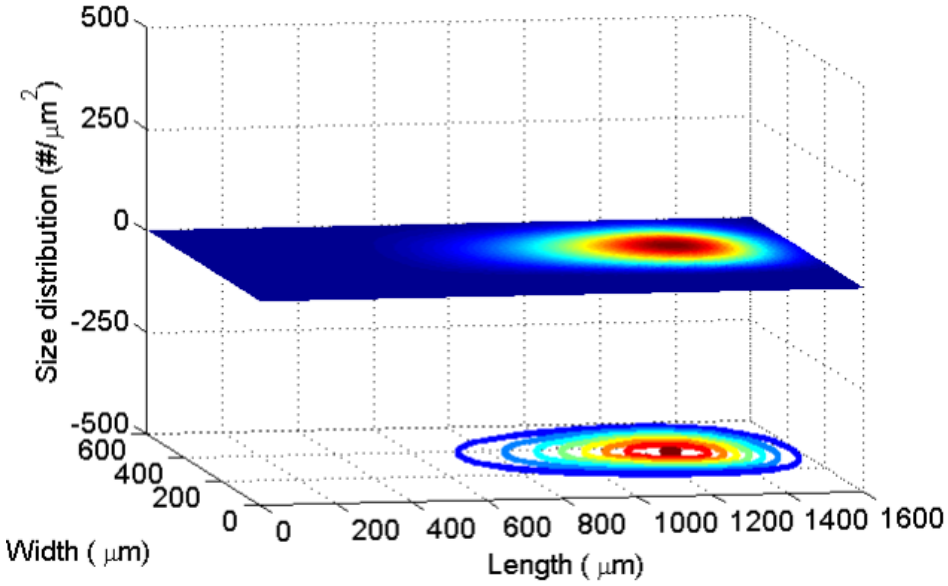

(e)

Figure 3.11. Crystal size distributions $f(L,W,t)$ of MSG slurry from model simulation using the kinetic parameters in Table 3.2 for the 5-cycle estimation temperature-cycling experiment, with the points as in Fig. 3.2: (a) 1a; (b) 2f; (c) 3b; (d) 4d; (e) 5c.

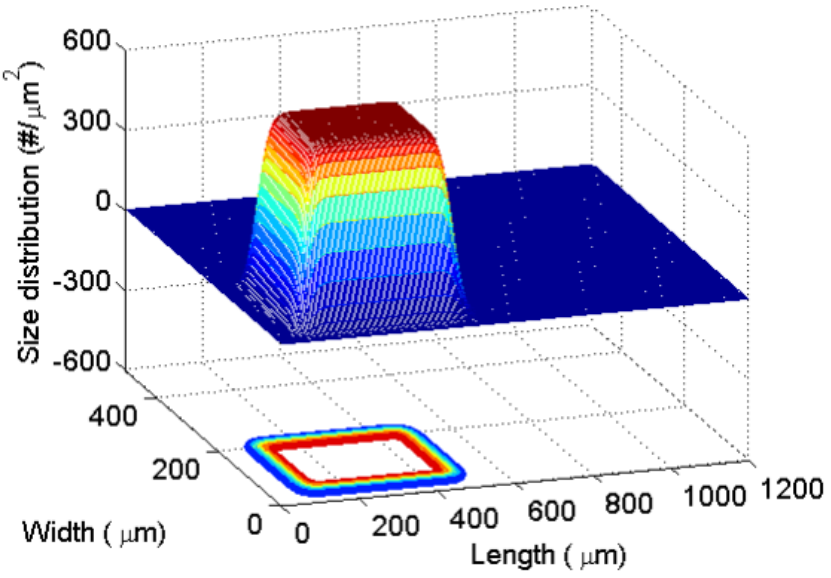

(a)

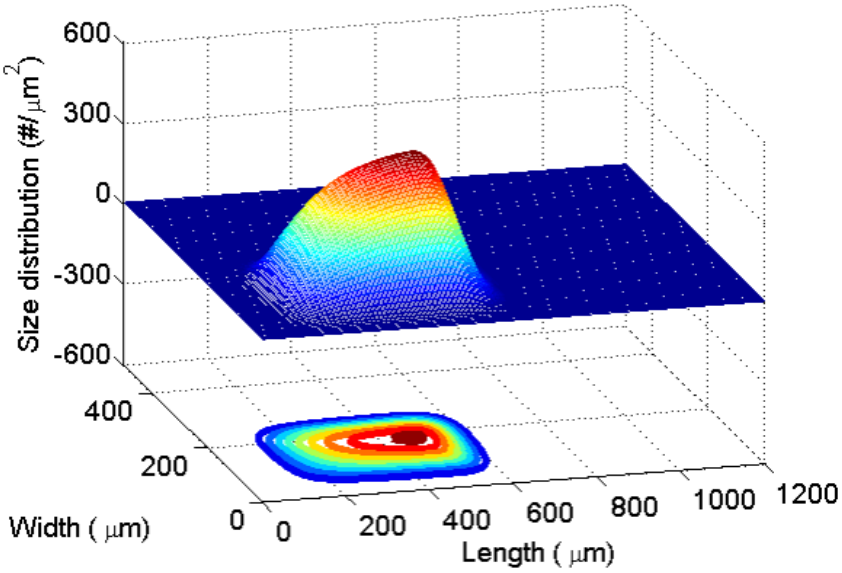
600
300
0
-300
-600
Size distribution (#/μm2)
400
200
0
Width (μm)
0
200
400
600
800
1000
1200
Length (μm)

(b)

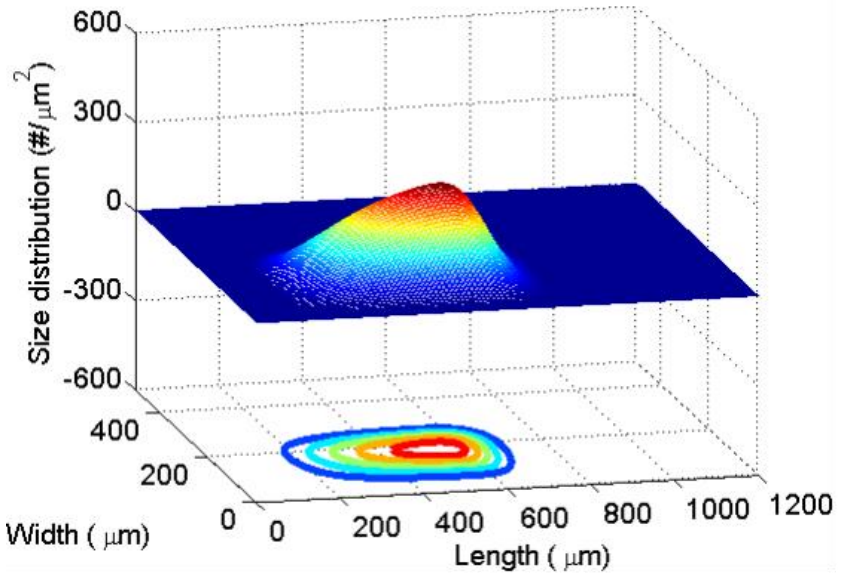
600
300
0
-300
-600
Size distribution (#/μm2)
400
200
0
Width (μm)
0
200
400
600
800
1000
1200
Length (μm)

(c)

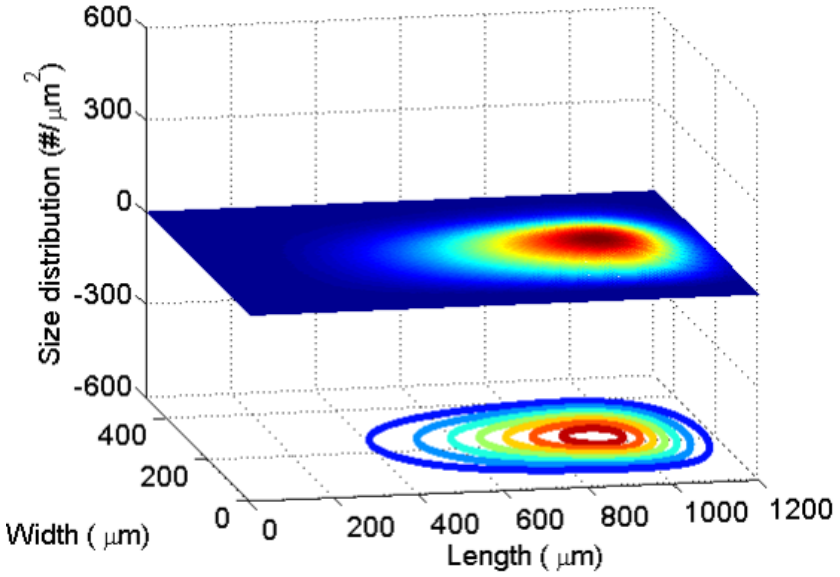

(d)

Figure 3.12. Crystal size distributions $f(L,W,t)$ of MSG slurry from model simulation using the kinetic parameters in Table 3.2 for the 7-cycle validation temperature-cycling experiment at the end of cycles, with the points as in Fig.3.6: (a) cycle 1; b) cycle 2; c) cycle 3; d) cycle 7.

3.3.4. Parameter estimation and accuracy quantification for the population balance model

The parameter error estimates in Table 3.8 were obtained from (3.4) to (3.9) using σ_C = 0.01 g MSG/g water and σ_L and σ_W in Fig. 3.9b, based on the experimental data from the single temperature-cycling estimation experiment. Such parameter error estimates should always be taken as being underestimates, since the statistical assumptions that the errors have zero expectation and are uncorrelated with each other and the independent variables [123] almost never exactly hold in practice. In particular, the derivation of a first-principles model always includes some simplifying assumptions that do not exactly hold, such as perfect spatially-uniform mixing, in which case the statistical assumptions will not hold exactly. Such parameter uncertainty estimates have been found to be useful in past crystallization studies [41], [100], and

so are discussed here with those caveats in mind. A direct comparison to error estimates in past studies is appropriate as the statistical assumptions made in this article are the same.

Table 3.8. Estimated confidence intervals for each parameter estimate in $\underline{\theta}$ [a]

Parameter	Optimal value	Lower bound	Upper bound
$\ln k_{GW0}$	30.78	30.72	30.84
$\ln k_{GL0}$	31.79	31.76	31.82
g_W	2.00	1.97	2.03
g_L	2.00	1.98	2.02
$\ln k_{DW}$	14.3	12.9	15.6
$\ln k_{DL}$	15.3	14.0	16.6

[a] $\underline{\theta}$ was calculated from $\theta_i^* - t_{\alpha_t/2,DOF}\sqrt{V_{\theta,ii}} \le \theta_i \le \theta_i^* + t_{\alpha_t/2,DOF}\sqrt{V_{\theta,ii}}$ (Montgomery and Runger, 2002), where $t_{\alpha_t/2,DOF}$ is the student *t* distribution and the degree of freedom (*DOF*) = 842 + 4 + 4 − 6 = 844 (N_c = 842). For a confidence level of $100(1-\alpha_t)\% = 95\%$, the value of *t* is 1.960. A confidence hyper-ellipsoid cannot be plotted, as $\underline{\underline{\theta}}$ has six dimensions.

From the single estimation temperature-cycling experiment, the estimated 95% confidence intervals for the pre-factor of each growth rate in Table 3.8 are smaller than values reported in past studies that employed up to four batch experiments [125]. The single cycling experiment collects experimental data for a longer period of time than most batch experiments, and was designed to have positive supersaturation with significant growth rate occurring for >90% of the entire time period (see Fig. 3.9a), hence producing data that is highly informative for growth rate estimation. The estimated 95% confidence intervals for the growth exponents are similar in magnitude to past studies [125]. The uncertainties in the dissolution rate constants are higher, up to 10%, which is quite accurate considering that the solute concentration closely follows the solubility curve during dissolution. The dissolution kinetics are so fast that the supersaturation is

never far from zero during dissolution, so the uncertainties in the dissolution rate constants are larger than for the parameters in the growth rate expressions.

3.3.5. Comparison of population balance model predictions with data from validation experiment

The small parametric uncertainties in Table 3.8 provide some confidence that the model predictions could be accurate enough to be used for design purposes. To make a more informed assessment, the parameter covariance matrix was also used to estimate the accuracy of the model predictions for the validation 7-cycle experiment. The parameter covariance matrix $\underline{\underline{V_\theta}}$ remains the same, while the sensitivity matrix is specific for each experiment. The sensitivity matrix for the 7-cycle experiment $\underline{\underline{F_7}}$ was calculated using the same central finite difference method. The prediction error covariance matrix $\underline{\underline{V_Y}}$ was calculated from $\underline{\underline{V_Y}} = \underline{\underline{F_7}}^{\mathrm{T}} \underline{\underline{V_\theta}} \underline{\underline{F_7}}$. The diagonal elements of $\underline{\underline{V_Y}}$ include the standard deviations of mean crystal length (σ_{L7}) and width (σ_{W7}) from the model prediction, all of which are listed in Table 3.9. The 95% prediction intervals for the predicted mean crystal length and width are estimated to be ±12.5 μm and ±2.5 μm, respectively, at Cycle 7, suggesting that the difference between the model predictions and experimental data in Fig. 3.10 is more likely to be due to uncertainties in the measurements rather than uncertainties in the model predictions.

Table 3.9. The standard deviation of the mean crystal length and width predicted by the model with its uncertainty description, with the time points being the same as in Fig. 3.12.[a]

Time points	Standard deviation of the mean crystal length (σ_{L7}), μm	Standard deviation of the mean crystal width (σ_{W7}), μm
Cycle 1	1.7249	0.4516
Cycle 2	2.8045	0.4993

Cycle 3	3.0404	0.4663
Cycle 7	6.2465	1.2851

[a]The prediction errors are much smaller than the noise in the mean crystal length and width measurements, so only bars on the estimated experimental measurement noise are shown in Figs. 3.9 and 3.10.

3.4. Summary

Temperature-cycling experiments were designed in which the mean crystal dimensions and aspect ratio significantly increased at the end of each cycle, in a much smaller number of cycles than in previous studies [97], [101]. FBRM, a commercial instrumentation that is readily available in pharmaceutical laboratories, was used for the in-situ simultaneous measurement of crystal shape and size for rod-like crystals during a temperature cycling experiment. The temperature-cycling experimental design may also be applied to semi-continuous and continuous crystallizers to modify crystal shape.

Dissolution and growth kinetics in a population balance model were estimated along the length and width directions for rod-shaped crystals based on experimental data from commercial instrumentation applied to a single experiment in which the temperature cycles. For the first time, both the growth and dissolution rates along multiple crystal axes were estimated from a multidimensional population balance model with a limited number of minimum-variance kinetic parameter estimates, based on solute concentration and crystal dimension measurements in a single experiment. The model outputs tracked well the experimentally measured mean crystal dimensions and solute concentrations. With the same parameter estimates, the model predicted the crystal dimensions for another temperature-cycling experiment reasonably well (Fig. 3.10). Both this observation and uncertainty analysis suggested that growth and dissolution rates estimated in a single temperature-cycling experiment might be suitable for designing a temperature-cycling protocol for optimizing the size and shape of the product crystals.

4. ENHANCED CSD CONTROL IN SEMI-CONTINUOUS CRYSTALLIZERS BY COMBINING CONTINUOUS SEEDING AND CONTROLLED GROWTH

4.1. Introduction

A control objective in the pharmaceutical industry is to manufacture crystals with a desired size distribution, so as to meet bioavailability requirements such as for inhalers or pulmonary delivery [126]–[128]. As described in these papers and elsewhere, the desired crystal size distribution for many pharmaceutical delivery applications is not necessarily the narrowest, and can have tight specifications within certain size ranges. Improved distribution control can also eliminate or reduce the amount of post-crystallization processing such as milling that can cause changes in polymorphic identity [129]–[134] and can enable the manufacture of size distributions with higher surface area during operations to reduce the likelihood of uncontrolled nucleation being induced by changes in contaminant profiles. Various methods have been proposed to control the size distribution during organic or inorganic crystallizations [62], [63], [75], [78], [79], [103], [135]–[137].

The controllability of the crystal size distribution is limited in industrial batch crystallizations, in which seed crystals are added near the start of the batch, especially when multiple concurrent phenomena can occur such as growth, aggregation, and nucleation, which can also have multiple concurrent mechanisms [138]. A theoretical study predicted that the controllability of the crystal size distribution could be greatly increased by employing continuous seeding, where crystals are continuously fed to a well-mixed tank crystallizer at any times during the batch [3]. The stirred tank was assumed to operate at a controlled size-independent growth rate by applying concentration feedback control [75], [77], which has produced negligible nucleation in numerous pharmaceutical crystallizations in academic and industrial laboratories [75], [77], [78], [80],

[139], [140]. Aggregation was assumed to be suppressed by judicious selection of seed crystals, in particular, feeding the seed crystals in a slurry and selecting crystals large enough to avoid sticking together. In the concentration feedback control strategy, the control system adjusted the temperature or addition rate to track a setpoint trajectory in the crystallization phase diagram [75]. The insensitivity of this approach to most variations in growth and nucleation kinetics and most practical disturbances has been demonstrated in experiments and simulations for many batch cooling and antisolvent crystallizations in polymorphic and non-polymorphic systems [8], [75].

The main objective of this paper is to experimentally demonstrate the ability of continuous seeding to produce a nearly uniform crystal size distribution, which is a shape that has never been reported as the product of a batch cooling crystallization. In this approach, the crystal nucleation and growth processes are decoupled. Seed crystals are continuously added at appropriate times to a well-mixed cooling crystallizer operating under conditions of growth with negligible nucleation. There are many ways to generate these seed crystals (in a slurry) continuously. One common approach is to combine solution and antisolvent streams in dual impinging jets, which can produce crystals of narrow size distribution for many solute-solvents systems [18], [24], [141]. At appropriate flow rates, the dual impinging jets can generate high-intensity micromixing of fluids to quickly achieve a nearly homogeneous composition of high supersaturation before the onset of primary homogeneous nucleation so that the exit crystals have a narrow and reproducible size distribution. In contrast to the literature, this paper utilizes a DIJ configuration that combines hot and cold saturated solutions to generate seed crystals with a narrow size distribution, to exploit the fact that the micromixing is not truly instantaneous, so that supersaturations high enough for primary homogeneous nucleation are generated before

complete mixing occurs. To our knowledge, this is the first time that experimental data have been reported for such a cooling DIJ.

4.2. Experimental methods

This section summarizes the experimental methods for characterization of the solubility, metastable limit, and growth kinetics for L-asparagine monohydrate (LAM) in aqueous solution by attenuated total reflection-Fourier transform infrared (ATR-FTIR) spectroscopy, chemometrics, and focused beam reflectance measurement (FBRM). Also discussed are the operations of the cooling DIJ and mixing-tank crystallizers that are coupled for the purposes of generating a target crystal size distribution.

4.2.1. Materials and instrumentation

Infrared spectra for L-asparagine monohydrate (LAM, from Sigma Aldrich) in de-ionized (DI) water were collected in a 2-liter stirred tank by an in situ Dipper-210 ATR immersion probe (Axiom Analytical) with ZnSe as the internal reflectance element attached to a Nicolet 6700 FTIR spectrophotometer, 64 scans collected for each spectrum, and DI water at 25°C used for the background (see Fig. 4.1). This solute-solvent system has selected because its solubility vs. temperature relationship is very similar to many pharmaceutical compounds.

(a)

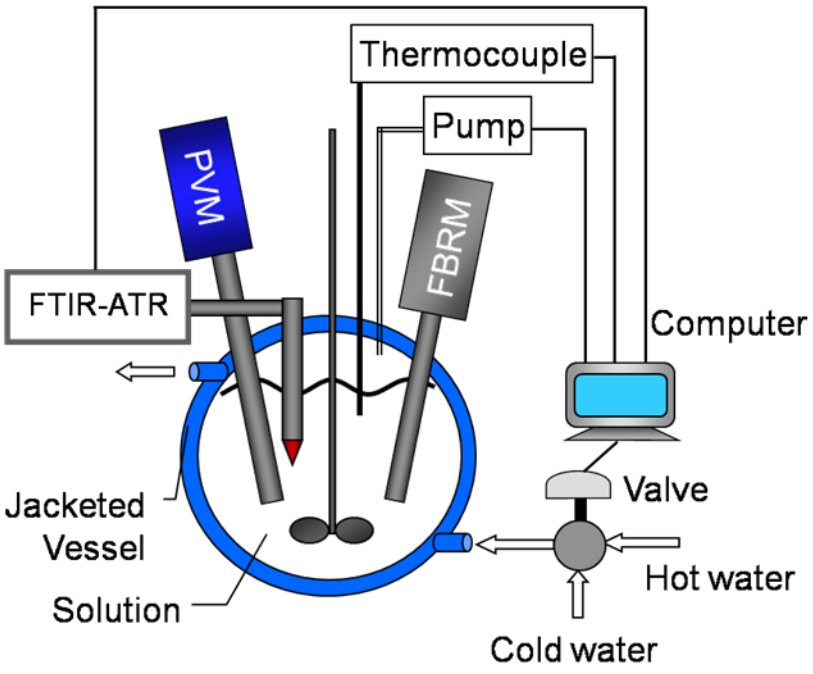

(b)

Figure 4.1. Photograph (a) and schematic (b) of stirred-tank crystallizer instrumented with in situ ATR-FTIR immersion probe, FBRM probe, and thermocouple. The PVM and pump was not used in this study.

During crystallization, the temperature of the slurry in the stirred tank was controlled by ratioing hot and cold water to the jacket of a round-bottom or cylindrical flask with a control valve using a proportional-integral control system designed via internal model control [80] and was measured every 2 seconds using a Teflon-coated thermocouple attached to a Data Translation 3004 data acquisition board via a Fluke 80TK thermocouple module [81]. The total counts/second of LAM crystals in solution were measured every 10 seconds using Lasentec FBRM with version 6.0b12 of the FBRM control interface software [80]. Images of crystal slurries were taken with a polarized microscope (Leica DMI 4000B) with cameras Qimaging ReRIGA 2000R (black and white) and Leica DFC 420 (color). Both FBRM and microscope can measure characteristic sizes in the range of about 1-2000 microns. Experimental data were archived and DIJ inlet flows specified using PI software from OSIsoft.

4.2.2. Calibration of ATR-FTIR for solute concentration

A bench-scale stirred-tank crystallizer was cooled at a constant rate of 0.5 °C/min for different known LAM concentrations (Table 4.1) in about 400 grams of aqueous solution, while being measured with in situ ATR-FTIR spectroscopy and FBRM, until an increase in the total counts/s indicated that the metastable limit was reached (the detailed experimental procedures are described elsewhere [77]. The width of the metastable zone at this cooling rate depended on solute concentration, so that a different number of infrared spectra was collected for each temperature.

Table 4.1. ATR-FTIR calibration samples for in situ solute concentration measurement.

Calibration sample	Solute concentration (g/g solvent)	Temperature range (°C)	Number of spectra
Cs1	0.0300	30.4-18.0	27
Cs2	0.0567	42.9-25.1	38

Cs3	0.0834	50.9-34.5	35
Cs4	0.1101	59.4-46.9	27
Cs5	0.1368	63.9-57.1	16

Several chemometrics methods were applied to the absorbance spectra (in the range 1200-1800 cm^{-1}) with known solute concentrations and temperatures to construct a linear calibration model for measurement of the solute concentration (see Fig. 4.2 for representative data and the regression coefficients, with the equipment and procedures being the same as for other solute-solvent systems [54], [77]. The calculations were carried out using in-house MATLAB 5.3 (The Mathworks, Inc.) code except for partial least-squares (PLS) regression, which was from the PLS Toolbox 2.0 (Eigenvector Research, Inc.). The correlation Forward Selection 2 PCR method with a noise level of 0.004 gave the smallest prediction interval of ± 0.00579 g/g solvent while being consistent with the accuracy of the solubility data. The calibration model had the form

$$C = \sum_{j=1200}^{1800} w_j a_j + w_T T + w_0 \quad , \tag{4.1}$$

where C is the solute concentration (g LAM/g water), a_j is the absorbance at frequency j (cm^{-1}), T is the temperature (°C), and w_j, w_T, and w_0 are regression coefficients.

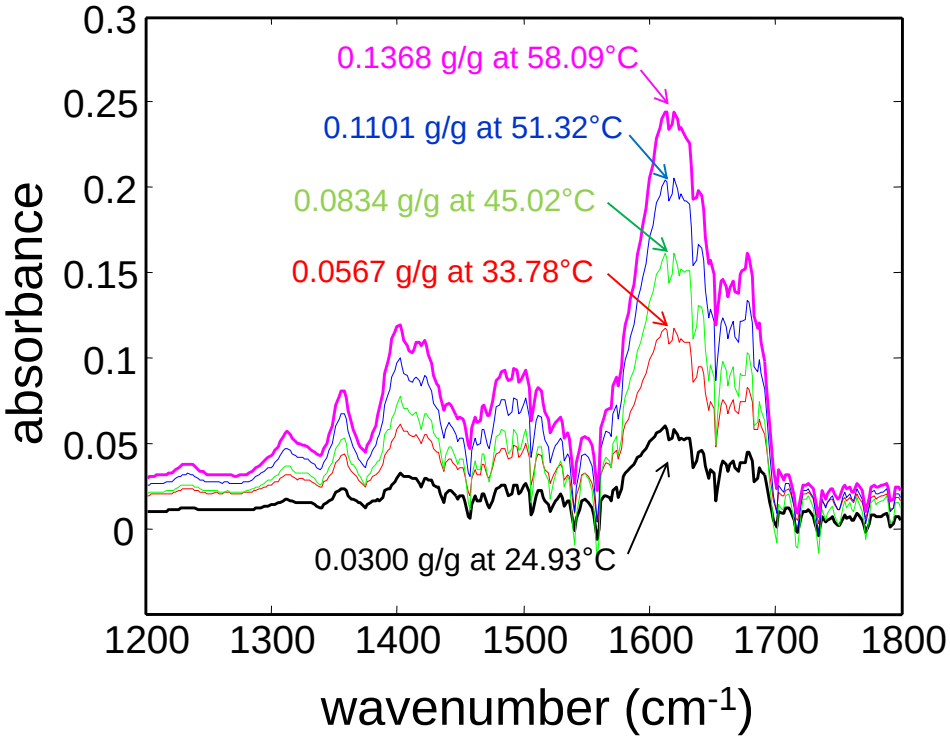

(a)

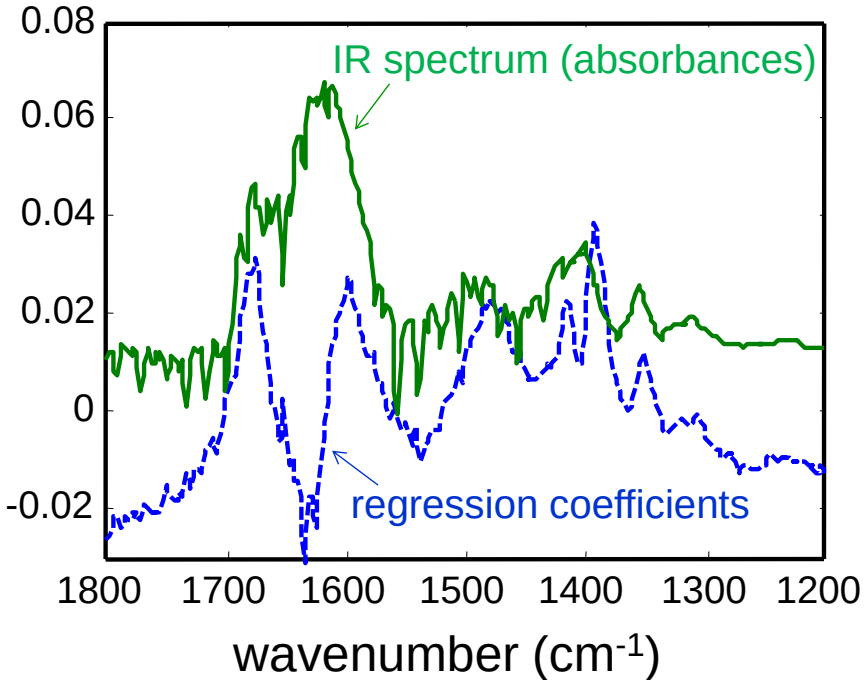

(b)

Figure 4.2. (a) Representative ATR-FTIR spectra of LAM aqueous samples used for calibration (units: g LAM/g water). (b) Regression coefficients of the calibration model relating absorbances

to solute concentration. The calibration model was constructed with chemometrics software [54], with error less than 0.5 mg LAM/g solvent.

4.2.3. Solubility measurement

The IR spectra were collected at different temperatures in an automated experimental system. At each elevated temperature, the slurry was equilibrated for at least one hour before IR spectra were recorded. The equilibration time was enough for the total counts/s to approach a constant value within the measurement noise. The solubility measurements were performed at five values of increasing temperature. The solvent mass and solute concentrations in the solubility experiments were very close to those used in the calibration experiments. The solute concentration was then calculated with the calibration model (Fig. 4.2b) to measure solubilities (see Fig. 4.3a).

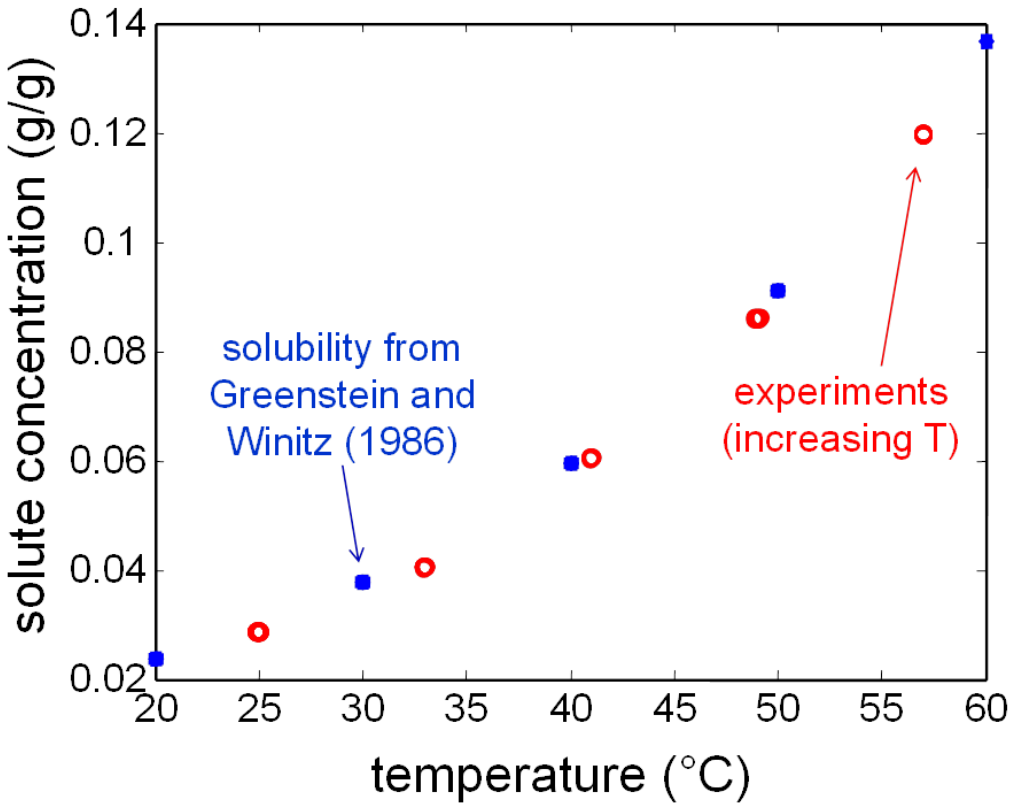

(a)

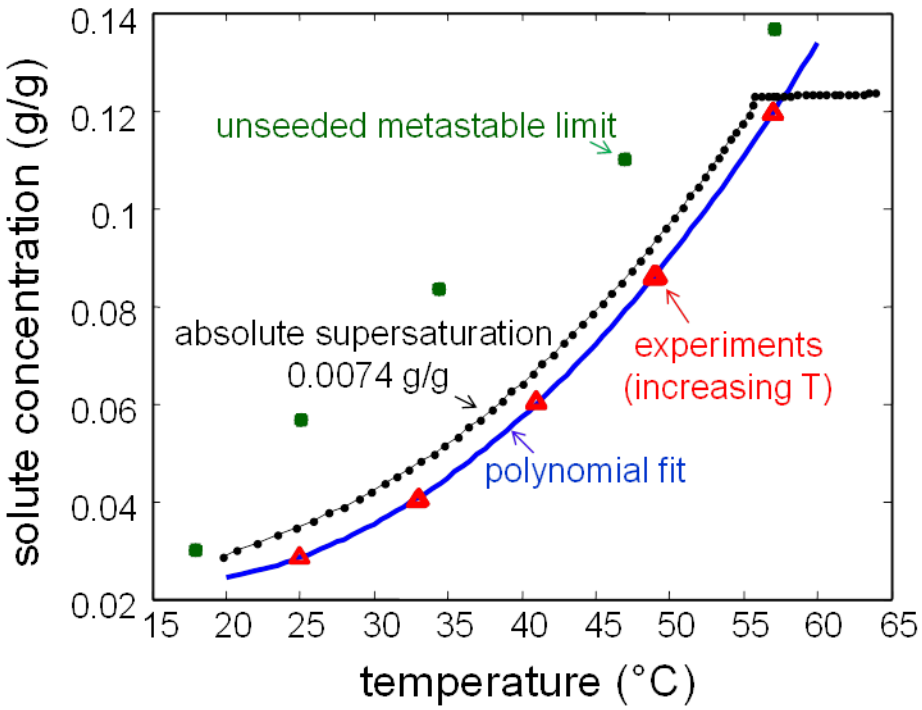

(b)

Figure 4.3. (a) LAM solubility curve compared to reference data from Greenstein and Winitz (1986). Reference data are slightly higher than solute concentrations determined from the calibration model, probably due to use of different grades of water. (b) Representative experimental solute concentrations and temperatures obtained during concentration feedback control for a constant supersaturation level of 0.0074 g/g and a seeding point at 55.5°C. Also shown is the unseeded metastable limit that defines the highest solute concentration for which the calibration model was valid, which is much higher than the solute concentrations used in the concentration feedback control experiments.

4.2.4. Seeded batch crystallizations

An initial set of seeded batch crystallizations were carried out to (i) verify that concentration feedback control could reliably track a constant absolute supersaturation with negligible nucleation and (ii) estimate average growth kinetics. An undersaturated solution with solute concentration 0.122 g LAM/g water was cooled at 0.5 °C/min from 65°C to below the saturation temperature (55.5°C, see Fig. 4.3b). The stirring conditions were very similar to the calibration experiments. Then seed crystals of LAM with mass 6.44% of the expected crystal yield were

added to the solution. The seed crystals (Fig. 4.4a) were generated from crash cooling of high temperature LAM-saturated solution, followed by filtration and vacuum drying at room temperature and then sieving. Crash cooling usually produces a wide size distribution of crystals; to make full use of material, dry seeds of adjacent sieve ranges were combined for the concentration control experiments.

During continuous seeding, the product CSD is a function of the supersaturation [3]. For each batch cooling crystallization, the control algorithm to follow a preset supersaturation profile started shortly after seeding, and continued throughout the rest of crystallization experiment (until the system cooled to about 18°C) [80]. The supersaturation set point profiles were selected within the metastable zone at different constant absolute supersaturations ($\Delta C = C - C_{sat}$) where C_{sat} denotes the solubility (g LAM/g water). In addition to visual inspection by optical microscopy after each experiment, FBRM data collected during each experiment confirmed that negligible nucleation occurred (see Fig. 4.4b).

These experiments with seeds obtained by crash cooling serve to demonstrate good concentration feedback control for the system and, at same time, estimation of temperature-averaged growth rates (For example, as used by [35], [142], [143]. As dry seed crystals have a tendency to agglomerate, slurry seed crystals were used in subsequent experiments. More specifically, for implementation towards the production of a target crystal size distribution, slurry seeds manufactured by dual impinging jets (Fig. 4.5, details below) with size less than 20 μm (Fig. 4.6) were fed to the stirred tank through the crystallizer neck (with residence time of about 1 second). The total mass of seeds added in slurry form was 3.39% of the total expected crystal yield. Similarly, the feedback control algorithm started shortly after seeding, and continued throughout the cooling crystallization experiment.

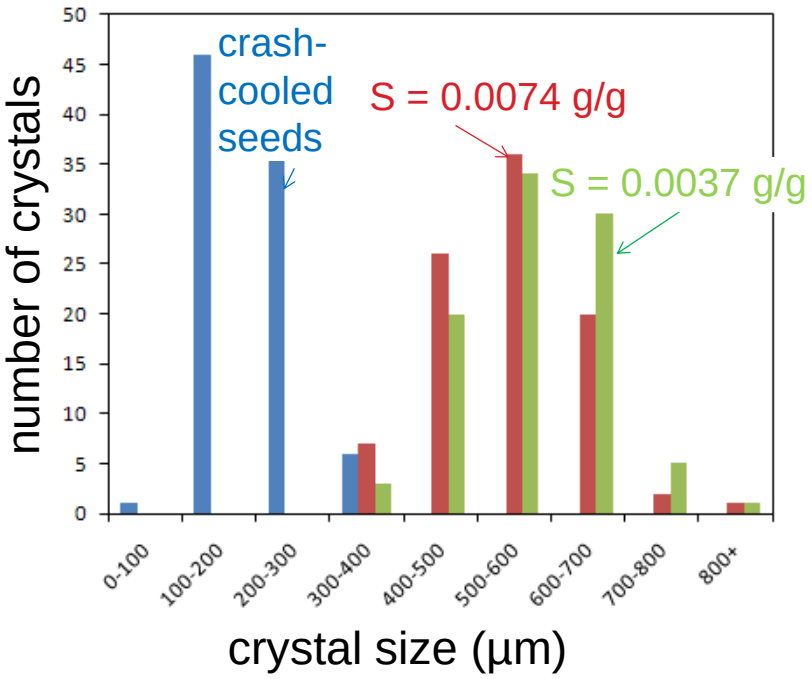

(a)

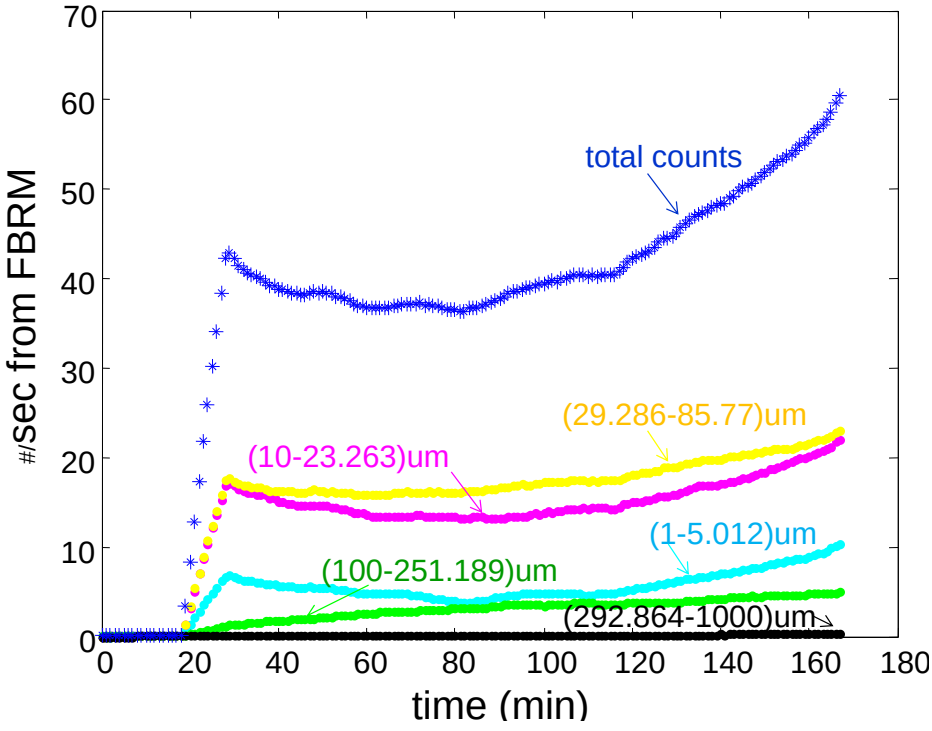

(b)

Figure 4.4. (a) Size distribution of LAM seeds (based on the largest dimension) and product crystals after concentration feedback control at two different values of constant supersaturation, measured from off-line optical microscopy. (b) FBRM counts during concentration feedback control at constant supersaturation of 0.0074 g LAM/g water.

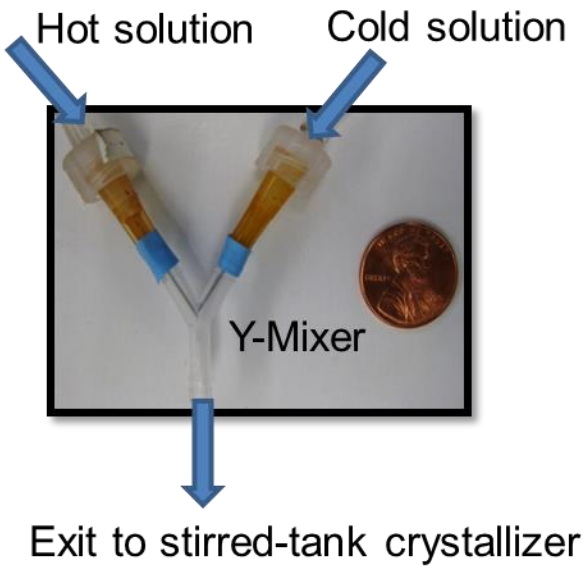

Figure 4.5. Photograph of DIJ configuration for continuous seeding coupled to a stirred-tank crystallizer. Needles were inserted into a standard plastic Y-mixer to generate the seed crystals in Fig. 4.6.

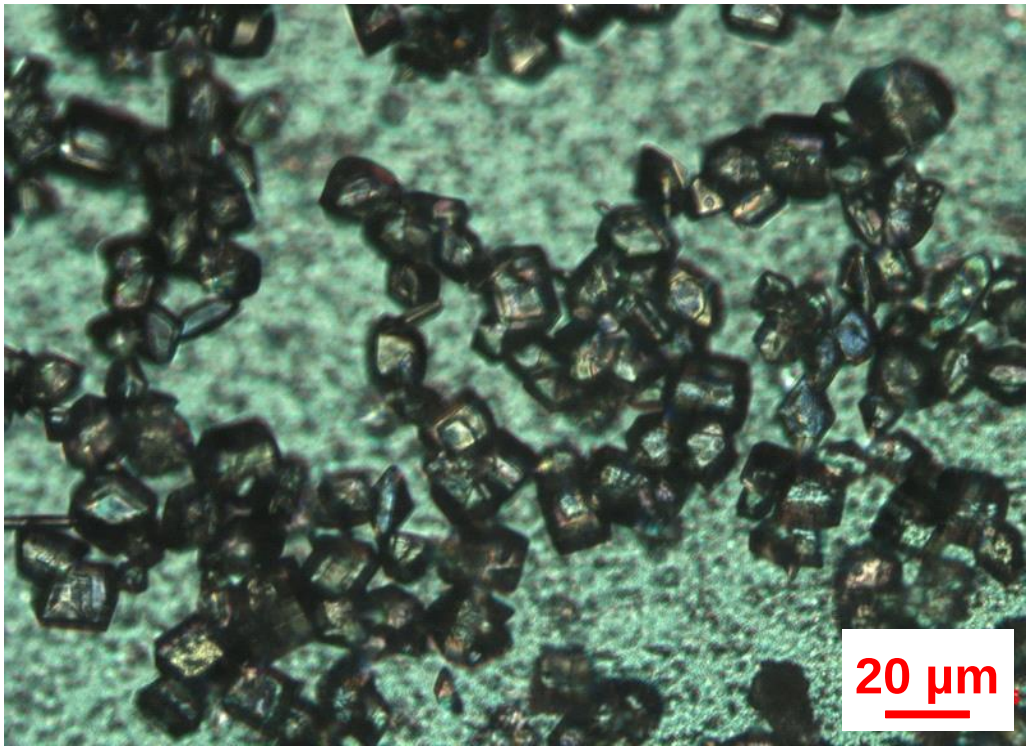

(a)

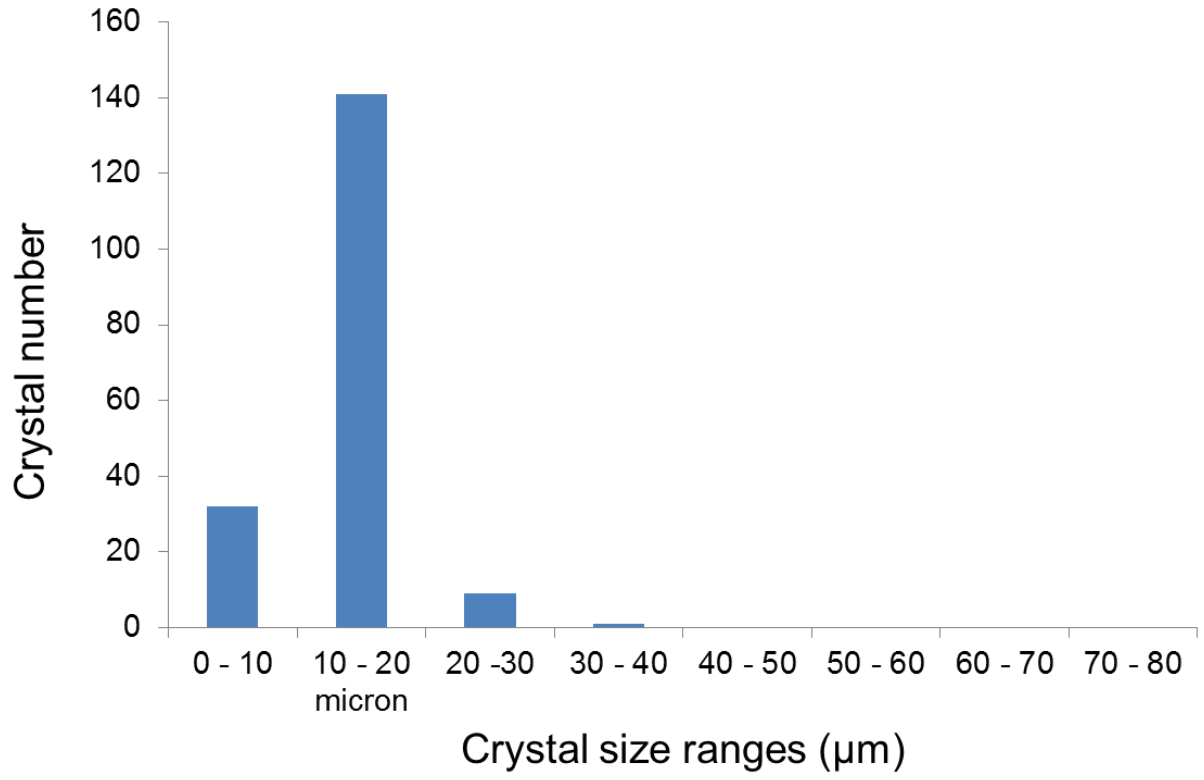

(b)

Figure 4.6. LAM crystals generated by DIJs (scale bar = 20 µm) (a) Microscopy image (with polarizers) and (b) Size distribution measured from off-line microscopy images.

4.2.5. Continuous seeding using dual impinging jets

The crystallizer configuration for the manufacture towards a target size distribution used in this particular experimental implementation (Fig. 4.5) employed a dual-impinging-jet (DIJ) mixer [18], [24], [141] in the shape of a Y to produce seed crystals that were continuously dropped into a 2-liter stirred-tank cooling crystallizer operating under concentration feedback control following a preset constant supersaturation (0.01 g LAM/g water) profile, to exactly correspond to the continuous seeding crystallizer configuration investigated in an earlier theoretical study by [3]. The stirred-tank crystallizer initially contained 1363 ml of saturated solution. The theoretical study indicated that the extra degrees of freedom provided by continuous seeding, instead of only seeding at the start of the crystallization, greatly increase the

controllability of the crystal size distribution. A uniform size distribution was selected for experimental validation of the approach as its shape is very different from the product size distributions produced by cooling crystallizations that only seed at the beginning of the batch. As the optimal jet velocity profile for producing the flattop CSD was nearly constant, to simplify the implementation the experiments employed a constant jet velocity of 1.9 m/s, with a volumetric flow rate of 5.8 ml/min and jet inner diameter of 0.254 mm. The total slurry volume added during the experiment was 88.5 ml. For crystallization with neither nucleation nor aggregation, multiplying the supersaturation and/or mass flow rate of seeds by a constant changes the height and width of the flattop distribution with negligible effect on its shape (for detailed mathematical expressions, see [3], so the theoretically optimal distribution shape can be directly compared to the experimentally obtained distribution for a different solute-solvent system (see Fig. 4.10, measured manually from off-line microscope images of hundreds of crystals). Due to the limited volume limit of the stirred-tank crystallizer, for proof-of-concept purposes, the continuous seeding was allowed to cover a 4.4% volume ratio of the reactor. The seeding time duration could also help tune the width of the product CSD.

Unlike antisolvent/reaction DIJ crystallizations, this experimental implementation generated seed crystals by mixing hot and cold saturated streams (solution concentrations of 0.20 g LAM/g water at 70 °C and 0.03 g LAM/g water at 25 °C). If the micromixing were perfect, then it is straightforward to show from a mass balance and Fig. 3a that the solute concentration of the well-mixed stream for this solute-solvent system would be near saturated conditions, with supersaturation too low ($(C - C_{sat})/C_{sat} = 1.4$) to generate nuclei by primary homogeneous nucleation. Crystals nucleate easily from this cooling DIJ configuration, suggesting that the

micromixing is sufficiently slow in this system that high enough supersaturation is generated near the interfaces between the two streams to induce nucleation.

4.3. Results and discussion

4.3.1. Solubility

The solubility curve of LAM in aqueous solution was fit to a quadratic function to give

$$C_{sat} = 3.084 \times 10^{-2} - 1.373 \times 10^{-3} T + 5.214 \times 10^{-5} T^2 \quad (4.2)$$

(see Fig. 4.3b). The maximum deviation of the experimental data points from the fitted solubility curves (0.0021 g LAM/g water) was within the prediction intervals. The solubility data were also fit to a van't Hoff equation [144]:

$$\ln C_0 = -(a/R)T^{-1} + (b/R)\ln T + c \quad (4.3)$$

where R is the ideal gas constant, T is in units of Kelvin, and C_0 is in units of mole fraction (see Fig. 4.7). The solubility data are in good agreement with [2]; the differences can be attributed to differences in the purity of water in the two sets of experiments. From the coefficients of the solubility curve, the apparent enthalpy of solution [144], $\Delta H^* = a + bT$ of LAM in aqueous solution was calculated to be 35.66 kJ/mol at 298.15 K, and apparent heat capacity as $C_p^* = b =$ 86 J/(mol-K). This calculated enthalpy of solution is in good agreement with calculation by applying the same method to the reference [2] (35.45 kJ/mol) and directly from measurement (33.89 kJ/mol).

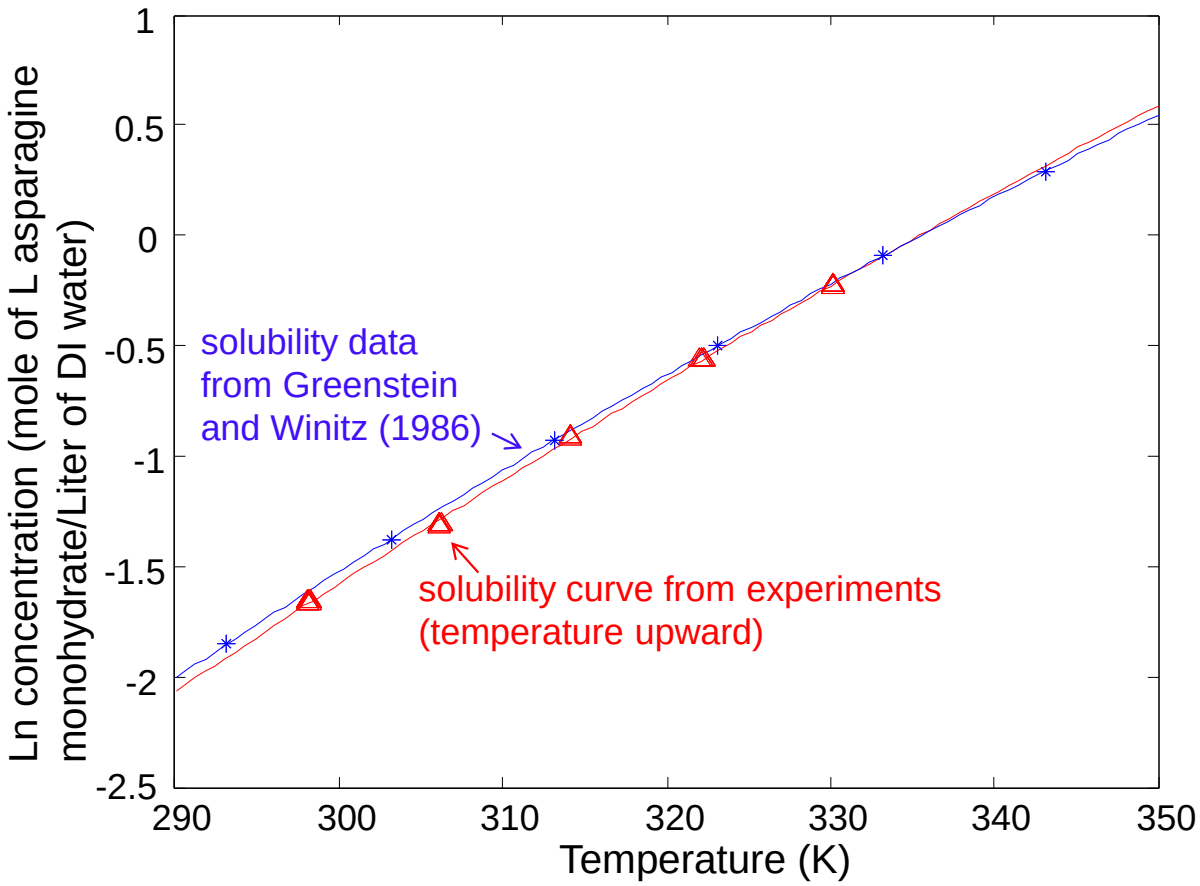

Figure 4.7. van't Hoff equation, $\ln C_0 = 9973.791 T^{-1} + 86.14549 \ln T - 56.68014$, fit to solubilities for LAM in aqueous solution obtained from ATR-FTIR spectroscopy (red triangles). A van't Hoff equation was also fit to previously published solubility data [2] that are shown as blue asterisks.

4.3.2. Initial seeded batch crystallizations.

Batch crystallizations seeded with dry crystals generated by crash cooling (Fig. 4.8) to follow preset constant absolute supersaturation profiles within the metastable zone were implemented using concentration feedback control with cooling rate based on the in situ measurement of the solute concentration (Fig. 4.3b). The solute concentration very closely tracked the setpoint trajectory in the phase diagram as has been observed for many other pharmaceutical compounds (e.g., [77], [80]).

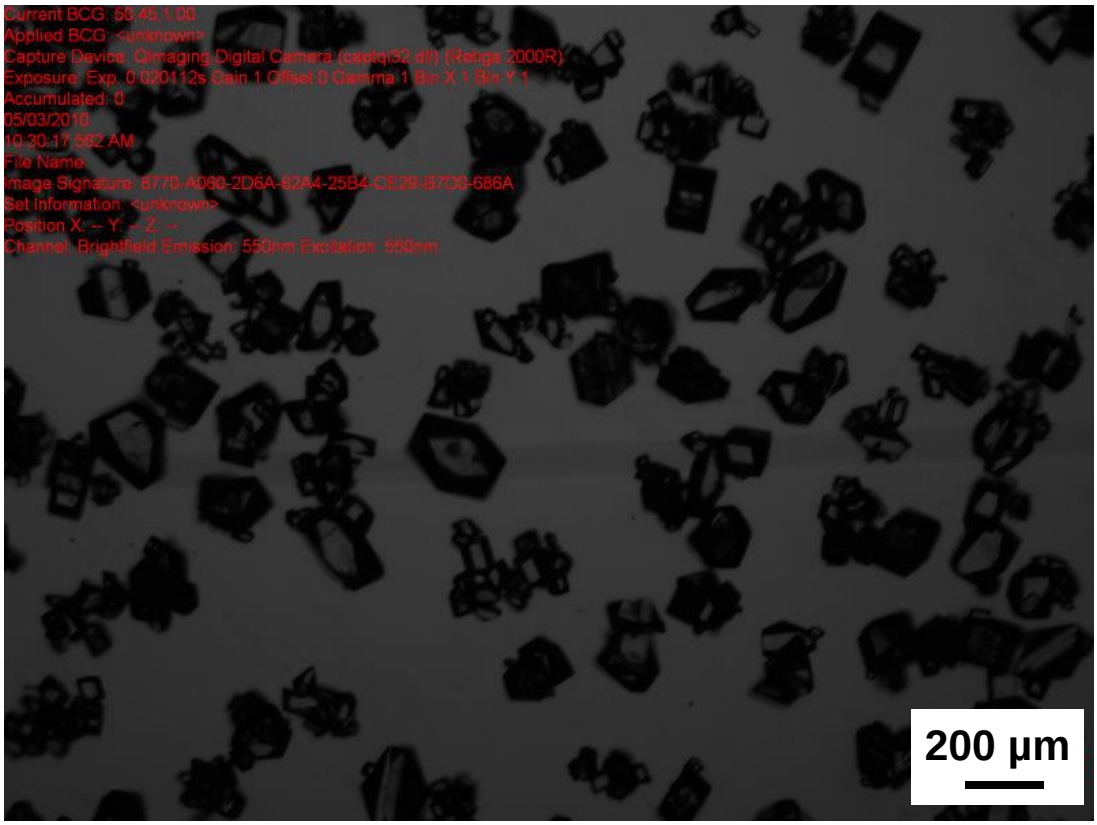

Figure 4.8. Microscope image of a batch of LAM seed crystals after sieving for the range of 125 to 180 µm (scale bar = 200 µm).

Two sets of supersaturation profiles were applied. Run 1 was implemented at a constant supersaturation (ΔC = 0.0074 g LAM/g water) that was very close to the middle of the metastable zone and Run 2 was implemented for half of this absolute supersaturation (ΔC = 0.0037 g LAM/g water). Microscope images of the product crystals are very similar between the two runs (see Fig. 4.9ab). Inspection of the microscope images and FBRM data (Fig. 4.4) indicated that that negligible nucleation occurred in the stirred-tank.

(a)

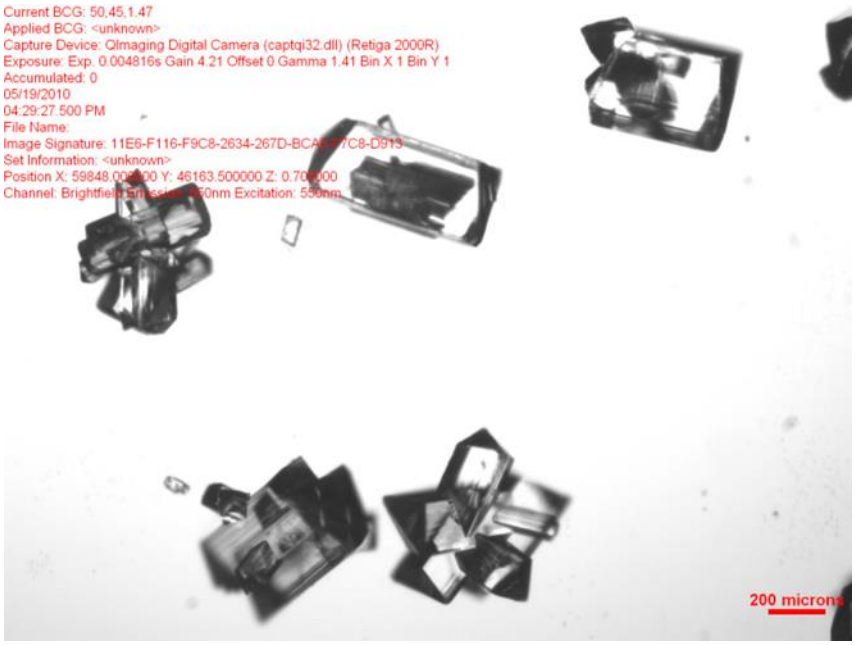

(b)

Figure 4.9. Microscope images of LAM product crystals produced by concentration feedback control experiments with constant supersaturation of (a) 0.0074 g LAM/g water and (b) 0.0037 g LAM/g water (scale bar = 200 μm).

The change in the mean crystal length during each experiment operating under constant absolute supersaturation in Fig. 4.4a was divided by the batch time to determine the average growth rate for each supersaturation. The estimated average growth rate G was plotted vs. supersaturation S to estimate the kinetic parameters in the power-law growth rate expression $G = k_g S^g$ for LAM crystals in aqueous solution, closely following a procedure described in [139], which determined that $g \approx 1$ and average $k_g = 6.353$ μm/s. The relationship between the average growth rate and absolute supersaturation implies that the concentration feedback control provides control of the average growth rate in the stirred-tank crystallizer.

The crystals shown in Fig. 4.8 were produced by crash cooling followed by vacuum drying and sieving, which caused some aggregation. Slurry seeds were used in the subsequent continuous seeding experiment because (*i*) they have a reduced potential for aggregation, and (*ii*) using a carrier fluid makes it easier to reliably deliver seed crystals at a smoothly controlled rate to a stirred-tank crystallizer.

4.3.3. Continuous seeding by dual impinging jets

Seed crystals produced by the DIJ mixer were highly uniform and smaller than 20 microns (Fig. 4.6). It is unlikely that the nucleation of these seed crystals occur under conditions of perfect mixing (that is, conditions in which the two liquids are mixed at the molecular scale before nucleation occurs). The temperature achieved by complete mixing would be about 47.5°C, which is the average of the two inlet stream temperatures of 25°C and 70°C in a 1:1 volume ratio, and the solubility at that temperature is about 0.082 g LAM/g water (see Fig. 4.3a). If the solute concentrations were perfectly mixed, the well-mixed concentration would be (0.2 + 0.03)/2 = 0.115 g LAM/g water, which is just above the unseeded metastable limit in Fig. 4.3b measured for a large-volume stirred-tank crystallizer at a low cooling rate. Smaller volumes and higher

cooling rates produce much higher metastable limits than for large volumes at low cooling rates (the former effect is described in papers on nucleation in microscale droplets, e.g., [25], and the latter effect is described in any textbook or paper that discusses metastable limits in some detail, e.g., [77]), which implies that the seed crystals were not nucleated under conditions of perfect mixing (which is defined in this context as the crystals nucleating after the fluids have perfectly mixed).

The ratio of the Prandtl to the Schmidt number, D/α, specifies the relative thickness of the concentration boundary layer to the thermal boundary layer, which is about 1/100, where D is the diffusivity of LAM in solution and α is the thermal diffusivity of the solution. This value indicates that the thermal boundary layer is much thicker than the concentration boundary layer. This implies that the temperature in the high concentration fluid side of the interface can drop while the concentration remains high, to produce a highly supersaturated solution. If symmetry about the interface between the two fluids is assumed, then the temperature near the interface is about equal to 47.5°C, and a solute concentration of 0.2 g LAM/g water is far enough above the metastable limit measured in Fig. 4.3b to indicate that primary homogenous nucleation can occur within the 1 second of residence time before the mixture enters the mixed-tank crystallizer. Collectively, this analysis provides evidence that the two liquids were not mixed at the molecular scale before crystal nucleation occurred.

The seeds in slurry generated by the DIJ mixer were continuously added to the experimentally validated concentration-controlled stirred-tank crystallizer (Fig. 4.1) for manufacturing the product crystal size distribution. For this experimental validation, the use of a flattop size distribution as the target enabled a direct comparison to the previously published theoretical results [3] (see Fig. 4.10 for the optimal CSD for some realistic seed crystals). Most

of the product crystals are within the size range of 50 to 150 μm, with similar smoothing at high and low sizes as predicted by theory for a seed distribution with nonzero width (Fig. 4.10). The experimental product crystal size distribution has very similar deviations from the target size distribution as predicted by theory. The theory of Woo et al. [3] assumed no growth rate dispersion and that the crystallizer was perfectly well-mixed, and the experimentally observed longer tail at large crystal sizes in Fig. 4.10 could be due to growth rate dispersion or some non-ideal mixing in the crystallizers. A microscope image in Fig. 4.11 shows crystals with a highly uniform shape with minimum aggregation and no fine crystals as would be produced by nucleation. These results provide an experimental validation of the increased controllability of the size distribution obtainable by continuous seeding.

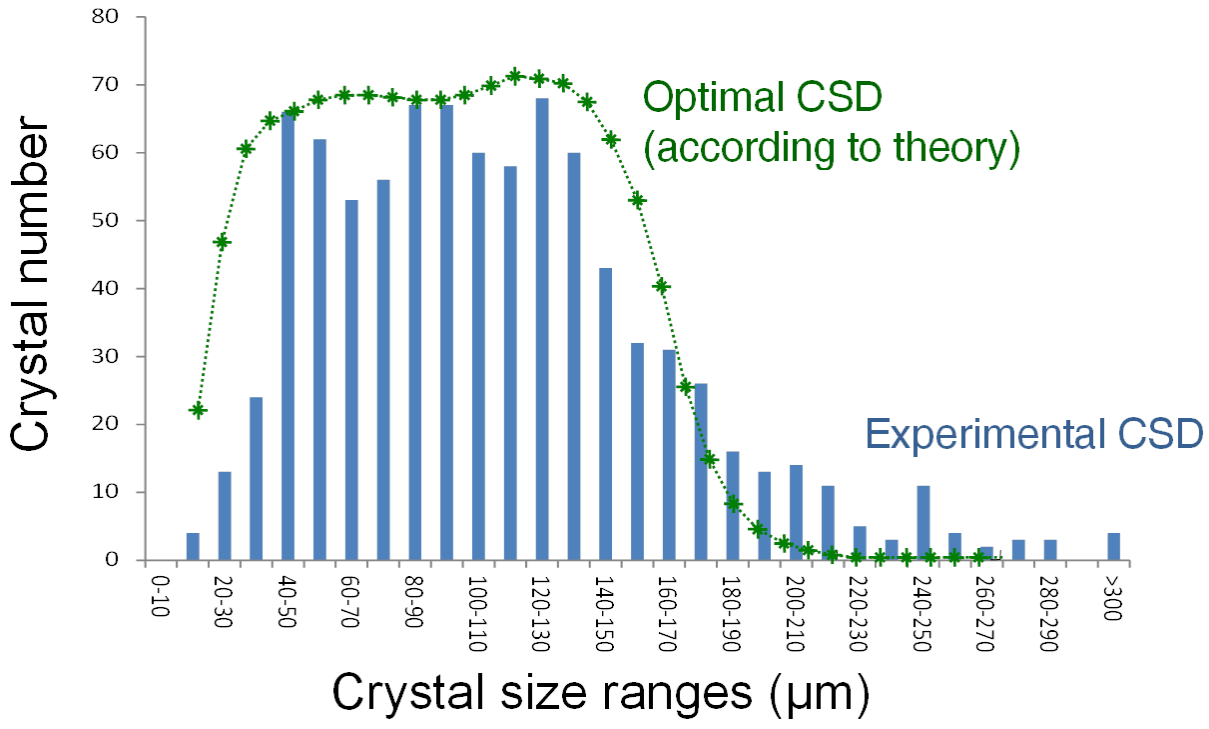

Figure 4.10. Comparison of optimal flattop CSD (green plot, from [3]) and experimental CSD measured by off-line optical microscopy (blue histogram).

Figure 4.11. Microscopy image (with polarizers) of LAM product crystals at the end of concentration control after continuous DIJ seeding (scale bar = 100 µm).

4.4. Summary

A semi-continuous crystallizer configuration that combines continuous seeding using dual impinging jets (DIJ) with concentration control in a stirred tank was experimentally demonstrated for the manufacture of L-asparagine monohydrate (LAM) crystals with the objective of manufacturing crystals with a uniform size distribution. The DIJ combined hot and cold saturated solutions to produce highly uniform LAM crystals with an average size of 20 microns that were grown using the concentration controlled stirred tank operated to have minimum nucleation. The approach included the automated collection of data for the determination of the solubility curve, metastable limit, and temperature-averaged growth kinetics for LAM crystals in aqueous solution. The size distribution of the product crystals were very similar to that predicted as being achievable in a published theoretical study.

The experiments confirm that greatly enhanced control of the crystal size distribution can be achieved by using continuous seeding. In this approach, the DIJ crystallizer can be replaced by any alternative technique for the continuous generation of seeds, as long as the rate of production of seed crystals can be specified and the seed crystals are uniform and smaller than the desired length resolution in the target product size distribution. Examples of alternative continuous seeding equipment include vortex mixers and wet milling crystals from a previous batch. Dual-impinging-jet and vortex mixers generate crystals of high uniformity of size and shape and produce a higher overall crystal yield per batch than wet milling crystals from a previous batch. By keeping a low supersaturation for the entire time history of each crystal, using wet milling crystals from a previous batch as seed may generate product crystals of higher average molecular purity.

5. MATHEMATICAL MODELING AND ANALYSIS OF COOLING CRYSTALLIZATION WITHIN DUAL-IMPINGING JET MIXERS

5.1. Introduction

A key objective in pharmaceutical crystallization is to control the crystal size distribution (CSD), to improve process efficiency and product quality. An effective way to improve the control of CSD is through combining continuous seeding and growth with concentration control [3]. One well-studied approach for continuous seeding is to combine solution and anti-solvent streams in a dual-impinging jet (DIJ) mixer [3], [18], [20], [141], [145]. The underlying principle is that, at appropriate flow rates, such a DIJ mixer can generate high-intensity micro-mixing of fluids to quickly achieve a nearly spatially homogeneous composition of high supersaturation before the onset of primary nucleation. An inexpensive DIJ mixer can be used to rapidly generate a large amount of small crystals and remove any need for post-crystallization milling, which simplifies the overall manufacturing process and avoids a potential route for the generation of an undesirable polymorphic transformation [18], [141].

Rather than anti-solvent crystallization as commonly used, a cooling DIJ mixer was recently demonstrated that combined hot and cold saturated solutions to generate small uniform seed crystals [4]. All of the crystals from the cooling DIJ mixer were about 10 microns in length, placing them in the approximate size range for direct application in inhalers [127]. Theoretically, if the mixing was perfect (that is, solution concentrations and temperature were completely mixed at the molecular scale in the mixer), the average supersaturation level would be too low to nucleate crystals in a cooling DIJ mixer. The surprising result of nucleating crystals by combining hot and cold saturated solutions in a DIJ mixer motivates the theoretical analysis of the system in this article. Also, it would be useful at the early stage of research and development

to be able to quickly decide on compound-solvent combinations for DIJ mixers without time-consuming trial-and-error as is currently used in process development [145]. These two motivations lead to the main objectives of this article: (1) to improve the understanding of primary nucleation in a free-surface cooling DIJ mixer, and (2) to develop design criteria for cooling DIJ mixers to quickly rule out unsuitable compound-solvent combinations based on their physicochemical properties. The primary emphasis is on the free-surface DIJ mixer configuration, as it is simple and flexible to implement experimentally, although the results are relevant to other DIJ mixer configurations.

A mathematical model is developed for crystallization in a DIJ mixer that combines thermodynamics, kinetics, fluid dynamics, and heat and mass transfer. The mathematical model is in the form of partial differential equations, simplified by exploiting symmetries and employing scaling analysis. The theoretical analysis is supported with process simulation. The two-dimensional energy and molar balances are solved using COMSOL input with an analytical solution for the velocity field, to generate spatial distributions of temperature, concentration, and supersaturation near the hot-cold interface within a cooling DIJ mixer. Compared to past work with similar DIJ geometries (e.g., confined dual jets) that mainly used numerical simulations to investigate flow and heat/mass transfer characteristics [3], [146]–[149], analytical expressions are derived that are composed of simple functions that provide physical insight, which are compared and supported with numerical results. Based on these analytical solutions of velocity, temperature, and concentration spatial distributions, design criteria are developed to increase the probability of primary nucleation in cooling DIJ mixers.

5.2. Theory

An analytical solution for the local flow field near the interface between two impinging jets can be derived for a partial differential equation that is simplified by exploiting symmetries. Assumptions are also presented and justified that are subsequently used to determine temperature and concentration spatial distributions via analytical and numerical approaches.

5.2.1. Assumptions with justifications for deriving an analytical solution of the DIJ local velocity field

A schematic of a DIJ mixer is in Fig. 5.1a, with an example set of operating parameters in Table 5.1 and the analytically computed jet shape and example set of crystal results in Fig. 5.S1). Nucleation can only occur very close to the interface between the two jets, since the supersaturation is zero far from the interface and can only increase when the jets are close enough to transfer heat and solute with each other. The region with the highest potential of nucleation is of most interest, which is where the residence time is the longest, shown as an orange box in Fig. 5.1a and referred to as 'local' here. Like some past studies that have mathematically modeled similar geometries (e.g., single free-surface jet impingement on a normal plane [150]–[152] or dual-impinging jets [153]), three assumptions are made to simplify the analysis:

(i) The fluid is assumed to be irrotational and in steady state.

(ii) The flow is assumed to be axisymmetric and the two impinging jets are assumed to have the same velocity field but in opposing directions.

(iii) The flow is assumed to be incompressible with constant values of density and viscosity.

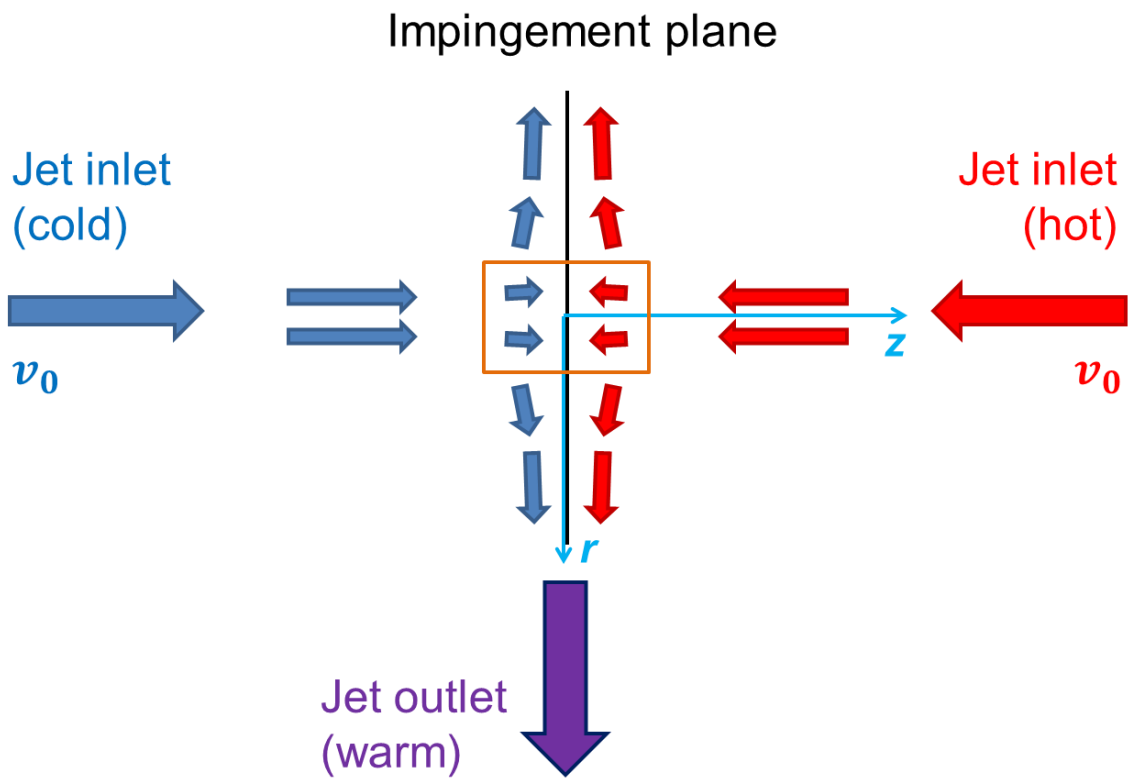
Impingement plane
Jet inlet
(cold)
v_0
Jet inlet
(hot)
v_0
z
r
Jet outlet
(warm)

(a)

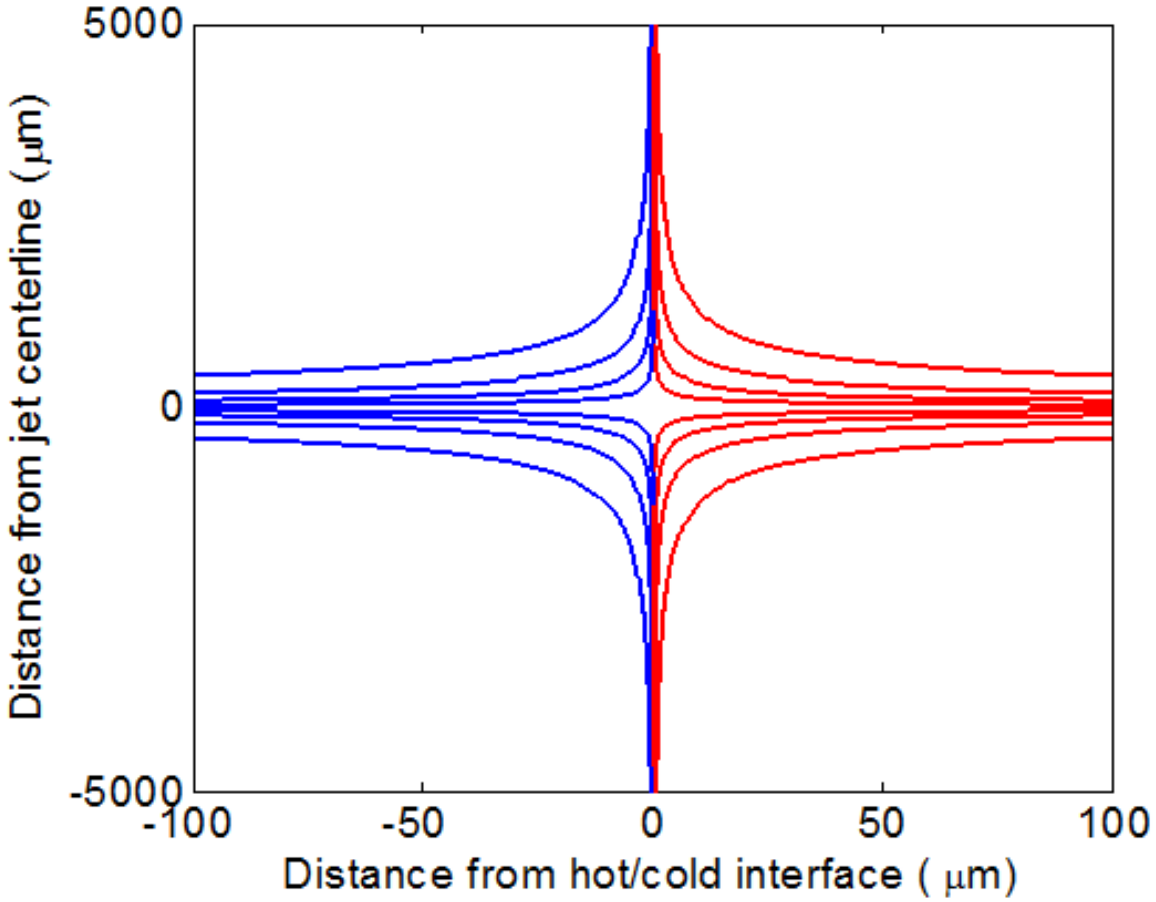

(b)

Figure 5.1. (a) Schematic of a free-surface cooling DIJ mixer. The centerlines of hot (70°C, red, right side) and cold (25°C, blue, left side) jets align. Both jets have the same volumetric flow rate, so the impingement plane is a symmetry plane perpendicular to the jet centerline. (b) Streamlines of the hot (red, right side) and cold jets (blue, left side) of the cooling DIJ mixer in (a), from the analytical solutions of the flow field (5.3) and (5.4).

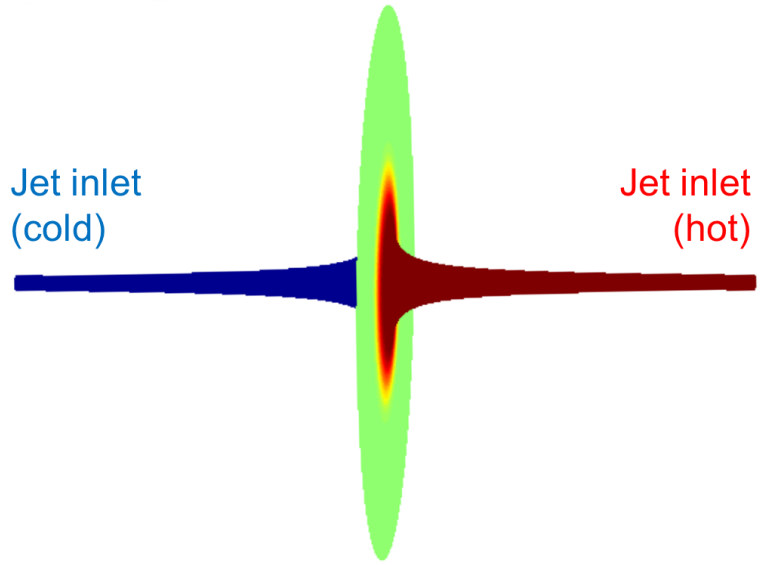

(a)

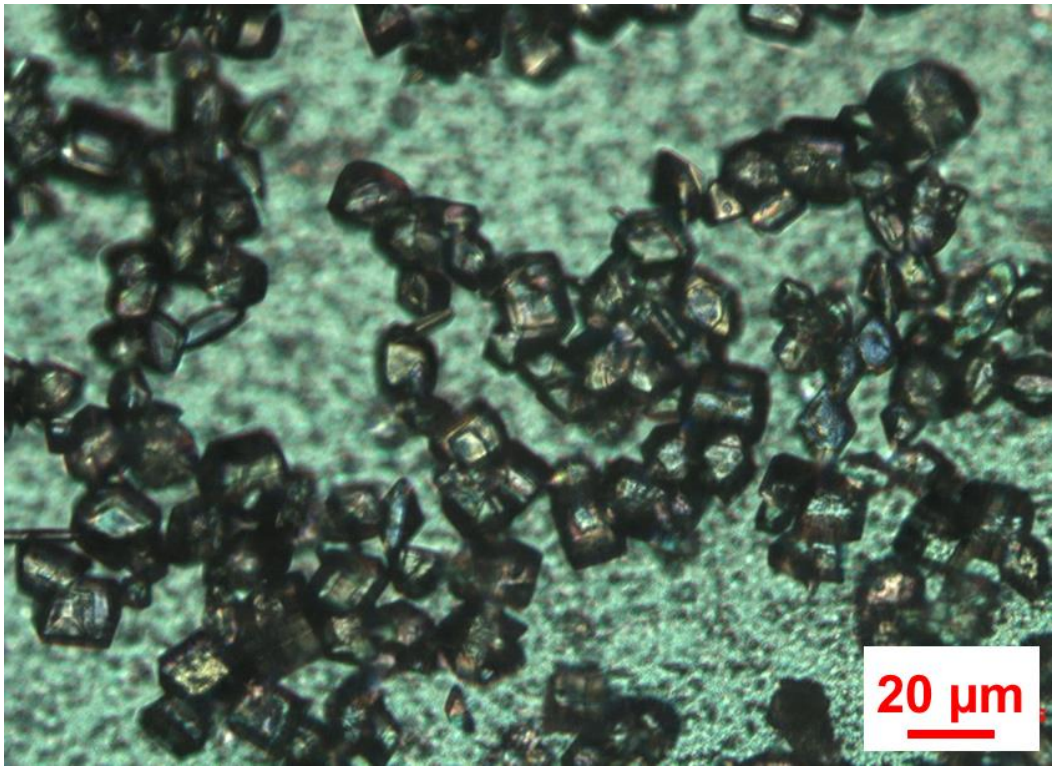

(b)

Figure 5.S1. (a) Liquid flows for a free-surface cooling DIJ mixer. Liquid from the cold jet (blue) is on the left side and hot jet (red) on the right side. The flow rates from the two opposite jets are the same, so the liquid flow at the impingement plane has circular cross-sections along the z axis. (b) Microscope image (with polarizers) of LAM crystals generated by a DIJ mixer [4].

In a past study that demonstrated the nucleation of crystals by mixing hot and cold saturated solutions [4], the Reynolds number indicates that the flow was in a laminar regime, which is the regime of interest in this article. As an example, the Reynolds number at the exit, $\mathrm{Re} = \frac{\rho U L}{\mu}$, is on the order of 600 (using jet velocity v_z and inner diameter $2r_0$, with density and dynamic viscosity values in Table 5.2) or smaller [154]. No splattering is expected at such a low Reynolds number [155].

Table 5.1. Experimental parameters for the cooling crystallization of L-asparagine monohydrate (LAM, from Sigma Aldrich) in a free-surface DIJ mixer with aligned centreline.[a]

Physical properties	Values
Molecular weight $\left(\frac{\mathrm{g}}{\mathrm{mol}}\right)$	150.13
Hot jet temperature, T_{hot} (°C)	70
Hot jet concentration, c_{hot} $\left(\frac{\text{g LAM}}{\text{g water}}\right)$	0.20 (slightly supersaturated)
Cold jet temperature, T_{cold} (°C)	25
Cold jet concentration, c_{cold} $\left(\frac{\text{g LAM}}{\text{g water}}\right)$	0.03 (saturated)
Area-average jet velocity, v_z $\left(\frac{\mathrm{m}}{\mathrm{s}}\right)$	1.9 (or slightly higher)
Inner diameter of the jet nozzle, $2r_0$ (μm)	254
Jet nozzle-to-interface distance, z_0 (μm)	5000
The largest distance away from the centerline at interface, R (μm)	5000

[a]The relation between the solubility of LAM in deionized (DI) water (c_{sat}, in g LAM/g water) and temperature (T, in °C) is $c_{sat} = 3.084 \times 10^{-2} - 1.373 \times 10^{-3} T + 5.214 \times 10^{-5} T^2$ [4]. Thus the solubility of LAM at the average mixing temperature (approximately 47.5°C, the average of the temperatures of two streams) is about 0.08 g LAM/g water.

Table 5.2. Physical constants associated with the crystallization of glycine in water [6].

Physical properties	Values
Density, $\rho\left(\frac{\mathrm{kg}}{\mathrm{m}^3}\right)$	977.8 (70°C), 997.1 (25°C)
Dynamic viscosity, $\mu\left(\frac{\mathrm{N{\cdot}s}}{\mathrm{m}^2}\right)$	0.4×10^{-3} (70°C), 0.58×10^{-3} (47.5°C), 0.9×10^{-3} (25°C)
Thermal conductivity, $k\left(\frac{\mathrm{mW}}{\mathrm{m{\cdot}K}}\right)$	663.1 (70°C), 607.2 (25°C)
Heat capacity, $C_p\left(\frac{\mathrm{kJ}}{\mathrm{kg{\cdot}K}}\right)$	4.19 (70°C), 4.18 (25°C)
thermal diffusivity, $\alpha=\frac{k}{\rho C_p}\left(\frac{\mathrm{m}^2}{\mathrm{s}}\right)$	1.6×10^{-7} (70°C), 1.5×10^{-7} (25°C)
Diffusion coefficient of glycine in water at infinite dilution, $D\left(\frac{\mathrm{cm}^2}{\mathrm{s}}\right)$	1.05×10^{-5} (25°C)
Acceleration due to gravity, $g\left(\frac{\mathrm{m}}{\mathrm{s}^2}\right)$	9.81

The axisymmetric assumption simplifies the analysis while being a good approximation for free liquid (unconfined) opposed-jet DIJ configuration with a flow rate ratio of 1:1. The two jet flows are considered symmetric with respect to the impingement plane (aka contact plane between the low temperature/low concentration fluid and the high temperature/high concentration fluid), with each side of the impingement plane similar to a circular jet perpendicular to a flat surface of radius R (Figs. 5.1ab). The symmetry allows the convenient use of cylindrical coordinates (Fig. 5.1a), where the z direction is that of jet centerline (positive direction on the right side of the impingement plane), and the r direction is perpendicular to z, pointed outward from the centerline. The angular velocity parallel to the interface (v_θ) is zero.

The assumption of spatially uniform density simplifies the analysis while being a good approximation for the impingement of two saturated solutions containing the same solute and solvent. As a specific example, the density of LAM aqueous solution (or slurry with very small

amount of nuclei) in Table 5.1 is a weak function of temperature and concentration, so the densities for cold, hot, or mixed LAM solutions/slurries are nearly identical, and of similar magnitude as the density of water at the average temperature. Liquid flow with uniform density is incompressible by definition. The dynamic viscosity of LAM aqueous solution is a stronger function of solute concentration and temperature compared to density, but in this cooling DIJ mixer, the viscosity difference between hot and cold streams does not affect the velocity field. The temperature and concentration variations are small are do not affect the velocity field.

5.2.2. Analytical solution of the DIJ local velocity field

Under the assumptions, an analytical solution for the velocity field can be derived using streamline analysis [153]. A derivation of the analytical solution is given here for completeness. For an axisymmetric irrotational flow, the continuity equation can be written as $E^2\psi = 0$, which in cylindrical coordinates is

$$\frac{\partial^2\psi}{\partial r^2} - \frac{1}{r}\frac{\partial\psi}{\partial r} + \frac{\partial^2\psi}{\partial z^2} = 0 \tag{5.1}$$

with boundary conditions

(i) No penetration: $v_{z(r,0)} = 0$, so $\frac{1}{r}\frac{\partial\psi}{\partial r}(r,0) = 0$

(ii) Symmetry: $\frac{\partial\psi}{\partial z}(0,z) = 0$

Note that the symmetry plane $z = 0$, and the axis $r = 0$ are both streamlines.

Assuming a trial solution of the form $\psi(r,z) = f(r)g(z)$, then $\frac{\partial\psi}{\partial r} = f'g$, $\frac{\partial^2\psi}{\partial r^2} = f''g$, $\frac{\partial\psi}{\partial z} = fg'$, $\frac{\partial^2\psi}{\partial z^2} = fg''$ which can be plugged into the continuity equation (1) to give $f''g - \frac{f'g}{r} + fg'' = 0$. Divide by fg on both sides to give

$$\frac{f''}{f} - \frac{f'}{rf} = -\frac{g''}{g} \tag{5.2}$$

Because the left-hand side is a function of r while the right-hand side is a function of z, both sides must equal the same constant for the trial solution to be valid. For the simplest solution satisfying this condition, begin with the constant 0, and solve for f and g [153].

For the right-hand side of (5.2), $g'' = 0$ implies that $g(z) = bz + d$ where b and d are unknown constants. The boundary condition (i), $\frac{1}{r}\frac{\partial \psi}{\partial r}(r, 0) = 0$, implies that $f'(r)g(0) = 0$ for all r, so $d = 0$. For the left-hand side of (5.2), $\frac{f''}{f} - \frac{f'}{rf} = 0$ implies that $f'' = \frac{f'}{r}$. Once way to solve this equation is to insert the trial solution $f = \sum a_n r^n$ into $f'' = \frac{f'}{r}$ and match terms, which gives that $f(r) = Br^2$. The boundary condition (ii), $\frac{\partial \psi}{\partial z}(0, z) = 0$, implies that $f(0)g'(z) = 0$ for all z, so $f(0) = 0$, which is satisfied by $f(r) = Br^2$. Hence the trial solution $\psi(r, z) = f(r)g(z) = bBr^2 z$ satisfies the continuity equation (5.1) and both boundary conditions.

Having the fluid flow move towards the impingement plane and moving radially outward implies that the one independent constant $C = -bB > 0$, so the stream function is $\psi(r, z) = -Cr^2 z$ [153]. Then the velocity components are

$$v_r = -\frac{1}{r}\frac{\partial \psi}{\partial z} = Cr \ (> 0) \tag{5.3}$$

$$v_z = \frac{1}{r}\frac{\partial \psi}{\partial r} = -2Cz \ (< 0 \text{ for } z > 0) \tag{5.4}$$

As an example of the determination of the constant C, consider an experimental system with a nozzle-to impingement plane distance of $z = z_0 = 5$ mm with a jet velocity along the jet centerline of $v_{z_0} = -1.9 \text{ m/s}$; then the constant C determined from equation (5.4) is $C = -\frac{v_{z_0}}{2z_0} = 190 \text{ s}^{-1}$.

5.2.3. Assumptions for calculation of temperature and concentration spatial fields

The temperature and concentration spatial distribution of liquid within a DIJ mixer is calculated via both analytical and numerical approaches. The governing equations of heat and mass transfer are

$$v_r \frac{\partial T}{\partial r} + v_z \frac{\partial T}{\partial z} = \alpha \left[\frac{1}{r}\frac{\partial}{\partial r}\left(r\frac{\partial T}{\partial r}\right) + \frac{\partial^2 T}{\partial z^2}\right] \tag{5.5}$$

$$v_r \frac{\partial c}{\partial r} + v_z \frac{\partial c}{\partial z} = D \left[\frac{1}{r}\frac{\partial}{\partial r}\left(r\frac{\partial c}{\partial r}\right) + \frac{\partial^2 c}{\partial z^2}\right] \tag{5.6}$$

where α is thermal diffusivity and D is the molecular diffusivity. The boundary conditions for the temperature $T(r, z)$ are

$$\frac{\partial T}{\partial r}(0, z) = 0,\ T(r, z_0) = T_{hot} = 70℃,\ T(r, -z_0) = T_{cold} = 25℃,$$

where some example temperature values are given. For the experimental configurations of interest, the boundary conditions can be approximated to very high accuracy by

$$\frac{\partial T}{\partial r}(0, z) = 0,\ T(r, \infty) = T_{hot} = 70℃,\ T(r, -\infty) = T_{cold} = 25℃.$$

The corresponding boundary conditions for concentration $c(r, z)$ are

$$\frac{\partial c}{\partial r}(0, z) = 0\,, \quad c(r, \infty) = c_{hot} = 0.20 \text{ g LAM/g water}\,, \quad c(r, -\infty) = c_{cold} = 0.03 \text{ g LAM/ g water},$$

where some example concentration values are given.

For both the heat and mass transfer equations (5.5)–(5.6), assume that (i) the analytical solution for the velocity field (5.3)–(5.4) is valid for the region of interest (Fig. 5.1a); (ii) the air/liquid interfaces are assumed to be streamlines from the analytical solution for the velocity field, starting from the edge of the inlet nozzles; (iii) the thermal diffusivity α is approximated as a constant. Assumption (iii) is a very accurate approximation for most systems; for example, α

varies by less than ±3.5% and the molecular diffusivity D is constant over a wide range of temperature for the system in Table 5.2.

All numerical simulations were made using the finite element method as implemented in COMSOL V4.3, using two additional assumptions:

(i) Uniform temperature and concentration at the nozzle inlets

(ii) No mass or heat flux at the air/liquid interfaces (including very far from centerline)

The latter assumption holds because air is an excellent insulator. Analytical solutions involve additional approximations described in the next section, where the analytical solutions are derived and compared to the numerical simulations.

5.3. Results and discussion

In this section, scaling analysis is applied to simplify the heat and mass transfer equations from two dimensional (2D) to one dimensional (1D) so that relatively simple analytical solutions can be derived. For the region of interest, the 1D analytical solutions is shown to be comparable to the 2D numerical solutions except near the outlet flows. Based on the analytical solutions for the temperature and concentration spatial fields, the supersaturation profile is analyzed for regions of high potential for nucleation, which leads to design criteria for inducing nucleation in cooling DIJ mixers.

5.3.1. Flow field and residence time

A good understanding of the velocity field is a prerequisite for the analysis of heat and mass transfer. The liquid gets decelerated as it approaches the impingement plane (hot/cold interface) (Fig. 5.1a). Then the fluid flow is diverted radially and accelerated, due to the fluid mass balance and finite volume of the region of interest (orange box in Fig. 5.1a, with small r and z).

Equations (5.3) and (5.4) are analytical solutions for the velocity field that are valid for the region of interest.

The liquid velocity in the *z*-direction is very small near the impingement plane, making the residence time very large for liquid moving along the jet centerline (Fig. 5.1b). According to (5.3) and (5.4), the residence time is infinity exactly on the jet centerline. In reality, liquid will not flow exactly along the centerline (due to fluid elements having finite size, fluctuation, etc.), so the residence time of a fluid element in the zone of interest is finite but still much longer than any other area. Consider that, for liquid that starts at a distance of R_1 from centerline, its residence time up to radial position R is $t_r = \int_{R_1}^{R} dr/v_r = \frac{\ln \frac{R}{R_1}}{C}$. Even slightly away from centerline (e.g., $R_1 = 1$ μm, much smaller than the jet nozzle diameter), the total residence time decreases significantly (t_r = 44.8 ms).

5.3.2. Scaling analysis for the temperature and concentration spatial fields

The independence of the heat and mass transfer governing equations (5.5)–(5.6) enables independent analysis of the heat and mass transfer. In the region of interest (Fig. 5.2a), the temperature gradient along impingement plane ($\frac{\partial T}{\partial r}$) is negligible compared to along the centerline ($\frac{\partial T}{\partial z}$), because the dominating direction of heat transfer (conduction) is from hot jet to cold jet [153]. In this way, the two-dimensional energy conservation equation (5.5) can be simplified to a one-dimensional equation,

$$v_z \frac{\partial T}{\partial z} = \alpha \frac{\partial^2 T}{\partial z^2}, \tag{5.7}$$

along the centerline. This simplified equation (5.7) has the unique analytical solution

$$\frac{T - T_{cold}}{T_{hot} - T_{cold}} = \frac{1}{2}\left(\mathrm{erf}\left(\frac{z}{z_{refh}}\right) + 1\right) \tag{5.8}$$

where $z_{refh} = \sqrt{\frac{\alpha}{c}}$. For the system in Table 5.2, $z_{refh} = 28.1$ μm.

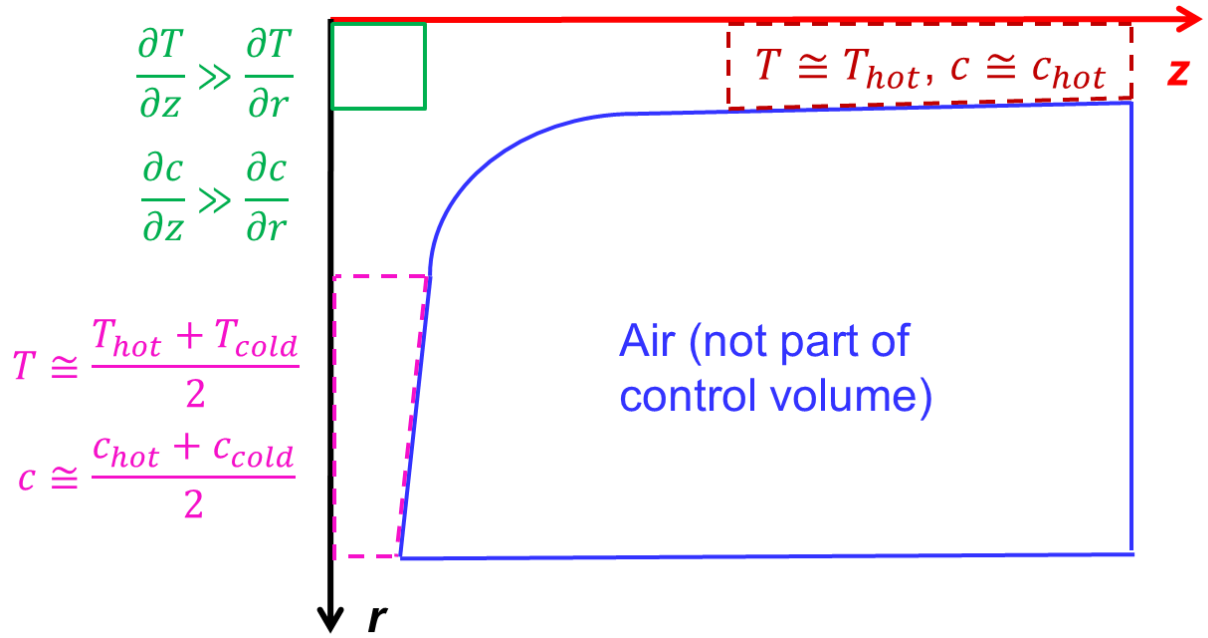

(a)

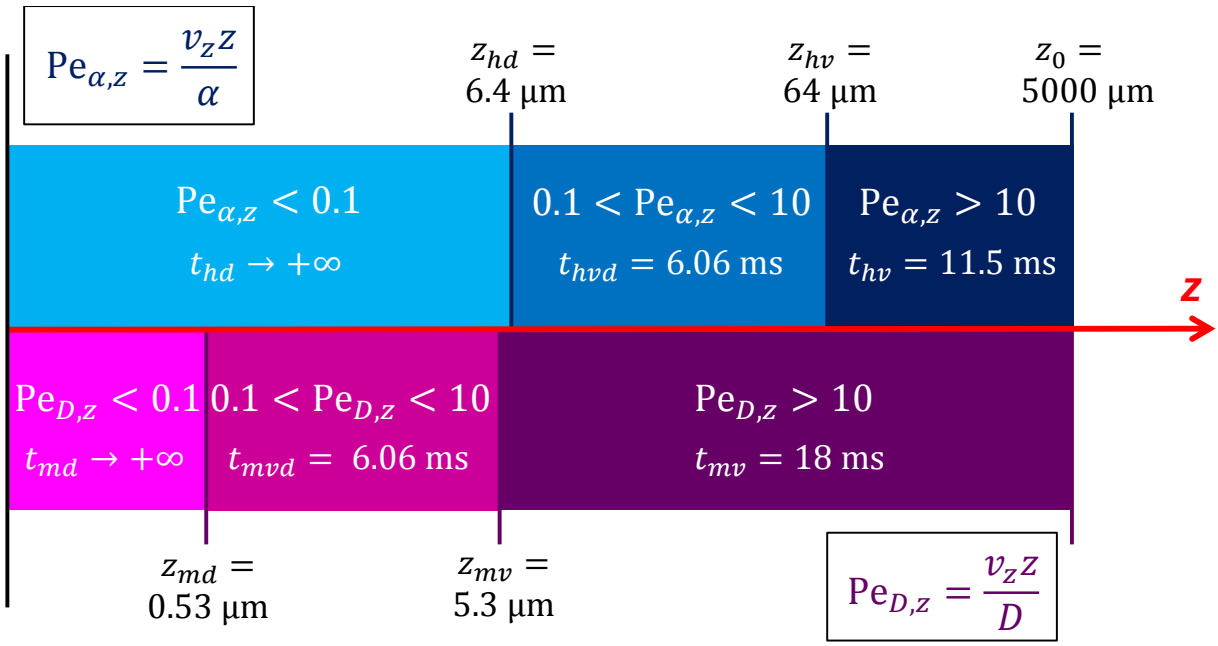

(b)

Figure 5.2. (a) Schematic for scaling analysis and defining the region of interest (only the hot jet side is shown due to symmetry). The *z* axis is the jet centerline. The blue region (large *r* and *z*) is air, which is not in the control volume. Temperatures and concentrations in the purple (large *r*, small *z*) and brown (large *z*, small *r*) regions are approximately spatially uniform, serving as boundary conditions (with values listed). The green region (small *r*, small *z*) of low velocity and long residence time is of interest for nucleation. (b) Time and length scales of heat transfer (blue) and mass transfer (pink) for liquid near to the jet centerline. The leftmost vertical line is the impingement plane, which is in the direction of the *r* axis, and the rightmost vertical line is the hot jet inlet (e.g., 5 mm away from the impingement plane). The residence time is denoted by *t*. The length of each regime are not drawn to linear scale, so as to show the small regimes with low Pe clearly (e.g., for heat transfer, $z \leq z_{hv} = 6.4$ μm). Example numerical values are given to show how to calculate the length scales and residence times: When liquid is far away from the impingement plane, the convection term dominates, $\frac{UL}{\alpha} \geq 10$, and $2Cz^2 \geq 10\alpha$, which is equivalent to $z \geq z_{hv} = 64$ μm. The residence time in this regime is $t_{hv} = \int_{z_{hv}}^{z_0} dz/(-v_z) = \frac{\ln \frac{z_0}{z_{hv}}}{2C} = 11.5$ ms.

This analytical solution (5.8) is in the form of an error function, indicating a sharp temperature gradient at the impingement plane (z = 0) and nonlinear along the z axis (Fig. 5.3c). The error function also indicates temperature gradient drops to nearly zero at a distance of around z_{refh} from the impingement plane (supported by Figs. 5.3abc). For the region of interest (near r = z = 0), the 1D analytical model (Fig. 5.3c) generates a very similar temperature profile to the 2D simulation from COMSOL (Fig. 5.3b).

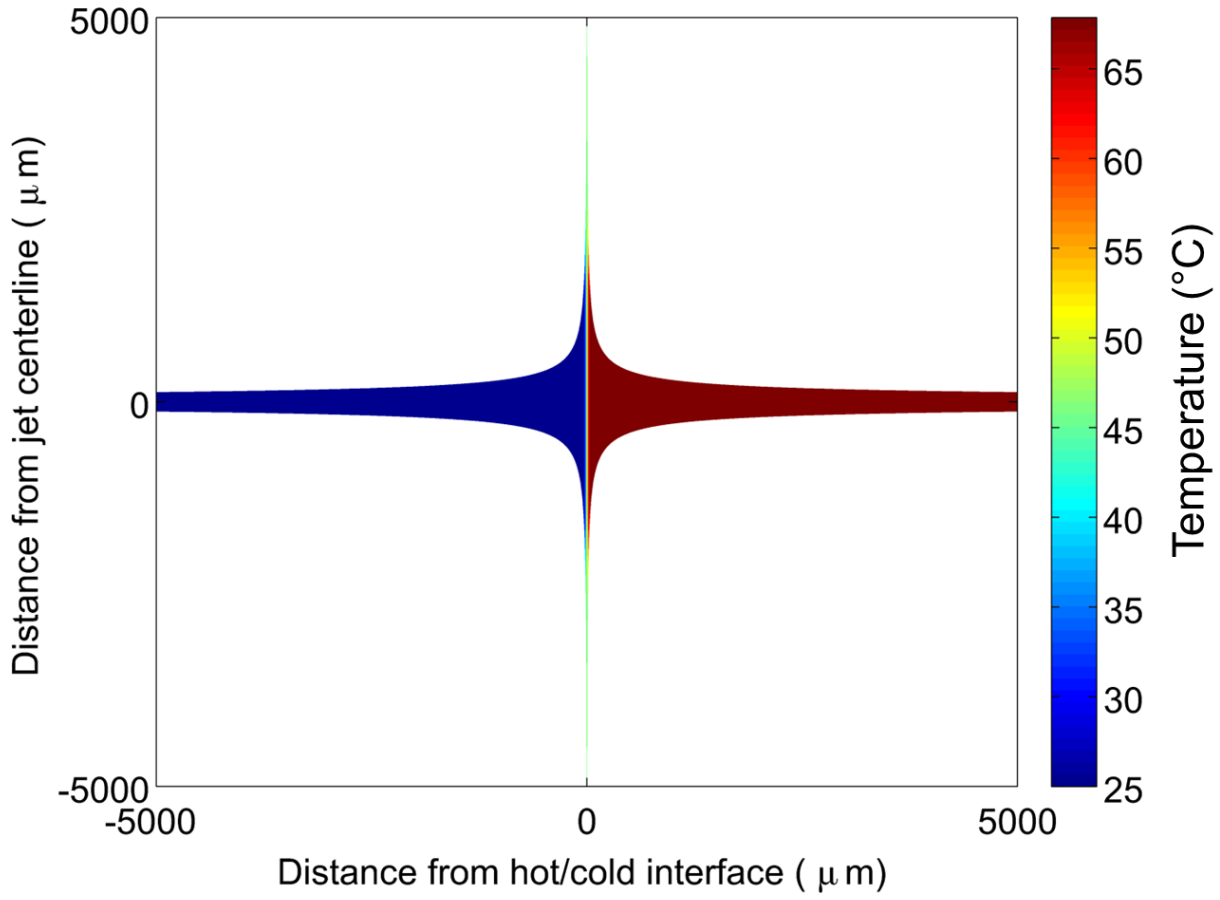
5000
0
-5000
-5000
0
5000
Distance from jet centerline (μ m)
Distance from hot/cold interface (μ m)
65
60
55
50
45
40
35
30
25
Temperature (°C)

(a)

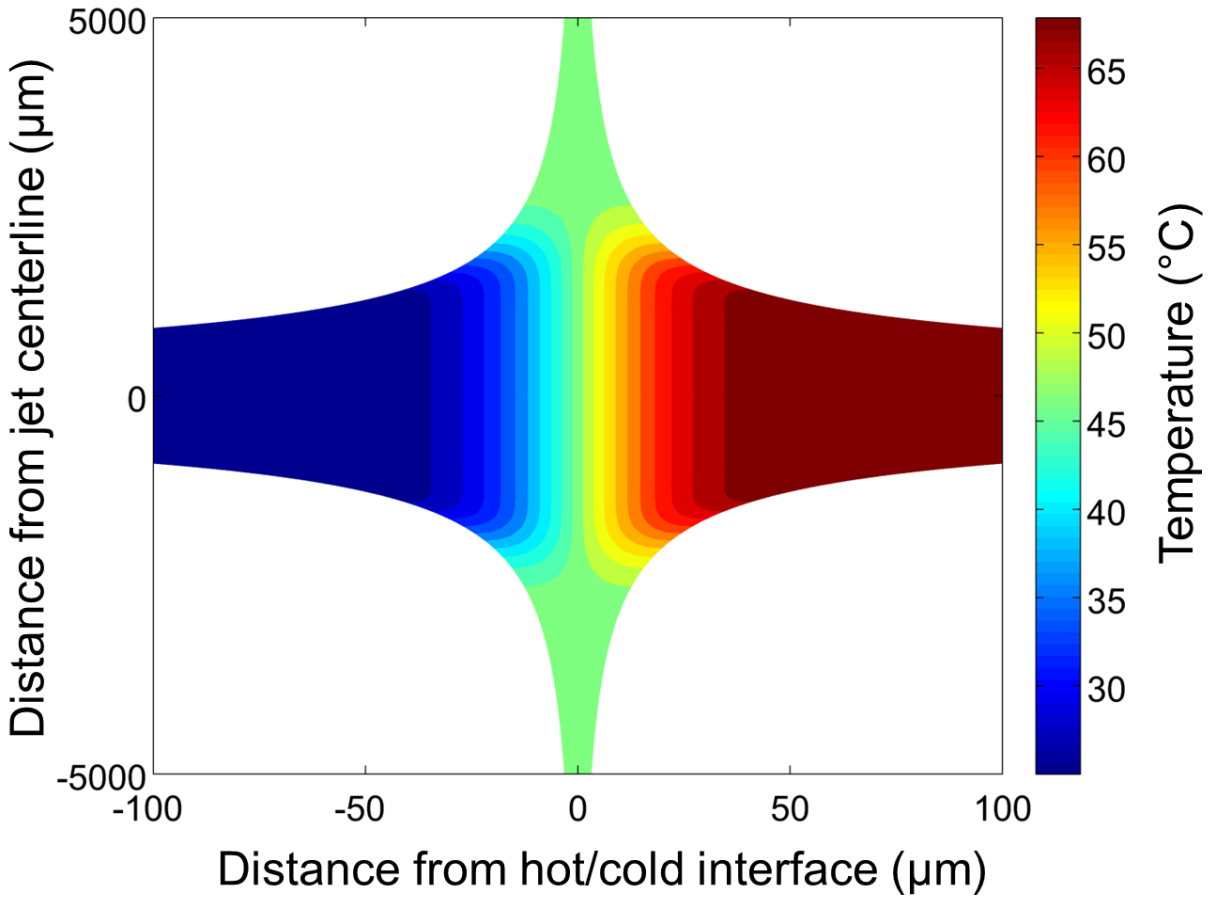
5000
0
-5000
-100
-50
0
50
100
Distance from jet centerline (μm)
Distance from hot/cold interface (μm)
65
60
55
50
45
40
35
30
Temperature (°C)

(b)

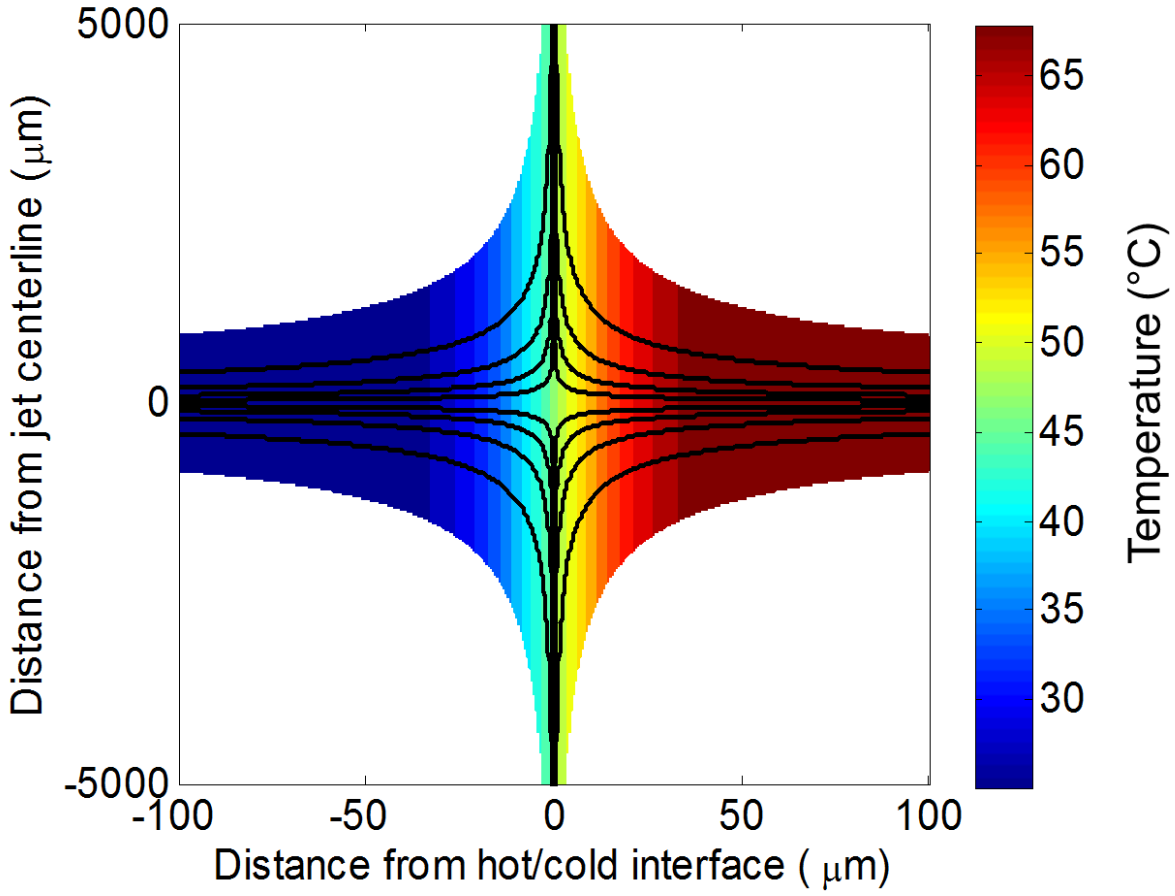

(c)

Figure 5.3. Temperature field: (a) computed by 2D simulation using the finite element method implemented in COMSOL, at the full length range with the dimensions being the nozzle-to-nozzle distance and the contact area diameter; (b) computed by 2D simulation using the finite element method implemented in COMSOL, very near the impingement plane (small range of *z*, as if 'stretching' Fig. 5.3a horizontally); (c) 1D analytical solution near the impingement plane, with the streamlines shown in black. The temperature is indicated by color (red indicates high temperature, and blue indicates low temperature), in unit of °C, and the black lines are streamlines. The cold impinging jet is on the left, and the hot impinging jet on the right. The white color shows air at room temperature. The edges between air and liquid are streamlines starting from the edge of the inlet nozzles.

Similar scaling analysis applies for the concentration field, to give

$$v_z \frac{\partial c}{\partial z} = D \frac{\partial^2 c}{\partial z^2} \tag{5.9}$$

Similar to the temperature equation, the simplified concentration equation (5.9) has the unique analytical solution

$$\frac{c-c_{cold}}{c_{hot}-c_{cold}} = \frac{1}{2}\left(\text{erf}\left(\frac{z}{z_{refm}}\right)+1\right) \tag{5.10}$$

where $z_{refm} = \sqrt{\frac{D}{C}}$. For the system in Table 5.2, $z_{refm} = 2.35$ μm.

The assumptions and governing equations for heat and mass transfer are very similar, and heat transfer is decoupled from mass transfer, thus the analytical solutions for the temperature and concentration profiles (5.8) and (5.10) are expected to be very similar. The trend of the concentration variation is very similar to the temperature, with sharp gradient at the impingement plane and nonlinear gradient along the *z* axis) as shown in Figs. 5.3 and 5.4. For the region of interest, the 1D analytical model (Fig. 5.4c) generates a very similar concentration profile to the 2D simulation from COMSOL (Fig. 5.4b). Thus for assessing the potential of primary nucleation, the analytical model is sufficiently accurate.

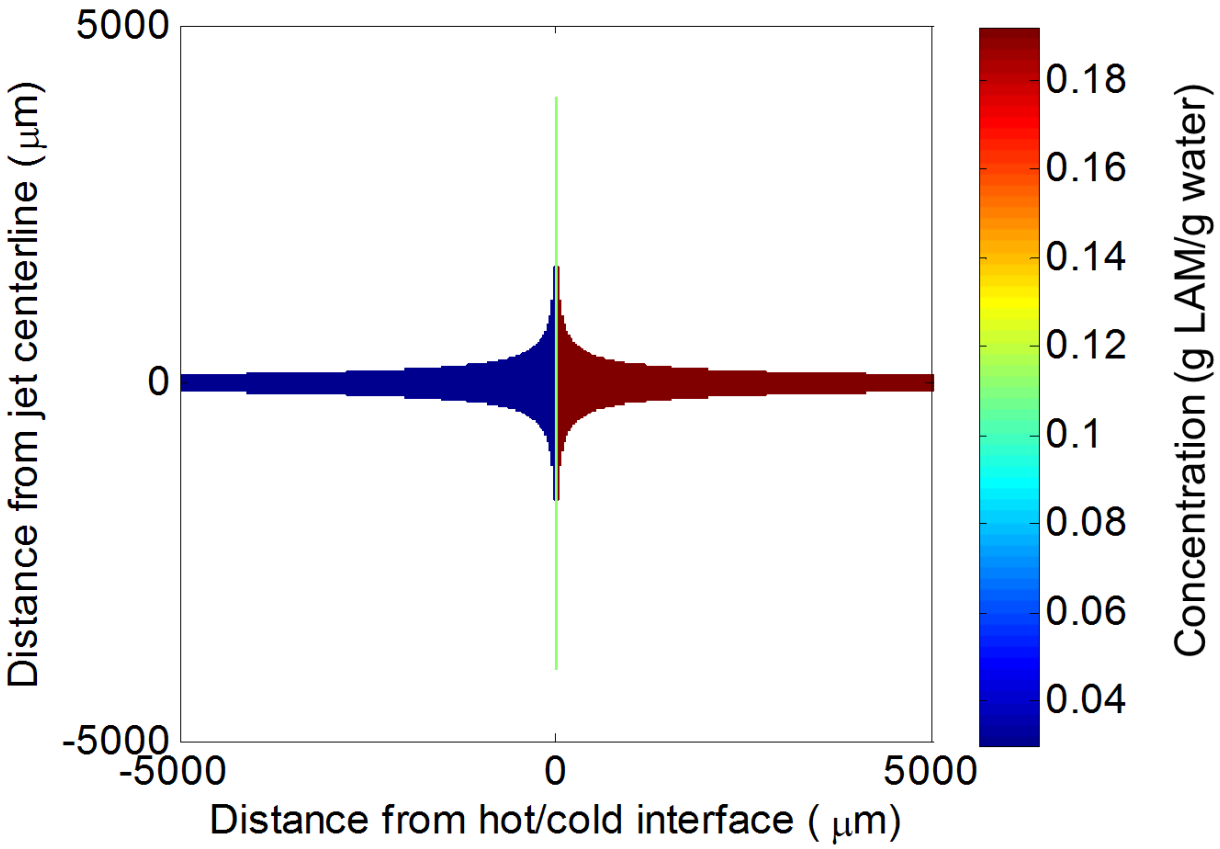
5000
0
-5000
-5000
0
5000
Distance from jet centerline (μm)
Distance from hot/cold interface (μm)
0.18
0.16
0.14
0.12
0.1
0.08
0.06
0.04
Concentration (g LAM/g water)

(a)

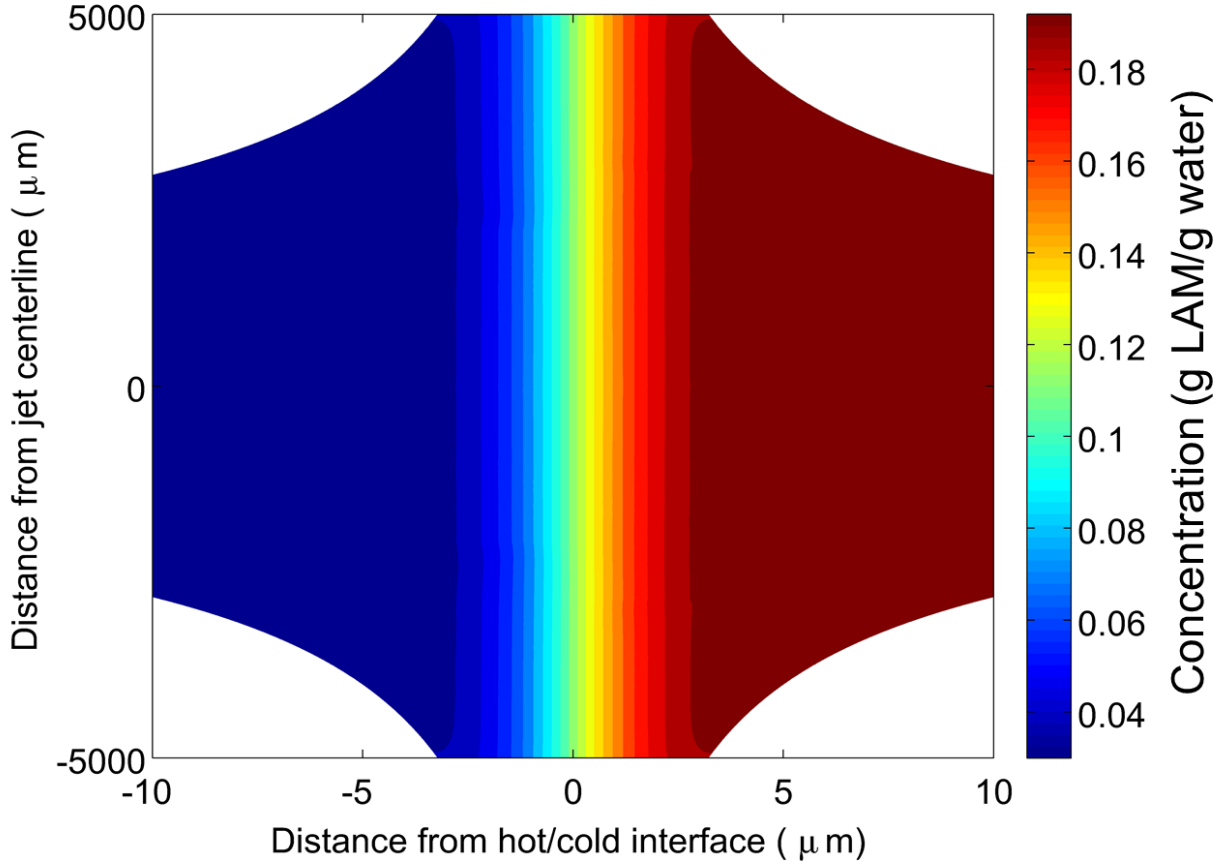
5000
0
-5000
-10
-5
0
5
10
Distance from jet centerline (μm)
Distance from hot/cold interface (μm)
0.18
0.16
0.14
0.12
0.1
0.08
0.06
0.04
Concentration (g LAM/g water)

(b)

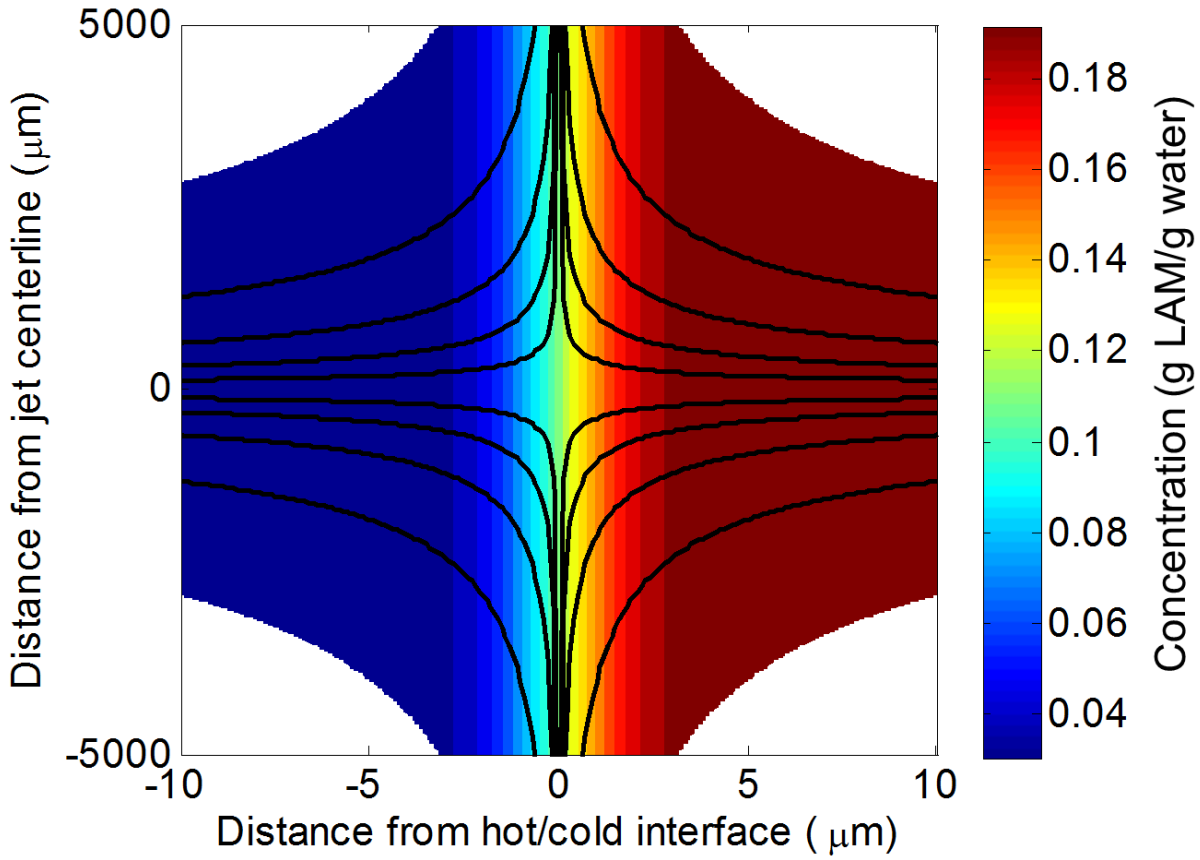

(c)

Figure 5.4. Concentration field: (a) computed by 2D simulation using the finite element method implemented in COMSOL, at the full length range (same as in Fig. 5.3a); (b) computed by 2D simulation using the finite element method implemented in COMSOL, very near the impingement plane; (c) 1D analytical solution near the impingement plane, with the streamlines shown in black. The concentration is indicated by color (red indicates high concentration, and blue indicates low concentration), in unit of g LAM/g water. As in Fig. 5.3, the cold impinging jet is on the left and the hot impinging jet on the right, and the edges between air and liquid are streamlines starting from the edge of the inlet nozzles. The streamlines in 5.4c (black) are the same as in Fig. 5.3c.

The difference between heat and mass transfer exists in the length scale along centerline (in the example system, z_{refh} = 28.1 μm for the temperature gradient change, and z_{refm} = 2.35 μm for the concentration gradient change, as shown in Figs. 5.3–5.5), which comes from the difference in heat and mass transfer rates. This difference can be indicated by the large value of

Lewis number (Le = 143), which is the ratio between thermal diffusivity and mass diffusivity (α/D), and also the ratio of the Schmidt to the Prandtl numbers.

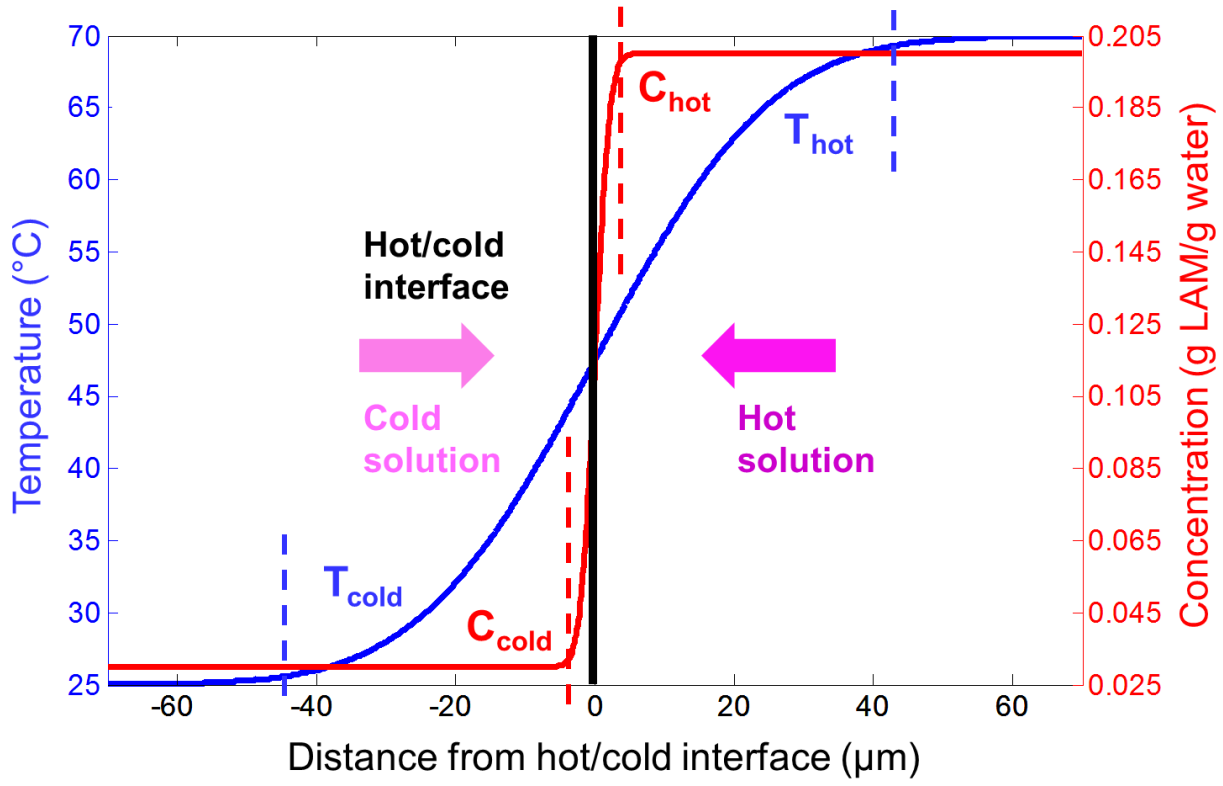

Figure 5.5. Temperature (blue) and concentration (red) profiles (solid lines) and edges of the boundary layers (dashed lines), based on the 1D approximation (Figs. 5.3c and 5.4c) along the jet centerline. The black line is the impingement plane.

5.3.3. Supersaturation spatial distribution and design criteria

The supersaturation spatial distribution was calculated (Figs. 5.5 and 5.6) based on the analytical solutions for the temperature and concentration profiles in the region of interest (Figs. 5.3c and 5.4c). Due to the different rates of heat and mass transfer, the temperature of the hot solution can drop towards the average temperature of the two solutions before its solution concentration has significantly changed (Fig. 5.5). Supersaturation can be much higher than the

spatially averaged supersaturation (e.g., 0.035 g LAM/g water) close to the impingement plane at the hot stream side (e.g., 0.10 g LAM/g water, from Fig. 5.6 or Region A in Fig. 5.7), where the temperature is low (thus the solubility) while the concentration remains high (Figs. 5.5 and 5.7). Between the impingement plane and Region A on the hot stream side (Region B in Fig. 5.7), the residence time is very high (due to low velocity) with positive supersaturation (though not as high as in Region A).

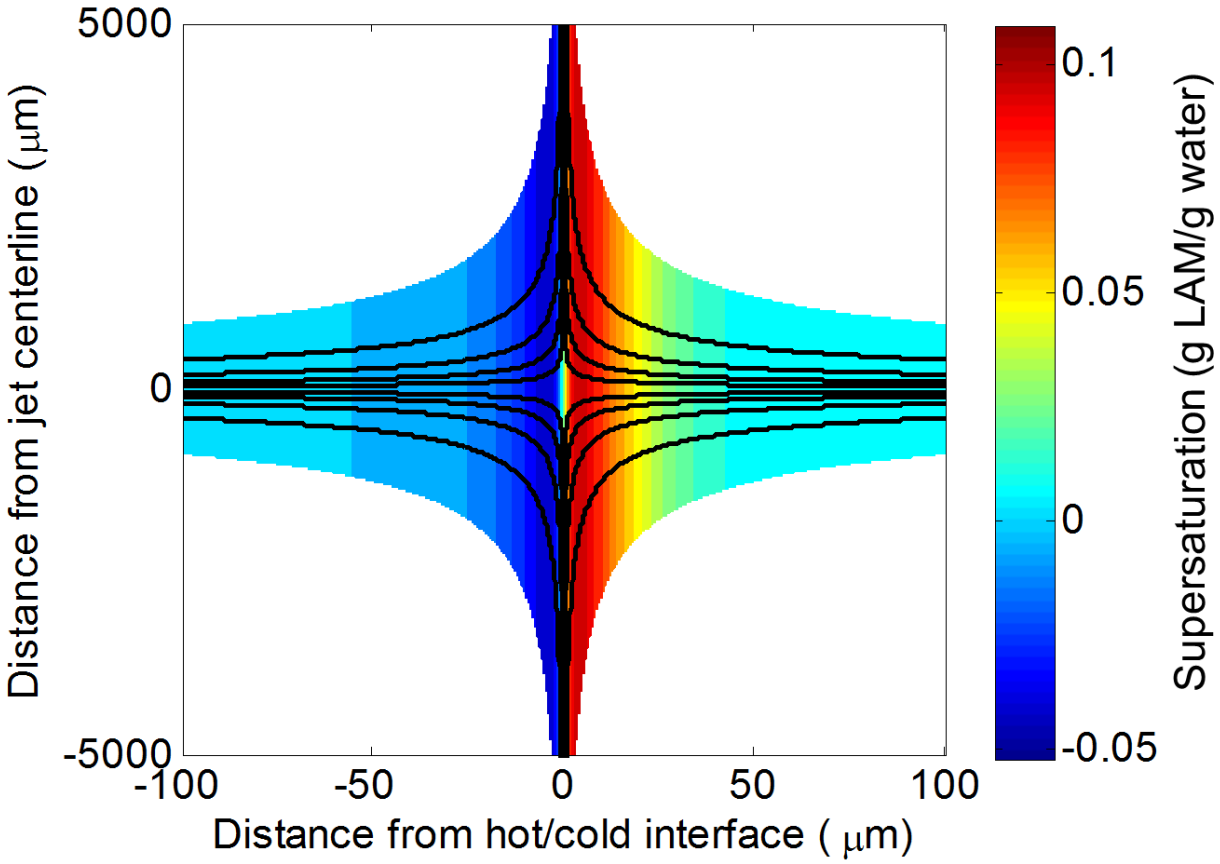

Figure 5.6. Supersaturation spatial field for the cooling DIJ mixer based on the 1D analytical solutions (Figs. 5.3c and 5.4c). The streamlines in black are the same as in Figs. 5.3c and 5.4c, with an additional streamline at the edges between air and liquid. The absolute supersaturation is indicated by color (red indicates high supersaturation, and blue indicates low supersaturation), in unit of g LAM/g water.

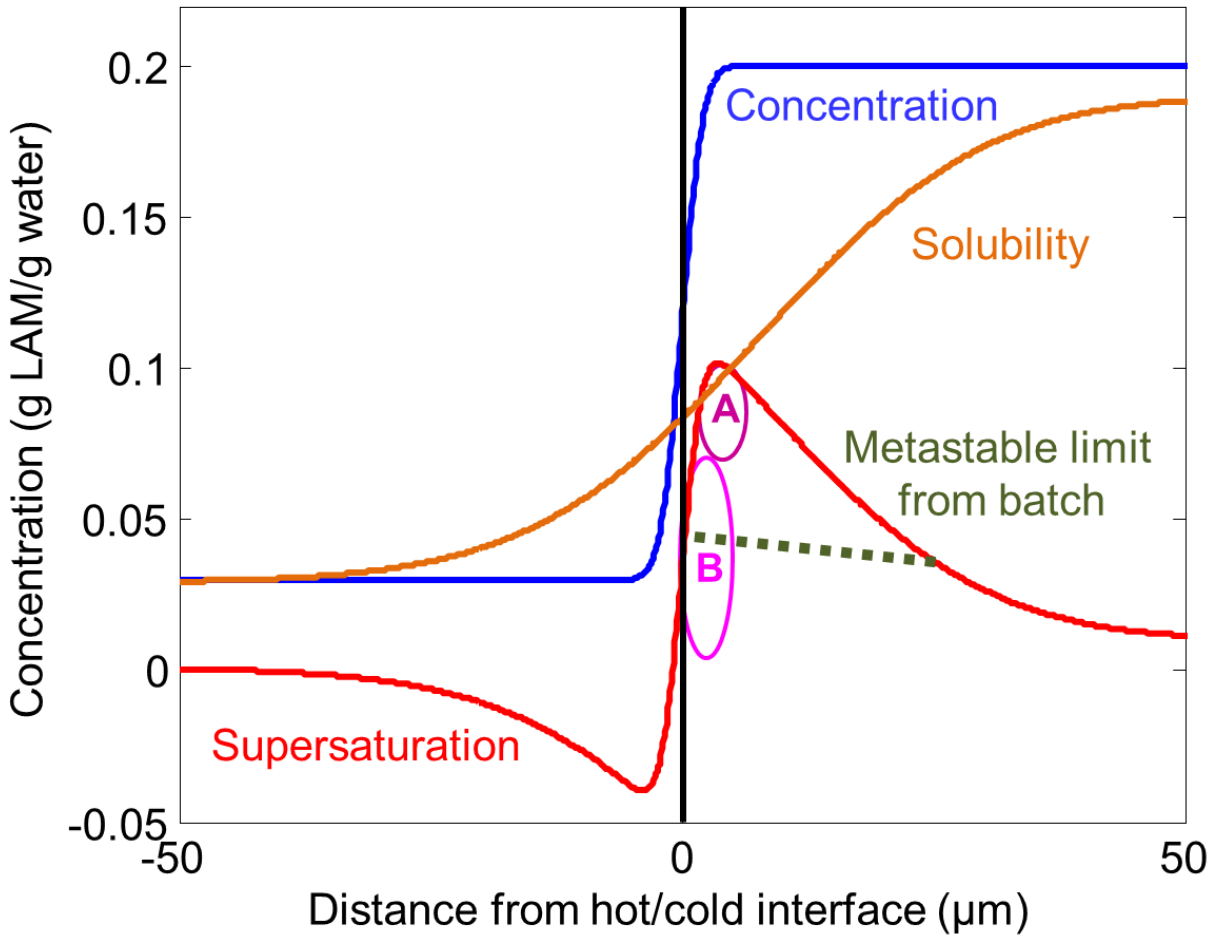

Figure 5.7. Concentration (blue curve), solubility (dark orange curve) and supersaturation (red curve) profiles along the jet centerline based on the 1D analytical solutions. Region A (dark purple) is the high supersaturation region, located between the thermal and concentration boundary layers, closer to the latter. Region A is just above the metastable limit for cooling DIJ, which is higher than the metastable limit in a cooling bath (dark green dashed line) due to smaller volume and faster cooling rate. Region B (light purple) is a long residence time region with slow velocity, located very near the jet centerline and the impingement plane.

As long as one of these two regions (high local supersaturation or long local residence time) exists for the solute/solvent system at operating conditions, the nucleation of crystals in a DIJ mixer may be feasible by combining hot and cold saturated solutions. This analysis leads to two design considerations for preferentially nucleating in a cooling DIJ mixer:

(i) Calculate the Lewis number for the solute/solvent system. A large value of α/D favors the generation of a high-supersaturation region (Region A in Fig. 5.7).

(ii) Choose inlet temperatures and concentrations for the two jets so that the average supersaturation is as high as possible at the set jet velocity (or flow rate) ratio. For 1:1 ratio of flow rates from the two jets, the average concentration of hot and cold streams should be set as high as possible relative to the solubility at the average temperature, that is, so that the inequality $\frac{1}{2}(c_{hot} + c_{cold}) > c_{sat,\frac{T_{hot}+T_{cold}}{2}}$ holds with as large of a gap as possible. [The inequality is almost always satisfied for organic compounds with convex solubility curves, such as LAM for the concentrations in Table 5.1, $\frac{1}{2}(0.2 + 0.03) = 0.115 > 0.08$.]

The average of the inlet concentrations does not need to be above the metastable limit in the crystallization phase diagram, but the peak concentration in the spatial domain should be. For Region A in Fig. 5.7 to exist, the maximum concentration must be higher than the metastable limit at its corresponding temperature, which is described by the analytical expression

$$\max_z \left\{\frac{1}{2}\left(\mathrm{erf}\left(\frac{z}{z_{refm}}\right) + 1\right) - \frac{c_{meta}(T(z)) - c_{cold}}{c_{hot} - c_{cold}}\right\} > 0 \qquad (5.11)$$

which is derived from the 1D analytical solution for the concentration.

For a particular system, if this condition (5.11) does not hold, then it is very unlikely that nucleation will occur in the cooling DIJ mixer. Approaches are available to increase the potential for primary nucleation. One approach to increase both the peak supersaturation and the left-hand side term of equation (5.11) is to increase c_{hot} by making the hot solution supersaturated (but not so supersaturated as to nucleate) [4]. If aggregation or oiling out phenomena is observed during DIJ mixing, then the concentration at the high temperature should be reduced.

A second approach to facilitate primary nucleation is to reduce the inlet jet velocity (but not so low that the jets no longer impinge). The lower the jet velocity (thus a smaller C in Eq. 5.3 and larger z_{refm} in Eq. 5.11), the longer the residence time.

Another approach is to increase the nozzle-to-impingement plane distance z_0 to decrease C and increase z_{refm}. The use of this approach is limited as longer distance will make the jet centerline alignment more difficult. When using the second and third approaches, one has to be reminded that c_{meta} is also a function of z.

5.4. Summary

The primary nucleation of crystals by combining saturated hot and cold solutions in a cooling DIJ mixer is analyzed, mostly in terms of derived analytical expressions for the velocity, temperature, concentration, and supersaturation fields. The analytical solutions with a 1D approximation of the temperature and concentration fields are accurate in the region of interest, as confirmed by 2D numerical solutions by the finite element method.

Design criteria were developed to provide guidance for achieving or for ruling out conditions not suitable for nucleation within a cooling DIJ mixer: (i) The Lewis number $\alpha/D >> 1$, so that the heat transfer is much faster than mass transfer, and (ii) The solute concentration on the hot side of the interface should be higher than the metastable limit. Several approaches were suggested to facilitate nucleation: (i) increase the concentration of the hot inlet stream, (ii) decrease the inlet jet velocity; and (iii) increase the distance between the two jets. The design criteria provide guidance, at the early stage of process development, for researchers to quickly identify compound-solvent combinations that will not nucleate crystals within DIJ mixers, based on their physicochemical properties.

The analysis of the cooling DIJ mixer may be extended to other free-surface DIJ mixer configurations such as use of oblique angles between the inlet nozzles or flow rate ratios other than 1:1. In the latter case, the symmetry analysis and flow field calculation will be different [150], [152], [156], [157], which will, together with jet geometry (nozzle-to-interface distance) [150], affect the constant C in the velocity field expressions. The design criteria may also shed light on analysis of other devices that generate small uniform-sized crystals through mixing hot and cold streams, such as radial or coaxial mixers [7].

6. CONTINUOUS-FLOW TUBULAR CRYSTALLIZATION IN SLUGS SPONTANEOUSLY INDUCED BY HYDRODYNAMICS

6.1. Introduction

Compared to batch and semibatch crystallizers, continuous-flow crystallizers have the potential for higher reproducibility, process efficiency, and flexibility, as well as lower capital and production cost [158]–[165]. Many continuous-flow crystallizer designs have been proposed in recent years with the goals of improving pharmaceutical processing or control of crystal product properties. For example, a continuous oscillatory baffled crystallizer has been proposed that employs a piston to agitate the crystal slurry in a long pipe with baffles [159]. Such a crystallizer can typically operate at lower shear rates than a single stirred-tank crystallizer, but is limited to lower solids densities and effective viscosities and has limited degrees of freedom for feedback control. An alternative design that employed laminar flow through a tube was demonstrated for paracetamol crystallization, but it was warned that inducing crystallization in a continuous slurry undergoing laminar flow in a tube by cooling through its walls was very prone to clogging for some solute-solvent systems [163]. With the notion that the best control of crystal size distribution should be obtained in a continuous-flow design that has negligible back-mixing with a residence time distribution approaching that of an ideal plug-flow crystallizer, several designs have tried to generate plug flow-like conditions. One continuous crystallizer design consists of slurry flowing through a tube with Kenics-type static mixers through its length to induce a more uniform velocity profile, with improved controllability obtained by introducing antisolvent at multiple points along the tube length [158]. A tubular crystallizer less prone to clogging ensured plug-flow behavior by forcibly segmenting the flow into liquid slugs separated by an immiscible fluid [160]–[162], [166]. Due to recirculation, the slurry in each slug is mixed

even in the absence of any static mixer [167], [168]. However, the separation of immiscible solvent takes additional process time when multiple liquids are used, and the slug production devices, usually with more than three channels, were relatively complicated. A significant advantage of all of these continuous-flow crystallizer designs is the lack of a stirring blade, resulting in negligible attrition compared to the mixed-suspension mixed-product-removal crystallizers widely employed for inorganic crystallization [169].

Most existing continuous-flow crystallizers are not specifically designed to provide many degrees of freedom for the control of crystal shape and size distribution in the presence of process disturbances and variations in crystallization kinetics associated with changes in contaminant profile of the feed streams. An improved continuous-flow crystallizer design would minimize operational problems while retaining the advantages of the best previous continuous crystallizers. At the same time, there are advantages to continuous-flow designs that enable the direct application of best-practices operations developed for the optimal control of batch and semi-batch crystallization.

Towards these goals, this chapter describes the design and implementation of a slug-flow crystallizer in which a multiphase mixture of liquid and gas in a tube spontaneously separates into slugs of liquid or slurry separated by slugs of gas [170]–[176]. The slug-flow crystallizer has all the advantages of a segmented-flow crystallizer, but does not require any specialized equipment to induce slug formation and avoids the use of liquid/liquid separators. In the proposed design, hydrodynamically stable slugs form spontaneously immediately upon the contact of the liquid/slurry and the gas. The crystallizer is designed so that nucleation and growth processes are decoupled to enhance the individual control of each phenomenon. This chapter demonstrates the crystallizer design for a cooling crystallization, which is inherently more

challenging than antisolvent crystallization due to the latter's easier nucleation to generate seed crystals.

6.2. Experimental methods and equipment setup

For better control of product CSD, the cooling crystallization process is decoupled into three parts: crystal nucleation, slug formation, and crystal growth (Fig. 6.1). Nuclei were generated within laminar flow by direct cooling, or within a coaxial or radial jet mixer by mixing hot and cold solutions. The slurry stream containing nuclei acting as seed crystals are combined with an air stream at flow rates selected to spontaneously form stable slugs. The motion of the slug through the tube mixes the solution without requiring any of the stirring blades that cause attrition in mixed-tank crystallizers. With each slug going through the tube with the same residence time, and with no stirring blades to cause attrition, the crystals in the slugs would be expected to grow to a large uniform size. The following experimental methods and equipment setup were selected to demonstrate the feasibility of this process design.

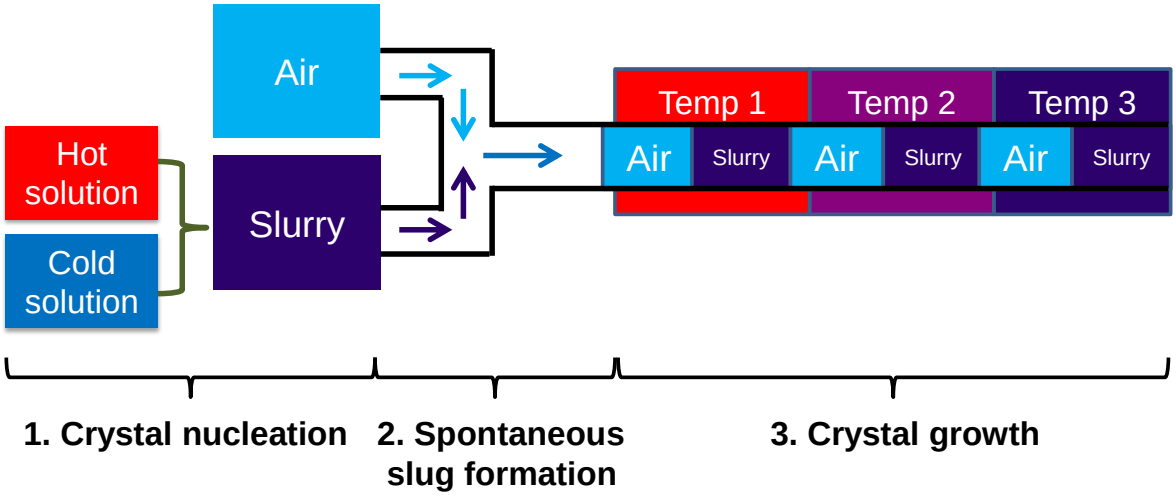

Figure 6.1. Schematic of slug-flow cooling crystallization. Crystal nucleation is induced by combining hot and cold LAM-aqueous solutions (photographs in Fig. 6.2). Slug formation spontaneously occurred by combining LAM slurry and air streams (Fig. 6.3a). Crystal growth occurs in the slurry in each slug going through the tube for a specified residence time (Fig. 6.3b).

The solute is L-asparagine monohydrate (LAM, purity ≥99% (TLC), from Sigma Aldrich) and the solvent is de-ionized (DI) water, which were selected because this solute-solvent combination is a well-studied model system that is challenging due to the very strong tendency of LAM crystals (product form, Fig. 6.S1) to aggregate in this solvent [4].

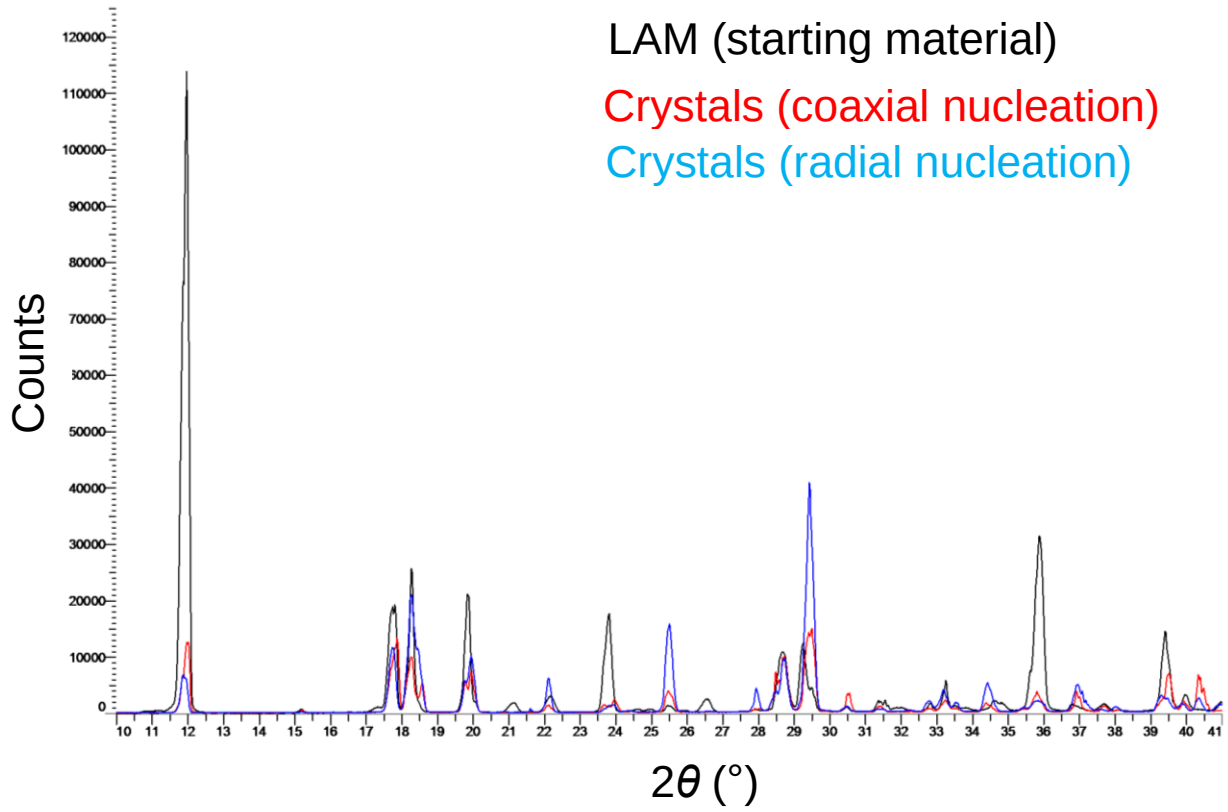

Figure 6.S1. X-ray powder diffraction (XRPD) of LAM starting material (black) and product crystals with nucleation from coaxial mixing (red, Fig. 6.8) and radial mixing (cyan, Fig. 6.11). The X-ray equipment was a Bruker D8 diffractometer using Cu K_α radiation (40kV, 40 mA). The angle (2θ) is from 10° to 41°, at a step size of 0.02°. The diffractogram was also compared to a published diffractogram for LAM [177] to further confirm the crystal structure.

6.2.1 Nuclei generation

In a preliminary experiment, a high solids amount (high initial concentration, 0.16 g LAM/g DI, as shown in Table 6.1) in each slug was used to demonstrate slug stability and CSD improvement in the growth stage. In another preliminary experiment, a low solids amount (low initial concentration, 0.09 g LAM/g DI, as shown in Table 6.1) was applied to facilitate in-line and off-line imaging and to compare the nucleation obtained from coaxial and radial mixers, to identify the most promising mixer type for subsequent experiments.

Table 6.1. Main experimental conditions for cooling nucleation.[a]

Experiment	Preliminary	Coaxial	Radial
Concentration of hot stream (g LAM/g DI)	0.16 or 0.09	0.16	0.16
Concentration of cold stream (g LAM/g DI)	N/A	0.02	0.02
Temperature of hot stream (°C)	65 or 44	65	66
Temperature of cold stream (°C)	N/A	23	22
Pump for hot stream	Peristaltic	Peristaltic	Peristaltic
Pump for cold stream	N/A	Peristaltic	Syringe
Tubing for hot and cold streams	Tygon	Tygon	BioPharm
Volumetric flow rate of hot stream (ml/min)	23.5	7.2	3.7
Volumetric flow rate of cold stream (ml/min)	N/A	6.8	3.3
Average velocity of hot stream (m/s)	0.05	0.02	0.02
Average velocity of cold stream (m/s)	N/A	2.14	0.78
Nucleation site (mixer)	Fig. 6.2a	Fig. 6.2b	Fig. 6.2c
Mixer inner diameter of hot inlet (mm)	3.1	3.1	2
Mixer inner diameter of cold inlet (mm)	N/A	0.26	0.3

[a]The preliminary experiment did not have a cold stream (the hot stream was directly cooled in an ice bath, see Fig. 6.2a). 'Peristaltic' refers to a peristaltic pump (Masterflex pump drive 7521-40, Easy Load II pump head with Model # 77200-50), and 'Syringe' refers to a syringe pump (Model NE-4000, from New Era Pump Systems, Inc.). 'Tygon' refers to Masterflex Tygon tubing, and 'BioPharm' refers to Masterflex BioPharm Plus platinum-cured silicone tubing. The volumetric flow rate reported for the syringe pump was pre-calibrated, and the volumetric flow rate reported for the peristaltic pump was estimated from the mass flow rate and temperature measured right before or after the experiment. The average velocities are calculated from the volumetric flow rates and mixer inner diameters.

The nucleation experimental conditions are listed in Table 6.1. For the radial mixing experiment (LAM nuclei were generated by combining hot and cold saturation solutions (66°C, 0.16 g LAM/g DI; and 22°C, 0.02 g LAM/g DI, respectively) through a coaxial or radial jet mixer (Figs. 6.2bc). This approach, first demonstrated in Ref. [4], contrasts with other continuous tubular cooling crystallizations that require a separate batch crystallizer to produce seed crystals to feed into the continuous crystallizer. Peristaltic pumps enable simple operation of

tubing at high temperature, while a syringe pump provides smooth flow rates. A peristaltic pump (Masterflex pump drive 7521-40, Easy Load II pump head with Model #77200-50) and a silicone tube (Masterflex BioPharm Plus platinum-cured silicone tubing, 3.1 mm inner diameter) were used to transfer hot solution to the mixer at a rate of about 3.7 ml/min. The tubing choice was based on the following criteria: low extractable and spallation, high temperature endurance, surface hydrophobicity (a more convex water slug shape is obtained by using a more hydrophobic surface) [178], and long life of the pump tubing. Around the pump head, a silicone tube with smaller inner diameter (2 mm) was used to increase the pump rotation rate for the same flow rate, to reduce the amplitude of flow pulsations. A syringe pump (Model NE-4000, from New Era Pump Systems, Inc.) was used to transfer cold solution to the mixer at a rate of 3.3 ml/min. The operational details of the other experiments in Table 6.1 are similar to the radial mixing experiment, but with the different values given in the associated column of the table.

(a)

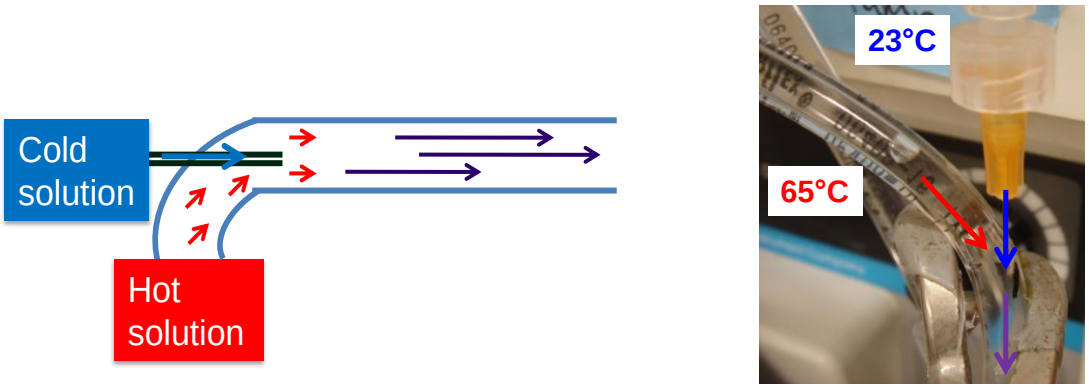

(b)

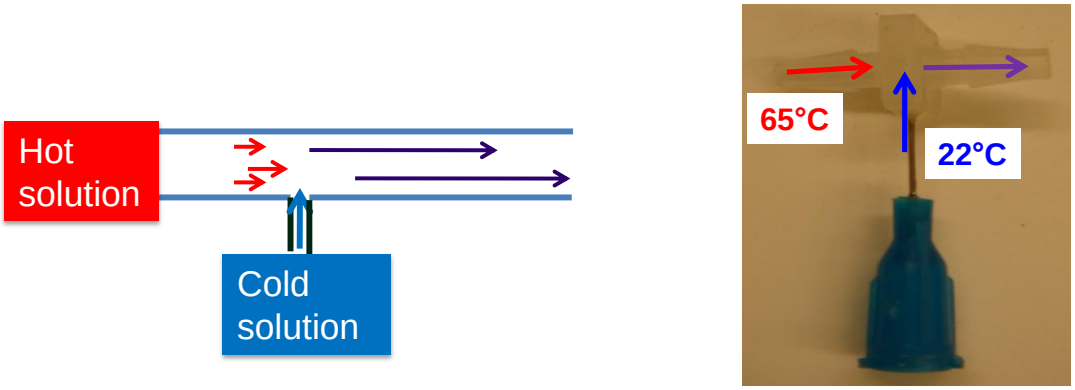

(c)

Figure 6.2. Photographs and schematics of setup for nucleation induced by cooling: (a) laminar flow tube; (b) coaxial mixer, the inner diameters of the two inlets are 3.1 mm (hot) and 0.26 mm (cold), respectively; (c) radial mixer, the inner diameters of the two inlets are 2 mm (hot) and 0.3 mm (cold), respectively.

6.2.2 Slug generation

A key element in the proposed crystallizer design is to exploit the hydrodynamically stable spontaneous generation of slugs. Many hydrodynamically stable flow regimes can occur when a liquid and gas are combined in a tube [172], [173], [179], as shown in Fig. 6.3, with the stability of the flow regimes determined by the ranges of inlet gas and liquid flow rates, tubing diameter, and fluids properties. For crystallization from liquid solution, most of the flow regimes have relatively poor spatial mixing of the liquid and allow liquid solution to remain close to the tube

walls for long periods of time, which would encourage crystallization on the surface of the inner tube (aka fouling), eventually clogging the tube. In contrast, slug flow has an internal circulation of liquid [168] that limits the time that liquid stays close to the tube wall, which results in the fluid dynamics within each slug operating like a small well-mixed crystallizer, with limited fouling.

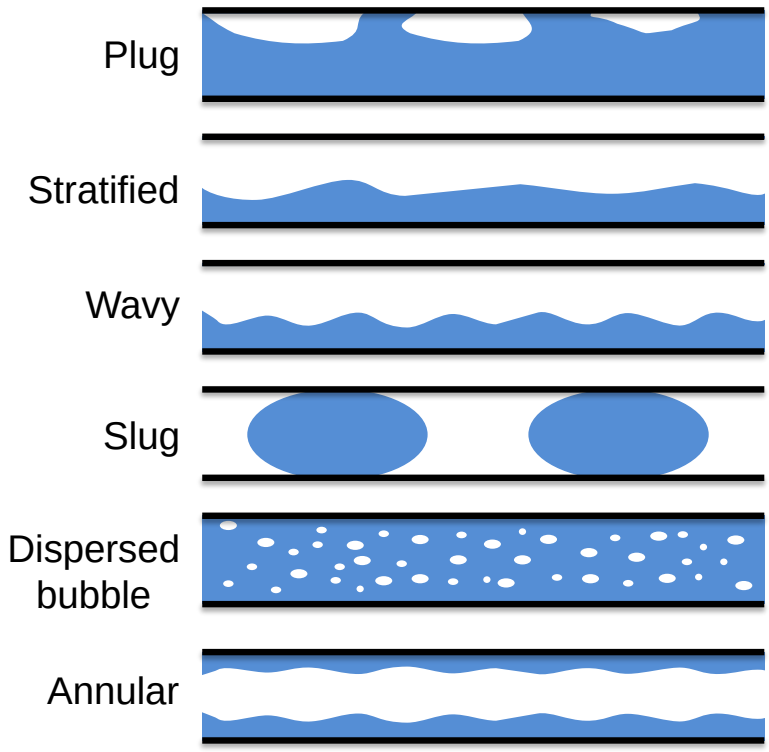

Figure 6.3. Schematics of hydrodynamically stable flow patterns of a gas (white color) and liquid (blue color) mixture in a horizontal round tubing. The notations and images of the flow were based on [179]. The air and liquid in slug flow can swap places depending on the affinity of the liquid for the material on the inner surface of the tube, e.g., a water slug with a strongly hydrophobic surface would appear as shown, with convex/roundish water slugs moving through the tube. For a strongly hydrophilic surface with water as the liquid, the air slugs would be convex. Regardless of surface affinities, the slugs become asymmetric at sufficiently high velocities, as observed in Fig. 6.10.

Fig. 6.4a shows an experimental demonstration of the spontaneous formation of hydrodynamically stable slugs after streams of slurry and air are passed through two branches of a T mixer that had a similar inner diameter as the tubes. Stable slugs were maintained throughout crystallization within each slug as it transports through the tubing to its exit. Air was transferred to the mixer through the same peristaltic pump with dual pump heads, with flow oscillation suppressed by offsetting their rollers, and a silicone tube with filters (pore sizes 3 μm and 0.2 μm) to prevent dust particles from getting into the tubes at the pump heads, and from contacting slurry at the mixer, respectively. Within a large hydrodynamically stable regime [173] for slugs in a 3.1 mm (inner diameter) tube, the length ratio of liquid and gas slugs was adjustable by specifying the flow rates (or pump rotation rates) between slurry and air. A pump rpm ratio of 1:1 between hot solution and air was used to generate stable liquid slugs of similar sizes with all aspect ratios of about 1 (Figs. 6.5ab). A horizontal wrapping of tubing around a bucket produced hydrodynamically stable slugs with no combination or partitioning (Figs. 6.4b and 6.5ac).

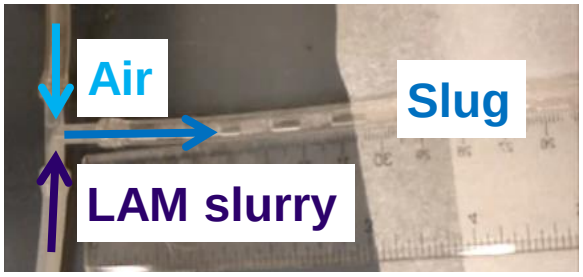

(a)

(b)

(c)

Figure 6.4. (a) Slug formation from streams of LAM slurry and air through a T mixer. The white slugs contain LAM-aqueous slurry, and the transparent slugs are air. (b) Slurry-containing slugs in the growth stage. The white slugs have high solids densities in this photograph. (c) Crystals in the funnel after filtration obtained under operations of high solids density in each slug.

(a)

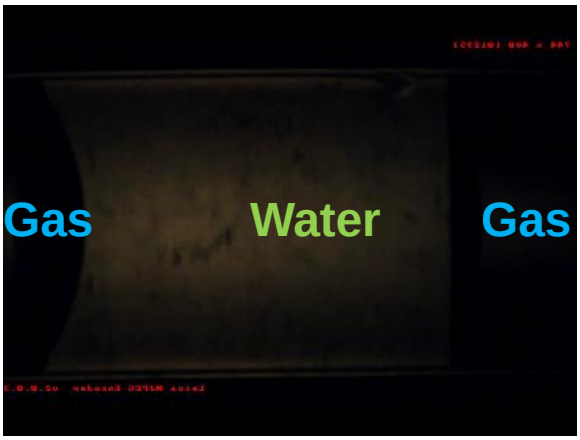

(b)

(c)

Figure 6.5. (a) Photograph of stable water slugs (aspect ratio about 1) separated by air slugs (aspect ratio about 4) in packed silicone tube, with black background to improve contrast. (b) Microscope image of water slug (slug in the center) and parts of air slugs (dark regions at both

edges) inside a silicone tube. The flow direction is from left to right. The front of the water slug is less curved towards the flow direction than the back [171], as indicated from the thickness of black shades at water/air interfaces. At higher flow rates, the shape of the water slug would be dominated by the velocity (e.g., the drag from wall) rather than the hydrophobicity of the tubing material. (c) Horizontal wrapping of silicone tube around a cylinder of the same diameter. The photograph (a) is a close-up of (c) indicated by the edge of the black background.

6.2.3 Crystal growth

The growth experimental conditions were reported in Table 6.2. Again the radial mixing experiment was used to justify the optimized design. The residence time after slug formation was on the order of 5 minutes (to prevent generation of large amount of waste materials) in 15.2 meter of transparent hydrophobic silicone tube (Dow Corning Pharma-80 tubing, 3.1 mm inner diameter). While the slugs were moving inside the silicone tube towards the exit, videos of them were recorded under an in-line trinocular stereomicroscope (Microscope model #XV331AC20C, from Cyber Scientific Corp.; Camera model #DFK 22BUC03, from The Imaging Source, LLC) at 1 meter before the exit. After the slurry slugs exited the end of tube, they were collected one by one into polystyrene wells (1.5 cm diameter, with the aqueous slugs covered with corn oil after collection to suppress evaporation) for off-line imaging under the stereomicroscope.

Table 6.2. Experimental conditions for slug formation and growth by cooling.[a]

Experiment	Preliminary	Coaxial	Radial
Pump for air stream	Peristaltic	Peristaltic	Peristaltic
Pump rotation rate for air stream (rpm)	66	78	53.4 (dual head)
Tubing for slug movement	Tygon	Tygon	Pharma-80
Tubing length (m)	15.2	15.2	15.2
Residence time (min)	1.7	2.9	5.0
Tube inner diameter (mm)	3.1	3.1	3.1

[a]'Peristaltic' and 'Tygon' are the same terms as in Table 6.1, and 'Pharma-80' refers to Dow Corning Pharma-80 tubing. Residence time counts the time between when the hot solution reaches the mixer and the exit of the tubing.

Crystallizations are generally more poorly mixed for higher solids densities. Since each slug operates as a small well-mixed batch crystallizer, each slug will not be as well mixed for a high solids density, in which case a fines dissolution step can be inserted into the crystal growth stage to enlarge the final product crystals and reduce aggregation. The end stage of the preliminary experiment had fines dissolution implemented as a fast heating of the slurry slugs to 50°C, followed by going through 2 meters of tubing in each of the two temperature baths at 39°C and 22°C, respectively, and then to room temperature (Fig. 6.6). The temperature in each bath was held constant using peristaltic pumps (same model as before) and hot and cold water reservoirs (Fig. 6.6), controlled with Proportional-Integral controller tuned as in past studies [77]. The temperature baths were not used in experiments with coaxial and radial mixing, as the product crystals from those experiments were uniformly large without fines dissolution.

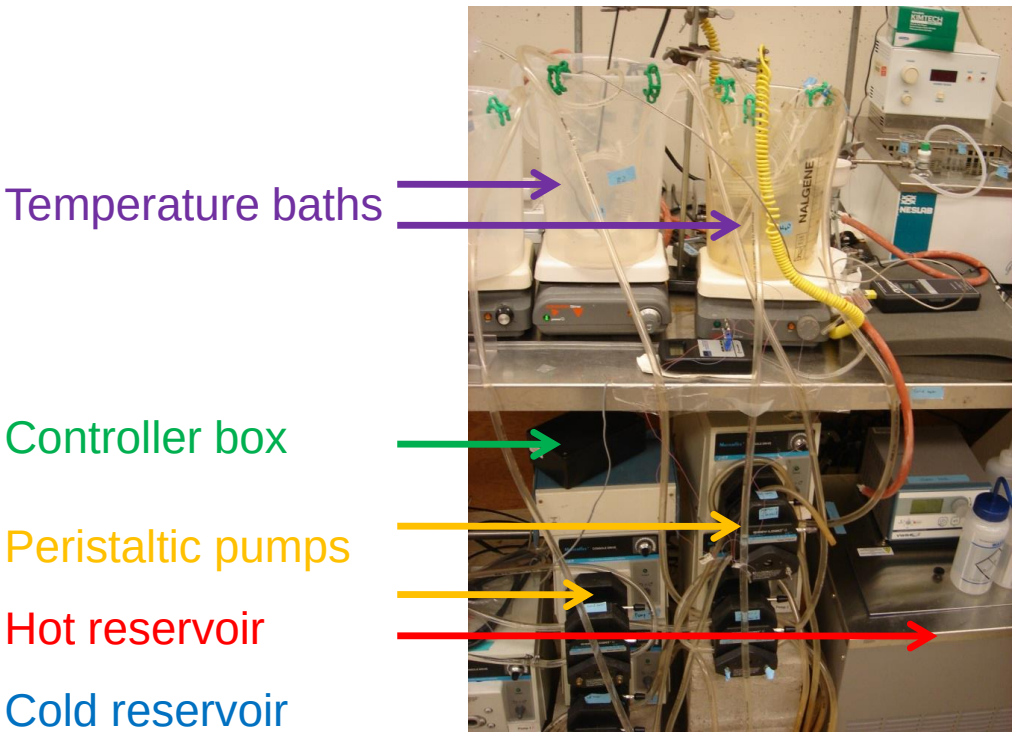

Figure 6.6. Photograph of the experimental setup with two temperature baths. The hot reservoir is in a temperature-controlled bath (lower right), and the cold reservoir is in an ice bucket at the lower left (not shown in the picture). Each of the two temperature baths at the top of the photograph is controlled with only one dual-head peristaltic pump using Proportional-Integral controllers tuned by Internal Model Control [180][181]. The dual head transfers both inlet and outlet water, keeping the water level of the reservoir constant. The temperature of the slugs in the tube increases or decreases relatively slowly due to the low thermal conductivity of the tube wall. Only one temperature bath is needed for coarse temperature control; additional temperature baths enable finer tuning of the spatial temperature profile of the slugs as they move through the tube.

6.3. Results and discussion

Below are results and discussion from the experimental demonstrations of the slug-flow crystallizer that include (1) a nonmonotonic spatial temperature profile to reduce aggregation and promote growth, (2) a comparison of coaxial and radial mixers for in-situ generation of seed crystals, and (3) the improvement of hydrodynamics for reducing variations in product quality.

6.3.1 Preliminary Experiment with Temperature Baths to Reduce Aggregation and Promote Growth

After crystal nucleation in a tube under laminar flow (no mixer, Re number of about 150, see Fig. 6.2a) and slug formation (Fig. 6.4a), the solids amount increases in the slugs as they move along the tube length, indicated by the whiter color of slurry slugs (Fig. 6.4b, top) observed visually after a short period of growth. Under high initial solute concentrations, the slugs were able to carry 12.3 wt% crystals in the slurry, with crystals nearly occupying the whole slug (Fig. 6.4b) at a reasonably fast flow rate (Table 6.1). The total yield (mass of product crystals/total mass of solute) from this preliminary experiment was 87%, close to the theoretical yield of a batch cooling experiment from the same hot solution (87.5%).

The final product crystals after growth from laminar flow nucleation were small and aggregated (Fig. 6.7a) (LAM has a strong tendency towards aggregation [4]). Heating followed by natural cooling in the tubing after the first stage of growth was expected to increase the crystal size [97][11], which was observed experimentally (Fig. 6.7b). Heating followed by cooling in two baths of controlled temperatures was able to further increase the average crystal size and reduce aggregation (Fig. 6.7c). Some small crystals remained, which motivated the implementation of mixers to provide better control of nucleation, which is described next.

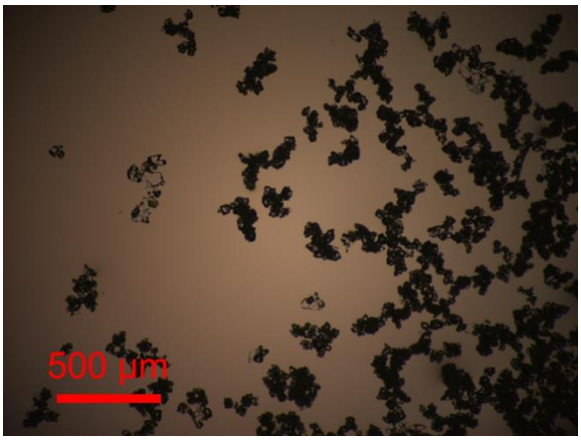

(a)

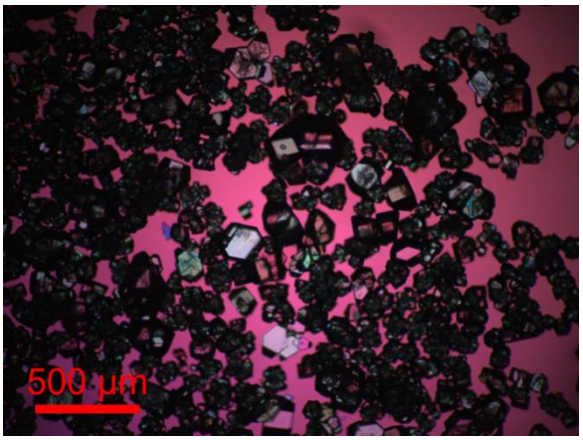

(b)

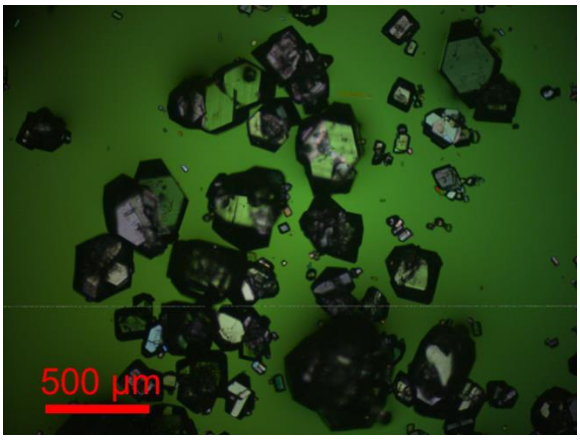

(c)

Figure 6.7. Microscope (with polarizers) images of product crystals from the preliminary experiment (after laminar flow nucleation and growth in slugs) with (a) no heating; (b) heating to 50°C followed by natural cooling in the tubing; (c) heating to 50°C followed by two temperature baths of set temperatures (39°C and 22°C).

6.3.2 Improved Hydrodynamics (e.g., Coaxial Mixing) to Improve Nucleation from Laminar Flow

The product crystals obtained when nucleation was induced by coaxial mixing (Fig. 6.8) improved the seed crystal quality (Fig. 6.9), with less aggregation and narrower CSD in each slug, compared to nucleation in laminar flow (Figs. 6.7a and 6.S2). Crystals nucleated by impinging a hot and a cold solution at an approximately equimolar ratio (Table 6.1) in a small volume can be more uniform in size than crystals nucleated by cooling from a single solution, as high local supersaturation (much higher than the average supersaturation) can be obtained near the interface between hot and cold solutions when the thermal diffusivity is much larger than the molecular diffusivity, as experimentally demonstrated and explained in a previous study [4]. By combining two streams, the coaxial mixer also has more intense mixing than would be obtained using one stream [182], with a Re ~ 600, which is expected to lead to more uniform-sized crystals due to more crystals following a similar supersaturation trajectory in the crystal phase diagram.

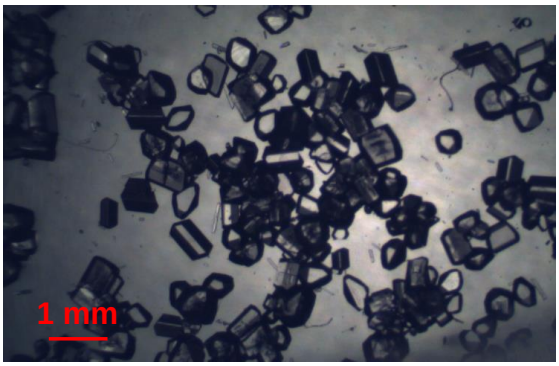

(a)

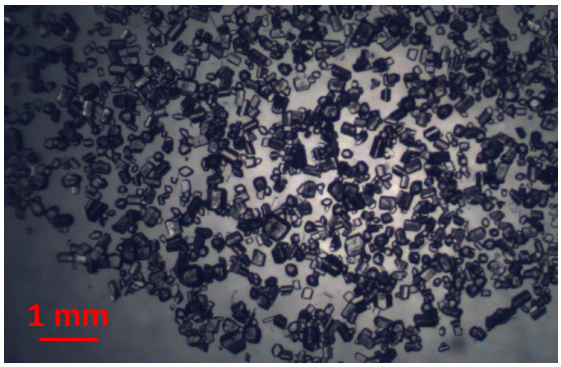

(b)

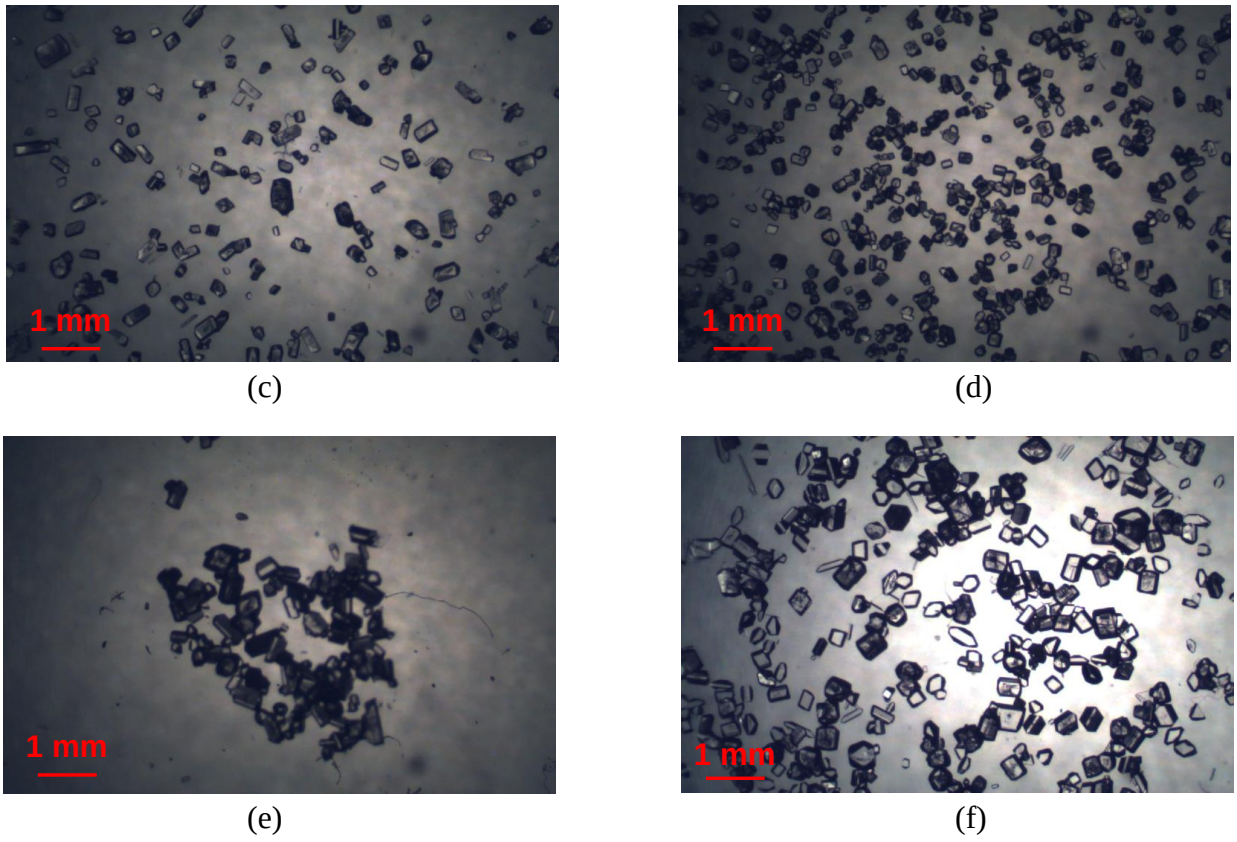

Figure 6.8. Stereomicroscope images of product crystals with nucleation induced by coaxial mixing in slug number (a) 21, (b) 81, (c) 141, (d) 201, (e) 261, (f) 311 (last slug). The scale bar = 1 mm. Detailed experimental conditions are provided in the coaxial experiment column in Tables 6.1 and 6.2.

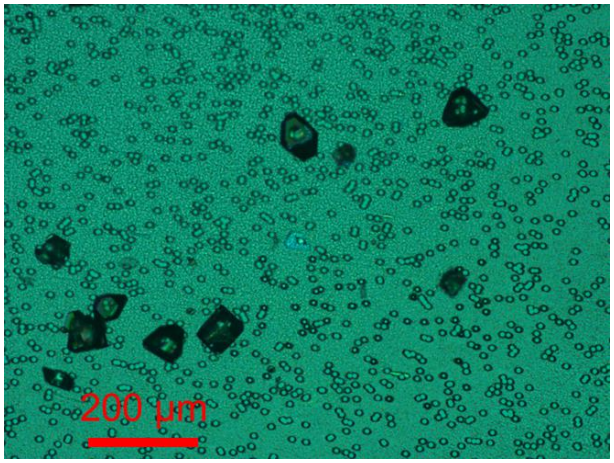

Figure 6.9. Seed crystals generated by cooling nucleation in a coaxial mixer. The background is a membrane filter with a pore size of 10 µm. The flow setups are in Fig. 6.2b. Although the

quantitative size of measured seed crystals is a combination of both nucleation and growth (with local supersaturation not easy to measure at fine spatial resolution), this image does qualitatively show the coaxial mixing reduces crystal aggregation and CSD width compared to laminar flow.

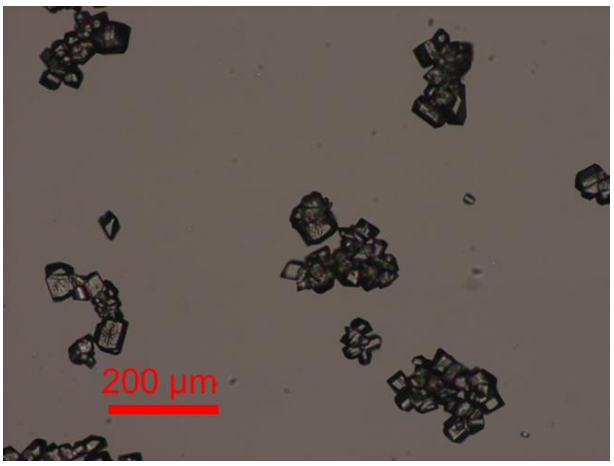

Figure 6.S2. Seed crystals generated by cooling nucleation in laminar flow. The starting concentration is 0.09 g LAM/g DI (the rest of experimental conditions are also listed in Table 6.1, in the preliminary experiment column). Although the quantitative size of measured seed crystals is a combination of both nucleation and growth (with local supersaturation not easy to measure within small-diameter tubes), this image does show the qualitative extent of aggregation.

While each slug obtained using the coaxial mixer (Fig. 6.8) had orders-of-magnitude less aggregation than the preliminary experiment (Fig. 6.7), the crystal number per unit volume and mean crystal size were variable from one slug to another (Fig. 6.8). With nucleation using a coaxial mixer, the crystal size distribution was narrow within nearly each slug (Fig. 6.8a-f). The variation in size of crystals before slug formation (Fig. 6.9) is similar to that within a single slug (Fig. 6.8, Table 6.3), which suggests that the mixing within each slug (from internal recirculation [176]) may be sufficient for maintaining a spatially uniform environment of temperature and concentration after nucleation. In particular, if the mixing had not been sufficient, there would have been a small number of crystals much larger than shown in Fig. 6.8, such as observed at the bottom of poorly mixed batch crystallizers. The slug-to-slug variability suggested that some

experimental component was inducing oscillations to the experimental system, which led to an effort to reduce flow pulsations from the peristaltic pumps (the experimental details are in Sections 6.2.1 and 6.2.2, with the results discussed in next section).

Table 6.3. Product crystal size and shape statistics for slug-flow crystallization, for nucleation using coaxial mixing (corresponding to the experimental results reported in Fig. 6.8).[a]

Slug number	21	81	141	201	261	311	All
Crystal image	Fig. 6.8a	Fig. 6.8b	Fig. 6.8c	Fig. 6.8d	Fig. 6.8e	Fig. 6.8f	Figs. 6.8a-f
Crystal mean length (μm)	442	205	231	279	341	318	303
Standard deviation, length (μm)	100	62	107	81	132	96	99
Crystal mean width (μm)	316	136	144	184	217	222	203
Standard deviation, width (μm)	82	46	58	52	69	76	65
Correlation coefficient of length and width	0.43	0.21	0.72	0.58	0.65	0.54	0.52
Coefficient of variation in length	0.23	0.30	0.46	0.29	0.39	0.30	0.34
Coefficient of variation in width	0.26	0.34	0.40	0.28	0.32	0.34	0.33
Mean aspect ratio	1.47	1.60	1.65	1.56	1.61	1.62	1.59

[a]The correlation coefficient of length and width varies widely from slug to slug, which indicates a wide range of crystal aspect ratios among different slugs (a correlation coefficient of length and width of one would correspond to all crystals having exactly the same aspect ratio).

6.3.3 Improved Hydrodynamics (e.g., Reducing Flow Variation) to Reduce Slug-to-Slug Variability

With the objective of reducing slug-to-slug variability, flow pulsations were reduced by replacing the peristaltic pump for cold liquid solution with a syringe pump, and by implementing offsetting dual heads of the peristaltic pump for the gas flow. Since another goal was to reduce variability generally, the slug shape was modified to improve mixing within each slug. In particular, better mixing is expected from a slug whose aspect ratio is close to one, such as for the slugs in Figs. 6.5b and 6.10b, rather than larger aspect ratios as for the slugs in Figs. 6.4b and 6.10a. An aspect ratio closer to one was expected to make the crystals more spread out within each slug, which was experimentally confirmed (Figs. 6.10ab). The effect of aspect ratio on mixing within each slug was more obvious with higher flow rates.

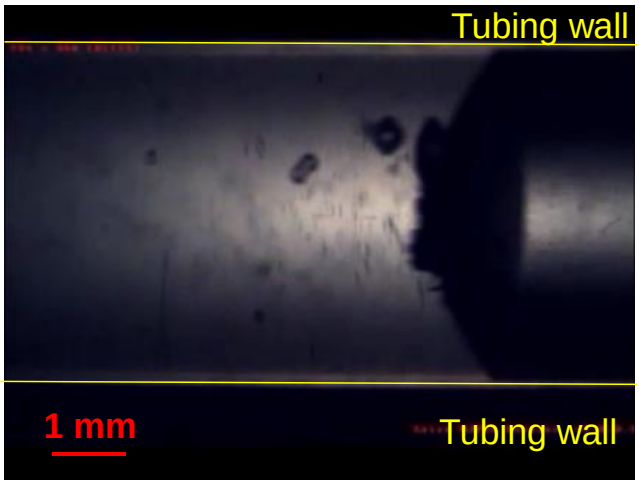

(a)

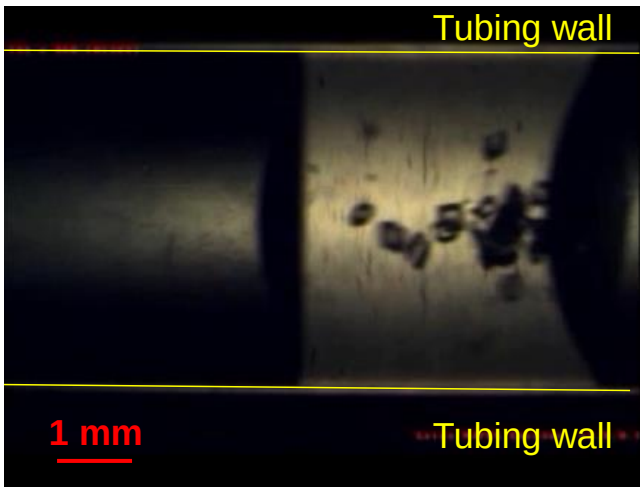

(b)

Figure 6.10. In-line stereomicroscope images of crystals in slugs with an aspect ratio of about (a) 4 (the slug is too long to fit into the image and is off to the left) and (b) almost 1. The scale bar ≈ 1 mm. Relatively low solids density was used in both experiments so that the crystals could be clearly imaged.

In addition, the coaxial mixer was replaced by a radial mixer, which provides much better mixing for systems of comparable velocities [183]. Compared with the coaxial mixer (Fig. 6.8a-f, Table 6.3), the radial mixer experiment produced similar mean aspect ratios and coefficient of variations in length and width (Fig. 6.11a-f, Table 6.4) within each slug but larger mean crystal dimensions and much lower slug-to-slug variability in mean crystal shape (i.e., aspect ratio). The reduction of slug-to-slug variability of the product crystal shape in the radial mixer experiment may be attributed to its reduced flow variability. The use of either coaxial or radial mixers reduced aggregation by orders-of-magnitude compared to laminar flow (compare Figs. 6.8 and 6.11 with Fig. 6.7).

Table 6.4. Product crystal size and shape statistics for slug-flow crystallization, for nucleation using radial mixing (corresponding to the experimental results reported in Fig. 6.11).[a]

Slug number	16-18	106-108	286-288	466-468	646-648	726-728	All

Crystal image	Fig. 11a	Fig. 11b	Fig. 11c	Fig. 11d	Fig. 11e	Fig. 11f	Figs. 11a-f
Crystal mean length (μm)	225	479	588	545	502	325	444
Standard deviation, length (μm)	103	146	202	160	181	92	152
Crystal mean width (μm)	176	388	471	371	330	220	326
Standard deviation, width (μm)	90	152	181	146	173	71	142
Correlation coefficient of length and width	0.92	0.86	0.90	0.81	0.74	0.76	0.83
Coefficient of variation in length	0.46	0.30	0.34	0.29	0.36	0.28	0.34
Coefficient of variation in width	0.51	0.39	0.39	0.39	0.52	0.32	0.43

[a]The correlation coefficient of length and width is near one for each slug, which indicates a high consistency in aspect ratio among different slugs (a correlation coefficient of length and width of one would correspond to all crystals having exactly the same shape).

Table 6.S1. Mean size for seed crystals by cooling nucleation in laminar flow (corresponding to the experimental results reported in Fig. 6.S2).[a]

Crystal image	Fig. A2
Crystal mean length (μm)	48
Standard deviation, length (μm)	16
Crystal mean width (μm)	34
Standard deviation, width (μm)	15
Correlation coefficient of length and width	0.71

[a]Crystal sizes were based on individual crystals within the loosely bound aggregates. The crystal dimensions are much smaller than when a radial or coaxial mixer was used (Tables 6.3 and 6.4).

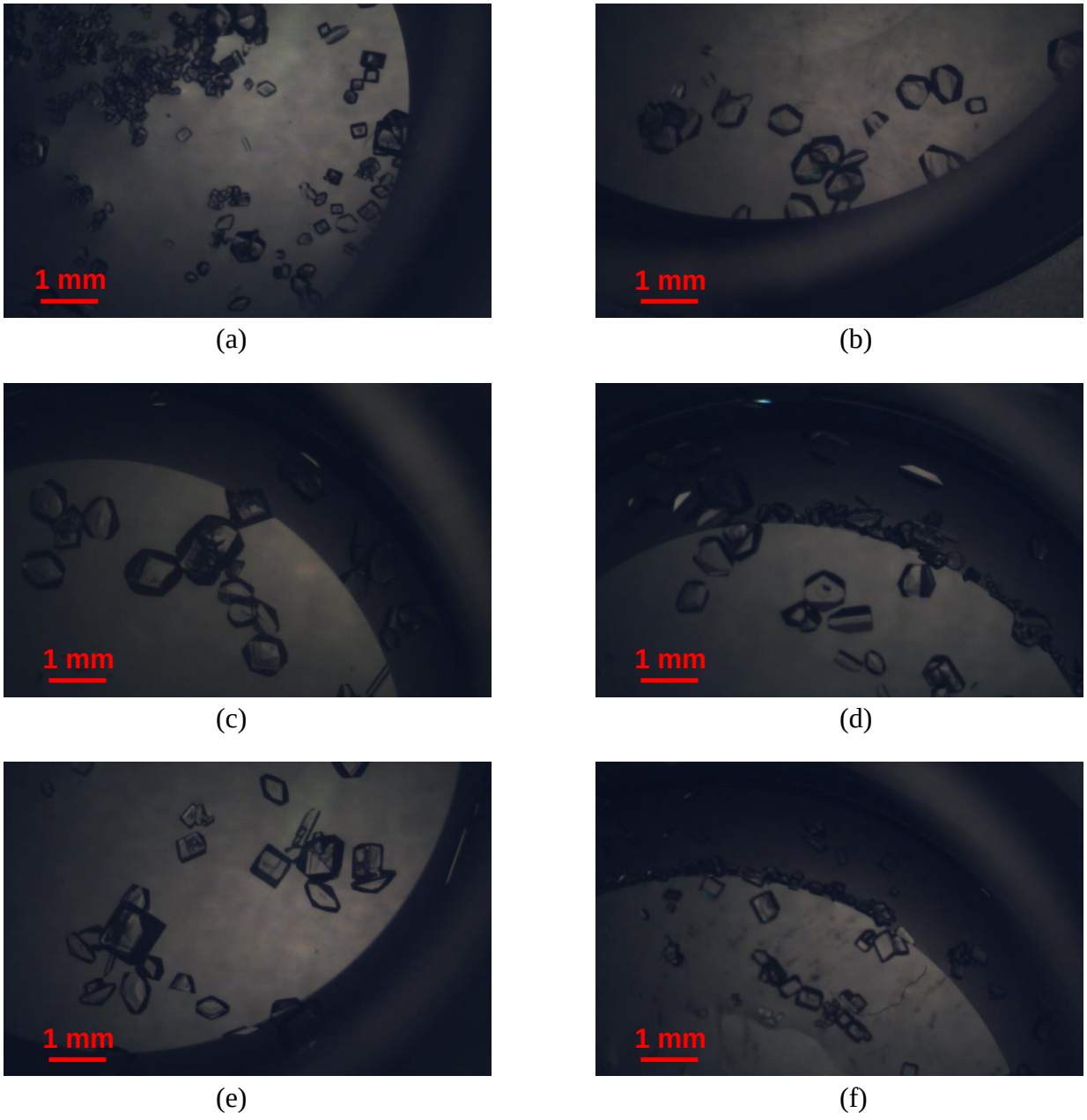

Figure 6.11. Stereomicroscope images of product crystals with nucleation by radial mixing in slug number (a) 16–18, (b) 106–108, (c) 286–288, (d) 466–468, (e) 646–648, (f) 726–728 (last slug). The scale bar = 1 mm. The total number of slugs is much larger than for the coaxial mixing experiments, for a similar amount of feed solutions, due to the smaller aspect ratios of the slugs. The dark ring-shape shades are due to the different refractive index between corn oil and water. Brighter areas are covered with corn oil. Crystals on top of the slurry (usually tiny) will

tend to align at the interface between the oil and water. Detailed experimental conditions are provided in the radial experiment column in Tables 6.1 and 6.2.

6.4. Summary

High-quality non-aggregating LAM crystals were produced in a continuous-flow cooling crystallizer that employed alternating slugs of slurry and air moving through a tube with a residence time of 2 to 5 minutes. The most novel aspects of the experimental system are that (1) the crystals were nucleated by mixing hot and cold solutions in coaxial and radial mixers instead of rapid cooling of a single solution [161], [163] or feeding seeds obtained by batch crystallization as done in many past continuous-flow cooling crystallization studies [184], and (2) the slugs were spontaneously induced by hydrodynamic forces rather than by alternating the feed between the two inlet flows [162]. As used in some past studies [160], [162], air was employed as the separating fluid so that no liquid-liquid separations are needed downstream from the crystallization.

The slugs generated spontaneously by hydrodynamic forces were highly uniform in size and shape, and the slugs maintained that uniformity during crystallization as the slugs moved through the tubular crystallizer. The slug size and shape were controllable by just changing the ratio of volumetric flows rates of the inlet streams of slurry and air. An in-line imaging system was employed to study the effect of slug aspect ratio, which confirmed the expectation that aspect ratios near one produced better mixing than larger aspect ratios. The size uniformity of the product crystals was enhanced by the introduction of the coaxial or radial jet mixers to improve nucleation, and by employing in-line fines dissolution involving a nonmonotonic spatial temperature profile (cooling, then heating, then cooling). The crystals grown from nuclei produced in a radial mixer were more uniform in size compared to a coaxial mixer (compare

Figs. 6.11 and 6.8). The high degree of mixing and small size of each slug promoted high spatial uniformity of temperature within each slug.

The experimental system can be used to simplify scale-up as the slug volume can be selected as the same volume as the batch crystallizer used in bench-scale experiments for initial process development. The residence time of 2 to 5 minutes is orders of magnitude shorter than the hours taken in a stirred-tank crystallization, enabled by the much higher supersaturations that can be generated within a slug while maintaining pure-growth conditions (the slug does not have a stirring blade, which is the primary source of secondary nuclei and attrition particles in a mixed-tank crystallizer). With further optimization, it is likely that the residence time could be brought down to less than one minute. The slug-flow crystallizer has higher equipment utilization, as the experimental system can generate crystals with narrow CSD with orders-of-magnitude higher supersaturation and growth rate than obtainable using a stirred tank of the same volume. Instead of scale-up, throughput can be further increased by scale-out, that is, using more slugs. While scale-out has already been discussed many times in the literature for microscale systems [185], this approach is much more industrially relevant for the length scales considered in this article, at least for the typical production rate for a pharmaceutical compound.

7. INDIRECT ULTRASONICATION IN CONTINUOUS SLUG-FLOW CRYSTALLIZATION

7.1. Introduction

In the pharmaceutical industry, the continuous generation of crystals of target size distribution has the potential to simplify and/or reduce post-crystallization operations [186], [187]. Crystal growth can be effectively controlled in a segmented/slug flow [5], [161], [167], [184] that can be operated at low enough supersaturation to remove or greatly suppress secondary nucleation [7], but the control of primary nucleation to generate the initial seed crystals is more limited [188]. The joining of two streams in dual impinging jet, coaxial, or radial micromixers has been demonstrated to produce seed crystals of uniform crystal size distribution (CSD) [4], [7], but with a nucleation rate that depends on the liquid flow rate [4], [7], [18], [189]. In addition, the primary nucleation rate in many micromixer designs is very sensitive to inlet flow alignment, and clogging can potentially occur in low velocity regions of the micromixers.

Ultrasonication is a technology for facilitating primary nucleation that has been useful in various industrial and academic studies [21], [190]–[193]. The nucleation rate is a function of ultrasonication parameters rather than just liquid flow rate, which provides extra degrees of freedom for controlling the CSD. Ultrasonication-assisted crystallization seldom has clogging problems, and actually has the opposite effect and is commonly used to remove particles from containers for cleaning purposes [191]. Ultrasonication facilitates primary nucleation by inducing acoustic cavitation in the liquid solution using high-frequency mechanical vibrations from converters (connected sonication generator) [194].

The effect of ultrasonication operation parameters on crystallization process and crystal size has been widely studied (e.g., see [191], [194]–[197] and citations there), which indicates that

the primary nucleation rate is sensitive to the power amplitude. This observation suggests that the power amplitude is a good choice for control of the primary nucleation rate in a continuous crystallization, which is the approach taken in this article.

In most studies of sonocrystallization, an ultrasonication probe (or horn) is in direct contact with the liquid solution, which may induce secondary nucleation from metal contact or contaminate the solution with metal after long time of use [191], [198]. The closer the liquid solution is to the probe tip, the more ultrasonication energy per unit volume is transferred to the solution, which is more spatially localized than when a sonication bath is used. This article uses an ultrasonication horn and so has spatial localization of ultrasonication energy, but does not directly contact the horn with the liquid solution. The ultrasonication probe tip is placed close enough to the liquid solution so as to transfer significant power and induce primary nucleation, but the tip and liquid solution are separated by a thin wall of plastic.

This article describes the implementation of this indirect ultrasonication-assisted primary nucleation into a slug-flow cooling crystallizer to demonstrate rapid generation of a large amount of crystals of larger size than the nuclei. The most closely related study is described in a high quality paper published by Khinast and co-workers [5] that also employs indirect ultrasonication and crystal nucleation and growth in a liquid solution flowing through a plastic tubing. The main differences compared to [5] is that this article (1) uses an ultrasonic probe focused on a small spatial location instead of placing a long tube in a sonication bath, (2) has order of magnitude lower time in which the solution is in contact with ultrasonication, (3) uses a simpler experimental system, and (4) uses horizontal instead of vertical coils of tubing. The pros and cons of the different configurations are discussed at the end of the Results and Discussion section.

7.2. Experimental Materials and Methods

7.2.1. Materials. The solute is L-asparagine monohydrate (LAM, purity ≥99%, from Sigma Aldrich), which forms crystals in the solvent, de-ionized (DI) water, that have a strong tendency to aggregate [4].

7.2.2. Equipment. A slug-flow cooling crystallizer that decouples crystal nucleation, slug formation, and crystal growth to allow control of the individual processes is shown in Fig. 7.1. The main differences with past similar experimental systems are described in the Introduction section.

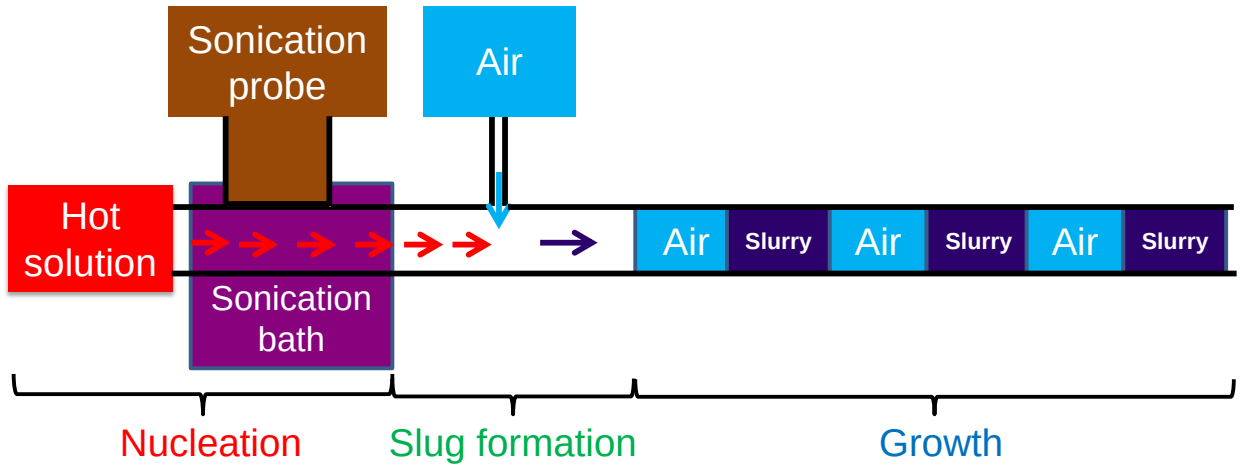

(a)

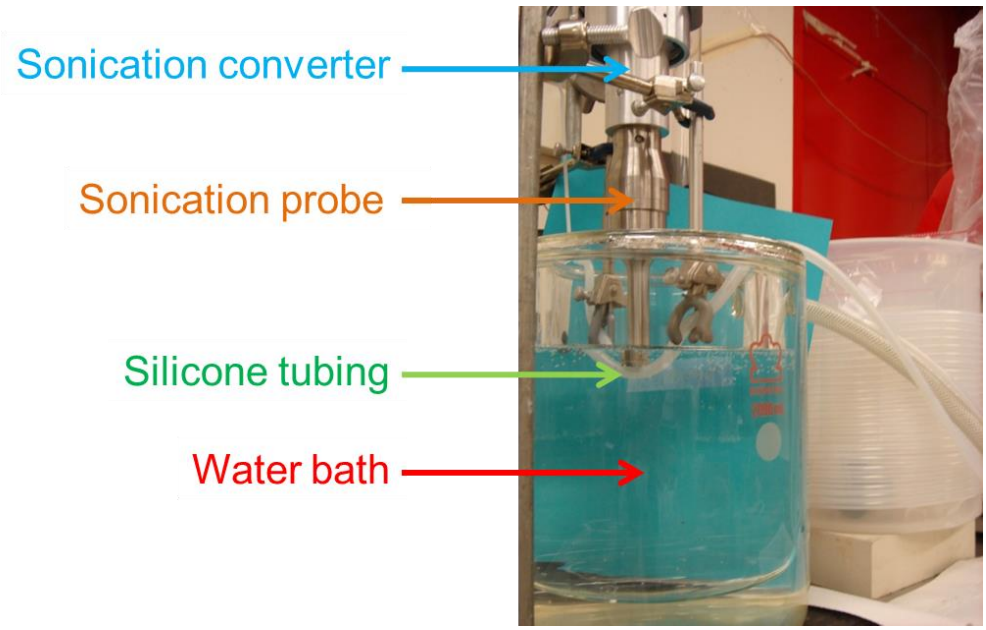

(b)

Figure 7.1. (a) Schematic of the slug-flow cooling crystallizer with ultrasonication-assisted nucleation. (b) Photograph of the experimental setup for ultrasonication. For maximum acoustic energy transmitted from the ultrasonication probe to the solution inside silicone tubing, the probe was placed in direct contact with the outer wall of silicone tubing, in water whose temperature was kept constant. The water outside the tubing is used to draw thermal energy generated by the ultrasonication away from the ultrasonication zone. The right background shows downstream tubing whose temperature can be controlled by placement in a temperature-controlled water bath [7].

The ultrasonication equipment for nucleation (Sonics® VCX 750, Fig. 7.1b) is composed of a generator, a converter, and a probe. Its generator has a working frequency of 20 kHz (widely used for sonocrystallization studies, such as [191], [194], [195], [197], [199]) and an input electric power of 750 Watt. The generator's output power to the probe (Sonics® 630-0597) increases as the amplitude increases (Table 7.1). Different amplitude values are set on the control panel of the generator keypad. The probe tip diameter is 13 mm, which is large enough for the center of the tip to cover the outer diameter (6 mm) of the silicone tubing.

Table 7.1. Experimental conditions and size and shape statistics for the ultrasonication-assisted nucleation of seed crystals.[a]

Experiment number	1	2	3	4	5	6
Ultrasonication amplitude setpoint (% maximum)	0	20	40	50	60	80
Ultrasonication power output (Watts)	0	9	26	39	45	68
Image of generated seed crystals	Fig. 7.2a	Fig. 7.2b	Fig. 7.2c	Fig. 7.2d	Fig. 7.2e	Fig. 7.2f
Mean length (μm)	34	53	42	24	20	20
Standard deviation, length (μm)	20	25	20	8	12	11
Standard error, length (μm)	2.3	1.6	1.3	0.5	0.8	0.9
Mean width (μm)	23	33	27	15	12	13
Standard deviation, width (μm)	18	18	16	6	8	8
Standard error, width (μm)	2.1	1.2	1.0	0.4	0.5	0.7
Coefficient of variation in length	0.60	0.46	0.47	0.32	0.59	0.54
Coefficient of variation in width	0.79	0.54	0.56	0.41	0.65	0.65
Mean aspect ratio	1.87	1.84	1.69	1.83	1.82	1.66

[a]The ultrasonicator vendor recommended that the ultrasonication be operated at or below a setpoint of 80% maximum amplitude (the power reading takes a few seconds to reach stable counts) continuously for our experimental time of 7 minutes or longer, thus continuous ultrasonication at 100% maximum amplitude was not carried out. The power output was calculated, as suggested by the vendor, to be the difference in power reading from the generator screen between when probe is in solution and in air at the same amplitude. The mean length and width are on a number basis. The standard errors are estimates of the uncertainties in the mean width and length measurements determined using Monte Carlo sampling [200].

A T-mixer of 2.7 mm inner diameter was employed for slug generation with its two inlets connected to the slurry and air. A peristaltic pump (Masterflex pump drive 7521-40, Easy Load II pump head with Model #77200-50) was used to transfer hot slurry to the T-mixer through a silicone tube (Masterflex BioPharm Plus platinum-cured silicone tubing, 3.1 mm inner diameter). Filtered air at room temperature was transferred to the T-mixer through the same peristaltic

pump with dual pump heads (their rollers were offset to suppress flow oscillation). Downstream of the T-mixer was 15.2 m of silicone tubing (Dow Corning Pharma-80 tubing, 3.1 mm inner diameter) in room-temperature air used for downstream crystal growth [7].

Product crystals were characterized using a stereomicroscope (microscope model #XV331AC20C from Cyber Scientific Corporation and camera model #DFK 22BUC03 from The Imaging Source, LLC).

7.2.3. Procedure. Nucleation from a supersaturated liquid solution is induced by the ultrasonication probe, which is followed by the formation of alternating slugs of air and slurry. The inlet air and liquid flow rates are selected so that the slugs form spontaneously as the hydrodynamically stable multiphase flow [1]. The supersaturated liquid solution was generated by slowly cooling a solution of 0.09 g LAM/g DI from 52°C to 45°C, which was the temperature of the bath in which the ultrasonication probe tip was placed (Fig. 7.1b). It is well established that ultrasonication reduces the width of the metastable zone [190], and the resulting absolute supersaturation of 0.015 g LAM/g DI at 45°C was selected to be lower than but close to the unseeded metastable limit of cooling nucleation observed in past experiments [4] so that primary nucleation is induced in the solution in front of the ultrasonication probe only when the probe is in operation. The mass flow rate of the inlet liquid solution was 4.03 g/min, and the ultrasonication residence time, that is, the time in which the liquid solution experiences cavitation as observed by eye, is 3 seconds.

LAM nuclei generated from ultrasonication of supersaturated LAM solution traversed the tubing for 0.7 m before slug formation. The distance of 0.7 m was selected to be long enough that the presence of air downstream in the tube does not significantly dampen the energy transferred to the liquid by the ultrasonication probe. The slug generation experimental setup is

the same as in a previous slug-flow experiment that used a radial mixer [7], except that the experimental system in this article also uses slugs of water before and after the LAM-containing slugs so that the pressure drops from the inlets to the tube outlet are nearly constant, so that the velocities of the slugs are constant throughout the entire experiment instead of having time periods during startup and shutdown with higher slug velocities. The crystals grow in the slugs of slurry while traversing through the tubing, for a residence time of ~8.5 minutes between slug formation and outlet. At the outlet of the tubing, slurry slugs were collected into polystyrene wells (1.5 cm in diameter) for off-line imaging under the stereomicroscope [7].

7.3. Results and discussion

The nuclei from indirect ultrasonication-assisted cooling nucleation at different amplitudes are compared in Section 7.3.1 to determine good values for subsequent crystal growth in the slug-flow crystallization process in Section 7.3.2.

7.3.1. Sonication-assisted continuous seed generation by cooling crystallization

For the same experimental system, inlet steams, and operating conditions, more nuclei were formed with ultrasonication than without (see Fig. 7.2), which is consistent with past studies that indicate a shortened induction time with ultrasonication [192]. For Experiment #1 at zero ultrasonication power (Table 7.1), most of the membrane filter contained no crystals, which is consistent with the average supersaturation of 0.015 g LAM/g DI being below the metastable limit for this experimental system under these operating conditions (e.g., at 45°C) [4]. Fig. 7.2a shows the few images that contained any crystals, with the seed crystals that were obtained having over an order of magnitude variation in crystal size. Crystals were consistently nucleated for the experiments with ultrasonication (Figs. 7.2b to 7.2f), with the crystals becoming smaller with increasing ultrasonication power (Table 7.1, Figure 7.S1). Some abnormally large crystals

were observed for an ultrasonication power amplitude setpoint of 40% and less (Figs. 7.2a to 7.2c), but not for 50% and higher ultrasonication power (Figs. 7.2d to 7.2f), indicating that the higher power should be used in this experimental system if the objective is to manufacture uniformly sized crystals.

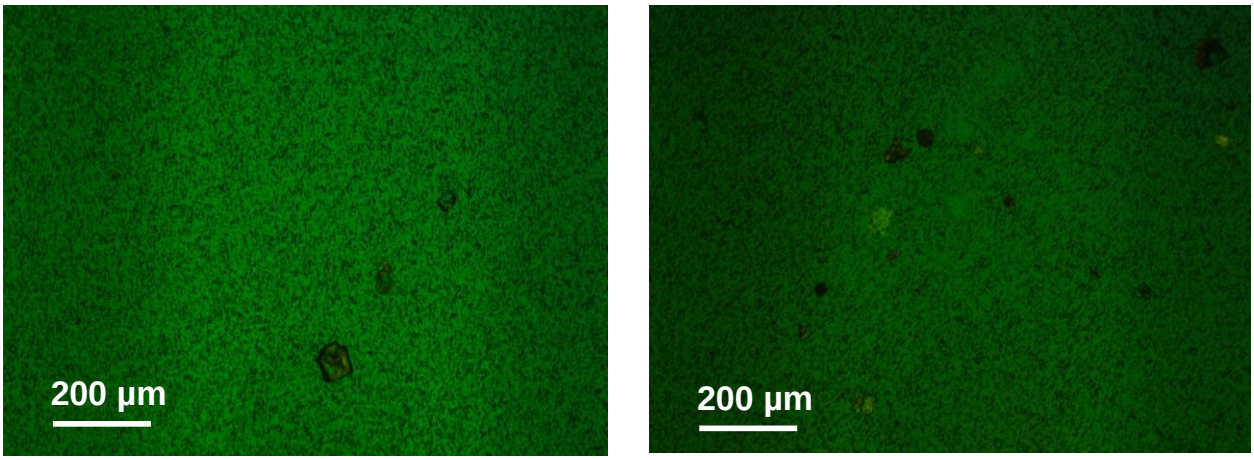

(a)

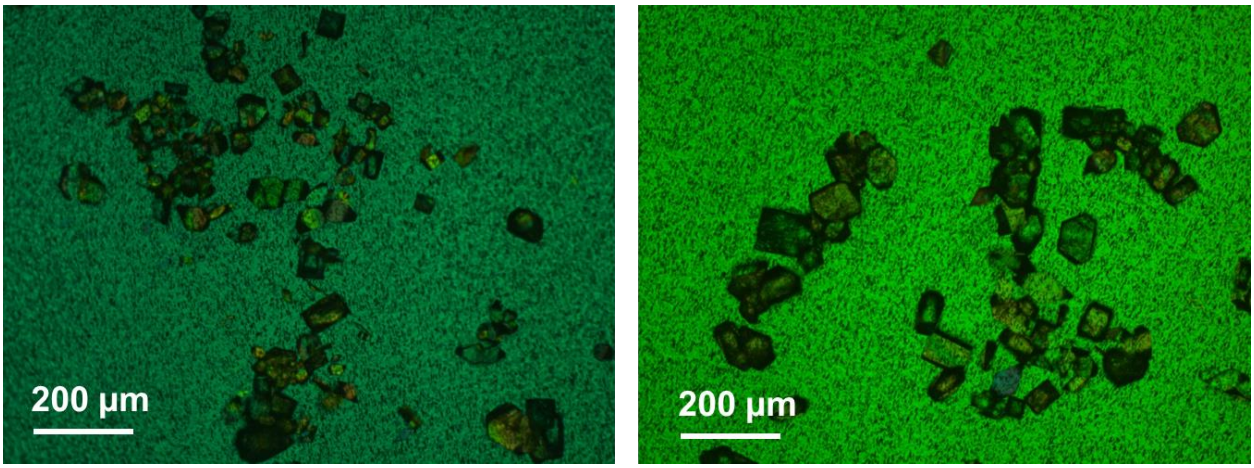

(b)

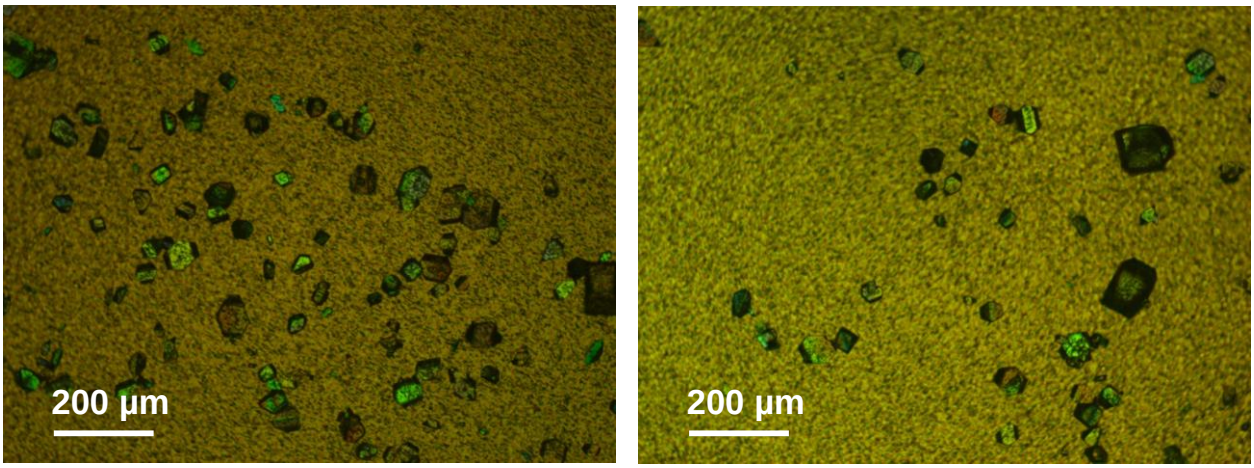

(c)

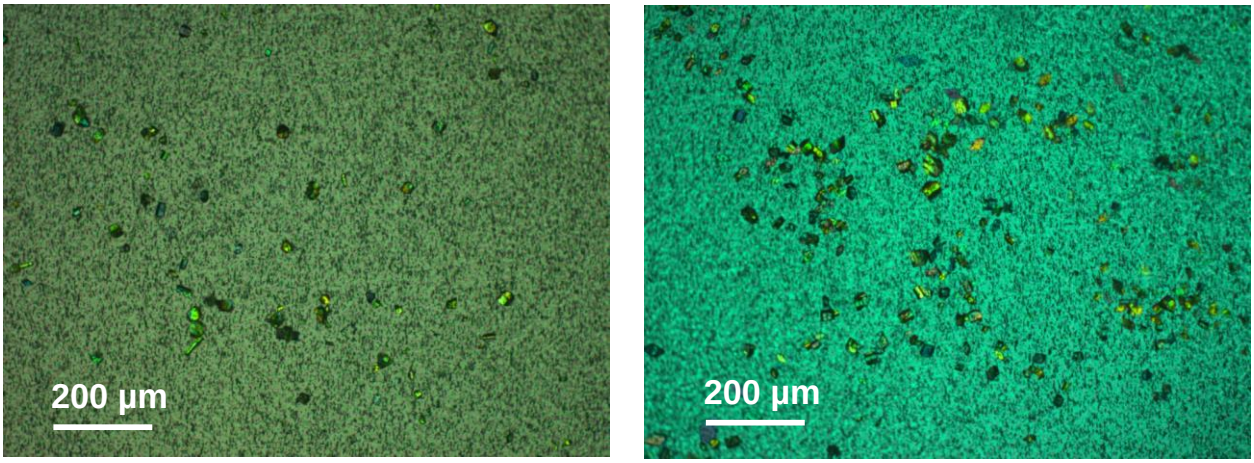

(d)

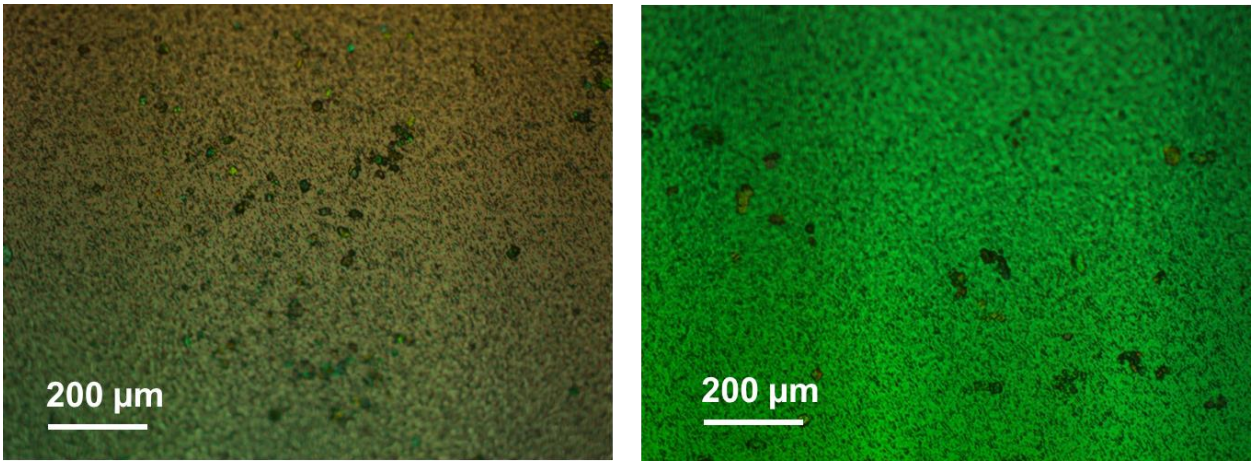

(e)

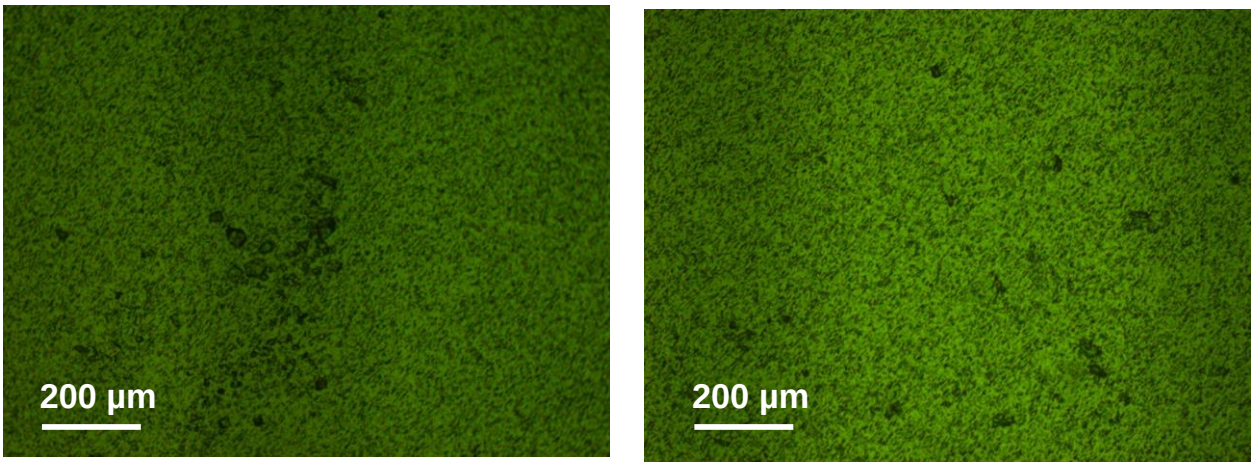

(f)

Figure 7.2. Microscope (with polarizers) images of seed crystals generated by cooling nucleation with ultrasonication (before slug formation in Fig. 7.1a) at different ultrasonication amplitude setpoints (values listed in Table 7.1): (a) Experiment #1, (b) Experiment #2, (c) Experiment #3, (d) Experiment #4, (e) Experiment #5, and (f) Experiment #6. The background of each figure is a membrane filter with a pore size of 2 µm. Images at two different spots on the membrane are shown for each experiment. The images for Experiment #1 with zero ultrasonication power were selected among the few that showed any crystals on the membrane filter. The images for the experiments with nonzero ultrasonication power contained crystals, with representative images shown in (b) to (f). The ultrasonication setup, excluding the slug-flow section, is shown in Fig. 7.1b. The seed crystal size and shape statistics are reported in Table 7.1.

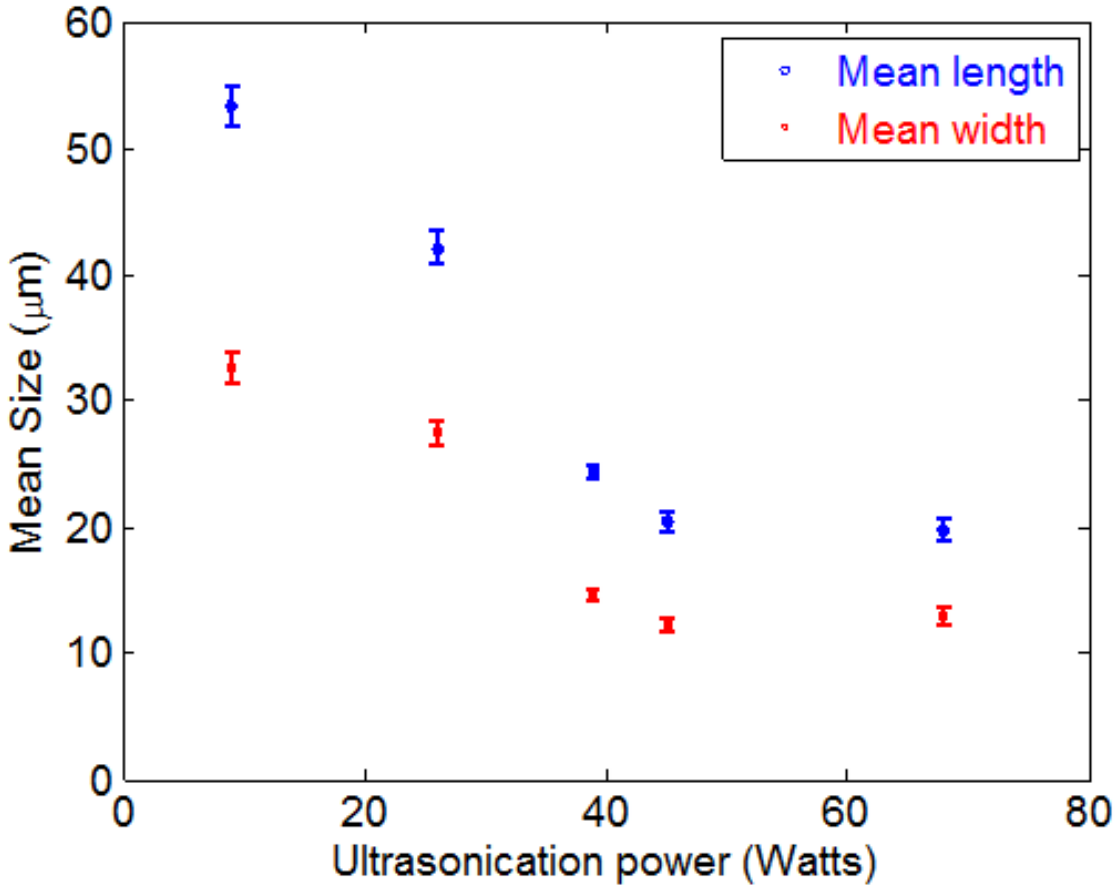

Figure 7.S1. Mean crystal length (blue circle) and width (red square) of seed crystals at various ultrasonication power amplitudes. The power input and crystal length and width statistics (e.g., standard errors for the error bars) are reported in Table 7.1.

Ultrasonication increased the nuclei number and size uniformity (compare coefficient of variations for Experiments 1 with 2 to 6 in Table 7.1). In the range of ultrasonication power amplitude setpoint from 20% to 50%, higher ultrasonication power reduced the size of the seed crystals (Figs. 7.2d to 7.2f, Table 7.1), which is consistent with sonocrystallization results published for other compounds [194]–[197], [199]. This observation is consistent with a higher ultrasonication power generating more bubbles that can act as direct or indirect sites for nucleation, so that the solute crystalizes on a larger number of nuclei. Increased ultrasonication

power would be expected to increase the nucleation rate as long as the fluid inside and outside of the tubing has a high enough mass flow rate and heat capacity to draw enough thermal energy away from the ultrasonication zone. No clear trend was observed in the mean aspect ratio with varying ultrasonication power (Table 7.1). The lowest coefficient of variations for the mean and length of crystals occurred for ultrasonication power amplitude setpoint of 50%.

When the amplitude was 60% or 80% of the maximum (Figs. 7.2e and 7.2f), no evident increases in the size uniformity were observed (Table 7.1). A possible explanation is that the mass flow rate and heat capacity of the water were insufficient to draw enough thermal energy away from the ultrasonication zone, so the local temperature increased, which increased the solubility and lowered the supersaturation and nucleation rate per nucleation site, which counteracted the increasing number of nucleation sites generated by the larger power input. The images showed more aggregation for the 60% or 80% power amplitude, which could be associated with increased particle-particle contacts resulting from increased cavitation. Based on having the lowest coefficient of variation and low aggregation (Table 7.1), the ultrasonication power amplitude setpoint of 50% was selected to provide seeds in subsequent slug-flow crystallization experiments to manufacture product crystals.

7.3.2. Product crystals obtained after growth in slugs

The product crystals generated without ultrasonication showed a high variability in size (see Fig. 7.3), which is consistent with the large variability in the size of crystals observed immediately before the slug formation zone (Fig. 7.2a and associated caption). In contrast, crystals from ultrasonication-assisted nucleation are much more uniform in size, while also having a small degree of aggregation (Fig. 7.4), which is consistent with the higher size uniformity of seed crystals continuously generated by ultrasonication (Fig. 7.2d). The unimodal

character of the crystal size distribution within each slug (Fig. 7.4) indicates that secondary nucleation was small in the slug growth zone (Fig. 7.1), which is consistent with a past observation [7] that recirculation within each slug provides sufficient mixing without requiring the use of any mixing blade that would induce secondary nucleation [201]. This operation allows the slug-flow crystallization to occur at orders of magnitude higher supersaturation and shorter residence times than traditional crystallizers, without inducing significant secondary nucleation [7].

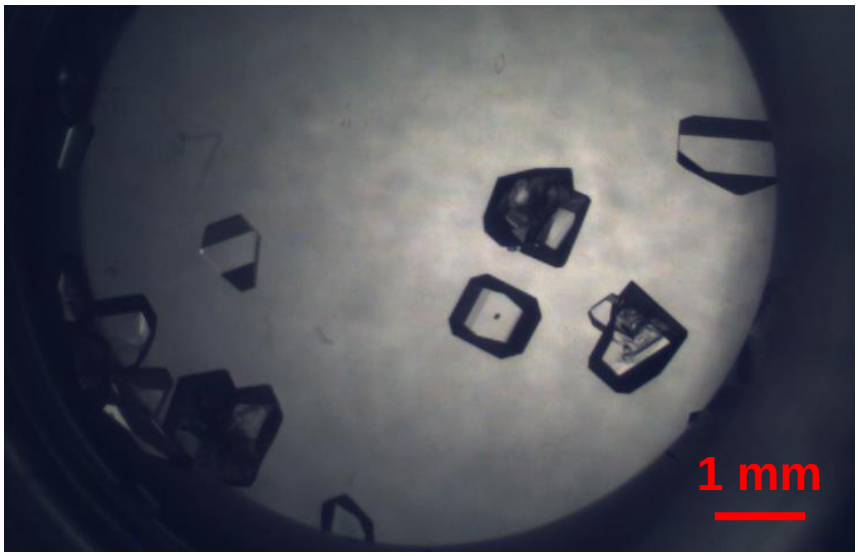

(a)

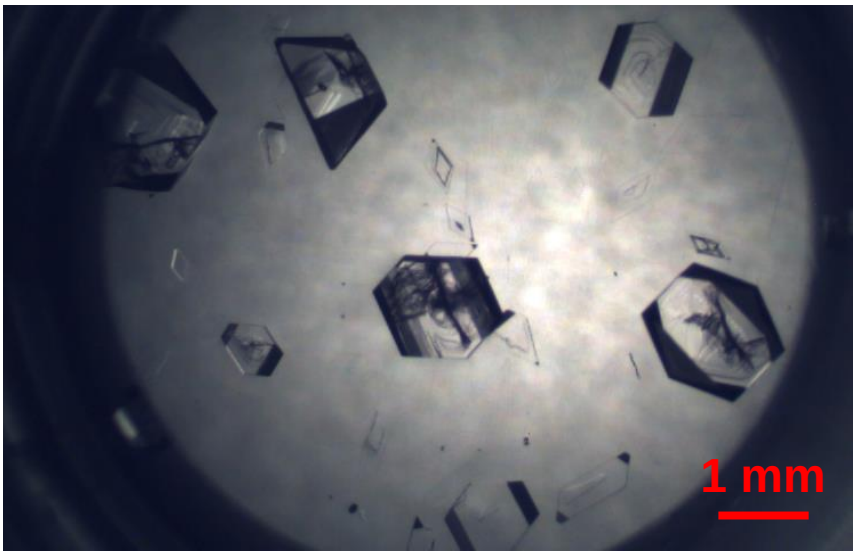

(b)

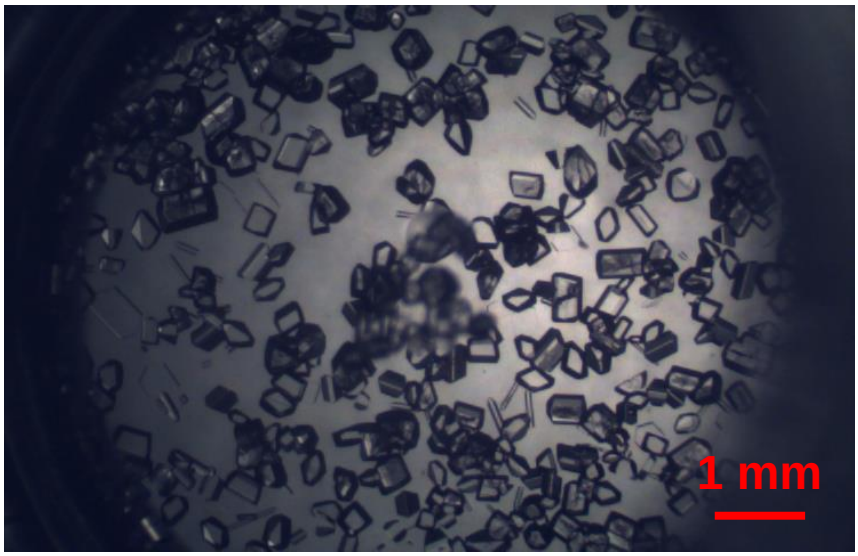

(c)

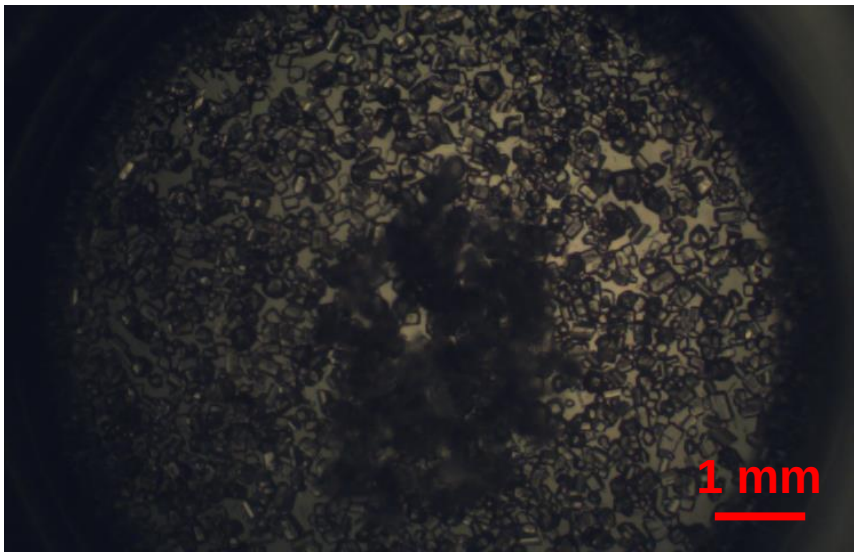

(d)

Figure 7.3. Stereomicroscope images of product crystals obtained by cooling nucleation without ultrasonication followed by slug flow in a 15.2 m long tube (Experiment #1, with conditions in Table 7.1) for slug numbers (a) 106–109, (b) 170–173, (c) 234–237, and (d) 298–301.

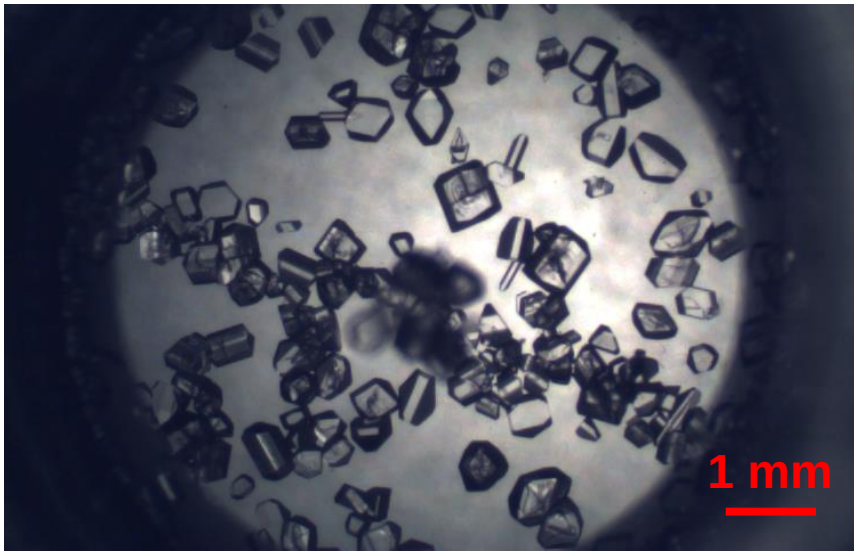

(a)

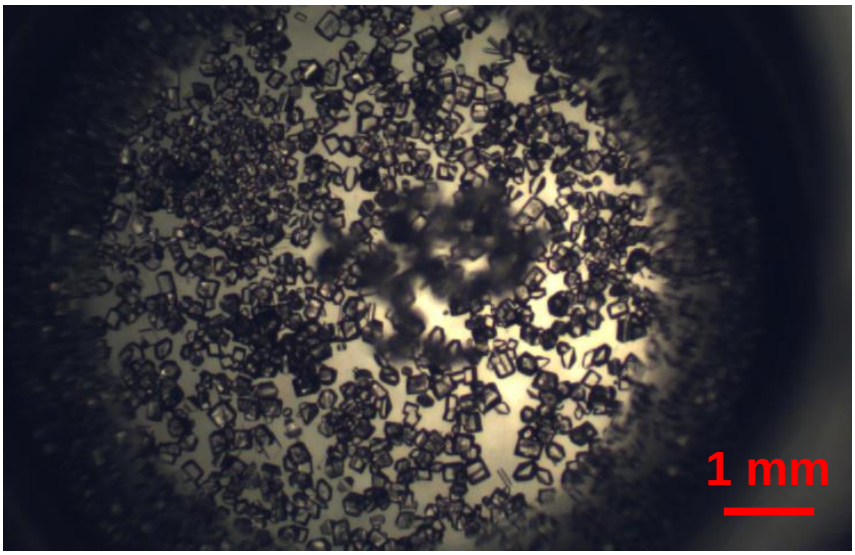

(b)

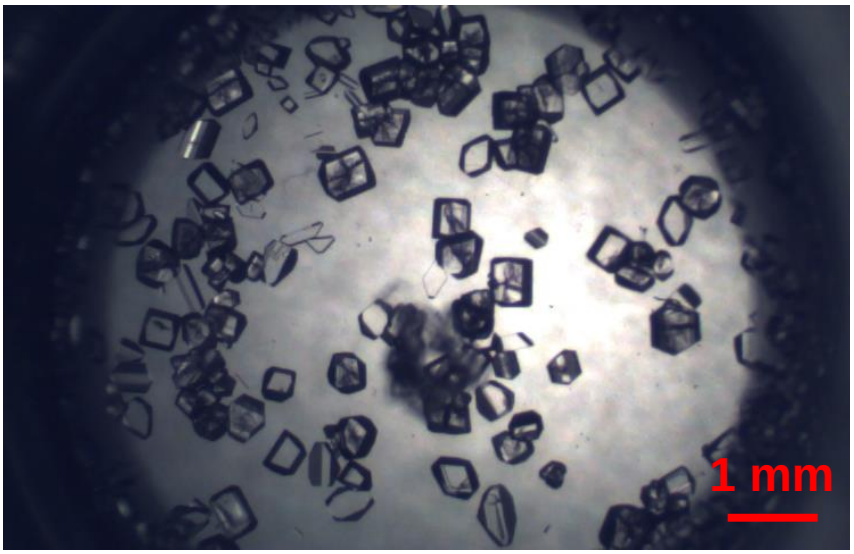

(c)

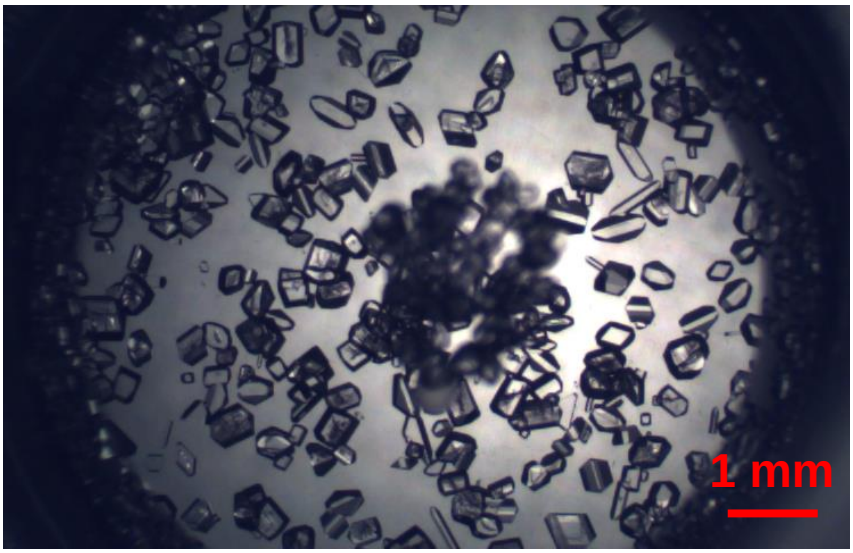

(d)

Figure 7.4. Stereomicroscope images of product crystals obtained at an ultrasonication power amplitude setpoint of 50% followed by slug flow in a 15.2 m long tube (Experiment #4, with conditions in Table 7.1) for slug numbers (a) 108–110, (b) 180–182, (c) 252–254, and (d) 324–326. The product crystal size and shape statistics are reported in Table 7.1.

By first selecting the ultrasonication power amplitude for nucleation and then combining with slug flow for crystal growth, product crystals were obtained with high size uniformity, comparable with the best results from past experiments that combined ultrasonication with subsequent growth in slugs [5]. Compared to a past study [5], this design requires simpler experimental configuration for the slug-flow section, with no fines dissolution equipment, by instead generating tunable seed size with spatially localized ultrasonication. The one ultrasonic probe can be replaced by two ultrasonic probes in series along the tubing with only one probe in ultrasonic mode and the other in rest mode, alternating between the modes of the two probes, to extend their lifetime. This two-probe design does not significantly increase the complexity of operation while facilitating scale-up, which is a typical problem in ultrasonication-associated research [193].

Table 7.2 compares the product crystals with seeds generated by spatially localized ultrasonication with seeds generated using a radial micromixer for the same conditions as Experiment 4. The product crystals generated by spatially localized ultrasonication are about 28%–35% smaller in mean length and width and have 15%–23% narrower crystal size distributions based on smaller coefficients of variation. The mean aspect ratios are similar.

Table 7.2. Comparison of product crystals obtained using the nucleation conditions in Experiment #4 of Table 7.1, with representative images of crystals in Fig. 7.4d, with product crystals reported in [7].[a]

Nucleation method for slug flow crystallization	Micromixer (radial mixer)	Spatially localized ultrasonication
Crystal image	Fig. 11 in Ref [7]	Fig. 7.4d
Mean length (μm)	444	321
Standard deviation, length (μm)	152	92
Standard error, length (μm)	13.0	6.4
Mean width (μm)	326	211
Standard deviation, width (μm)	142	69
Standard error, width (μm)	12.0	4.8
Coefficient of variation in length	0.34	0.29
Coefficient of variation in width	0.43	0.33
Mean aspect ratio	1.46	1.60

[a]The mean width and length are on a number basis.

An advantage of using ultrasonication to generate nuclei is that the nucleation rate can be manipulated by the ultrasonication power, which is a control variable that can be changed independently from the mass flow rate through the tubular crystallizer. The nuclei generation rate produced by a micromixer cannot be varied independently from the mass flow rates of the inlet streams, regardless of whether the micromixer is radial, coaxial, or dual-impinging-jet type. In a

crystallizer that uses a micromixer, any operating variable that affects the nuclei generation rate also affects the crystal production rate. The nuclei generation rate can be affected by changing the design of the micromixer, but such equipment design parameters are then fixed during operation.

The measured process yield (mass of product crystals/total inlet mass of solute) for the slug-flow crystallizer with ultrasonication nucleation (73.8%) was close to the theoretical maximum yield of a batch cooling crystallizer of the same initial concentrations (74.4%). In contrast to employing micromixers that combine hot and cold inlet solutions, applying ultrasonication to a single hot inlet solution in a continuous crystallizer can better approach the maximum yield obtainable in a batch cooling crystallizer. For the slug-flow crystallizer, the maximum yield is obtained by having a sufficiently long tube near the exit held at the desired exit cooling temperature.

Another advantage of employing ultrasonication over micromixers is that the former is less likely to clog. By using a consistent inner diameter of tubing in the slug-flow crystallizer, as in Fig. 7.1, there are no constrictions available to induce clogging. Although the potential for clogging in micromixers can be reduced by employing computational fluid dynamics simulations to improve the micromixer design [17], a surer approach to avoid clogging is to replace the micromixer by employing ultrasonication instead.

In a past study [5] that also employed indirect ultrasonication and crystal nucleation and growth in a liquid solution flowing through a plastic tubing, primary nucleation occurs within 3 meters of plastic tubing placed inside of a sonication bath. The ultrasonication power per unit volume varies widely with spatial position inside of a sonication bath, and having crystals nucleate throughout a long tubing length means that the crystals leaving the sonication bath have

widely varying residence time and sizes. In particular, crystals that nucleate near the inlet of the tubing enters the sonication bath have much more time to grow in size than crystals that nucleate near the tubing outlet. This article uses a sonication probe tip focused in a small spatial location, which enables primary nucleation to occur within a small section of tubing. The much narrower side distribution that results is shown in Fig. 7.5, which compares product crystal size distributions (CSDs) obtained in [5] with the product CSD obtained in this study.

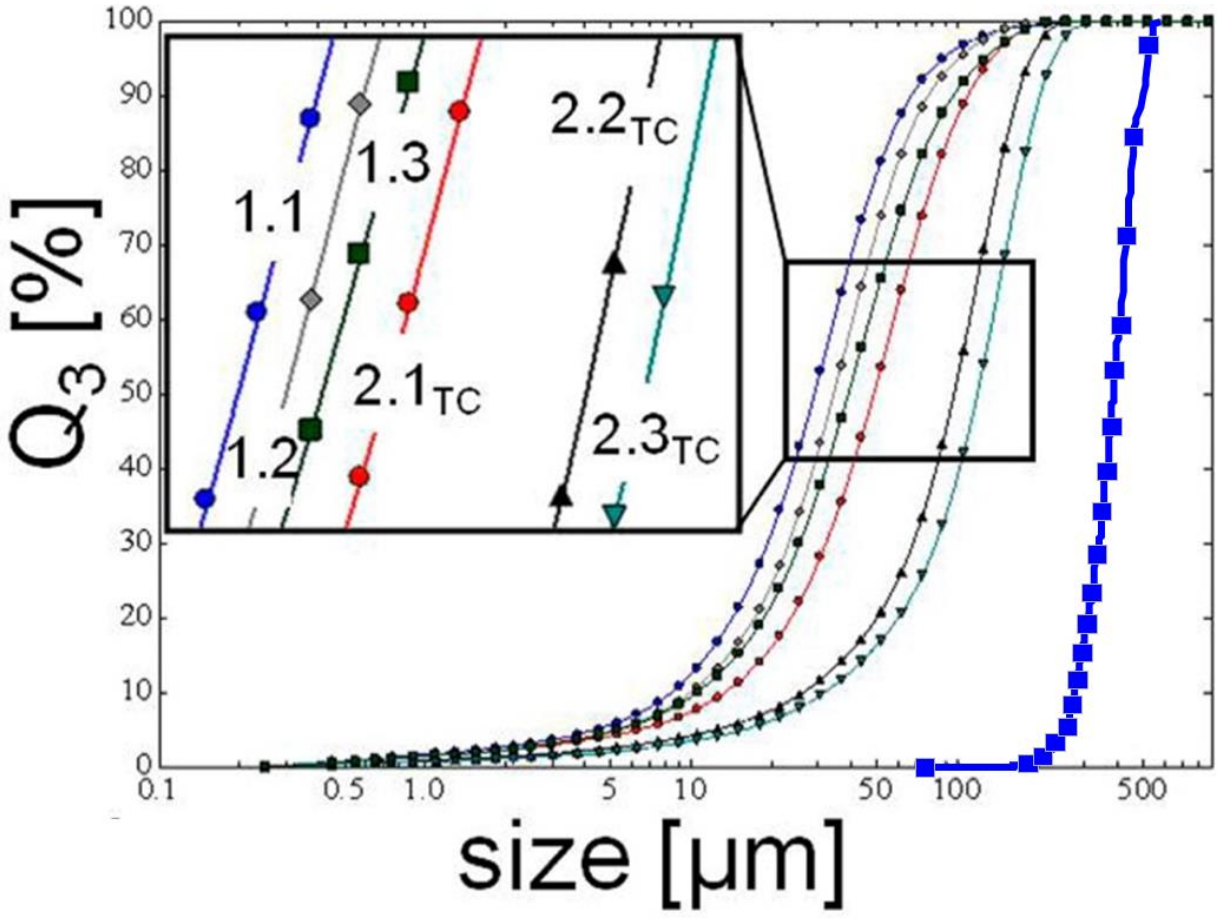

Figure 7.5. Comparison of the cumulative product crystal size distribution on a mass basis (labeled as Q3) obtained using the nucleation conditions in Experiment #4 of Table 7.1 (blue square, with representative images of crystals in Fig. 7.4d) with product crystals reported in Fig. 4b of [3]. A mass basis was used to allow a direct comparison with the results of this manuscript with Fig. 4b of [3]. The CSD for the product crystals in this manuscript is much narrower even

though the crystals are grown much larger and have a greater opportunity to be affected by growth dispersion.

Another difference with a past study [5] is that the experimental system in this article uses a simpler single solution stream instead of two streams, and so has one less pump and less tubing, and does not require a mixer to combine two liquid streams. The experimental apparatus in [5] has higher flexibility of operation but also has higher complexity. Instead of applying ultrasonication to liquid solution for a half minute or more as in past studies [191], this article subjects the liquid solution to ultrasonication for a much shorter time (e.g., a few seconds), to reduce heating of the solution and widening of the CSD. Another difference with a past study [5] is that this article uses horizontal coils of tubing, as in [7], instead of vertical coils. The advantage of a horizontal coils is that the slug velocities are much more spatially uniform and the advantage of vertical coils is that the crystals are forced to opposite sides of the slug during each coil [184].

7.4. Summary

This article presents a slug-flow crystallizer that employs indirect ultrasonication to continuously generate seed crystals. The ultrasonication probe is pressed up against a tube to generate a localized ultrasonication zone within supersaturated solution in the tube for the generation of crystal nuclei (Fig. 7.1). The ultrasonication design with an intermediate power amplitude (Fig. 7.2d) continuously generated a larger number of uniform-sized seed crystals than using micromixers or direct cooling in a past study [7], with minimal aggregation for a solute-solvent combination known to have a high tendency towards aggregation. The ultrasonication design also enables the seed generation rate to be varied in real time independently of the

production rate, providing an additional degree of freedom that can be used in feedforward and/or feedback control design.

The ultrasonication-assisted nucleation design was implemented into a continuous slug-flow crystallization process to generate uniform-sized product crystals within each slug (Fig. 7.4). The ultrasonication-assisted slug-flow crystallizer was operated at sufficiently high supersaturation for the entire crystallization to have a residence time of only ~8.5 min, without inducing significant secondary nucleation. The overall production rate can be increased by operating at a higher inlet mass flow rate while using a longer tube for crystal growth. The crystallizer can be operated continuously for a long time period with equipment of similar complexity, such as by placing two ultrasonic probes in series along the tubing with only one probe in ultrasonic mode and the other in rest mode, alternating between the modes of the two probes, so as to extend the probe lifetimes.

By increasing size uniformity, the indirect ultrasonication-assisted slug-flow crystallizer has potential as a final crystallization step to produce crystals for use in direct compression tableting [202], which would remove the need for milling and/or granulation steps from the drug product manufacturing process chain. The use of indirect ultrasonication, as demonstrated for segmented-flow crystallization in a past study [5], avoids the potential for sample contamination from metals detaching from the ultrasonication equipment [198], which can be a significant concern in pharmaceutical applications. The use of an ultrasonication probe, in contrast to an ultrasonication bath used in a past study [5], allows the ultrasonication zone to be more spatially localized, which can produce a narrower size distribution of seed crystals (Figure 7.S1, Table 7.2), and hence narrower product crystal size distribution (Figure 7.5, Table 7.2).

8. CONCLUSIONS

My Ph.D. research is on the design and experimental validation of batch, semi-continuous, and continuous crystallizers with controlled crystal shape and size distribution. Each project started from the perspective of the whole system, whose configuration was designed based on requirements for the final product quality. The system was then decomposed into subsystems that were understood in detail before adding more functionality and complexity. One key strategy is to exploit dual-impinging jets and multiphase flow to decouple nucleation and growth so that the phenomena can be individually controlled. Another key strategy was to increase the degrees of freedom in the dynamic operation of the crystallizers.

8.1. Enhancing control of crystal shape in a batch crystallizer

In Chapter 3, temperature-cycling experiments in batch crystallizers were designed to alternate between positive and negative supersaturations to substantially change crystal shape with only a small number of cycles. FBRM, a readily available commercial instrumentation, was paired with ATR-FTIR spectroscopy and PVM to monitor the crystallization growth and dissolution during the temperature-cycling experiment.

The growth and dissolution kinetics were estimated in a multidimensional population balance model based on solute concentration and crystal dimension measurements. This model fitted the experimental data with a limited number of parameters of small uncertainty. In addition, with the estimated kinetic parameters, the model predicted the crystal size and shape distribution in a different temperature-cycling experiment reasonably well. The results suggested that growth and dissolution rates estimated in a single temperature-cycling experiment might be suitable for designing a temperature-cycling protocol for optimizing the size and shape of the product

crystals. This method may be suitable for guiding the design of temperature-cycling experiments to change particle shape in a wide variety of systems.

8.2. Enhancing control of CSD in a semi-continuous crystallizer

In Chapter 4, a semi-continuous crystallizer configuration that combines continuous seeding using a dual impinging jet with growth rate control in a stirred tank was experimentally demonstrated for the challenging problem of obtaining a target uniform product CSD. Uniform seed crystals generated by DIJ were further grown to a desired size in the stirred tank with suppressed nucleation. The construction of calibration models and the measurement of solubility and metastable limit were obtained by an automated system that followed preset supersaturation profiles by using feedback control. The experiments confirm that greatly enhanced control of the crystal size distribution can be achieved by using continuous seeding. The same approach works for other seed generation methods, such as a rotor stator or wet milling.

The results in Chapter 4 appear to be the first report of using a DIJ mixer to nucleate crystals by cooling. Chapter 5 provides a physical explanation for this discovery that a cooling DIJ mixer can generate small crystals of uniform size and shape by combining hot and cold saturated solutions. The surprising result of nucleating crystals even at a low average supersaturation in a DIJ mixer led to the analysis of the system that showed that nucleation was enabled by having much faster energy transfer than mass transfer rates, resulting in a local supersaturation sufficiently high to nucleate crystals.

The cooling DIJ mixer may work for some compounds that are not suitable with anti-solvent operations. Design criteria were developed for cooling DIJ mixers to quickly identify suitable compound-solvent combinations based on their physicochemical properties. These criteria could

save time and material by avoiding or reducing trial-and-error experiments, which is helpful at the early stage of pharmaceutical process development (details in Chapter 5).

8.3. Enhancing control of CSD in a slug-flow continuous crystallizer

Chapter 6 presents the design of a slug-flow continuous crystallizer that exploits multi-phase hydrodynamics to experimentally demonstrate the generation of large uniform crystals of LAM in less than five minutes. Temperature and concentration are uniform inside each slug due to recirculation, without using a mixing blade. Coaxial or radial mixers were developed to combine liquid streams and continuously generate uniform seed crystals immediately upstream of the growth zone. Scale up of slug flow crystallization process is straightforward—run the process continuously and sustainably for a longer time. In addition, in-situ imaging and analysis methods were developed for sub-millimeter flowing crystals inside millimeter-size moving slugs in tubular crystallizers and a simple but effective syringe heater was designed to keep solutions at a constant elevated temperature while pumping with minimum pulsing (details in Chapter 6).

An alternative nucleation design that can decouple nucleation and flow rates (thus product rate) is to replace the micromixer with the application of an ultrasonication probe through the tube wall. The nucleation design allows fast tuning of nuclei number by sonication power amplitude. This sonication-assisted nucleation design may be implemented in other advanced continuous slug-flow crystallizers to generate product crystals of target uniform size (details in Chapter 7).

8.4. Overall conclusion and future perspective

Experimental validation has confirmed that the proposed designs suppress secondary nucleation, attrition, and aggregation/agglomeration—phenomena that worsen the ability to control the CSD but are dominant in most existing crystallizer designs. My experiments are

supported by mathematical modeling and analysis. The technologies and strategies developed for successful pharmaceutical crystallization may shed light on advancing other areas such as biopharmaceutical development and manufacturing.

REFERENCES

[1] S. Talreja, D. Y. Kim, A. Y. Mirarefi, C. F. Zukoski, and P. J. A. Kenis, "Screening and optimization of protein crystallization conditions through gradual evaporation using a novel crystallization platform," *J. Appl. Crystallogr.*, vol. 38, pp. 988–995, 2005.

[2] J. P. Greenstein and M. Winitz, *Chemistry of the Amino Acids*. Malabar, FL: Robert. E. Krieger Publishing Company, 1986.

[3] X. Y. Woo, R. B. H. Tan, and R. D. Braatz, "Precise tailoring of the crystal size distribution by controlled growth and continuous seeding from impinging jet crystallizers," *CrystEngComm*, vol. 13, no. 6, pp. 2006–2014, 2011.

[4] M. Jiang, M. H. Wong, Z. Zhu, J. Zhang, L. Zhou, K. Wang, A. N. Ford Versypt, T. Si, L. M. Hasenberg, Y. E. Li, and R. D. Braatz, "Towards achieving a flattop crystal size distribution by continuous seeding and controlled growth," *Chem. Eng. Sci.*, vol. 77, pp. 2–9, 2012.

[5] R. J. P. Eder, S. Schrank, M. O. Besenhard, E. Roblegg, H. Gruber-Woelfler, and J. G. Khinast, "Continuous sonocrystallization of acetylsalicylic acid (ASA): Control of crystal size," *Cryst. Growth Des.*, vol. 12, no. 10, pp. 4733–4738, 2012.

[6] W. M. Haynes, Ed., *CRC Handbook of Chemistry and Physics*, 95th ed. Boca Raton, FL: CRC Press/Taylor and Francis, 2015.

[7] M. Jiang, Z. Zhu, E. Jimenez, C. D. Papageorgiou, J. Waetzig, A. Hardy, M. Langston, and R. D. Braatz, "Continuous-flow tubular crystallization in slugs spontaneously induced by hydrodynamics," *Cryst. Growth Des.*, vol. 14, no. 2, pp. 851–860, 2014.

[8] M. Jiang, X. Y. Woo, N. C. S. Kee, L. M. Goh, J. D. Tice, L. Zhou, R. B. H. Tan, C. F. Zukoski III, M. Fujiwara, Z. K. Nagy, P. J. A. Kenis, and R. D. Braatz, "The role of automatic process control in Quality by Design," in *Comprehensive Quality by Design for Pharmaceutical Product Development and Manufacture*, G. V Reklaitis, Ed. Chichester: John Wiley & Sons Ltd., in press.

[9] J. De Calderon Anda, X. Z. Wang, and K. J. Roberts, "Multi-scale segmentation image analysis for the in-process monitoring of particle shape with batch crystallisers," *Chem. Eng. Sci.*, vol. 60, no. 4, pp. 1053–1065, 2005.

[10] M. Oullion, F. Puel, G. Févotte, S. Righini, and P. Carvin, "Industrial batch crystallization of a plate-like organic product. In situ monitoring and 2D-CSD modelling: Part 1: Experimental study," *Chem. Eng. Sci.*, vol. 62, no. 3, pp. 820–832, 2007.

[11] M. Jiang, X. Zhu, M. C. Molaro, M. L. Rasche, H. Zhang, K. Chadwick, D. M. Raimondo, K.-K. K. K. Kim, L. Zhou, Z. Zhu, M. H. Wong, D. O'Grady, D. Hebrault, J. Tedesco,

and R. D. Braatz, “Modification of crystal shape through deep temperature cycling,” *Ind. Eng. Chem. Res.*, vol. 53, no. 13, pp. 5325–5336, 2014.

[12] M. Jiang, C. Gu, and R. D. Braatz., “Mathematical modeling and analysis of cooling crystallization within dual impinging jet mixers,” final manuscript under review by Novartis Pharmaceuticals.

[13] M. Jiang, C. D. Papageorgiou, J. Waetzig, A. Hardy, M. Langston, and R. D. Braatz, “Indirect ultrasonication in continuous slug-flow crystallization,” *Cryst. Growth Des.*, in press. DOI: 10.1021/acs.cgd.5b00263.

[14] R. A. Lionberger, S. L. Lee, L. Lee, A. Raw, and L. X. Yu, “Quality by design: Concepts for ANDAs,” *AAPS J.*, vol. 10, no. 2, pp. 268–276, 2008.

[15] H. G. Brittain, *Polymorphism in Pharmaceutical Solids*, 2nd ed. London and New York: Informa Healthcare, 2009.

[16] J. Bernstein, *Polymorphism in Molecular Crystals*. Chester, England: International Union of Crystallography, 2008.

[17] X. Y. Woo, R. B. H. Tan, and R. D. Braatz, “Modeling and computational fluid dynamics−population balance equation−micromixing simulation of impinging jet crystallizers,” *Cryst. Growth Des.*, vol. 9, no. 1, pp. 156–164, 2009.

[18] M. Midler Jr., E. L. Paul, E. F. Whittington, M. Futran, P. D. Liu, J. Hsu, and S. H. Pan, “Crystallization Method to Improve Crystal Structure and Size,” U.S. Patent 5314506 A, May 24, 1994.

[19] D. J. am Ende, T. C. Crawford, and N. P. Weston, “Reactive Crystallization Method to Improve Particle Size,” U.S. Patent 6558435, May 6, 2003.

[20] R. Dauer, J. E. Mokrauer, and W. J. Mckeel, “Dual Jet Crystallizer Apparatus,” U.S. Patent 5578279, Nov 26, 1996.

[21] M. D. Lindrud, S. Kim, and C. Wei, “Sonic Impinging Jet Crystallization Apparatus and Process,” U.S. Patent 6302958 B1, Oct. 16, 2001.

[22] C. Lindenberg and M. Mazzotti, “Experimental characterization and multi-scale modeling of mixing in static mixers. Part 2. Effect of viscosity and scale-up,” *Chem. Eng. Sci.*, vol. 64, no. 20, pp. 4286–4294, 2009.

[23] H. Chiou, H.-K. Chan, R. K. Prud’homme, and J. A. Raper, “Evaluation on the use of confined liquid impinging jets for the synthesis of nanodrug particles,” *Drug Dev. Ind. Pharm.*, vol. 34, no. 1, pp. 59–64, 2008.

[24] A. J. Mahajan and D. J. Kirwan, "Nucleation and Growth Kinetics of Biochemicals Measured at High Supersaturations," *J. Cryst. Growth*, vol. 144, no. 3–4, pp. 281–290, 1994.

[25] L. Goh, K. Chen, V. Bhamidi, G. He, N. C. S. Kee, P. J. A. Kenis, C. F. Zukoski, and R. D. Braatz, "A stochastic model for nucleation kinetics determination in droplet-based microfluidic systems," *Cryst. Growth Des.*, vol. 10, no. 6, pp. 2515–2521, 2010.

[26] M. J. Anderson, C. L. Hansen, and S. R. Quake, "Phase knowledge enables rational screens for protein crystallization," *Proc. Natl. Acad. Sci. U. S. A.*, vol. 103, no. 45, pp. 16746–16751, 2006.

[27] C. L. Hansen, E. Skordalakest, J. M. Berger, and S. R. Quake, "A robust and scalable microfluidic metering method that allows protein crystal growth by free interface diffusion," *Proc. Natl. Acad. Sci. U. S. A.*, vol. 99, no. 26, pp. 16531–16536, 2002.

[28] A. J. Alvarez, A. Singh, and A. S. Myerson, "Polymorph screening: Comparing a semi-automated approach with a high throughput method," *Cryst. Growth Des.*, vol. 9, no. 9, pp. 4181–4188, 2009.

[29] K. Kim, I. S. Lee, A. Centrone, T. A. Hatton, and A. S. Myerson, "Formation of nanosized organic molecular crystals on engineered surfaces," *J. Am. Chem. Soc.*, vol. 131, no. 51, pp. 18212–18213, 2009.

[30] L. Li and R. F. Ismagilov, "Protein crystallization using microfluidic technologies based on valves, droplets, and slipChip," *Annu. Rev. Biophys.*, vol. 39, no. 1, pp. 139–158, 2010.

[31] G. He, R. B. H. Tan, P. J. A. Kenis, and C. F. Zukoski, "Generalized phase behavior of small molecules and nanoparticles," *J. Phys. Chem. B*, vol. 111, no. 43, pp. 12494–12499, 2007.

[32] S. Talreja, P. J. A. Kenis, and C. F. Zukoski, "A kinetic model to simulate protein crystal growth in an evaporation-based crystallization platform," *Langmuir*, vol. 23, no. 8, pp. 4516–4522, 2007.

[33] S. Talreja, S. L. Perry, S. Guha, V. Bhamidi, C. F. Zukoski, and P. J. A. Kenis, "Determination of the phase diagram for soluble and membrane proteins," *J. Phys. Chem. B*, vol. 114, no. 13, pp. 4432–4441, 2010.

[34] L. X. Yu, R. A. Lionberger, A. S. Raw, R. D'Costa, H. Wu, and A. S. Hussain, "Applications of process analytical technology to crystallization processes," *Adv. Drug Deliv. Rev.*, vol. 56, no. 3, pp. 349–369, 2004.

[35] H. B. Matthews and J. B. Rawlings, "Batch crystallization of a photochemical: Modeling, control, and filtration," *AIChE J.*, vol. 44, no. 5, pp. 1119–1127, 1998.

[36] S. H. Chung, D. L. Ma, and R. D. Braatz, "Optimal seeding in batch crystallization," *Can. J. Chem. Eng.*, vol. 77, no. 3, pp. 590–596, 1999.

[37] J.-P. Corriou and S. Rohani, "A new look at optimal control of a batch crystallizer," *AICHE J.*, vol. 54, no. 12, pp. 3188–3206, 2008.

[38] D. Sarkar, S. Rohani, and A. Jutan, "Multi-objective optimization of seeded batch crystallization processes," *Chem. Eng. Sci.*, vol. 61, no. 16, pp. 5282–5295, 2006.

[39] H. M. Hulburt and S. Katz, "Some problems in particle technology. A statistical mechanical formulation," *Chem. Eng. Sci.*, vol. 19, no. 8, pp. 555–574, 1964.

[40] A. D. Randolph and M. A. Larson, *Theory of Particulate Processes: Analysis and Techniques of Continuous Crystallization*, 2nd ed. New York: Academic Press, 1974.

[41] J. B. Rawlings, S. M. Miller, and W. R. Witkowski, "Model identification and control of solution crystallization processes: a review," *Ind. Eng. Chem. Res.*, vol. 32, no. 7, pp. 1275–1296, 1993.

[42] R. D. Braatz and S. Hasebe, "Particle size and shape control in crystallization processes," in *Sixth International Conference on Chemical Process Control, AIChE Symposium Series*, J. B. Rawlings, B. A. Ogunnaike, and J. W. Eaton, Eds. New York: AIChE Press, 2002, pp. 307–327.

[43] Z. K. Nagy and R. D. Braatz, "Distributional uncertainty analysis using power series and polynomial chaos expansions," *J. Process Control*, vol. 17, no. 3, pp. 229–240, 2007.

[44] M. W. Hermanto, M. S. Chiu, X. Y. Woo, and R. D. Braatz, "Robust optimal control of polymorphic transformation in batch crystallization," *AIChE J.*, vol. 53, no. 10, pp. 2643–2650, 2007.

[45] Z. K. Nagy and R. D. Braatz, "Worst-case and distributional robustness analysis of finite-time control trajectories for nonlinear distributed parameter systems," *IEEE Trans. Control Syst. Technol.*, vol. 11, no. 5, pp. 694–704, 2003.

[46] Z. K. Nagy and R. D. Braatz, "Open-loop and closed-loop robust optimal control of batch processes using distributional and worst-case analysis," *J. Process Control*, vol. 14, no. 4, pp. 411–422, 2004.

[47] G. Févotte, "In situ Raman spectroscopy for in-line control of pharmaceutical crystallization and solids elaboration processes: A review," *Chem. Eng. Res. Des.*, vol. 85, no. 7, pp. 906–920, 2007.

[48] D. R. Thompson, E. Kougoulos, A. G. Jones, and M. W. Wood-Kaczmar, "Solute concentration measurement of an important organic compound using ATR-UV spectroscopy," *J. Cryst. Growth*, vol. 276, no. 1–2, pp. 230–236, 2005.

[49] D. D. Dunuwila, L. B. Carroll, and K. A. Berglund, "An investigation of the applicability of attenuated total reflection infrared spectroscopy for measurement of solubility and supersaturation of aqueous citric acid solutions," *J. Cryst. Growth*, vol. 137, no. 3–4, pp. 561–568, 1994.

[50] L. Feng and K. A. Berglund, "ATR-FTIR for determining optimal cooling curves for batch crystallization of succinic acid," *Cryst. Growth Des.*, vol. 2, no. 5, pp. 449–452, 2002.

[51] P. Billot, M. Couty, and P. Hosek, "Application of ATR-UV spectroscopy for monitoring the crystallisation of UV absorbing and nonabsorbing molecules," *Org. Process Res. Dev.*, vol. 14, no. 3, pp. 511–523, 2010.

[52] G. Févotte, "New perspectives for the on-line monitoring of pharmaceutical crystallization processes using in situ infrared spectroscopy," *Int. J. Pharm.*, vol. 241, no. 2, pp. 263–278, 2002.

[53] H. Gron, P. Mougin, A. Thomas, G. White, D. Wilkinson, R. B. Hammond, X. Lai, and K. J. Roberts, "Dynamic in-process examination of particle size and crystallographic form under defined conditions of reactant supersaturation as associated with the batch crystallization of monosodium glutamate from aqueous solution," *Ind. Eng. Chem. Res.*, vol. 42, no. 20, pp. 4888–4898, 2003.

[54] T. Togkalidou, M. Fujiwara, S. Patel, and R. D. Braatz, "Solute concentration prediction using chemometrics and ATR-FTIR spectroscopy," *J. Cryst. Growth*, vol. 231, no. 4, pp. 534–543, 2001.

[55] J. Calderon De Anda, X. Z. Wang, X. Lai, and K. J. Roberts, "Classifying organic crystals via in-process image analysis and the use of monitoring charts to follow polymorphic and morphological changes," *J. Process Control*, vol. 15, no. 7, pp. 785–797, 2005.

[56] X. Z. Wang, J. Calderon De Anda, and K. J. Roberts, "Real-time measurement of the growth rates of individual crystal facets using imaging and image analysis: A feasibility study on needle-shaped crystals of L-glutamic acid," *Chem. Eng. Res. Des.*, vol. 85, no. 7, pp. 921–927, 2007.

[57] A. R. Parsons, S. N. Black, and R. Colling, "Automated measurement of metastable zones for pharmaceutical compounds," *Chem. Eng. Res. Des.*, vol. 81, no. 6, pp. 700–704, 2003.

[58] R. Gunawan, L. David, M. Fujiwara, and D. B. Richard, "Identification of kinetic parameters in multidimensional crystallization processes," *Int. J. Mod. Phys. B*, vol. 16, no. 1–2, pp. 367–374, 2002.

[59] S. W. Wong, C. Georgakis, G. D. Botsaris, K. Saranteas, and R. Bakale, "Online estimation and monitoring of diastereomeric resolution using FBRM, ATR-FTIR, and Raman spectroscopy," *Ind. Eng. Chem. Res.*, vol. 47, no. 15, pp. 5576–5584, 2008.

[60] K. Pöllänen, A. Häkkinen, S.-P. Reinikainen, M. Louhi-Kultanen, and L. Nyström, "A study on batch cooling crystallization of sulphathiazole: Process monitoring using ATR-FTIR and product characterization by automated image analysis," *Chem. Eng. Res. Des.*, vol. 84, no. 1, pp. 47–59, 2006.

[61] T. Togkalidou, R. D. Braatz, B. K. Johnson, O. Davidson, and A. Andrews, "Experimental design and inferential modeling in pharmaceutical crystallization," *AIChE J.*, vol. 47, no. 1, pp. 160–168, 2001.

[62] J. Worlitschek and M. Mazzotti, "Model-based optimization of particle size distribution in batch-cooling crystallization of paracetamol," *Cryst. Growth Des.*, vol. 4, no. 5, pp. 891–903, 2004.

[63] P. A. Larsen, D. B. Patience, and J. B. Rawlings, "Industrial crystallization process control," *IEEE Control Syst. Mag.*, vol. 26, no. 4, pp. 70–80, 2006.

[64] T. Togkalidou, H.-H. Tung, Y. Sun, A. T. Andrews, and R. D. Braatz, "Parameter estimation and optimization of a loosely bound aggregating pharmaceutical crystallization using in situ infrared and laser backscattering measurements," *Ind. Eng. Chem. Res.*, vol. 43, no. 19, pp. 6168–6181, 2004.

[65] F. Lewiner, G. Févotte, J. P. Klein, and F. Puel, "Improving batch cooling seeded crystallization of an organic weed-killer using on-line ATR FTIR measurement of supersaturation," *J. Cryst. Growth*, vol. 226, no. 2–3, pp. 348–362, 2001.

[66] P. Barrett, B. Smith, J. Worlitschek, V. Bracken, B. O'Sullivan, and D. O'Grady, "A review of the use of process analytical technology for the understanding and optimization of production batch crystallization processes," *Org. Process Res. Dev.*, vol. 9, no. 3, pp. 348–355, 2005.

[67] M. Kempkes, J. Eggers, and M. Mazzotti, "Measurement of particle size and shape by FBRM and in situ microscopy," *Chem. Eng. Sci.*, vol. 63, no. 19, pp. 4656–4675, 2008.

[68] H. M. Alatalo, H. Hatakka, M. Louhi-Kultanen, J. Kohonen, and S. P. Reinikainen, "Closed-loop control of reactive crystallization. Part I: Supersaturation-controlled crystallization of L-glutamic acid," *Chem. Eng. Technol.*, vol. 33, no. 5, pp. 743–750, 2010.

[69] Z. P. Chen, J. Morris, A. Borissova, S. Khan, T. Mahmud, R. Penchev, and K. J. Roberts, "On-line monitoring of batch cooling crystallization of organic compounds using ATR-FTIR spectroscopy coupled with an advanced calibration method," *Chemom. Intell. Lab. Syst.*, vol. 96, no. 1, pp. 49–58, 2009.

[70] A. Borissova, S. Khan, T. Mahmud, K. J. Roberts, J. Andrews, P. Dallin, Z.-P. Chen, and J. Morris, "In situ measurement of solution concentration during the batch cooling

crystallization of L-glutamic acid using ATR-FTIR spectroscopy coupled with Chemometrics," *Cryst. Growth Des.*, vol. 9, no. 2, pp. 692–706, 2008.

[71] L. L. Simon, Z. K. Nagy, and K. Hungerbuhler, "Endoscopy-based in situ bulk video imaging of batch crystallization processes," *Org. Process Res. Dev.*, vol. 13, no. 6, pp. 1254–1261, 2009.

[72] L. L. Simon, Z. K. Nagy, and K. Hungerbuhler, "Comparison of external bulk video imaging with focused beam reflectance measurement and ultra-violet visible spectroscopy for metastable zone identification in food and pharmaceutical crystallization processes," *Chem. Eng. Sci.*, vol. 64, no. 14, pp. 3344–3351, 2009.

[73] L. L. Simon, K. A. Oucherif, Z. K. Nagy, and K. Hungerbuhler, "Bulk video imaging based multivariate image analysis, process control chart and acoustic signal assisted nucleation detection," *Chem. Eng. Sci.*, vol. 65, no. 17, pp. 4983–4995, 2010.

[74] K. Chow, H. H. Y. Tong, S. Lum, and A. H. L. Chow, "Engineering of pharmaceutical materials: An industrial perspective," *J. Pharm. Sci.*, vol. 97, no. 8, pp. 2855–2877, 2008.

[75] Z. K. Nagy, J. W. Chew, M. Fujiwara, and R. D. Braatz, "Comparative performance of concentration and temperature controlled batch crystallizations," *J. Process Control*, vol. 18, no. 3–4, pp. 399–407, 2008.

[76] M. Fujiwara, Z. K. Nagy, J. W. Chew, and R. D. Braatz, "First-principles and direct design approaches for the control of pharmaceutical crystallization," *J. Process Control*, vol. 15, no. 5, pp. 493–504, 2005.

[77] M. Fujiwara, P. S. Chow, D. L. Ma, and R. D. Braatz, "Paracetamol crystallization using laser backscattering and ATR-FTIR spectroscopy: Metastability, agglomeration, and control," *Cryst. Growth Des.*, vol. 2, no. 5, pp. 363–370, 2002.

[78] H. Grön, A. Borissova, and K. J. Roberts, "In-process ATR-FTIR spectroscopy for closed-loop supersaturation control of a batch crystallizer producing monosodium glutamate crystals of defined size," *Ind. Eng. Chem. Res.*, vol. 42, no. 1, pp. 198–206, 2003.

[79] V. Liotta and V. Sabesan, "Monitoring and feedback control of supersaturation using ATR-FTIR to produce an active pharmaceutical ingredient of a desired crystal size," *Org. Process Res. Dev.*, vol. 8, no. 3, pp. 488–494, 2004.

[80] N. C. S. Kee, R. B. H. Tan, and R. D. Braatz, "Selective crystallization of the metastable alpha-form of L-glutamic acid using concentration feedback control," *Cryst. Growth Des.*, vol. 9, no. 7, pp. 3044–3051, 2009.

[81] N. C. S. Kee, P. D. Arendt, R. B. H. Tan, and R. D. Braatz, "Selective crystallization of the metastable anhydrate form in the enantiotropic pseudo-dimorph system of L-

phenylalanine using concentration feedback control," *Cryst. Growth Des.*, vol. 9, no. 7, pp. 3052–3061, 2009.

[82] Z. K. Nagy and R. D. Braatz, "Advances and new directions in crystallization control," *Annu. Rev. Chem. Biomol. Eng.*, vol. 3, pp. 55–75, 2012.

[83] N. Doki, H. Seki, K. Takano, H. Asatani, M. Yokota, and N. Kubota, "Process control of seeded batch cooling crystallization of the metastable α-form glycine using an in-situ ATR-FTIR spectrometer and an in-situ FBRM particle counter," *Cryst. Growth Des.*, vol. 4, no. 5, pp. 949–953, 2004.

[84] X. Y. Woo, Z. K. Nagy, R. B. H. Tan, and R. D. Braatz, "Adaptive concentration control of cooling and antisolvent crystallization with laser backscattering measurement," *Cryst. Growth Des.*, vol. 9, no. 1, pp. 182–191, 2009.

[85] M. R. A. Bakar, Z. K. Nagy, A. N. Saleemi, and C. D. Rielly, "The impact of direct nucleation control on crystal size distribution in pharmaceutical crystallization processes," *Cryst. Growth Des.*, vol. 9, no. 3, pp. 1378–1384, 2009.

[86] X. Y. Woo, R. B. H. Tan, P. S. Chow, and R. D. Braatz, "Simulation of mixing effects in antisolvent crystallization using a coupled CFD-PDF-PBE approach," *Cryst. Growth Des.*, vol. 6, no. 6, pp. 1291–1303, 2006.

[87] R. D. Braatz, R. C. Alkire, E. Seebauer, E. Rusli, R. Gunawan, T. O. Drews, X. Li, and Y. He, "Perspectives on the design and control of multiscale systems," *J. Process Control*, vol. 16, no. 3, pp. 193–204, 2006.

[88] D. L. Ma, D. K. Tafti, and R. D. Braatz, "High-resolution simulation of multidimensional crystal growth," *Ind. Eng. Chem. Res.*, vol. 41, no. 25, pp. 6217–6223, 2002.

[89] R. Gunawan, I. Fusman, and R. D. Braatz, "High resolution algorithms for multidimensional population balance equations," *AIChE J.*, vol. 50, no. 11, pp. 2738–2749, 2004.

[90] A. S. Michaels and A. R. Colville Jr., "The effect of surface active agents on crystal growth rate and crystal habit," *J. Phys. Chem.*, vol. 64, no. 1, pp. 13–19, 1960.

[91] C. Sano, N. Nagashima, T. Kawakita, and Y. Iitaka, "Effects of additives on the crystal habit of monosodium L-glutamate monohydrate," *J. Cryst. Growth*, vol. 99, no. 1–4 pt 2, pp. 1070–1075, 1990.

[92] I. Weissbuch, L. Addadi, M. Lahav, and L. Leiserowitz, "Molecular recognition at crystal interfaces," *Science*, vol. 253, no. 5020, pp. 637–645, 1991.

[93] D. L. Ma and R. D. Braatz, "Worst-case analysis of finite-time control policies," *IEEE Trans. Control Syst. Technol.*, vol. 9, no. 5, pp. 766–774, 2001.

[94] F. Lewiner, G. Févotte, J. P. Klein, and F. Puel, "An online strategy to increase the average crystal size during organic batch cooling crystallization," *Ind. Eng. Chem. Res.*, vol. 41, no. 5, pp. 1321–1328, 2002.

[95] H. Takiyama, K. Shindo, and M. Matsuoka, "Effects of undersaturation on crystal size distribution in cooling type batch crystallization," *J. Chem. Eng. Japan*, vol. 35, no. 11, pp. 1072–1077, 2002.

[96] G. Yang, N. Kubota, Z. Sha, M. Louhi-Kultanen, and J. Wang, "Crystal shape control by manipulating supersaturation in batch cooling crystallization," *Cryst. Growth Des.*, vol. 6, no. 12, pp. 2799–2803, 2006.

[97] R. C. Snyder, S. Studener, and M. F. Doherty, "Manipulation of crystal shape by cycles of growth and dissolution," *AIChE J.*, vol. 53, no. 6, pp. 1510–1517, 2007.

[98] J. Wan, X. Z. Wang, and C. Y. Ma, "Particle shape manipulation and optimization in cooling crystallization involving multiple crystal morphological forms," *AIChE J.*, vol. 55, no. 8, pp. 2049–2061, 2009.

[99] N. Bajcinca, V. de Oliveira, C. Borchert, J. Raisch, and K. Sundmacher, "Optimal control solutions for crystal shape manipulation," *Comput. Aided Chem. Eng.*, vol. 28, pp. 751–756, 2010.

[100] Z. K. Nagy, M. Fujiwara, and R. D. Braatz, "Monitoring and advanced control of crystallization processes," in *Handbook of Industrial Crystallization*, 3rd ed., A. Myerson and D. Erdemir, Eds. Cambridge University Press, in press.

[101] M. A. Lovette, M. Muratore, and M. F. Doherty, "Crystal shape modification through cycles of dissolution and growth: Attainable regions and experimental validation," *AIChE J.*, vol. 58, no. 5, pp. 1465–1474, 2012.

[102] D. B. Patience and J. B. Rawlings, "Particle-shape monitoring and control in crystallization processes," *AIChE J.*, vol. 47, no. 9, pp. 2125–2130, 2001.

[103] K. Lee, J. H. Lee, M. Fujiwara, D. L. Ma, and R. D. Braatz, "Run-to-run control of multidimensional crystal size distribution in a batch crystallizer," *Proc. Am. Control Conf.*, vol. 2, pp. 1013–1018, 2002.

[104] F. Puel, G. Févotte, and J. P. Klein, "Simulation and analysis of industrial crystallization processes through multidimensional population balance equations. Part 1: A resolution algorithm based on the method of classes," *Chem. Eng. Sci.*, vol. 58, no. 16, pp. 3715–3727, 2003.

[105] H. Briesen, "Simulation of crystal size and shape by means of a reduced two-dimensional population balance model," *Chem. Eng. Sci.*, vol. 61, no. 1, pp. 104–112, 2006.

[106] C. Y. Ma, X. Z. Wang, and K. J. Roberts, "Multi-dimensional population balance modeling of the growth of rod-like L-glutamic acid crystals using growth rates estimated from in-process imaging," *Adv. Powder Technol.*, vol. 18, no. 6, pp. 707–723, 2007.

[107] C. Y. Ma and X. Z. Wang, "Crystal growth rate dispersion modeling using morphological population balance," *AIChE J.*, vol. 54, no. 9, pp. 2321–2334, 2008.

[108] C. Y. Ma, X. Z. Wang, and K. J. Roberts, "Morphological population balance for modeling crystal growth in face directions," *AIChE J.*, vol. 54, no. 1, pp. 209–222, 2008.

[109] J. J. Liu, C. Y. Ma, Y. D. Hu, and X. Z. Wang, "Effect of seed loading and cooling rate on crystal size and shape distributions in protein crystallization-A study using morphological population balance simulation," *Comput. Chem. Eng.*, vol. 34, no. 12, pp. 1945–1952, 2010.

[110] J. J. Liu, C. Y. Ma, Y. D. Hu, and X. Z. Wang, "Modelling protein crystallisation using morphological population balance models," *Chem. Eng. Res. Des.*, vol. 88, no. 4, pp. 437–446, 2010.

[111] J. De Calderon Anda, X. Z. Wang, X. Lai, K. J. Roberts, K. H. Jennings, M. J. Wilkinson, D. Watson, and D. Roberts, "Real-time product morphology monitoring in crystallization using imaging technique," *AIChE J.*, vol. 51, no. 5, pp. 1406–1414, 2005.

[112] J. Eggers, M. Kempkes, and M. Mazzotti, "Measurement of size and shape distributions of particles through image analysis," *Chem. Eng. Sci.*, vol. 63, no. 22, pp. 5513–5521, 2008.

[113] P. A. Larsen, J. B. Rawlings, and N. J. Ferrier, "An algorithm for analyzing noisy, in situ images of high-aspect-ratio crystals to monitor particle size distribution," *Chem. Eng. Sci.*, vol. 61, no. 16, pp. 5236–5248, 2006.

[114] F. Puel, P. Marchal, and J. Klein, "Habit transient analysis in industrial crystallization using two dimensional crystal sizing technique," *Chem. Eng. Res. Des.*, vol. 75, no. 2, pp. 193–205, 1997.

[115] X. Z. Wang, K. J. Roberts, and C. Ma, "Crystal growth measurement using 2D and 3D imaging and the perspectives for shape control," *Chem. Eng. Sci.*, vol. 63, no. 5, pp. 1173–1184, 2008.

[116] T. Togkalidou, H.-H. Tung, Y. Sun, A. Andrews, and R. D. Braatz, "Solution concentration prediction for pharmaceutical crystallization processes using robust chemometrics and ATR FTIR spectroscopy," *Org. Process Res. Dev.*, vol. 6, no. 3, pp. 317–322, 2002.

[117] D. L. Ma, D. K. Tafti, and R. D. Braatz, "Optimal control and simulation of multidimensional crystallization processes," *Comput. Chem. Eng.*, vol. 26, no. 7–8, pp. 1103–1116, 2002.

[118] S. Qamar, S. Noor, Q. U. Ain, and A. Seidel-Morgenstern, "Bivariate extension of the quadrature method of moments for batch crystallization models," *Ind. Eng. Chem. Res.*, vol. 49, no. 22, pp. 11633–11644, 2010.

[119] C. Sano, N. Nagashima, T. Kawakita, and Y. Iitaka, "Crystal and molecular structures of monosodium L-glutamate monohydrate," *Anal. Sci.*, vol. 5, no. 1, pp. 121–122, 1989.

[120] M. Shoji, T. Eto, and H. Takiyama, "A kinetic study of the influence of modulated undersaturation operation on crystal size distribution in cooling-type batch crystallization," *J. Chem. Eng. Japan*, vol. 44, no. 3, pp. 191–196, 2011.

[121] S. Qamar, S. Mukhtar, and A. Seidel-Morgenstern, "Efficient solution of a batch crystallization model with fines dissolution," *J. Cryst. Growth*, vol. 312, no. 20, pp. 2936–2945, Jan. 2010.

[122] Z. K. Nagy, E. Aamir, and C. D. Rielly, "Internal fines removal using population balance model based control of crystal size distribution under dissolution, growth and nucleation mechanisms," *Cryst. Growth Des.*, vol. 11, no. 6, pp. 2205–2219, 2011.

[123] J. V Beck and K. J. Arnold, *Parameter Estimation in Engineering and Science*. New York: Wiley, 1977.

[124] S. M. Miller and J. B. Rawlings, "Model identification and control strategies for batch cooling crystallizers," *AIChE J.*, vol. 40, no. 8, pp. 1312–1327, 1994.

[125] J. N. Sherwood and R. I. Ristic, "The influence of mechanical stress on the growth and dissolution of crystals," *Ind. Cryst.*, vol. 56, no. 7, pp. 2267–2280, 2001.

[126] L. M. Nagao, S. Lyapustina, M. K. Munos, and M. D. Capizzi, "Aspects of particle science and regulation in pharmaceutical inhalation drug products," *Cryst. Growth Des.*, vol. 5, no. 6, pp. 2261–2267, 2005.

[127] N. Rasenack, H. Steckel, B. W. Muller, and B. W. Müller, "Micronization of anti-inflammatory drugs for pulmonary delivery by a controlled crystallization process," *J. Pharm. Sci.*, vol. 92, no. 1, pp. 35–44, 2003.

[128] B. Y. Shekunov and P. York, "Crystallization processes in pharmaceutical technology and drug delivery design," *J. Cryst. Growth*, vol. 211, no. 1–4, pp. 122–136, 2000.

[129] M. Alleso, F. Tian, C. Cornett, and J. Rantanen, "Towards effective solid form screening," *J. Pharm. Sci.*, vol. 99, no. 9, pp. 3711–3718, 2010.

[130] D. J. am Ende and S. J. Brenek, "Strategies to control particle size during crystallization processes," *Am. Pharm. Rev.*, vol. 7, no. 3, pp. 98–104, 2004.

[131] M. Descamps, J. F. Willart, E. Dudognon, and V. Caron, "Transformation of pharmaceutical compounds upon milling and comilling: The role of Tg," *J. Pharm. Sci.*, vol. 96, no. 5, pp. 1398–1407, 2007.

[132] S.-Y. Lin, C.-H. Hsu, and W.-T. Ke, "Solid-state transformation of different gabapentin polymorphs upon milling and co-milling," *Int. J. Pharm.*, vol. 396, no. 1–2, pp. 83–90, 2010.

[133] J. Linol, T. Morelli, M. N. Petit, and G. Coquerel, "Inversion of the relative stability between two polymorphic forms of (±) modafinil under dry high-energy milling: Comparisons with results obtained under wet high-energy milling," *Cryst. Growth Des.*, vol. 7, no. 9, pp. 1608–1611, 2007.

[134] F. Tian, H. Qu, M. Louhi-Kultanen, and J. Rantanen, "Insight into crystallization mechanisms of polymorphic hydrate systems," *Chem. Eng. Technol.*, vol. 33, no. 5, pp. 833–838, 2010.

[135] E. Aamir, Z. K. Nagy, and C. D. Rielly, "Optimal seed recipe design for crystal size distribution control for batch cooling crystallisation processes," *Chem. Eng. Sci.*, vol. 65, no. 11, pp. 3602–3614, 2010.

[136] S. Rohani, S. Horne, and K. Murthy, "Control of product quality in batch crystallization of pharmaceuticals and fine chemicals. Part 2: External control," *Org. Process Res. Dev.*, vol. 9, no. 6, pp. 873–883, 2005.

[137] C. Wibowo, W. C. Chang, and K. M. Ng, "Design of integrated crystallization systems," *AIChE J.*, vol. 47, no. 11, pp. 2474–2492, 2001.

[138] J. D. Ward, D. A. Mellichamp, and M. F. Doherty, "Choosing an operating policy for seeded batch crystallization," *AIChE J.*, vol. 52, no. 6, pp. 2046–2054, 2006.

[139] N. C. S. Kee, P. D. Arendt, L. M. Goh, R. B. H. Tan, and R. D. Braatz, "Nucleation and growth kinetics estimation for L-phenylalanine hydrate and anhydrate crystallization," *CrystEngComm*, vol. 13, pp. 1197–1209, 2011.

[140] G. X. Zhou, M. Fujiwara, X. Y. Woo, E. Rusli, H.-H. Tung, C. Starbuck, O. Davidson, Z. Ge, and R. D. Braatz, "Direct design of pharmaceutical antisolvent crystallization through concentration control," *Cryst. Growth Des.*, vol. 6, no. 4, pp. 892–898, 2006.

[141] B. K. Johnson and R. K. Prud'homme, "Chemical Processing and Micromixing in Confined Impinging Jets," *AIChE J.*, vol. 49, no. 9, pp. 2264–2282, 2003.

[142] R. J. Farrell and Y.-C. Tsai, "Modeling, simulation and kinetic parameter estimation in batch crystallization processes," *AIChE J.*, vol. 40, no. 4, pp. 586–593, 1994.

[143] Y. Qiu and Å. Rasmuson, "Estimation of crystallization kinetics from batch cooling experiments," *AIChE J.*, vol. 40, no. 5, pp. 799–812, 1994.

[144] D. J. W. Grant, M. Mehdizadeh, A. H.-L. Chow, and J. E. Fairbrother, "Non-linear van't Hoff solubility-temperature plots and their pharmaceutical interpretation," *Int. J. Pharm.*, vol. 18, no. 1–2, pp. 25–38, 1984.

[145] H.-H. Tung, E. L. Paul, M. Midler, and J. A. McCauley, *Crystallization of Pharmaceuticals: An Industrial Perspective*. Hoboken, NJ: Wiley, 2009.

[146] Y. Wu, *Impinging Streams: Fundamentals, Properties, Applications*. New York: Elsevier, 2007.

[147] Y. Liu and R. O. Fox, "CFD Predictions for Chemical Processing in a Confined Impinging-Jets Reactor," *AIChE J.*, vol. 52, no. 2, pp. 731–744, 2006.

[148] D. L. Marchisio, L. Rivautella, and A. A. Barresi, "Design and scale-up of chemical reactors for nanoparticle precipitation," *AIChE J.*, vol. 52, no. 5, pp. 1877–1887, 2006.

[149] S. M. Hosseinalipour and A. S. Mujumdar, "Flow and thermal characteristics of steady two dimensional confined laminar opposing jets: Part I. Equal jets," *Int. Commun. Heat Mass Transf.*, vol. 24, no. 1, pp. 27–38, 1997.

[150] B. W. Webb and C. F. Ma, "Single-phase liquid jet impingement heat transfer," *Adv. Heat Transf.*, vol. 26, pp. 105–217, 1995.

[151] D. J. Phares, G. T. Smedley, and R. C. Flagan, "The inviscid impingement of a jet with arbitrary velocity profile," *Phys. Fluids*, vol. 12, no. 8, pp. 2046–2055, 2000.

[152] C. duP Donaldson and R. S. Snedeker, " Study of free jet impingement. Part 1. Mean properties of free and impinging jets," *J. Fluid Mech.*, vol. 45, pp. 281–319, 1971.

[153] W. M. Deen, *Analysis of Transport Phenomena*, 2nd ed. New York: Oxford University Press, 2012.

[154] J. M. Bergthorson, K. Sone, T. W. Mattner, P. E. Dimotakis, D. G. Goodwin, and D. I. Meiron, "Impinging laminar jets at moderate Reynolds numbers and separation distances," *Phys. Rev. E*, vol. 72, no. 6, p. 66307, 2005.

[155] J. H. Lienhard V., "Heat Transfer by Impingement of Circular Free-Surface Liquid Jets," in *18th National and 7th ISHMT-ASME Heat and Mass Transfer Conference*, IIT Guwahati, India, January 2006. Available online at http://web.mit.edu/lienhard/www/jets.pdf.

[156] S. Devahastin and A. S. Mujumdar, "A numerical study of flow and mixing characteristics of laminar confined impinging streams," *Chem. Eng. J.*, vol. 85, no. 2–3, pp. 215–223, 2002.

[157] D. A. Johnson, "Experimental and numerical examination of confined laminar opposed jets part I. Momentum imbalance," *Int. Commun. Heat Mass Transf.*, vol. 27, no. 4, pp. 443–454, 2000.

[158] A. J. Alvarez and A. S. Myerson, "Continuous plug flow crystallization of pharmaceutical compounds," *Cryst. Growth Des.*, vol. 10, no. 5, pp. 2219–2228, 2010.

[159] S. Lawton, G. Steele, P. Shering, L. Zhao, I. Laird, and X.-W. Ni, "Continuous crystallization of pharmaceuticals using a continuous oscillatory baffled crystallizer," *Org. Process Res. Dev.*, vol. 13, no. 6, pp. 1357–1363, 2009.

[160] R. Vacassy, J. Lemaître, H. Hofmann, and J. H. Gerlings, "Calcium carbonate precipitation using new segmented flow tubular reactor," *AIChE J.*, vol. 46, no. 6, pp. 1241–1252, 2000.

[161] J. Schiewe and B. Zierenberg, "Process and Apparatus for Producing Inhalable Medicaments," U.S. Patent 20030015194 A1, Jan 23, 2003.

[162] J. Lemaître, N. Jongen, R. Vacassy, and P. Bowen, "Production of Powders," U.S. Patent 6458335 B1, Oct 1, 2002.

[163] J. R. Méndez del Río and R. W. Rousseau, "Batch and tubular-batch crystallization of paracetamol: Crystal size distribution and polymorph formation," vol. 6, no. 6, pp. 1407–1414, 2006.

[164] R. J. P. Eder, S. Radl, E. Schmitt, S. Innerhofer, M. Maier, H. Gruber-Woelfler, and J. G. Khinast, "Continuously seeded, continuously operated tubular crystallizer for the production of active pharmaceutical ingredients," *Cryst. Growth Des.*, vol. 10, no. 5, pp. 2247–2257, 2010.

[165] S. Ferguson, G. Morris, H. Hao, M. Barrett, and B. Glennon, "In-situ monitoring and characterization of plug flow crystallizers," *18th Int. Symp. Ind. Cryst.*, vol. 77, pp. 105–111, 2012.

[166] S. Guillemet-Fritsch, M. Aoun-Habbache, J. Sarrias, A. Rousset, N. Jongen, M. Donnet, P. Bowen, and J. Lemaître, "High-quality nickel manganese oxalate powders synthesized in a new segmented flow tubular reactor," *Solid State Ionics*, vol. 171, no. 1–2, pp. 135–140, 2004.

[167] C. J. Gerdts, V. Tereshko, M. K. Yadav, I. Dementieva, F. Collart, A. Joachimiak, R. C. Stevens, P. Kuhn, A. Kossiakoff, and R. F. Ismagilov, "Time-controlled microfluidic

seeding in nl-volume droplets to separate nucleation and growth stages of protein crystallization," *Angew. Chemie - Int. Ed.*, vol. 45, no. 48, pp. 8156–8160, 2006.

[168] M. N. Kashid, I. Gerlach, S. Goetz, J. Franzke, J. F. Acker, F. Platte, D. W. Agar, and S. Turek, "Internal circulation within the liquid slugs of a liquid−liquid slug-flow capillary microreactor," *Ind Eng Chem Res*, vol. 44, no. 14, pp. 5003–5010, 2005.

[169] A. S. Myerson, *Handbook of Industrial Crystallization*, 2nd ed. Woburn, MA: Butterworth-Heinemann, 2002.

[170] T. Yonemoto, M. Kubo, T. Doi, and T. Tadaki, "Continuous synthesis of titanium dioxide fine particles using a slug flow ageing tube reactor," *Chem. Eng. Res. Des.*, vol. 75, no. 4, pp. 413–419, 1997.

[171] M. Kubo and T. Yonemoto, "Continuous synthesis of TiO2 fine particles and increase of particle size using a two-stage slug flow tubular reactor," *Chem. Eng. Res. Des.*, vol. 77, no. 4, pp. 335–341, 1999.

[172] A. E. Dukler, D. Moalem Maron, and N. Brauner, "A physical model for predicting the minimum stable slug length," *Chem. Eng. Sci.*, vol. 40, no. 8, pp. 1379–1385, 1985.

[173] K. A. Triplett, S. M. Ghiaasiaan, S. I. Abdel-Khalik, and D. L. Sadowski, "Gas–liquid two-phase flow in microchannels Part I: two-phase flow patterns," *Int. J. Multiph. Flow*, vol. 25, no. 3, pp. 377–394, 1999.

[174] C.-X. Zhao and A. P. J. Middelberg, "Two-phase microfluidic flows," *Microfluid. Eng.*, vol. 66, no. 7, pp. 1394–1411, 2011.

[175] M. Gopal and W. P. Jepson, "The study of dynamic slug flow characteristics using digital image analysis—Part I: Flow visualization," *J. Energy Resour. Technol.*, vol. 120, no. 2, pp. 97–101, 1998.

[176] A. Günther, M. Jhunjhunwala, M. Thalmann, M. A. Schmidt, and K. F. Jensen, "Micromixing of miscible liquids in segmented gas-liquid flow," *Langmuir*, vol. 21, no. 4, pp. 1547–1555, 2005.

[177] A. S. de Menezes, F. M. Ardito, A. O. dos Santos, A. J. D. Moreno, R. J. C. Lima, M. A. Hayashi, and L. P. Cardoso, "Characterization of the time-dependent L-asparagine monohydrate crystal phase transition," *J. Appl. Crystallogr.*, vol. 44, pp. 954–957, 2011.

[178] S. Kuhn, R. L. Hartman, M. Sultana, K. D. Nagy, S. Marre, and K. F. Jensen, "Teflon-coated silicon microreactors: Impact on segmented liquid-liquid multiphase flows," *Langmuir*, vol. 27, no. 10, pp. 6519–6527, 2011.

[179] A. J. Ghajar, "Non-boiling heat transfer in gas-liquid flow in pipes - A tutorial," *J. Brazilian Soc. Mech. Sci. Eng.*, vol. 27, no. 1, pp. 46–73, 2005.

[180] M. Morari and E. Zafiriou, *Robust process control*. Englewood Cliffs, N.J.: Prentice Hall, 1989.

[181] W. S. Levine, Ed., *The Control Handbook*. Boca Raton, Florida: CRC Press/IEEE Press, 1996.

[182] J. Baldyga and W. Orciuch, "Barium sulphate precipitation in a pipe - An experimental study and CFD modelling," *Chem. Eng. Sci.*, vol. 56, no. 7, pp. 2435–2444, 2001.

[183] K. Mahesh, "The interaction of jets with crossflow," *Annu. Rev. Fluid Mech.*, vol. 45, pp. 379–407, 2013.

[184] R. J. P. Eder, E. K. Schmitt, J. Grill, S. Radl, H. Gruber-Woelfler, and J. G. Khinast, "Seed loading effects on the mean crystal size of acetylsalicylic acid in a continuous-flow crystallization device," *Cryst. Res. Technol.*, vol. 46, no. 3, pp. 227–237, 2011.

[185] N. Jongen, M. Donnet, P. Bowen, J. Lemaître, H. Hofmann, R. Schenk, C. Hofmann, M. Aoun-Habbache, S. Guillemet-Fritsch, J. Sarrias, A. Rousset, M. Viviani, M. T. Buscaglia, V. Buscaglia, P. Nanni, A. Testino, and R. Herguijuela, "Development of a continuous segmented flow tubular reactor and the 'Scale-out' concept - In search of perfect powders," *Chem. Eng. Technol.*, vol. 26, no. 3, pp. 303–305, 2003.

[186] D. McCormick, "Evolutions in direct compression," *Pharm. Technol.*, vol. 29, no. 4, pp. 52–62, 2005.

[187] Z. Sun, N. Ya, R. C. Adams, and F. S. Fang, "Particle size specifications for solid oral dosage forms: A regulatory perspective," *Am. Pharm. Rev.*, vol. 13, no. 4, pp. 68–73, 2010.

[188] A. S. Myerson and B. L. Trout, "Nucleation from Solution," *Science*, vol. 341, no. 6148, pp. 855–856, 2013.

[189] A. J. Mahajan and D. J. Kirwan, "Micromixing effects in a two-impinging-jets precipitator," *AIChE J.*, vol. 42, no. 7, pp. 1801–1814, 1996.

[190] N. S. Deora, N. N. Misra, A. Deswal, H. N. Mishra, P. J. Cullen, and B. K. Tiwari, "Ultrasound for improved crystallisation in food processing," *Food Eng. Rev.*, vol. 5, no. 1, pp. 36–44, 2013.

[191] J. R. G. Sander, B. W. Zeiger, and K. S. Suslick, "Sonocrystallization and sonofragmentation," *Ultrason. Sonochem.*, vol. 21, no. 6, pp. 1908–1915, 2014.

[192] G. Ruecroft, D. Hipkiss, T. Ly, N. Maxted, and P. W. Cains, "Sonocrystallization: The use of ultrasound for improved industrial crystallization," *Org. Process Res. Dev.*, vol. 9, no. 6, pp. 923–932, 2005.

[193] D. Ensminger and L. J. Bond, “Applications of high- intensity ultrasonics: Basic mechanisms and effects,” in *Ultrasonics: Fundamentals, Technologies, and Applications*, 3rd ed., New York: CRC Press, 2011.

[194] E. Miyasaka, S. Ebihara, and I. Hirasawa, “Investigation of primary nucleation phenomena of acetylsalicylic acid crystals induced by ultrasonic irradiation-ultrasonic energy needed to activate primary nucleation,” *J. Cryst. Growth*, vol. 295, no. 1, pp. 97–101, 2006.

[195] S. Devarakonda, J. M. B. Evans, and A. S. Myerson, “Impact of ultrasonic energy on the crystallization of dextrose monohydrate,” *Cryst. Growth Des.*, vol. 3, no. 5, pp. 741–746, 2003.

[196] I. Nishida, “Precipitation of calcium carbonate by ultrasonic irradiation,” *Ultrason. Sonochem.*, vol. 11, no. 6, pp. 423–428, 2004.

[197] M. D. Luque de Castro and F. Priego-Capote, “Ultrasound-assisted crystallization (sonocrystallization),” *Ultrason. Sonochem.*, vol. 14, no. 6, pp. 717–724, 2007.

[198] H. M. Santos, C. Lodeiro, and J.-L. Capelo-Martínez, “The power of ultrasound,” in *Ultrasound in Chemistry: Analytical Applications*, J.-L. Capelo-Martínez, Ed. KGaA, Weinheim, Germany: Wiley, 2008.

[199] N. Amara, B. Ratsimba, A. M. Wilhelm, and H. Delmas, “Crystallization of potash alum: Effect of power ultrasound,” *Ultrason. Sonochem.*, vol. 8, no. 3, pp. 265–270, 2001.

[200] G. Bohm and G. Zech, *Introduction to Statistics and Data Analysis for Physicists*. Hamburg, Germany: Verlag Deutsches Elektronen-Synchrotron, 2010.

[201] S. K. Bermingham, *A Design Procedure and Predictive Models for Solution Crystallisation Processes*, Ph.D. thesis, Delft University of technology, The Netherlands, 2003.

[202] C. Sun and D. J. W. Grant, “Effects of initial particle size on the tableting properties of L-lysine monohydrochloride dihydrate powder,” *Int. J. Pharm.*, vol. 215, no. 1–2, pp. 221–228, 2001.